Distribution Agreement

In presenting this thesis or dissertation as a partial fulfillment of the requirements for an advanced degree from Emory University, I hereby grant to Emory University and its agents the non-exclusive license to archive, make accessible, and display my thesis or dissertation in whole or in part in all forms of media, now or hereafter known, including display on the world wide web. I understand that I may select some access restrictions as part of the online submission of this thesis or dissertation. I retain all ownership rights to the copyright of the thesis or dissertation. I also retain the right to use in future works (such as articles or books) all or part of this thesis or dissertation.

Signature:

_____ _____

James Scott Cordova Date

The Use of 5-Aminolevulinic Acid and Spectroscopic Magnetic Resonance Spectroscopy in the Management of Patients with Glioblastoma

By

James Scott Cordova
Doctor of Philosophy

Graduate Division of Biological and Biomedical Science
Molecular and Systems Pharmacology

_____

Hyunsuk Shim, Ph.D.
Advisor

_____ _____

Robert Gross, M.D., Ph.D.
Committee Member

Sumin Kang, Ph.D.
Committee Member

_____

Leonard Howell, Ph.D.
Committee Member

Accepted:

_____

Lisa Tedesco, Ph.D.
Dean of the James T. Laney School of Graduate Studies.

_____

Date

The Use of 5-Aminolevulinic Acid and Spectroscopic Magnetic Resonance Spectroscopy in the Management of Patients with Glioblastoma

By

James Scott Cordova
B.S., Chemistry, University of Central Arkansas

Advisor: Hyunsuk Shim, Ph.D.

An abstract of a dissertation submitted to the Faculty of the James T. Laney School of Graduate Studies of Emory University in partial fulfillment of the requirements for the degree of Doctor of Philosophy in Molecular and Systems Pharmacology in 2016

Abstract

The Use of 5-Aminolevulinic Acid and Spectroscopic Magnetic Resonance Spectroscopy in the Management of Patients with Glioblastoma

By James Scott Cordova

Gliomas are the most common primary of brain tumors in adults with Glioblastoma (GBM), a World Health Organization grade IV glioma, being the most common and aggressive. Although a strict combination of surgery, radiation therapy, and chemotherapy is standard for GBM, the disease invariably leads to death over months or years. This is in part due to the incredibly invasive nature of the tumor, a quality that prevents its complete surgical removal and shrouds the extent of its infiltration on conventional imaging. However, the exciting and fast growing field of molecular imaging is gaining popularity in glioma management and may offer substantial insight into this elusive disease. Optical and magnetic resonance molecular imaging techniques are allowing clinicians to probe the biological underpinnings of GBM on the molecular level and use this information to guide therapy and stratify patient populations for targeted therapy. For example, 5-aminolevulinic acid (5-ALA) is under investigation as an optical technique for identifying the infiltrative margins of GBMs intraoperatively while spectroscopic magnetic resonance imaging (sMRI) is allowing the metabolic profiling of GBM tissue regions non-invasively. It is with the application of these two techniques that this work is primarily concerned. Here, sophisticated image analysis and biostatistical techniques are developed and used to evaluate the impact of adding 5-ALA and sMRI to the clinical management of patients with GBM, from surgery to response determination. Specifically, the efficacy of 5-ALA fluorescence-guided surgery in tumor resection is evaluated in a cohort of GBM patients, *ex vivo* 5-ALA fluorescence and objective histology image analysis are used to validate sMRI's identification of tumor infiltration, and metabolic abnormalities are used to judge the feasibility of including sMRI into radiation therapy planning. In its parts, this work describes a number of incremental technical advances in applying molecular imaging techniques to GBM management. As a whole, this work represents a paradigm shift in the image-based management of patients with GBM away from conventional clinical imaging to more quantitative molecular imaging modalities that non-invasively describe a number of intrinsic and substantive biological phenomena.

The Use of 5-Aminolevulinic Acid and Spectroscopic Magnetic Resonance Spectroscopy in the Management of Patients with Glioblastoma

By

James Scott Cordova
B.S., Chemistry, University of Central Arkansas

Advisor: Hyunsuk Shim, Ph.D.

A dissertation submitted to the Faculty of the James T. Laney School of Graduate Studies of Emory University in partial fulfillment of the requirements for the degree of Doctor of Philosophy in Molecular and Systems Pharmacology in 2016

Acknowledgements

Graduate school would have been much more difficult, if not impossible, without the many people who surrounded and supported me. To them, I would like to dedicate this manuscript as it belongs to them as much as it belongs to me.

First, I would like to thank my advisor, Hyunsuk Shim, who gave me the freedom and courage to pursue such a rewarding project. Thank you for pushing me to do more than I thought I could and supporting me when I felt it impossible. Next, to my committee members Leonard Howell, Sumin Kang, and Robert Gross, your advice always cleared my vision and your encouragement allowed me to keep a confident attitude toward my goals. I would especially like to thank Drs. Kang and Gross for immediately taking up the open committee spots after previous members left the University.

To all the others at the BITC, CSI, and the Winship Cancer Institute with whom I during my training, thank you for your friendship and good times. Without you, I would have prematurely gone crazy in my mid- to late-twenties instead of during residency. This is especially true for those good friends with whom I would imbibe and discuss the failures and hardships of the day. I thank you for being there with me.

Finally, I would have never arrived here at Emory or completed this voyage without my family. Mom and Dad, thank you for giving me your good genes. I see and hear both of you every day and I am forever grateful to have both for your support and belief in me. Along with Mamaw, you two make up a group of the most influential individuals in my young life. This is a group to which I will always be indebted, and I will appreciate and love forever.

Table of Contents

Table of Contents xiii

Table of Figures xix

Chapter 1 xvii

Introduction 1

1.1 Gliomas 1

1.2 Glioblastoma 6

1.3 Presentation, Diagnosis, and Clinical Management of GBM 16

1.3.1 Presentation 16

1.3.2 Diagnosis 17

1.3.3 Therapy and Clinical Management 18

1.3.4 Response to Therapy 22

1.4 Imaging in GBM Management 23

1.4.1. Important Physical Concepts in MRI 24

1.4.2. Conventional Imaging Sequences 43

1.4.3 MRI in GBM Standard-of-Care Therapy 56

1.4.4 MRI in Glioma Response Assessment 63

1.5 Molecular Imaging in Glioma 67

1.5.1 Intraoperative Optical Imaging 69

1.5.2 Magnetic Resonance Spectroscopy 75

1.5.3 Spectroscopic Magnetic Resonance Imaging 78

1.5.4 Overview of Spectroscopic Data Processing 96

1.5.5 Spectroscopic Methods Used in this Work 104

1.5.6 MR Spectroscopy in Glioma Management 107

1.6 Organization of The Dissertation 114

1.7 References 117

Chapter 2 152

Quantitative tumor segmentation for the evaluation of extent of GBM resection 152

2.1 Author's Contribution and Acknowledgement of Reproduction 152

2.2 Abstract 153

2.3 Introduction 153

2.4 Methods 156

2.4.1 Preoperative and Postoperative Imaging 156

2.4.2 Image Analysis 157

2.4.3 Computer-Assisted, Manual Contouring 157

2.4.4 Semi-automated Segmentation Method 158

2.4.5 Statistical Methods 161

2.5 Results 162

2.5.1 Fuzzy3 Shows Greatest Volume Agreement with Manual Contouring 162

2.5.4 Fuzzy3 Algorithm Performs Well Per Diagnostic Performance Metrics 174

2.6 Discussion....174

2.7 References....181

Chapter 3 190

Semi-Automated Volumetric and Morphological Assessment of Glioblastoma Resection with Fluorescence-Guided Surgery.... 190

3.1 Author's Contribution and Acknowledgement of Reproduction 190

3.2 Abstract....191

3.3 Introduction....191

3.4 Materials and Methods.... 194

3.4.1 Patient Selection.... 194

3.4.2 Fluorescence-Guided Surgery 195

3.4.3 Image Acquisition and Analysis 195

3.4.4 Statistical Methods 198

3.5 Results.... 199

3.5.1 Study Accrual.... 199

3.5.2 Primary endpoints: EOR and RTV 199

3.5.3 Secondary Endpoint: PFS and OS 205

3.5.4 Adverse events (AEs) 208

3.6 Discussion 212

5.6.1 Limitations and Strengths 215

3.6.2 Conclusions 215

3.7 References 217

Chapter 4 225

Whole-Brain Spectroscopic MRI Biomarkers Identify Infiltrating Margins in Glioblastoma Patients 225

4.1 Author's Contribution and Acknowledgement of Reproduction 225

4.2 Abstract 226

4.3 Introduction 226

4.4 Materials and Methods 229

4.4.1 Study Design 229

4.4.2 Image Acquisition and Processing 230

4.4.4 SOX2 Immunohistochemistry 232

4.4.5 Automated Histology Slide Analysis 234

4.4.6 sMRI-SOX2 Analysis 234

4.4.7 Statistical Methods 236

4.5 Results 236

4.5.1 sMRI shows metabolic abnormalities beyond anatomical MRI 236

4.5.2 Integration of sMRI into neuronavigation system 241

4.5.3 Automated histology image analysis gives objective marker of tumor infiltration 241

4.5.4 sMRI markers exhibit significant correlations with SOX2 density 244

4.5.5 Ex vivo tissue fluorescence correlates with sMRI markers and SOX2 density 246

4.5.6 Cho/NAA identifies regions at high-risk for tumor recurrence..... 246

4.5.7 Cho/NAA ratio in T2-hyperintense regions correlates with PFS..... 249

4.6 Discussion 249

4.6.1 Study Strengths and Limitations 252

4.6.1 Conclusions 253

4.7 References 255

Chapter 5 260

Impact of Integrating Whole-Brain Spectroscopic MRI into Radiation Treatment Planning for Glioblastoma 260

5.1 Author's Contribution and Acknowledgement of Reproduction 260

5.2 Abstract 261

5.3 Introduction 262

5.4 Methods and Materials 263

5.4.1 Patients 263

5.4.2 sMRI data acquisition and registration 264

5.4.3 Target and sMRI volume definitions 265

5.4.4 Data Analysis, Re-planning, and Recurrence Evaluation 266

5.5 Results 267

5.5.1 Volumetric and Spatial Analysis 270

5.5.2 Replanning 274

5.5.3 Preliminary Recurrence analysis 278

5.6 Discussion 278

5.6.1 Study Strengths and Limitations 280

5.6.2 Conclusions 281

5.7 References 282

Chapter 6 286

General Discussion and Future Directions 286

6.1 General Discussion 286

6.2 Future Directions 293

6.2.1 sMRI for Lower Grade Glioma Targeting 293

6.2.2 Automated Spectral Quality Analysis 296

6.2.3 RT Target Volume Segmentation and Automatic Metabolic Profiling 299

6.4 References 302

Chapter 7 307

Some Final Thoughts 307

Table of Figures

Table 1.1. WHO 2007 classification of diffuse gliomas. 4

Figure 1.1. Schematic showing the classification of diffuse gliomas of astrocytic and oligodendroglial lineages based on the WHO guidelines. 5

Figure 1.2. The prevalence and OS of the TCGA molecular subtypes in GBM. 9

Figure 1.3. Hypothesized pathways of gliomagenesis based on TCGA data leading to the formation of subtypes of GBM: mesenchymal, classical, proneural and GBM-O. 11

Figure 1.4. Three molecular subgroups of patients can be defined on the basis of IDH1 mutation and 1p/19q co-deletion status exhibit differing progression-free and OS 13

Figure 1.5. Kaplan–Meier Estimates of OS, According to MGMT Promoter Methylation Status. 15

Figure 1.6. Treatment algorithm for GBM. 20

Figure 1.7. Schematic representation of a single proton nuclear spin and precession. 27

Figure 1.8. Vector representation of proton magnetization in the rotating reference frame. 29

Figure 1.9. Longitudinal magnetization recovery and transverse magnetization decay in two separate tissue types. 32

Figure 1.10. Diagram showing loss of Mxy component of magnetization. 34

Figure 1.11. Spin-echo pulse sequence depicting both TE and TR. 36

Figure 1.12. Signal weighting based on TE and TR. 38

Figure 1.13. Common water relaxation-based imaging techniques. 41

Figure 1.14. Mechanics of inversion recovery resulting in T2W/FLAIR images. . 47

Figure 1.15. Impact of cellularity on water diffusion and DWI/ADC intensity.... 50

Figure 1.16. Examples of a concentration-time curve and AIF for a DSC perfusion experiment. 52

Figure 1.17. A basic two-compartment model of K_{trans}. 55

Figure 1.18. Neuronavigation using frameless system with instrument fiducials. 59

Figure 1.19. Heme biosynthetic pathway leading to the accumulation of PpIX. ...71

Figure 1.20. Characteristic spectra from MRS. 77

Table 1.2. Metabolites observed with proton MRS with chemical shifts, T2 length, and role within tissue. 80

Figure 1.21. Representative spectra of long (left) and short (right) TE pulse sequences..... 82

Figure 1.22. CHESS saturation sequence and its impact on different spins..... 84

Figure 1.23. Chemical structures of small molecules commonly evaluated using in vivo MRS. 86

Figure 1.24. Single voxel localization techniques. 92

Figure 1.25. Array of spectra acquired using a 2D-MRSI sequence of a suspicious brain lesion. 94

Figure 1.26. Basic pulse sequences for SVS, 2D-MRSI, and 3D-MRSI. 95

Figure 1.27. Flow chart for processing of MR signals for spectroscopic applications. 97

Figure 1.28. The impact of phase and baseline correction on spectral quality. 99

Figure 1.29. Fitting of raw frequency domain data 101

Figure 1.30. Results of MRSI spatial mapping procedure..... 103

Figure 1.31. Complete MIDAS MRI and MRSI processing protocol. 106

Figure 2.1. Segmentation procedure for preoperative and postoperative images.....159

Table 2.1. Preoperative contrast-enhancing tumor volumes (cm3) generated using manual, Otsu, and Fuzzy methods..... 164

Table 2.2. Postoperative tumor volumes generated using manual, Otsu, and Fuzzy methods. 165

Figure 2.2. Preoperative and postoperative manual tumor contour volume vs. semi-automated segmentation (Otsu 4, Fuzzy 4, or Fuzzy3 from top to bottom) by two separate readers. 166

Table 2.3. Mean CCCs with SEM and 95% confidence intervals for preoperative tumor volumes generated using automated methods versus manual contouring by two separate readers 167

Table 2.4. Mean CCCs with SEM and 95% confidence intervals for postoperative tumor volumes generated using automated methods versus manual contouring by two separate readers 168

Figure 2.3. Pre- and postoperative Dice and MED..... 171

Figure 2.4. Inter-rater reliability analysis. 173

Figure 3.1. Example of semi-automated tumor segmentation results used for volumetric and morphological analysis. 197

Table 3.1. Patient and tumor characteristics for 5-ALA FGS trial..... 201

Table 3.2. Univariate analyses of EOR and RTV outcomes. 202

Table 3.3. Final multivariate, general linear model describing RTV. 204

Table 3.4. Univariate Cox proportional hazard regression analysis for PFS and OS. 206

Table 3.5. Final multivariate Cox proportional hazard regression models of PFS and OS. 207

Table 3.6. Adverse events recorded during trial. 209

Table 3.7. Patients with hepatobiliary laboratory disturbances at 48 h and 6 weeks post-surgery 211

Figure 4.1. Procedure for tissue sampling and histological analysis using sMRI and 5-ALA FGS. 233

Figure 4.2. Metabolite signal normalization scheme used for sMRI analyses. 235

Figure 4.3 238

Figure 4.4. Representative sMRI spectra from normal and tumor tissue. 239

Table 4.1. Fold-change of each metabolite in different tumor regions on CE-T1w MRI for all preoperative patients 240

Figure 4.5. A normalized metric of tumor infiltration, SOX2 density, identifies tumor outside of conventional imaging. 243

Table 4.2. Pearson's correlation coefficients for all sMRI metabolites and SOX2 density. 245

Figure 4.6. Abnormalities in Cho/NAA describe regions at high risk for recurrence before RT in GBM. 248

Figure 4.7. Peritumoral Cho/NAA abnormalities are associated with PFS. 250

Table 5.1. sMRI-RT patient characteristics. 268

Figure 5.1. Image processing and analysis pipeline. 269

Table 5.2. Volumetric and spatial data 271

Figure 5.2. Co-registered CE-T1w MRI and Cho/NAA images of 40-year-old male with occipital GBM who received RT. 272

Figure 5.3. Co-registered CE-T1w MRI and Cho/NAA images of 56-year-old female with frontal GBM who received chemoradiation. 273

Table 5.3. Autosegmented sMRI contour extending outside of prescription isodoses. 275

Figure 5.3. Boxplots reflecting the percentage of the sMRI structure volume extending outside of the RT prescription isodoses 276

Table 5.4. Comparison of Target Coverage and Brainstem Doses. 277

Figure 6.1. Spectroscopic MRI in LGG. 294

Figure 6.2. Example of sMRI artifact. 297

Figure 6.3. Automatic metabolic ROI segmentation for RT target volume planning. 301

List of Abbreviations

Central Nervous System, CNS

Peripheral Nervous System, PNS

Central Brain Tumor Registry of US, CBTRUS

World Health Organization, WHO

Glioblastoma, GBM

Tumor protein 53, TP53

Phosphatase & tensin homolog, PTEN

Neurofibromin 1, NF1

Epidermal growth factor receptor, EGFR

Phosphoinositide-3-Kinase Reg α, PIK3R1

Phosphoinositide-3-Kinase Catalytic α, PIK3CA

High-grade glioma, HGG

The Cancer Genome Atlas, TCGA

Isocitrate dehydrogenase 1 & 2, IDH1 & 2

O6-methyl-guanine-DNA methyltransferase, MGMT

Wild-type, wt

GBM with oligodendroglial component, GBM-O

α-thalassemia/retardation X-Link, ATRX

capicua transcription repressor, CIC

Temozolomide, TMZ

Intracranial pressure, ICP

Computed tomography, CT

Magnetic resonance imaging, MRI

Contrast-enhanced MRI, CE-MRI

Radiation therapy, RT

Karnofsky performance scale, KPS

Progression-free survival, PFS

Overall survival, OS

Extent-of-resection, EOR

Gross total resection, GTR

Radiation Therapy Oncology Group, RTOG

Spin quantum number, $\overrightarrow{S_z}$

Magnetic moment vector, $\vec{\mu}$

Static magnetic field vector, $\overrightarrow{B_0}$

Larmor frequency, ω

Gyromagnetic constant, γ

Radiofrequency pulse, RF

Magnetization vector, $\vec{M}$

Electromotive force, EMF or ε

Electric flux, Φ

Spin-lattice relaxation time constant, T_1

Spin-spin relaxation time constant, T_2

Proton density, rho or $\boldsymbol{\rho}$

Repetition time, TR

Echo time, TE

Signal spin-echo sequence, $\boldsymbol{S_{SE}}$

Gadolinium-based contrast agents, GBCA

Intravenous, IV

Spectroscopic MRI, sMRI

Electronic environment constant, $\boldsymbol{\sigma}$

Fluid Attenuated Inversion Recovery, FLAIR

Diffusion-weighted image, DWI.

Contrast-enhanced T1-weighted, CE-T1w

Blood-brain barrier, BBB

T2w, T2-weighted

Cerebrospinal fluid, CSF

Inversion time, TI

Signal attenuation, SI

Apparent diffusion coefficient, ADC

Perfusion-weighted imaging, PWI

Dynamic susceptibility contrast-enhanced, DSC

Dynamic contrast-enhanced, DCE

GBCA concentration, [GABC]

T2-relaxation rate, $\Delta R2$

Cerebral blood volume, CBV

Cerebral blood flow, CBF

Arterial input function, AIF

Fourier transform, $\boldsymbol{FT}$

Extravascular, extracellular space, ECC

Intracellular space, IC

Gross tumor volume, GTV

Clinical target volume, CTV

Planning target volume, PTV

Region-of-interest, ROI

Response assessment in Neuro-oncology, RANO

Pseudoprogression, PsP

Histone deacetylase inhibitor, HDACi

Bevacizumab, BEV

Histone deacetylase, HDAC

US Food and Drug Administration, FDA

Pseudoresponse, PsR

Positron emission tomography, PET

Single photon emission CT, SPECT

MR spectroscopy, MRS

Intraoperative optical imaging, IOI

protoporphyrin IX, PpIX

Low-grade glioma, LGG

Fluorescence-guided surgery, FGS

Parts per million, ppm

Nuclear magnetic resonance, NMR

Myo-inositol, MI

Choline, Cho

Total choline, tCho

Creatine, CR

Glutamine, Gln

Glutamate, Glu

N-acetylaspartate, NAA

Lactate, Lac

Free lipids, Lip

Glutamine/Glutamate, Glx

Signal-to-noise ratio, SNR

Chemical shift selective suppression, CHESS

Outer volume suppression, OVA

Single voxel spectroscopy, SVS

MR Spectroscopic imaging, MRSI

Chemical shift imaging, CSI

Point-resolved spectroscopy, PRESS

Stimulated echo acquisition mode, STEAM

Mixing time, TM

Metabolite Imaging and Data Analysis System, MIDAS

Area under the curve, AUC

Cramer-Rao lower bound, CRLB

Selective short TI inversion recovery, STIR

Normal appearing white matter, NAWM

Magnetization-Prepared Rapid-Acquisition Gradient Echo, MPRAGE

Digital Imaging and Communications in Medicine, DICOM

Otsu multilevel thresholding, Otsu

Fuzzy C-means clustering, Fuzzy

Concordance correlation coefficient, CCC

Dice similarity index, Dice

Mean Euclidean Distance, MED

Standard error of the mean, SEM

Confidence Interval, C.I.

Residual Tumor Volume, RTV

Surface area, SA

5-Aminolevulinic acid, 5-ALA

Complete resection of contrast-enhancing tumor, CRET

Percent necrosis volume, NV%

Surface area-to-volume ratio, SAVR

Interquartile range, IQR

Hazard rate ratio, HR

Adverse event, AE

Hematoxylin, HXN

Standard deviation, SD

After radiation therapy, postRT

Positive predictive value, PPV

Receiver-operator characteristic, ROC

Sex Determining Region Y-Box 2, SOX2

Standardized metabolite abnormality, AI_{metab}

Before radiation therapy, preRT

Echo planar spectroscopic imaging, EPSI

Negative predictive value, NPV

Organ at risk, OAR

Chapter 1

Introduction

1.1 Gliomas

Gliomas are the most common type of primary intracranial neoplasm diagnosed in adults, accounting for approximately 50% of all newly diagnosed brain tumors (1). These highly infiltrative tumors originate from cells of glial (from *glia*, Greek for "glue") origin, normal, non-neuronal support cells that are differentiated from the neural tube and crest of the primordial ectoderm during embryogenesis (1; 2). These "neuroglia" function as caretakers of the central and peripheral nervous systems (CNS and PNS) maintaining homeostasis, forming myelin, and providing support and protection to neurons, the electrical workhorses of the nervous system (3). For example, astrocytes provide physical structure, metabolic support, and osmolality regulation within the brain while

oligodendrocytes generate the myelin sheaths responsible for speeding signal propagation along the neuronal axon (3). In gliomas, however, these cells divide uncontrollably, passing through cell signaling pathways unchecked, resulting in destructive and infiltrative lesions that disrupt the functioning of neuronal tissue, ultimately resulting in neurological symptoms.

Though glioma tumorigenesis is not completely understood, the characteristics of patients diagnosed with them and the course of their disease have been well studied. A report recently published by The Central Brain Tumor Registry of the United States (CBTRUS) found that from 2008 to 2012, the risk of diagnosis with glioma (per 100,000 people) was higher in adults than children (6.62 vs 3.70), higher in men than in women (7.79 vs 5.60), and higher in non-Hispanic whites (7.4) than African-Americans (3.98), Asian/Pacific Islanders (4.12), and American Indians/Alaska Natives (3.48) (4). More striking, however, is the mortality observed for gliomas. The 1, 2, and 5-year survival rates (per 100,000 people) for patients with glioma are 58.1%, 44.1%, and 34.4%, respectively. As the survival statistics suggest, these tumors are by and large incurable, and patients generally succumb to significant neurological morbidity (including seizures, headaches, memory loss, and visual disturbances) during the disease course before ultimately dying from brain herniation or disturbed autonomic functioning due to brainstem invasion (5).

Gliomas are classified using three main criteria: the region of the CNS the tumor is located, cell type of which the tumor is composed, and the histological grade of the tumor in tissue specimens. The location of a tumor is usually described relative to the tentorium, an extension of the dura mater that separates

the cerebellum from the cerebrum. “Supratentorial” gliomas are those that fall above the tentorium (i.e. within the cerebrum), “infratentorial” gliomas fall below the tentorium (i.e. in the cerebellum), and “pontine” gliomas fall within the pons of the brainstem.

The predominant cell type and grade of a glioma is evaluated histologically. Not only is histological evaluation the gold standard for brain tumor diagnosis, classifications based on histological features are used to stratify gliomas into different groups based on treatment responsiveness and prognosis. Cell type generally describes the composition of the glioma (e.g. astrocytes, oligodendrocytes, ependymocytes, etc.) while the grade describes the degree of structural abnormality present within each tissue section in terms of the World Health Organization (WHO) grading criteria (i.e. cellularity, mitotic activity, pleomorphism, necrosis, and endothelial proliferation) (1; 6). “Anaplasia” is often used to describe tissue that has little native tissue structure, high cellularity, an abundance of pleomorphic structures, and many mitotic figures. Examples of classifications with histologic descriptions can be found in **Table 1.1** and **Figure 1.1**.

Type	Grade	Description
Astrocytoma	II	Found diffusely infiltrating into surrounding neural tissue; increased hypercellularity, no mitosis
Oligodendroglioma	II	Occur in the white matter and cortex of the cerebral hemispheres, low mitotic activity, no necrosis
Oligoastrocytoma	II	Diffuse mixed tumor with mixed glial background
Anaplastic Astrocytoma /Oligodendroglioma	III	Highly infiltrating tumor with increased mitotic activity; no necrosis or vascular proliferation
Glioblastoma	IV	Infiltrating glial neoplasm with necrosis and micro-vascular proliferation; high rate of mitosis

Table 1.1. WHO 2007 classification of diffuse gliomas.

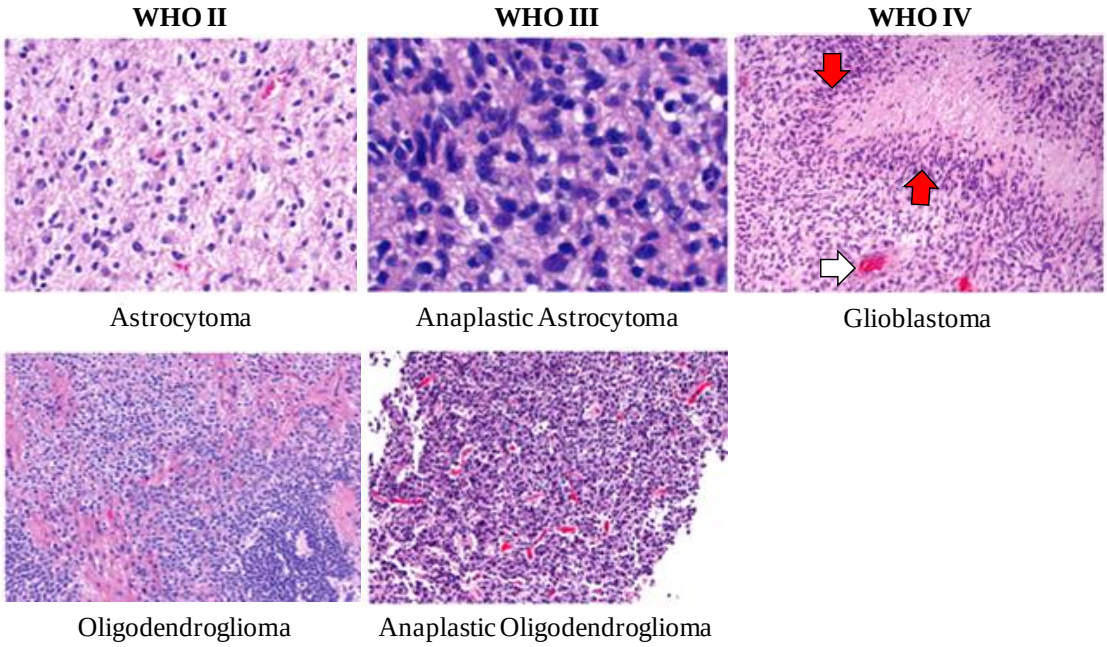

Figure 1.1. Schematic showing the classification of diffuse gliomas of astrocytic and oligodendroglial lineages based on the WHO guidelines. Representative micrographs for each tumor class are given. The hallmark histological features of glioblastoma, microvascular proliferation (white arrow), and pseudo palisading necrosis (red arrows) are indicated. Adapted by permission from Macmillan Publishers Ltd: Nature Reviews Cancer 2010 May;10(5):319-31. DOI: 10.1038/nrc2818., copyright 2010 *(7)*.

1.2 Glioblastoma

Of the gliomas, glioblastoma (GBM) is the highest grade, the most aggressive, and the most treatment resistant. Approximately 12,000 new cases are diagnosed each year in the U.S., making it not only the most common glioma in adults (55.1%), but also the most common primary malignant brain tumor in adults (15%) (4; 8). The incidence of GBM is 3.19 per 100,000 people, and the 1, 2, and 5-year survival rates for patients with GBM are well below those of all gliomas (37.2%, 15.2%, and 5.1%, respectively). As with the other gliomas, the incidence of GBM diagnosis increases with age (rates highest between ages 75 and 84) and the disease has a predilection for both males and white, non-Hispanic individuals (4). Though incremental progress has been made in the management of GBM over the last decade, unfortunately outcomes remain poor with local recurrence rates approaching 70% at 6-months post therapy and a median overall survival (OS) of only 14.6 months (9-11).

Per the WHO grading criteria, GBMs are infiltrating astrocytomas or oligodendrogliomas that exhibit the elevated mitotic activity of anaplastic lesions with the addition of vascular proliferation and tumor necrosis (6). Usually, GBMs are highly cellular tumors with marked nuclear atypia and “pseudo-palisading” necrosis characterized by the accumulation of tumor cells around zones of necrosis (**Figure 1.1**). Oftentimes thrombi are noted within vessels inside and adjacent to the tumor; these thrombi may also be associated with necrotic foci (6). In most cases, the tumor neovasculature is extensive and surrounding stroma is packed with reactive astrocytes, glioma stem cells, and tumor-associated endothelia (12;

13). The heterogeneous histology and refractory nature of these tumors make the management of GBM quite complex.

Although the classification of GBM with histopathology is straightforward, the genetic variation in GBM is abundant, and a number of molecular abnormalities stratify these tumors into clinically distinct subtypes. Though hundreds of genetic mutations are found within a single GBM, the most commonly mutated genes found in patients include TP53 (42%), PTEN (33%), NF1 (21%), EGFR (21%), PIK3R1 (10%), and PIK3CA (7%) (1). These mutations provide selective growth advantages that promote survival and proliferation in a hostile and hypoxic environment (14). Although some are closely associated with other high-grade gliomas (HGGs), each genetic alteration is regularly identified in patients with GBM. The variety of abnormalities seen within even a single tumor affirms the need for individualized treatment, and gives a starting point for rationally-designed pharmaceuticals and the identification of multigene predictors.

The recent trend towards genomic profiling has led to the exploration of classifying lesions into molecular groups based on genotype. Classification of high-throughput microarray data from The Cancer Genome Atlas (TCGA) has allowed the identification of both prognostic markers and molecular subgroups within histologically-defined GBM (15-17). Gene classification resulted in the identification of four distinct molecular subtypes (i.e. classical, mesenchymal, proneural, and neural) within GBM that exhibited differing age at diagnosis, response to therapy, and OS (**Figure 1.2**) (15; 18). Though this classification may allow for the identification of new targets with the additional benefit of predictive

markers for targeted therapies, the clinical utility of multigene molecular subtyping is still limited. Currently, the most important biomarkers to clinical outcome are Isocitrate dehydrogenase 1 and 2 (IDH1 and IDH2) mutations, co-deletion of the 1p and 19q chromosome arms (1p19q co-deletion), and O6-methyl-guanine-DNA methyltransferase MGMT promoter methylation status.

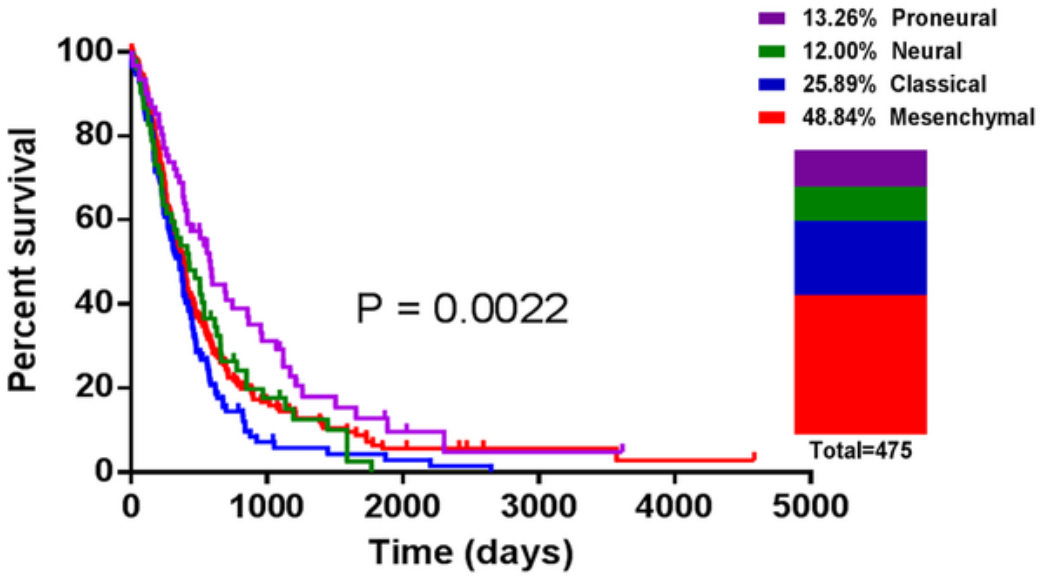

Figure 1.2. The prevalence and OS of the TCGA molecular subtypes in GBM. Reproduced from *Lin N, et al. (2014) PLoS ONE 9(4): e94871. DOI:10.1371/journal.pone.0094871* under the Creative Commons Attribution (CC BY) license (7).

The classification of gliomas in adults was transformed with the discovery and characterization of IDH mutations. In the mitochondria of wild-type (*wt*) cells, IDH catalyzes the oxidative decarboxylation of isocitrate to α-ketoglutarate in the tricyclic acid cycle. In mutant (*mt*) cells, IDH converts this substrate to 2-hydroxyglutarate, a metabolite hypothesized to alter DNA methylation, telomere length, and gene expression (19-21). Molecular profiling of these mutations, the most common of which is an arginine to histidine mutation at position 132, has given rise to not only a genetically distinct neoplasm, but also a cohort of tumors that behave quite differently clinically (22; 23). Gliomagenesis research has found that IDH mutations take part in the initial glial-tumor cell transformation with proposed models suggesting that IDH mutation occurs early in this process followed by further changes along stereotypic cytogenetic pathways corresponding to "oligodendroglial" or "astrocytic" differentiation (**Figure 1.3**) (24; 25). These tumors tend to take a more indolent, stepwise course to becoming GBM (e.g. secondary GBM/proneural and GBM with components of oligodendroglioma) and, consequently, exhibit longer OS. Conversely, IDH*wt* tumors appear to result from *de novo* mutations, are generally associated with EGFR and PTEN abnormalities, are more aggressive, exhibit mesenchymal and classical genetic signatures, and poorer survival outcomes. Of note, the populations studied throughout this work are generally primary GBMs that are IDHwt.

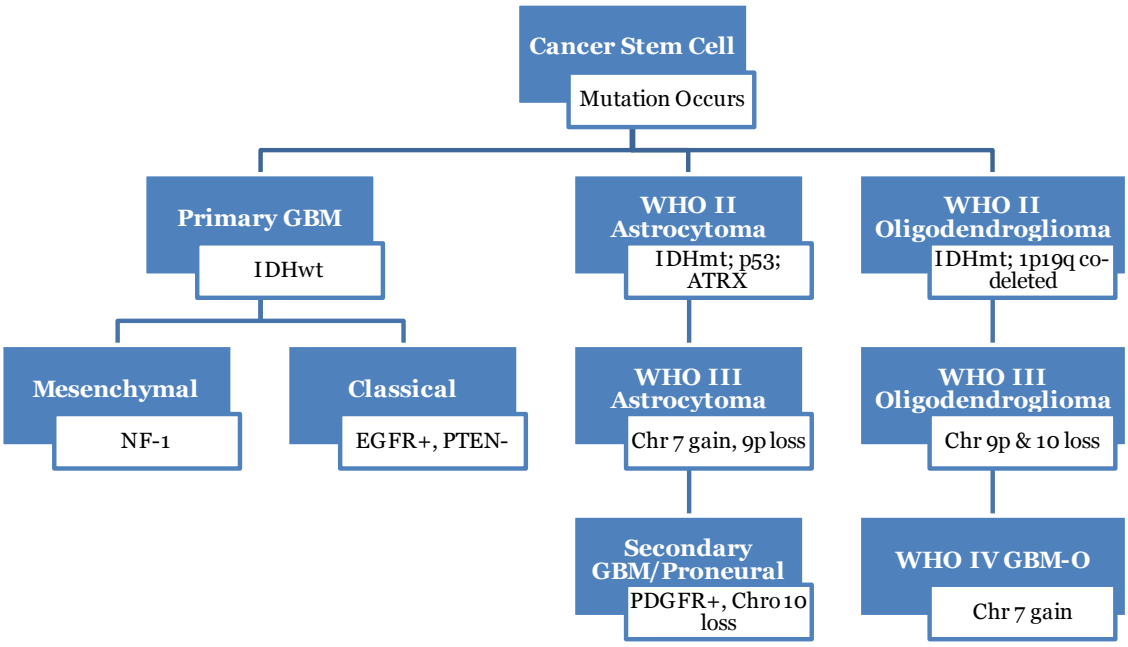

Figure 1.3. Hypothesized pathways of gliomagenesis based on TCGA data leading to the formation of subtypes of GBM: mesenchymal, classical, proneural and GBM-O. GBM, glioblastomas; IDH, isocitrate dehydrogenase; TCGA, The Cancer Genome Atlas, GBM-O, GBM with oligodendroglioma component, *mt*, mutant.

Co-deletion of 1p/19q is found in 70%-90% of oligodendrogliomas, and has recently been named an objective molecular marker for oligodendroglial lineage (26; 27). Furthermore, 1p/19q co-deletion is almost always found in the absence of ATRX and P53 abnormalities, markers associated almost exclusively with the astrocytic lineage (28; 29). In fact, a link between 1p/19q co-deletion and IDH mutations was recently hypothesized through the capicua transcription repressor (CIC), a single retained allele on 19q. This connection may in part explain the preponderance of IDH mutant, 1p/19q co-deleted tissues with oligodendroglial features (30). Clinically, oligodendrogliomas with a 1p/19q co-deletion behave in an indolent fashion and tend to respond well to chemotherapy and radiation therapy (RT), even more so than their IDH mutant, astrocytic counterparts (27; 31). As such, 1p/19q co-deletion is associated with the improved prognosis and longer OS in HGG (32). Of note, the populations studied throughout this work are generally primary GBMs which have 1p/19q intact.

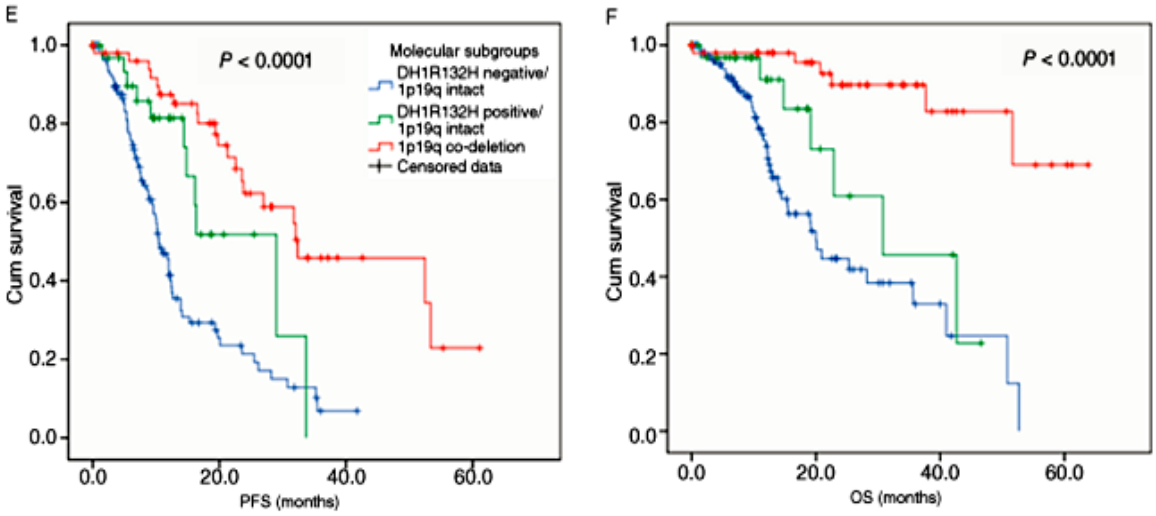

Figure 1.4. Three molecular subgroups of patients can be defined on the basis of IDH1 mutation and 1p/19q co-deletion status exhibit differing progression-free and OS (**E** and **F**). 1p/19q co-deleted cases are IDH mutant as well. Adapted with permission from John Wiley and Sons, Inc. from *Figarella-Branger, D., et al. (2015) Brain Pathology 25(4): DOI 10.1111/bpa.12227 (31).*

MGMT is a DNA repair enzyme located in 10q26 that is responsible for removing alkyl adducts at the O^6 position of guanine (33). This is significant in glioma management as the most commonly used chemotherapeutic, temozolomide (TMZ), is a potent alkylator at the O^6 position of guanine (34). Thus, those glioma cells that lack MGMT (via gene silencing, knock-out, or loss of function) cannot repair TMZ-induced DNA damage and are more sensitive to therapy than their wild-type counterparts. As such, numerous trials have shown that MGMT silencing through gene promoter hypermethylation portends improved survival in GBM patients due to TMZ sensitivity (**Figure 1.5**) (34-37). Per the seminal study from which the below **Figure 1.5** was taken, patients with MGMT promoter methylation experienced a 55% reduction in risk of death compared to their counterparts in the unmethylated cohort (34).

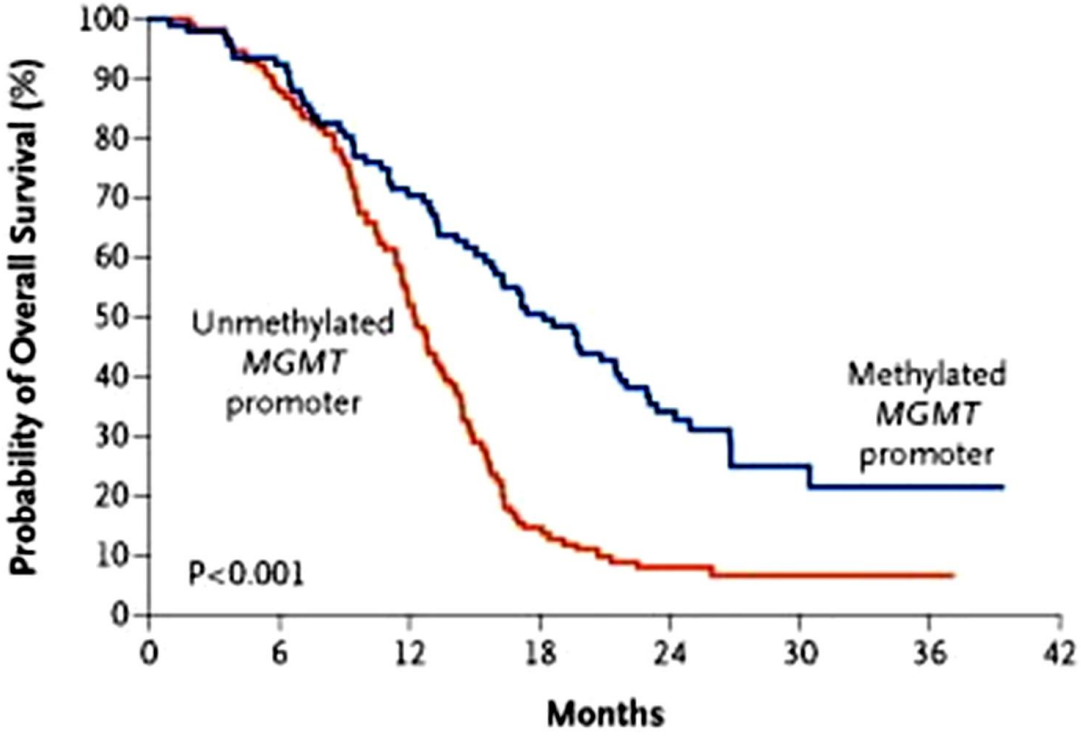

Figure 1.5. Kaplan–Meier Estimates of OS, According to MGMT Promoter Methylation Status. The difference in survival between patients with a methylated MGMT promoter and those with an unmethylated MGMT promoter was highly significant (P<0.001 by the log-rank test), indicating that the MGMT methylation status has prognostic value. Reproduced with permission from *Hegi, M.E., et al. (2005) NEJM 352 (10), DOI: 10.1056/NEJMoa043331* Copyright Massachusetts Medical Society *(34)*.

1.3 Presentation, Diagnosis, and Clinical Management of GBM

1.3.1 Presentation

Regardless of the molecular characteristics of the tumor, patients with GBM generally present with symptoms canonical for brain tumors: headache, seizure, and neurological deficits. The type and severity of symptoms is largely dependent on the location of the tumor and the rate at which it grows, however. Headaches in GBM can be caused by the increased intracranial pressure (ICP), dural irritation, intratumoral hemorrhage, or obstructive hydrocephalus, and are the most common complaint of patients with GBM (1; 12). They have also been reported to be more severe upon waking in the morning or even cause a patient to wake from sleep as the vasodilation common to sleep couples with tumor mass effect to substantially increase ICP. Unlike headaches, seizures and focal neurological deficits are less common and are highly dependent on the location of the tumor. For example, a large tumor in a noneloquent area, like the frontal lobe for example, may be asymptomatic until it reaches critical structures, while a small tumor in an eloquent area, like Broca's area, may cause pronounced symptomatology early on. The onset of focal deficits is initially subtle and progresses over time, paralleling the gradual growth of the lesion into eloquent regions.

The above symptoms are usually present with the normal associated finding on physical exam. Headache due to increased ICP can be confirmed through fundoscopy by the finding of papilledema (edema of the head of the optic nerve associated with engorgement of the retinal veins) (1; 12). Continuing with the previous small tumor example, a lesion of in the lateral aspect of the frontal lobe in the dominant hemisphere may result in expressive aphasia (i.e. the inability to

generate spoken or written language) due to infiltration of Broca's area or weakness in the muscles used to generate speech in the primary motor cortex. Cranial nerve palsies, most concerningly oculomotor palsy, are signs of more severe intracranial processes like uncal herniation or brainstem infiltration that may require immediate surgical correction.

1.3.2 Diagnosis

Radiographic imaging is generally the first step performed to evaluate patients with suspected brain tumors as it provides information regarding location, tumor type, and the impact of the lesion on surrounding structures. Because computed tomography (CT) is quick, effective, and affordable, it is generally the imaging modality of choice for screening patients with the above symptoms. With CT one can generally differentiate space occupying lesions like tumors from other pathologies with similar symptoms (e.g. ischemic stroke or intraparenchymal hemorrhage) and evaluate the extent to which the tumor has invaded bony structures. Contrast-enhanced magnetic resonance imaging (CE-MRI) is the diagnostic standard, however, because of its superior sensitivity, its soft-tissue contrast, and its versatility in terms of available imaging sequences (12; 38). GBMs are generally inhomogeneous, space occupying masses with irregularly enhancing rims that encompass a hypointense, necrotic core. Vasogenic edema surrounding this mass is normal, and due of mass effect, it is not uncommon for these tumors to impinge upon the ventricles, sometimes occluding a portion of it entirely. Through various image texture analyses, CE-MRI can give vital information on the cellularity, vascularity, and invasion of the tumor into normal

tissue as well. Anecdotally, these imaging findings on structural MRI are so distinct that a trained physician can predict the diagnosis of GBM before biopsy with reasonable accuracy.

The gold standard for brain tumor diagnosis is histology, however, and tissue sampling is required to definitively diagnose GBM. Non-cancerous lesions including infection, demyelinating disease, and vascular malformations can sometimes present much like a tumor on imaging, and in such cases biopsy not only confirms the diagnosis but also prevents unnecessary treatment. Tissue samples are generally acquired through stereotactic needle biopsy or craniotomy. As glial tumors are graded according to the most malignant portion of the tumor, it is essential that the specimen comes from a region of significant imaging abnormality (generally contrast-enhancing tissue) and is of adequate quality, in terms of size and consistency, for pathological assessment. If tissue exhibits the histological features of grade IV glioma as dictated by the WHO in **Table 1.1** to a trained neuropathologist, a diagnosis of GBM is confirmed and a discussion of the prognosis and treatment options begins.

1.3.3 Therapy and Clinical Management

The standard-of-care for GBM incorporates a three-pronged approach that is aimed at relieving mass effect, controlling visible disease, and enhancing the efficacy of adjuvant therapy. To this end, patients with GBMs that are deemed operable by a neurosurgeon receive maximal safe tumor resections followed by high dose RT with concurrent and adjuvant TMZ (**Figure 1.6**) (11; 39). Patients with inoperable tumors, those near critical structures or vasculature that prevent

substantial debulking, are offered RT and TMZ. Symptoms of mass effect such as seizures or hemiparesis are also treated with antiepileptics and corticosteroids with varying results (1; 12; 40). As there is no curative therapy for GBM, patients are strongly encouraged to participate in clinical trials throughout the duration of their care.

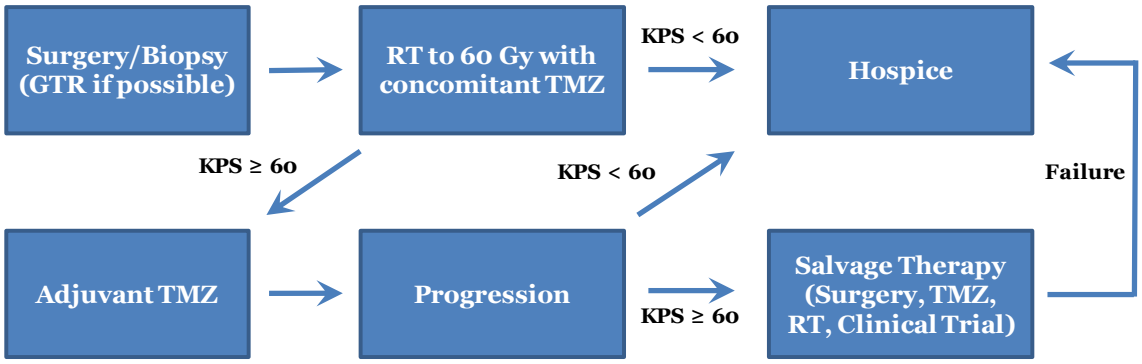

Figure 1.6. Treatment algorithm for GBM.

The mainstay of GBM therapy is surgical resection with the central goal of maximizing the removal of neoplastic tissue while minimizing the damage to surrounding normal tissue and vasculature. Using stereotactic neuronavigation, electrophysiological monitoring, and other advanced guidance techniques, surgeons cut through the skull, carefully navigate past eloquent tissue to the tumor bulk as defined by CE-MRI, and remove as much of the contrast-enhancing component as possible. A number of studies have shown recently that "more complete" resections (i.e. those that remove a larger portion of the contrast-enhancing tumor) may extend both progression-free survival (PFS) and OS in GBM patients (41-51). This may be because patients with lower tumor burden are more likely to respond to adjuvant therapy or because the immune system has a smaller neoplastic insult to combat. Regardless, achieving a high extent-of-resection (EOR) or a gross total resection (GTR) is incredibly difficult as neoplastic tissue is virtually indistinguishable from normal tissue. This leaves surgeons with a limited ability to evaluate surgical margins and determine when all resectable tissue has been removed. Given the prognostic significance of EOR and the difficulty in detecting residual tumor intraoperatively, many technologies have been developed recently to enhance tumor resection. Moreover, it has become standard practice for surgeons to order postoperative MR imaging to evaluate the residual contrast-enhancing tumor in the immediate postoperative period (52).

Though surgical resection is a cornerstone of GBM management, it is not possible to remove all tumor cells in this fashion, and adjuvant therapies including RT and chemotherapy have been developed to address residual disease. RT is cytotoxic primarily by the generation of DNA-damaging free radicals from

ionization of H_2O and O_2 molecules within tumor tissue (53). Cancer cells are more sensitive to these free radicals due to their perpetual state of DNA synthesis. Cranial irradiation of the resection cavity and any residual contrast-enhancing tissue to 60 Gy has been shown to increase survival by approximately 5 months compared to surgery alone, and a seminal study by Stupp et al. found that the addition of the alkylator, TMZ, to this RT regimen increased median survival by another 2.5 months (9; 10; 54). When given in thirty 2 Gy fractions over 6 weeks, RT is generally well tolerated with limited toxicity and only moderate gastrointestinal, hematologic, and constitutional side effects (55; 56). After the completion of RT, patients continue on 5 day cycles of TMZ -barring any hematologic perturbations like thrombocytopenia or leukopenia- until recurrence is noted on imaging.

1.3.4 Response to Therapy

Even with this aggressive surgical and chemoradiation protocol, the vast majority of GBM patients (up to 90%) will have visible recurrence on CE-MRI within 2 cm of their original tumor (41; 57). This is partly due to the highly infiltrative nature of the tumor that make it impossible to target the entire tumor for surgical resection or RT. It is also likely due to the extensive hypoxia present within these tumors as low oxygen concentrations limit the generation of the DNA-damaging free-radicals generated by RT. Furthermore, recently discovered GBM cancer stem cells are hypothesized to remain proliferatively quiescent, and thus immune to RT, while also being pluripotent and capable of repopulating the tumor well after the completion of treatment (58). Regardless of the mechanism, the vast

majority of GBM patients exhibit treatment failure within a year of therapy and search for salvage therapies or clinical trials before ultimately succumbing to this uniformly fatal disease.

The only primary GBM patients that do not experience such a fast, precipitous decline following surgery are those with MGMT methylated tumors (33; 34; 57). As stated in **1.2,** silencing of the MGMT gene through methylation of its promoter results in an increased sensitivity to the alkylating agent TMZ. In a seminal randomized study by Hegi et al., GBM patients with MGMT methylation who were treated with TMZ were found to have better median OS and 2-year survival rates than patients with unmethylated promoters (21.7 vs 12.7 months and 46.0% vs 13.8%, respectively; **Figure 1.5**) (34). Though all GBM patients receive TMZ currently, if a double-blinded randomized trial by the Radiation Therapy Oncology Group (RTOG 0525) confirms this relationship between MGMT methylation status and outcome, patients with unfavorable MGMT methylation status may be selected for trials of different drug combinations including MGMT expression modulators (NCT01402063, NCT02287428, and NCT01700569).

1.4 Imaging in GBM Management

Apart from the use of CT or MRI for the initial diagnosis of GBM, imaging plays an important role in the prognostication of disease, the direction of therapy, and the assessment of treatment response. In addition to the use of imaging because physical examination of the brain is impractical and dangerous, advanced imaging techniques also can tell us quite a bit about the physical, chemical, and biological makeup of the tumor. With no other imaging technique is this truer than

MRI. This is likely why MRI plays such an important role in the routine clinical care of patients and is a central modality in GBM research. Advanced MRI techniques are currently available that can be used to quantify many physical processes in GBM including tissue cellularity and vascularity, the generation of small-molecule metabolites, and the patterns of tumor growth and recurrence. This is all done by the physical manipulation of the hydrogen atom (^1H) with a complex series of magnetic fields, the basic understanding of which is essential for the appreciation of MRI in GBM management.

Note: A rigorous and complete description of MR phenomena would require quantum mechanics, though in most cases, a description in terms of classical physics describes the macroscopic behavior quite well. As such, the following sections are described in the classical sense only with occasional references to quantum mechanical principles. The references used for this chapter are textbooks or book sections written by Mamourian, de Graaf, Diaz, Gowland, and others (59-64). All information in sections **1.4.1** and **1.4.2** come from these texts unless otherwise specified with a separate citation.

1.4.1. Important Physical Concepts in MRI

Magnetization and Precession

An atom with an odd number of protons and/or neutrons in its nucleus possesses the basic physical quality of nuclear spin angular momentum, or spin, the underlying source of the MR phenomenon. In biological specimens, the most abundant nuclei that fits this description is ^1H, the proton opposite oxygen in water (H_2O), with a spin quantum number ($\overrightarrow{S_z}$) of ± 1/2. These nuclei can be pictured as

small spherical magnets that are spinning very fast, generating north and south magnetic poles, or a magnetic moment ($\vec{\boldsymbol{\mu}}$). Like the wobble of a spinning top that is decelerating to a stop, the spinning nucleus has an axis of precession along which $\vec{\boldsymbol{\mu}}$ passes.

When these nuclear spins are subjected to a static magnetic field ($\overrightarrow{\boldsymbol{B_0}}$), two important effects arise: *i.*) the spins have a tendency to precess around the applied field and *ii.*) the spins precess at a well-defined frequency ($\boldsymbol{\omega}$) defined by the function

$$\boldsymbol{\omega} = \frac{\boldsymbol{\gamma}}{\boldsymbol{2\pi}}\boldsymbol{B_0} \qquad \textbf{(Eq. 1.1)}$$

where $\boldsymbol{\gamma}$ is the gyromagnetic constant (42.577 MHz/Tesla for ^{1}H), a unique value for each nuclear species. This frequency is known at the *Larmor Frequency*, and the magnetization of the proton is resonant at this specific frequency. See **Figure 1.7A** for a schematic representation of this process.

When $\overrightarrow{\boldsymbol{B_0}}$ is applied to a set volume like a piece of tissue, the protons whose spins are normally oriented in random directions (**Figure 1.7B**) begin to precess around an axis parallel (lower energy state) or antiparallel (higher energy state) to the external magnetic field (**Figure 1.7C**). Although the spins split into two antiparallel populations, a preponderance reside in the lower energy state. This results in a non-zero sum of magnetic moments, ultimately resulting in a net magnetization of the tissue in the direction of $\boldsymbol{B_0}$. At 1 Tesla, the excess of protons in the parallel state is approximately 7 for every million protons, and it is the manipulation of the net tissue magnetization with other magnetic fields that gives rise to MR signal used for imaging.

Note that this nuclear precession is similar to the wobbling of the spinning top previously described. The angular momentum of the top is analogous to the magnetic moment of the proton while the gravitational field of the earth is analogous to $\boldsymbol{B_0}$. Just as a top precess around an axis of the surface normal, the proton precesses around the axis of the external magnetic field.

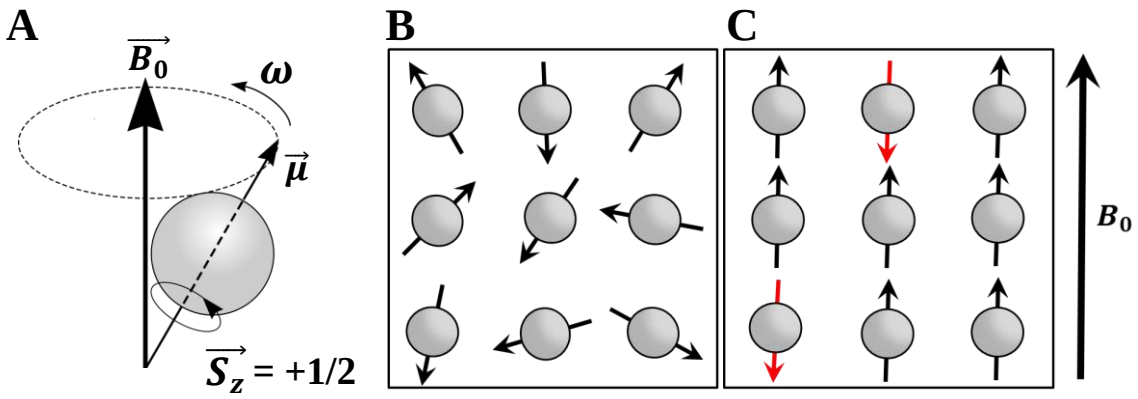

Figure 1.7. Schematic representation of a single proton nuclear spin and precession. Spinning protons precess about an external magnetic field (**A**). A population of protons under no external magnetic field have dipoles that are arranged randomly (**B**) while those under the influence of a static magnetic field, $\overrightarrow{B_0}$ orient either parallel or antiparallel to the field (**C**). The net magnetization in **C** would be pointing toward the top of the page.

Excitation and Relaxation

The application of another magnetic field, generally called a radiofrequency pulse (RF pulse), from the transverse direction and oscillating at the resonance frequency of the protons will "excite" the magnetization. Excitation is most easily visualized by establishing a frame of reference, a coordinate system, and nomenclature. The constant precession of the proton makes its excitation elliptical in nature, and it is easiest to understand the dynamics of the system by first imagining that we are rotating about the precession axis of the proton at a frequency equal to the $\boldsymbol{\omega}$**.** This "rotating frame" neutralizes the precession and makes it appear static. We can now superimpose our proton onto a 3-dimensional coordinate system with $\vec{M}$**,** the magnetization caused by the spinning proton, as a vector pointing along the z-axis in the same direction of $\boldsymbol{B_0}$ (**Figure 1.8A).** One can conceptualize the change in a proton's magnetization by describing two components of the vector $\vec{M}$: the longitudinal and transverse components. The longitudinal component of the magnetization ($\vec{M_z}$) is the projection of $\vec{M}$ onto the z-axis while the transverse component ($\vec{M_{xy}}$) is the projection of $\vec{M}$ onto the *xy,* or transverse, plane. For example, the blue vector **in Figure 1.8A** and **B** points straight along the z-axis, and thus does not have any transverse component. Conversely, the red vector ($\vec{M}'$in **Figure 1.8B)** lies entirely in the transverse plane and does not have a longitudinal component.

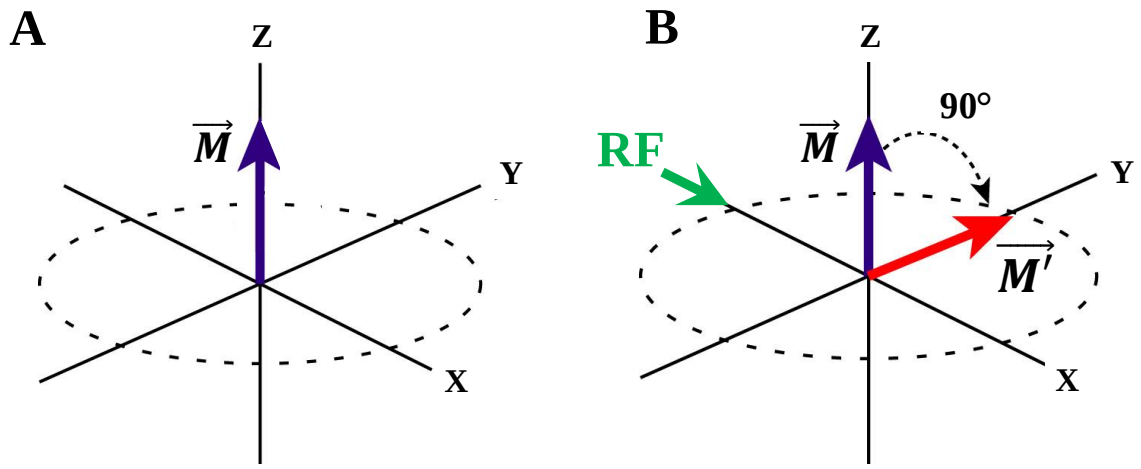

Figure 1.8. Vector representation of proton magnetization in the rotating reference frame. Equilibrium magnetization before excitation (**A**) and excitation of the spin with a 90° RF pulse along the x-axis (**B**).

Classically, excitation as viewed in the rotating frame, is the tipping of the magnetization vector $\vec{M}$ away from its equilibrium position along B_0 by an RF pulse to a position in the *xy* plane denoted $\vec{M}'$. **Figure 1.8B** depicts the excitation process with a 90° RF pulse along the x-axis in the rotating reference frame. The magnetization is still precessing around B_0 even though this is not shown using the rotating frame. Given the new transverse component of the magnetization, detection of the magnetization becomes possible via Faraday's law of induction. The precessing magnetization causes a change in the electric flux (**Φ**) of the receiver coils in the MR scanner inducing a small electromotive force (EMF or **ε**), where

$$\varepsilon = \frac{\partial \Phi}{\partial t} \qquad \textbf{(Eq. 1.2)}$$

The resulting signal is called the *free induction decay* and represents the basic MR signal recorded. It should be noted that only magnetization in the *xy* plane contributes to the MR signal as this is the only component that generates a magnetic field with the correct orientation to induce an electrical current in the receiver coils. Thus signal amplitude, as measured by the scanner, is directly related to M_{xy}.

Once the RF pulse is turned off, the spin system begins to "relax" to its equilibrium state along the z-axis. The mechanisms of relaxation are complex and are beyond the scope of this work; however, a brief explanation of the dominant mechanism relevant in biological tissues, magnetic dipole-dipole interactions, will be provided. Regardless of the mechanism, relaxation implies that the transverse component decays away while the longitudinal component grows back to its

equilibrium state. Two important MR parameters, $\boldsymbol{T_1}$and $\boldsymbol{T_2}$, describe this return to equilibrium and are known as the relaxation time constants.

$\boldsymbol{T_1}$ characterizes the return of magnetization vector to equilibrium along $\boldsymbol{B_0}$ and is called the spin-lattice time constant. As the name implies, $\boldsymbol{T_1}$ involves the exchange of energy between the spinning nuclei and the molecules (i.e. H_2O, proteins, lipids) in the surrounding lattice. Through collision, vibration, heat generation, and magnetic dipole interactions, the excited protons dissipate the energy induced by the RF pulse, and slowly return to their ground state. The longitudinal component of the magnetization behaves according to the differential equation

$$\frac{dM_z}{dt} = -\frac{M_z - M_o}{T_1} \qquad \textbf{(Eq. 1.3)}$$

where $\boldsymbol{M_o}$ is the equilibrium magnetization. The solution of this equation following a 90° excitation pulse gives the function

$$M_z = M_o(1 - e^{-\frac{t}{T_1}}) \qquad \textbf{(Eq. 1.4)}$$

The exponential growth of the longitudinal component of the magnetization is largely dependent on the value of $\boldsymbol{T_1}$, which can range from a few tenths of a second to several seconds in biological tissues. The differences in $\boldsymbol{T_1}$ between tissue types are part of what allows us to differentiate tissues like grey matter and white matter on T1-weighted MRI (**Figure 1.9**).

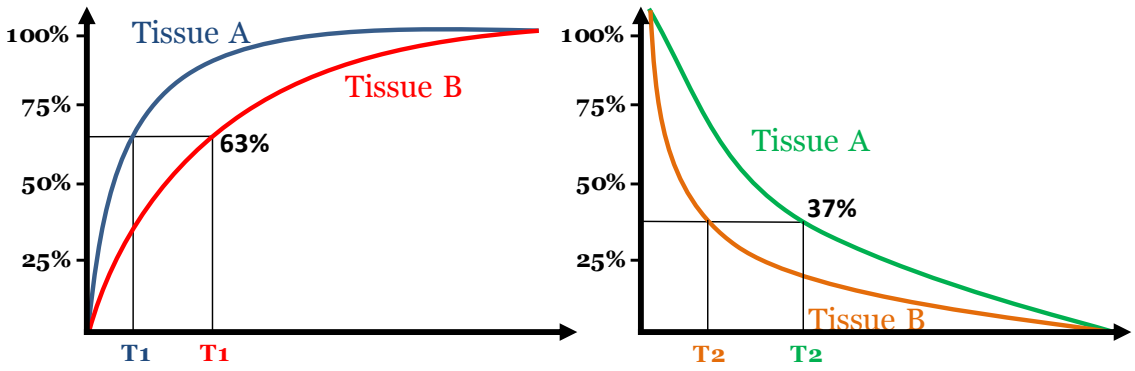

Figure 1.9. Longitudinal magnetization recovery and transverse magnetization decay in two separate tissue types. The M_z regrows to ~63% of its equilibrium value after time T_1 while M_{xy} has decays to ~37% of its excited value at time T_2.

$\boldsymbol{T_2}$ characterizes the decay of magnetization in the transverse plane and is called the spin-spin time constant. The same energy dissipation mechanisms at work in $\boldsymbol{T_1}$ are present in T_2 relaxation; however, the random interactions between some dipoles in the transverse plane add to the relaxation of these spins. This is because a change in the local magnetic field experienced by a spin causes its precession frequency to change. As some spins begin to precess faster and others slower, phase coherence is lost. This "spin-spin" interaction within the transverse plane dominates the $\boldsymbol{T_2}$ process and represents a broadening of the spins' resonance frequencies and a dephasing of the transverse components of the spins (**Figure 1.9**) that ultimately results in the decay of MR signal.

The transverse component of the magnetization vector can be described with the following equation

$$\frac{dM_{xy}}{dt} = -\frac{M_{xy}}{T_2} \qquad \textbf{(Eq. 1.5)}$$

The solution to which immediately following a 90° RF pulse is simply

$$M_{xy} = M_o\, e^{-\frac{t}{T_2}} \qquad \textbf{(Eq. 1.6)}$$

This exponential decay represents the decay of the dampened sinusoid in **Figure 1.10**.

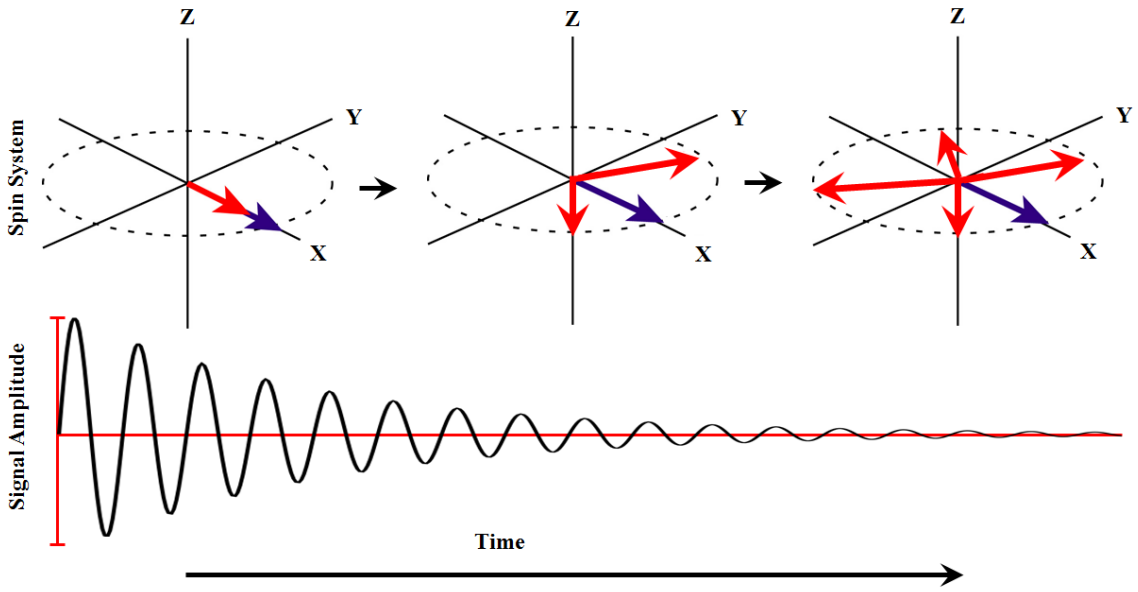

Figure 1.10. Diagram showing loss of transverse component (M_{xy}) of magnetization. Immediately after a 90° RF pulse, the spins in the transverse plane are all in phase. Due to spin-spin interactions, some protons begin to precess faster and others slower. This ultimately results in a dephasing of the spins over time and a decay of the MR signal.

Image Contrast and Signal Weighting

In clinical imaging, different sequences are used because of the different contrast that they produce and the different information this gives the physician about the tissue. One of the main strengths of MR imaging is that image contrast depends on many different modifiable parameters. By solely altering the time at which we administer the RF pulse and when we read the MR signal in the receiver coils, we can utilize the intrinsic $\boldsymbol{T_1}$ and $\boldsymbol{T_2}$ properties of tissues, as well as the tissues' proton density ($\boldsymbol{\rho}$), to generate signal contrast (65). The difference in signal between tissue can then be used to make a grey-scale signal intensity-based image, like that generated in conventional MRI. To understand how signal contrast is generated, one must first understand two essential components of RF pulse sequences: Repetition time (TR) and Echo time (TE).

TR represents the time between the centers of 2 RF excitation pulses in a pulse sequence while TE represents the time between the center of an excitation pulse and the subsequent echo (e.g. the point at which the MR signal is maximum). These values and their modulation can be most easily understood by evaluating a simple spin-echo pulse sequence (**Figure 1.11**). The basic spin-echo sequence consists of a 90° excitation RF pulse followed by a 180° refocusing pulse to maximize the subsequent echo. After the refocusing pulse at a time TE, the scanner records the signal induced in the receiver by the transverse component of the magnetization of the excited spins.

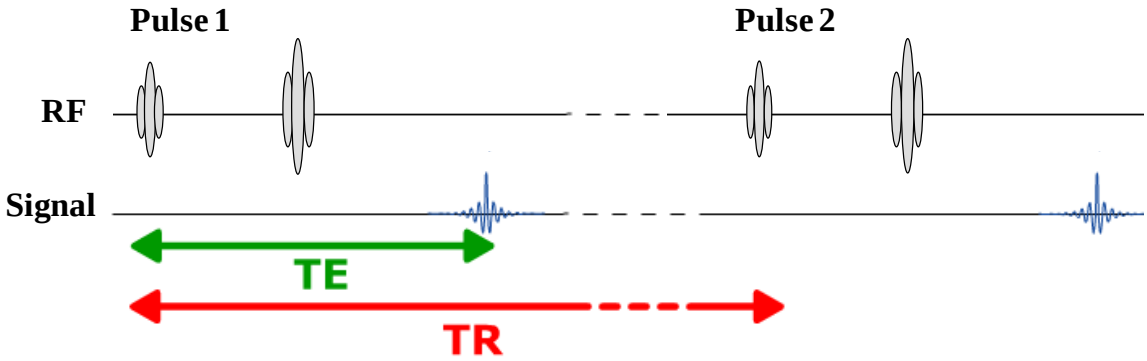

Figure 1.11. Spin-echo pulse sequence depicting TR and TE.

The modulation of TE and TR relative to the $\boldsymbol{T_1}$ and $\boldsymbol{T_2}$ properties of the tissues allows for the precise control of tissue contrast known as "weighting", and allows us to control which source of image contrast ($\boldsymbol{T_1}$, $\boldsymbol{T_2}$, **or** $\boldsymbol{\rho}$) contributes most to the image generated. This can most easily be appreciated by evaluating the model for signal intensity of a spin-echo sequence ($\boldsymbol{S_{SE}}$).

$$\boldsymbol{S_{SE}} = \boldsymbol{K\rho}\left(\mathbf{1} - \boldsymbol{e}^{-\frac{\boldsymbol{TR}}{\boldsymbol{T_1}}}\right)\boldsymbol{e}^{-\frac{\boldsymbol{TE}}{\boldsymbol{T_2}}} \qquad \textbf{(Eq 1.6)}$$

Per **Eq 1.6**, it is readily apparent that $\boldsymbol{T_1}$ effects are directly related to TR while $\boldsymbol{T_2}$ effects are related to TE. For example when TE is much shorter than $\boldsymbol{T_2}$, $\boldsymbol{e}^{-\frac{\boldsymbol{TE}}{\boldsymbol{T_2}}} \rightarrow 1$, and the $\boldsymbol{T_1}$ component of the signal dominates; when TE is made longer than $\boldsymbol{T_2}$, the exponential term remains and the $\boldsymbol{T_2}$ contributes to the signal. The latter scenario accentuates the signal decay between tissues with different $\boldsymbol{T_2}$ values and is thus called "T_2-weighting." Similarly when TR >> $\boldsymbol{T_1}$, the longitudinal magnetization of protons in all the tissues have recovered from the excitation pulse, and the $\boldsymbol{T_1}$effects are nulled. Conversely, short TRs accentuate the $\boldsymbol{T_1}$ effects resulting in T_1-weighting. Finally, when TR is long and TE is short, both $\boldsymbol{T_1}$ and $\boldsymbol{T_2}$ affects are minimized, making $\boldsymbol{\rho}$ the dominant factor in $\boldsymbol{S_{SE}}$, resulting in "proton density weighting." A summary of the TE and TR combinations that result in contrast weighting can be found in **Figure 1.12**.

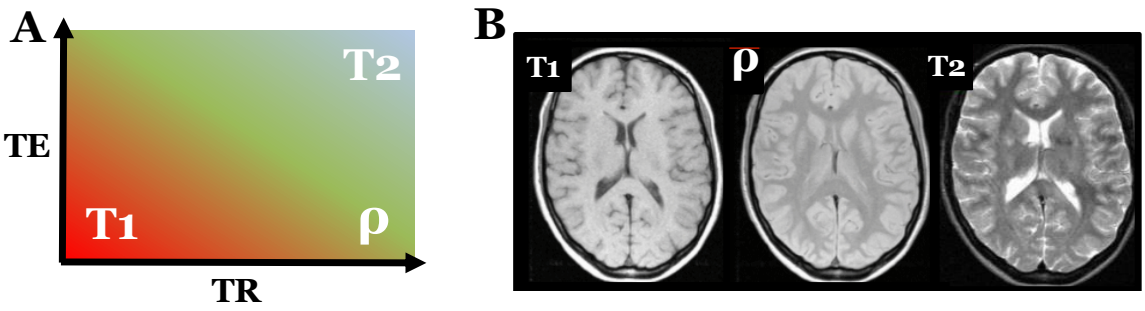

Figure 1.12. Signal weighting based on TE and TR. T_1-weighting results from a pulse sequence with short TE and TR, T_2-weighting results from long TE and long TR, and proton density (rho, ρ) weighting results from short TE and long TR (**A**). This variation in sequence parameters results in images with differing tissue contrast (**B**).

Water Diffusion

Molecular diffusion, or Brownian motion, refers to the movement of a molecule in a fluid as it is perturbed by thermal energy in its environment. The global displacement of water molecules over time in a fluid is random, and is most easily described in statistical terms with a displacement distribution. This distribution describes the proportion of molecules that have moved in a specific direction for a specific distance over a specified time interval. Diffusion of molecules in a homogenous medium is known to exhibit a Gaussian displacement distribution, represented as a sphere in 3D space, as there are no boundaries to prevent diffusion in any direction. Biological tissues are highly heterogeneous, in contrast, and consist of various compartments and barriers of different diffusivities. Water diffusion is impeded by these barriers and takes a particular structure and orientation based on the shape and diffusivity of compartment in which it resides. The structure and orientation of water diffusion can be tracked using special MR techniques and used to describe a number of physicobiological properties of tissues that are of clinical importance in GBM.

Magnetic Susceptibility and Gadolinium-based Contrast Agents

Magnetic susceptibility is a physical property that describes the extent to which a substance becomes magnetized when exposed to an external magnetic field. This property results because the movement of electrons in atomic orbitals generate an internal magnetic field that interacts with an external magnetic field. When these electrons are unpaired in their orbitals, a local net magnetic field is generated that augments the magnetic field, a phenomenon known as positive

susceptibility. Conversely, when electrons are paired in their orbitals, the opposing magnetic fields generated by the opposite spins negate a local net magnetic field, ultimately resulting in a diminishment of an external magnetic field. This is known as negative susceptibility. These materials are called paramagnetic and diamagnetic, respectively. Most tissues in the body, including water, are weakly diamagnetic and induce negligible susceptibility effects while metals like tungsten, cesium, and gadolinium are paramagnetic.

Paramagnetic materials like gadolinium have seen widespread use as contrast agents in MRI because of their ability to alter the relaxation of water in tissue. Gadolinium, the most commonly used paramagnetic element in clinical contrast agents, is a lanthanide that contains seven unpaired electrons in its *4f* orbital, giving it a strong magnetic moment. The direct and indirect interaction of the magnetic moments of gadolinium-based contrast agents (GBCA) with the magnetic moments of RF-excited water protons causes a shortening of the $\boldsymbol{T_1}$ and $\boldsymbol{T_2}$ in tissues where intravenous GBCAs accumulate. This ultimately results an accentuated $\boldsymbol{T_1}$ signal in regions where GBCAs can diffuse; most notably, the blood vessels and regions where the blood vessels are highly permeable. This increase in $\boldsymbol{T_1}$ signal, or "contrast-enhancement" as it is generally termed, is useful in not only characterizing different types of lesions with MRI, but also evaluating a number of physiological properties with the technique, like blood flow, tissue perfusion, and vessel permeability (**Figure 1.13**).

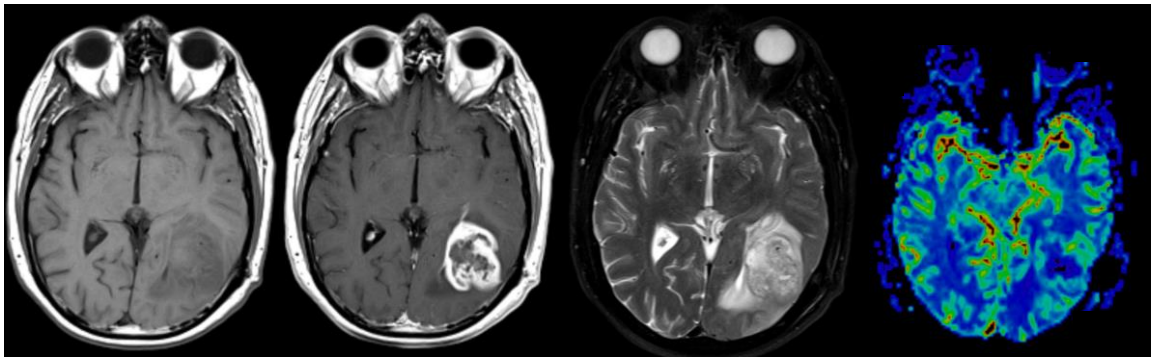

Figure 1.13. Common water relaxation-based imaging techniques. T_1 and T_2- weighted images highlight the intrinsic relaxation properties of the brain tumor without describing vascularity and vessel permeability. Intravenous (IV) administration of GBCAs allows for the identification of leaky brain tumor vasculature and characterizes a region of clinical importance. Tracking the flow and diffusion of GBCAs allows the computation of markers like cerebral blood flow that are useful in diagnosis and prognosis.

Chemical Shift

Chemical shift describes the subtle resonance frequency change observed for protons in a number of small molecules due to the local magnetic environment they experience as a product of the molecule's electronic composition. This shift is unique for each molecular group and has been used for years by chemists to identify unknown compounds and elucidate molecular structures. In MR spectroscopy, this chemical shift can be used to identify and quantify the presence of a number of small molecules associated with a variety of intracellular processes. An understanding of chemical shift is essential for an appropriate appreciation of the MR imaging technique most prevalent in this work: spectroscopic MRI (sMRI).

Physically, chemical shift is a displacement of the resonant frequency of a nucleus due to *shielding* created by the orbital motion of the surrounding electrons in response to the external magnetic field ($\boldsymbol{B_0}$)**.** This shielding decreases the magnitude of the magnetic field that nuclei experience, and subsequently their resonance frequency. This interaction with $\boldsymbol{B_0}$ is local, however, only affecting the molecule and its functional groups. This is unlike magnetic susceptibility which is a global property describing the magnetic behavior of a material. In the presence of an external magnetic field, the effective field $\boldsymbol{B_{eff}}$ experienced by a nucleus is

$$\boldsymbol{B_{eff}} = \boldsymbol{B_0}(\mathbf{1} - \boldsymbol{\sigma}) \qquad \textbf{(Eq. 1.7)}$$

where $\boldsymbol{\sigma}$ is a constant representing the electronic environment of the nucleus. If we propagate $\boldsymbol{B_{eff}}$ through **Equation 1.1**, we find that, indeed, resonance frequency is also affected.

$$\boldsymbol{\omega_{eff}} = \boldsymbol{\omega_0}(\mathbf{1} - \boldsymbol{\sigma}) \qquad \textbf{(Eq. 1.8)}$$

This displacement in resonance frequency in parts per million ($\boldsymbol{\delta}$) is generally expressed relative to a reference frequency ($\boldsymbol{\omega_{ref}}$) and is given by

$$\boldsymbol{\delta} = \frac{\omega_S - \omega_{ref}}{\omega_{ref}} \mathbf{x\ 10^6} \qquad \textbf{(Eq. 1.9)}$$

where $\boldsymbol{\omega_S}$ is the resonance frequency of the sample in question. In most in vivo spectroscopic imaging sequences, the reference resonance frequency is generally that of protons on H_2O, but some sequences use organic small molecules that have negligible concentrations in the body.

1.4.2. Conventional Imaging Sequences

With an understanding of the basic physical principles giving rise to MR signal and many of the process that can affect it, it is much easier to understand the variety of imaging sequences used for GBM management and the clinical significance each. The recommended imaging protocol for all brain tumors includes the following: Pre- and post-contrast 3D T1-weighted imaging, pre- and post-contrast 2D Axial T2-weighted FLuid Attenuated Inversion Recovery (FLAIR) imaging, and 2D Axial diffusion-weighted imaging (DWI) (66). Additional studies that may be of some use per response assessment guidelines include dynamic susceptibility perfusion weighted imaging, dynamic contrast-enhanced permeability imaging, and proton magnetic resonance spectroscopy (67).

<u>Pre- and Post-Contrast T1-weighted Imaging</u>

Contrast-enhanced, T1-weighted (CE-T1w) imaging sequences have been the standard for detection, characterization, and response assessment in GBM for

decades. A pre-contrast image is generally acquired before the IV administration of a GBCA to identify any $\boldsymbol{T_1}$ native hyperintense regions (i.e. fatty collections, blood products, microcalcification) that may obscure contrast-enhancement. A bolus of GBCA at approximately 0.1 mmol/kg body weight is then administered IV at a rate of 1 mL/s, and a second "contrast-enhanced" T1w acquisition with the same imaging parameters is performed. Disruption of the blood-brain barrier (BBB) can lead to accumulation of these agents in the interstitial spaces surrounding the leaky vasculature, resulting in substantial $\boldsymbol{T_1}$ shortening and increased signal intensity on T1w images (68). This phenomenon can be used to qualitatively observe regions of abnormally high signal as a surrogate marker of disease like malignancy, hemorrhage, or abscess (66).

Contrast-enhancement is of significant importance in the evaluation of gliomas as it has been shown not only to correlate significantly with glioma grade and mitotic activity, but also to show efficacy in predicting survival (69-71). Similarly, robust contrast-enhancement in the parenchyma is quite specific for the histological presence of GBM (75% - 100%) and the presence of a central region of low signal due to tissue necrosis is nearly pathognomonic for the disease (72-74). Not only does the presence of GBM cause an increase in the baseline permeability of the BBB, but significant angiogenesis and neovascularization associated with GBM results in an immature, leaky neovasculature (75). These structural abnormalities in the BBB allow GBCA leakage from the vascular space into the extravascular, extracellular space resulting in pronounced parenchymal enhancement. The hypointense region within the enhancing rim originates from a focus of hypoxic, tightly-packed glioma cells that outgrow their initial blood

supply, resulting in frank cell death and the observed necrosis (76). Interestingly, a radiogenomic study by Naeini, et al. linked the volumes of the enhancing and necrotic regions of GBMs with the mesenchymal molecular subtype previously discussed. This suggests that the quantitative assessment of these tumor regions may not only describe underlying biological processes, but considering the significantly different prognosis of patients with mesenchymal subtype vs others, these values may also be useful in evaluating survival (77).

Pre- and Post-Contrast T2-weighted FLAIR Imaging

Also standard for clinical diagnosis and monitoring of brain tumor are T2-weighted (T2w) or T2w/FLAIR imaging. These imaging studies assist in the detection and characterization of a number of tumor characteristics and effects including vasogenic edema, mass effect, and tumor heterogeneity (68). T2 relaxation is, however, not highly affected at the concentrations of GBCA that reach the parenchyma in the brain; thus, the administration of GBCAs does not generally augment T2w imaging (65). Images can also help with the identification of hemorrhage due to the unique T2 properties of protons in blood breakdown products like hemosiderin or methemoglobin (68; 78). An early study of T2w imaging sequences found that the overall accuracy of glioma grading by experienced neuroradiologists using T2w features alone was rather high (80% - 94%) (68). However, the abnormalities present in T2w imaging for GBM tend to be more severe in terms of intensity, size, and mass effect than those of lower grade gliomas. Moreover, studies have found that approximately 30% - 40% of contrast-enhancing brain tumors originate from nonenhancing, T2w hyperintense regions

of MRI, sometimes even in the presence of antiangiogenic therapy (79; 80). Thus, T2w abnormalities observed in brain tumor patients not only describe tumor-related effects, but also give insight into the location of potential contrast-enhancement in both low-grade gliomas (LGGs) and GBM.

T2w/FLAIR sequences have an inversion recovery pulse for negating the signal acquired from protons in the cerebrospinal fluid (CSF) (81; 82). By applying a 180° preparatory pulse before applying the 90° excitatory pulse, the signal from a single tissue with a specific T1 can be nullified if the excitatory pulse is applied as the net magnetization vector of the tissue passes through the *xy* plane. Because this tissue has no longitudinal component to excite into the transverse plane, these spins are not excited into the *xy* plane to generate MR signal (**Figure 1.14A**). For most tissues, the time at which the net magnetization vector crosses the *xy* plane after the 180° pulse occurs at the time $\boldsymbol{T_1}$***ln 2.** The time between the null point and the 180° pulse is termed the inversion time (TI), and is unique for each tissue. Though this technique results in a lower signal-to-noise ratio than T2w sequences, the suppression of free water and CSF results in a T2w image that is sensitive to edematous or inflammatory changes in white matter (81; 82).

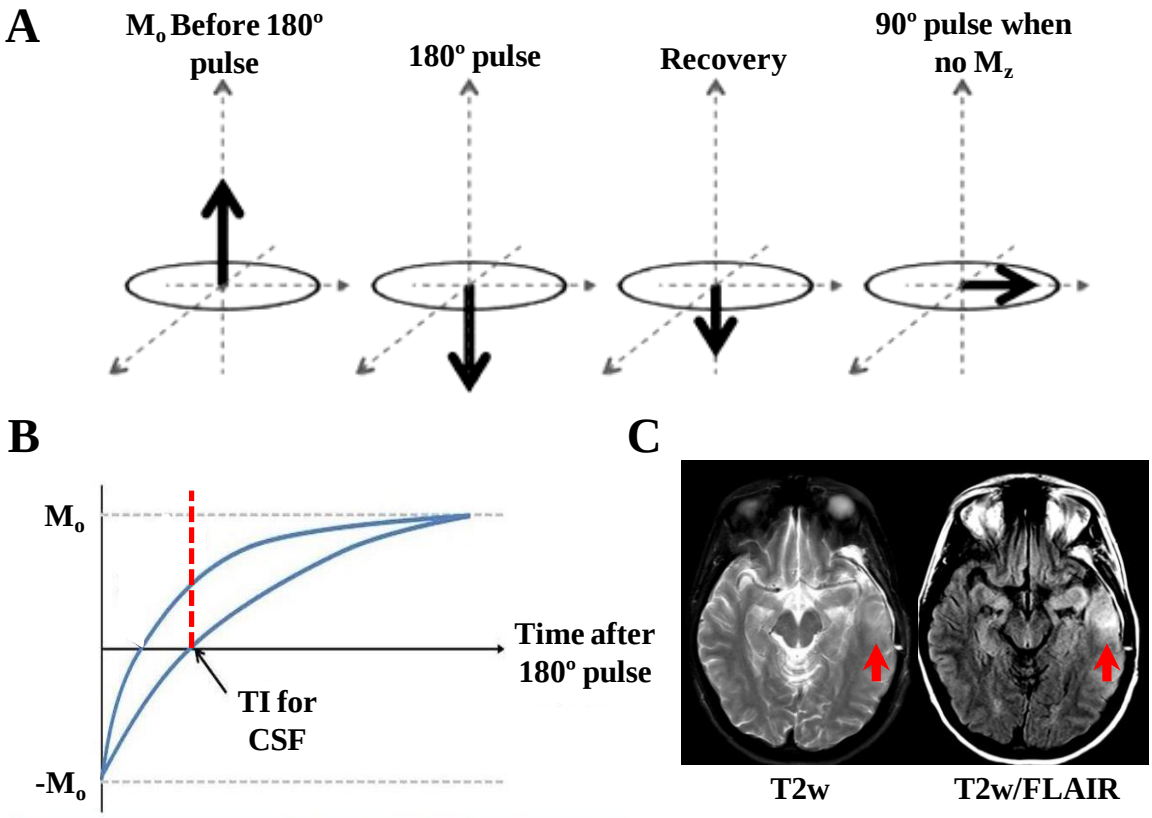

Figure 1.14. Mechanics of inversion recovery resulting in T2W/FLAIR images. The spins within the tissue that is selected for nullification are excited to the *–z* axis and have relaxed to the *xy* plane when the excitatory 90° pulse is applied, effectively preventing their contribution to the MR signal (**A**). When the 90° pulse is set at the TI marked in **B**, the signal from the CSF and other free water is nullified, and a T2w/FLAIR image can be generated (**C**).

Diffusion-Weighted Imaging

One of the most widely used physiologic MR imaging sequences in glioma is DWI. This is because DWI offers insight into the tumor microenvironment by elucidating the diffusion properties of water within tumor and normal surrounding tissue (83-85). The diffusion of water through an inhomogeneous magnetic field causes a dephasing of proton spins resulting in a signal attenuation (SA) that is proportional to the distance traveled (**Eq. 1.10**). In MRI, SA can be generated using unidirectional diffusion-sensitizing gradients that dephase spins along a predetermined spatial axis following the relationship

$$\boldsymbol{SA_x = S_o e^{-bD_x}} \qquad \textbf{(Eq. 1.10)}$$

where $\boldsymbol{S_o}$ is the baseline signal before the application of the sensitizing gradients, $\boldsymbol{b}$ reflects the strength and timing of these gradients, and D_x describes the physical diffusion coefficient, a parameter describing the flux of water particles through a given area per unit time, along the *x*-axis. Regions where water diffusion is limited, or *"restricted"*, due to impermeable membranes (i.e. grey matter) exhibit little SA while those where water diffuses freely, or is *"unrestricted"* (i.e. CSF), experience much more SA. Using the geometric mean of D_x, D_y, and D_z, a global statistical parameter known as the apparent diffusion coefficient (ADC) can be generated as follows

$$\boldsymbol{ADC = -\frac{1}{b}\ln\frac{S_{DWI}}{S_o}} \qquad \textbf{(Eq. 1.11)}$$

These diffusion measures provide information about tissue architecture and the orientation of intra- and extracellular spaces, and have shown considerable utility in describing parameters important to brain tumor management such as

tumor cellularity and nerve fiber orientation (86). In neuroimaging, restricted regions exhibit low ADC values, are dark on ADC maps, and are generally associated with regions of tightly compacted cells while unrestricted regions exhibit large ADC values, are bright on ADC maps, and are associated with the absence of cells. Clinically, the former represents tissues that have experienced an increase in intracellular water due to cytotoxic edema, as seen in cerebral infarction, or the reduction in the extracellular space due to increased cellularity, as seen in certain neoplasms (**Figure 1.15**) (87).

Though DWI is a common sequence acquired in glioma, studies regarding its use in diagnosis and management have been ambiguous (86-90). The utility of DWI in discriminating between LGG and HGG is limited as there is significant overlap in ADC values from these populations. In a study by Kono et al., GBM and grade II astrocytomas exhibited significant differences in ADC values; however, the authors reported that neither voxel nor texture-based measures of ADC was able to identify peritumoral neoplastic cell infiltration in patients (91). Similarly, Fan et al. showed some utility of DWI metrics in differentiating anaplastic astrocytoma from other non-enhancing tumors, yet ultimately concluded that the observed ADC in the peritumoral regions of these tumor types were not significantly different (92). Though the addition of diffusion measures using DWI to routing imaging may increase our understanding of the tumor microenvironment and contribute to diagnostic accuracy, the use of DWI for glioma measurement is quite limited, and DWI-guided therapy has failed to reach any meaningful clinical implementation (91).

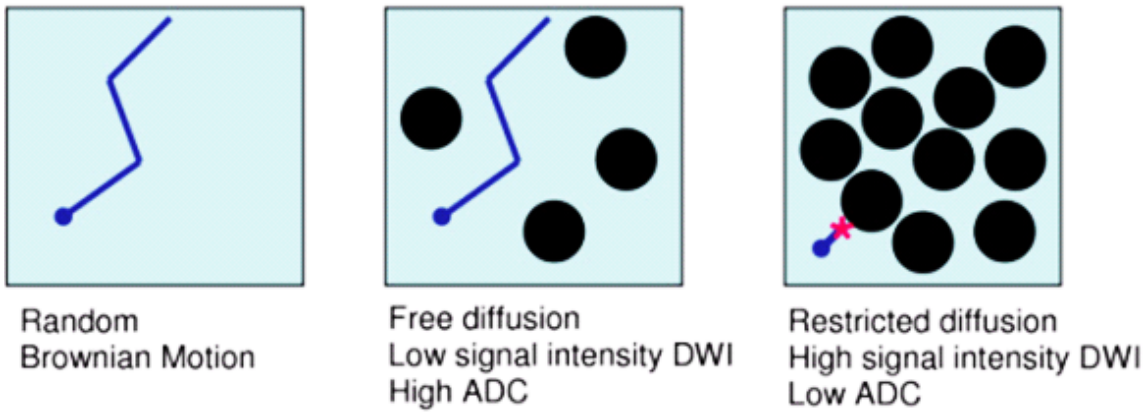

Figure 1.15. Impact of cellularity on water diffusion and DWI/ADC intensity. Low cellularity allows for the water molecules (blue circles) to flow in the extracellular space more freely resulting in high ADC (**A**). Higher cellularity (black circles) limits the extracellular space in which water can diffuse resulting in low ADC (**B**). Reproduced from *O'Flynn E.A., et al. 2011, Breast Cancer Res. 2011 13(1). DOI: 10.1186/bcr2815* under the Creative Commons Attribution (CC BY) license (93).

Perfusion-Weighted Imaging

An advanced MR imaging technique that has seen incredible development and clinical utilization in the last decade for glioma is that of perfusion-weighted imaging (PWI). Using the two main methods of PWI, T2w dynamic susceptibility contrast-enhanced (DSC) perfusion and T1w dynamic contrast-enhanced (DCE) imaging, physicians can evaluate and quantify a number of parameters describing the tumor vasculature. These methods rely on the IV injection of a GBCA bolus and describe the distribution of these tracers, in terms of T1 and T2 contrast changes, within bodily tissues over time. Regions with abnormal perfusion (e.g. tumor vasculature) show abnormal signal changes over time from which quantitative parameters can be derived describing various properties including blood volume and flow as well as blood vessel permeability and surface area.

DSC imaging begins with the administration of an IV GBCA bolus followed by a series of rapid image acquisitions over a given region of interest (e.g. the brain). As the contrast agent passes through the regional circulation, it generates local magnetic field distortions that result in spin dephasing, and consequently, signal loss. By measuring signal intensity over time and utilizing the relationship between the GBCA concentration ([GABC]) and the T2-relaxation rate (ΔR2), a concentration-time curve (**Figure 1.16**) can be generated using

$$[\boldsymbol{GBCA}] \propto \Delta \boldsymbol{R2} = -\frac{\mathbf{1}}{\boldsymbol{TE}} \ln \frac{\boldsymbol{S_t}}{\boldsymbol{S_o}} \qquad \textbf{(Eq. 1.12)}$$

where $\boldsymbol{S_o}$ is the baseline signal in a given voxel and $\boldsymbol{S_t}$ is the signal at time $\boldsymbol{t}$ at the same voxel**.**

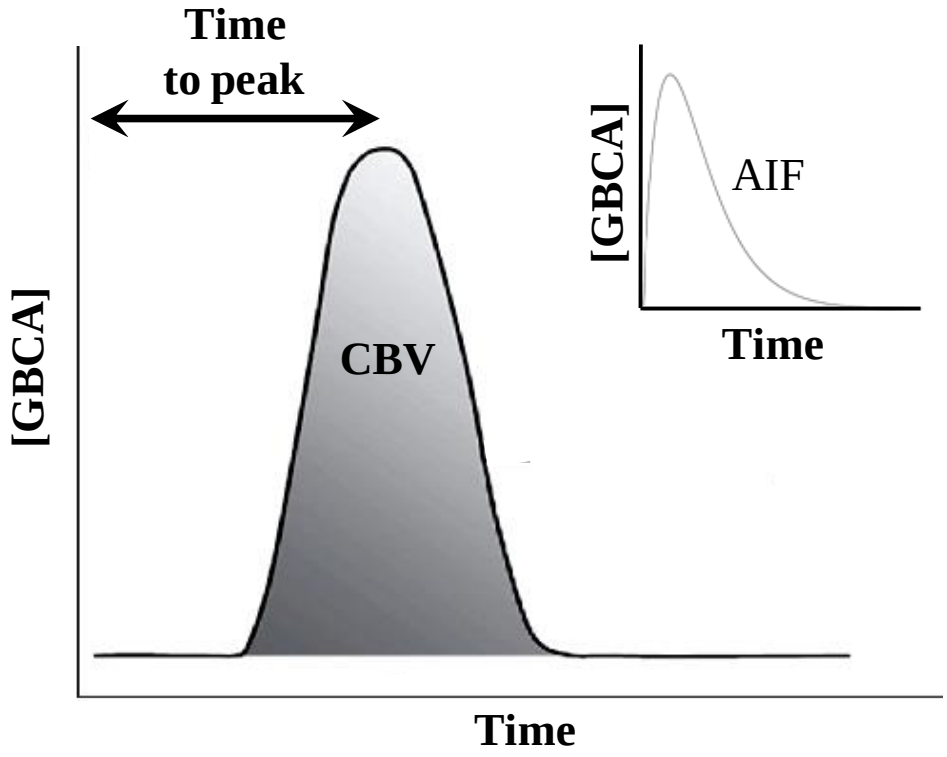

Figure 1.16. Examples of a concentration-time curve and AIF for a DSC perfusion experiment.

From this concentration-time curve, a number of perfusion parameters can be computed with various physiological meanings and uses. For example, it is well established that, ignoring recirculation effects, the volume of blood that passes through a voxel, or the cerebral blood volume (CBV), can be computed as the area under the concentration-time curve ($\boldsymbol{C_{tissue}}$), or

$$\boldsymbol{CBV \propto \int_0^{\infty} C_{tissue}(t)dt} \qquad \textbf{(Eq. 1.11)}$$

Moreover, one can approximate the flow of blood passing through a voxel, or the cerebral blood flow (CBF), if information describing the temporal shape of the input concentration curve, also known as the arterial input function (AIF), is available. Because the AIF is different for every voxel and cannot be directly measured, it is generally estimated by measuring the concentration-time curve in a large feeding artery of the brain, like the middle cerebral artery, and applying this function to all voxels of the brain. As $\boldsymbol{C_{tissue}}$ is a combination of the AIF and inherent tissue properties, a mathematical operation known as deconvolution, a topic that is beyond the scope of this work, is employed to separate these effects. By definition, CBF is the magnitude of the first time point of the solution of

$$\boldsymbol{CBF * R(t) = FT^{-1}\left(\frac{FT(C_{tissue}(t))}{FT(AIF(t))}\right)} \qquad \textbf{(Eq. 1.13)}$$

where $\boldsymbol{R(t)}$ represents the residual function after deconvolution while $\boldsymbol{FT}$ and $\boldsymbol{FT^{-1}}$ represent the one-dimensional forward and inverse Fourier transforms. Both CBV and CBF are routinely used clinically to identify regions of abnormal perfusion and vessel architecture in a number of pathologies including ischemia and neoplasia.

While DSC is based on the T2-relaxivity properties of GBCAs and describes first-pass parameters like flow and volume, DCE relies on the T1 relaxivity properties of GBCAs and describes the dynamic features of BBB contrast agent leakage. Like with DSC, a direct association between GBCAs and signal intensity allows for the generation of concentration-time curves, though the explicit relationship between the two varies based on the methods used to model tracer dynamics (94). Regardless of the model, many of the parameters derived using DCE can be appreciated within the context of a simple two-compartment pharmacokinetic model (**Figure 1.16**) describing the flow of GBCAs from the plasma to the tissue space. Per this model, the concentration of GBCA in the tissue ($\boldsymbol{C_t}$) is associated not only with the concentration of tracer within the plasma ($\boldsymbol{C_t}$) and the extravascular, extracellular space (EEC), but also permeability and surface area of blood vessels within the imaging voxel according to

$$\frac{dC_t}{dt} = PS\left(C_p - \frac{C_t}{v_e}\right) \qquad \textbf{(Eq. 1.13)}$$

where $\boldsymbol{P}$ is permeability, $\boldsymbol{S}$ is the surface area per unit mass, and $\boldsymbol{v_e}$ is the EEC volume fraction. Though $\boldsymbol{P}$ and $\boldsymbol{S}$ can be evaluated separately, the exact relationship between the two can be difficult to determine, so most models condense them into a $\boldsymbol{K_{trans}}$ term describing tracer transport from the capillary (**Figure 1.17**).

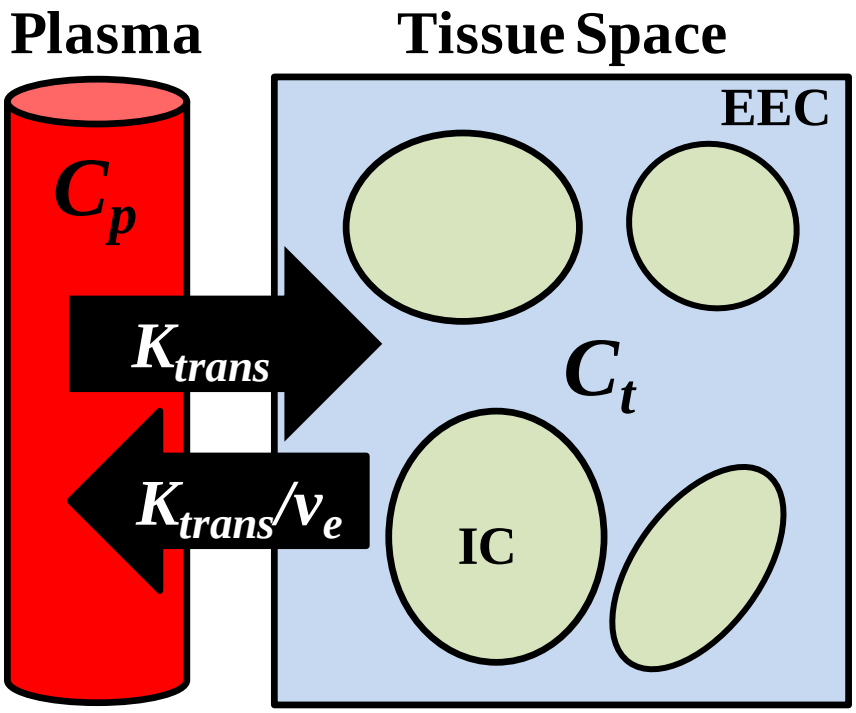

Figure 1.17. A basic two-compartment model of K_{trans}. This model describes the flow of GBCAs from the intravascular space to the tissue space which is composed of the extravascular extracellular space (EEC) and the intracellular space (IC).

The hemodynamic parameters generated using PWI are increasingly used as diagnostic aids and for monitoring therapeutic response in patients with glioma as vascular morphology and the degree of angiogenesis have been shown to correlate with the biological aggressiveness of gliomas (69; 95-97). Several studies have shown statistically significant correlations between tumor CBV glioma grade, tumor vascularity, histopathology, and OS with GBM showing much greater CBVs than any other tumor (98-102). Similarly, high pretreatment vessel permeability (elevated $\boldsymbol{K_{trans}}$) has been associated with worse PFS and OS (103). CBV has also been reported to be elevated in regions considered to be robustly infiltrated with tumor outside of contrast-enhancement in T2/FLAIR abnormalities (104). Interestingly, a study combining both DSC and DCE in GBM found that $\boldsymbol{K_{trans}}$ and CBV both correlated significantly with OS even though each metric describes different hemodynamic phenomena. Additionally, PWI has been used to evaluate treatment response in patients with HGG, particularly those with apparent radiation necrosis, though the relationship between hemodynamics, recurrence, and radiation necrosis in GBM is not yet clear (104-107).

1.4.3 MRI in GBM Standard-of-Care Therapy

Treatment of patients with GBM is traditionally divided into surgical, radiotherapeutic, and chemotherapeutic modalities. Currently, the standard-of-care for newly diagnosed GBM consists of maximal safe surgical resection followed by 60 Gy fractionated RT plus concomitant and adjuvant TMZ (9; 108). MRI plays an integral role in GBM management from diagnosis and treatment planning to prognosis and response assessment. What follows is a brief description of the use

of MRI in surgical and RT intervention as well as response assessment in patients with GBM.

Surgical Therapy

The central goals of GBM surgery are to sample tissue for histological diagnosis, relieve mass effect by maximizing the removal of neoplastic tissue while minimizing collateral damage to surrounding brain and vascular structures, and support adjuvant therapy by decreasing the tumor burden (1). These goals are generally accomplished with a craniotomy whereby a surgeon excises a substantial amount of tumor tissue through a relatively large surgical opening in the skull. If craniotomy is contraindicated, as in the case of an inoperable tumor that lies in critical brain structures, the surgeon may opt to obtain a small amount of tissue for histological diagnosis with a needle biopsy without tumor debulking. When craniotomy is possible, the surgeon must attempt to remove as much of the tumor as safely possible as many studies have shown substantial survival benefits for patients that have a large proportion of their tumor removed, or high extent-of-resection (EOR) (109). In GBM, as with all HGGs, the resection target is the contrast-enhancing component of the tumor on CE-T1w MRI.

Regardless of the procedure performed (biopsy or craniotomy), it is imperative that at all times the surgeon have firm grasp of the tumor distribution in the brain while in the operating room. One of the most widely used methods to do this is to use an intraoperative stereotactic neuronavigation with MRI guidance. This technique relates the position of the surgeon's instrument in space to the location of intracranial structures on MR images by establishing a fiducial-spatial coordinate system similar to that used in global positioning devices (**Figure 1.18**)

(110). Using fiducial markers on each instrument as a reference, the navigation tower is able to triangulate the position of the instrument relative to specific intracranial structures, like tumor or ventricle, within image space (111). This allows the surgeon not only to visualize the neoplastic tissue with his eye, but also direct resection or biopsy based on neuroimaging findings displayed on a monitor at the bedside. The ability to perform real-time intraoperative guidance increases the accuracy and safety of resection and biopsy, and such technology has become a standard in neurosurgery around the world (110).

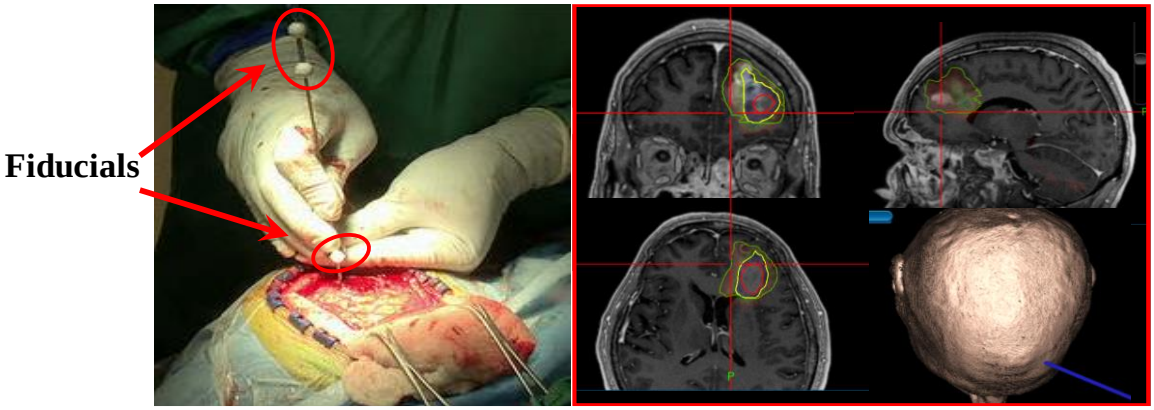

Figure 1.18. Neuronavigation using frameless system with instrument fiducials.

One of the central challenges in GBM surgery is that neoplastic tissue detected using MRI is often indistinguishable from normal brain. Studies evaluating the extent of brain tumor resection highlight the fact that in many cases, especially in diffusely invasive brain tumors, a significant amount of residual tumor remains even after GTR, with deleterious effects on patient outcome (46-48; 112-114). Moreover, surgeons have a limited ability to predict when all resectable tumor has indeed been removed. Consequently, a variety of technologies have been developed to improve surgical outcomes. Retrospective analyses suggest that intraoperative MRI, an approach in which brain tumor resection is performed in a highly specialized surgical suite containing an MRI machine, improves EOR and outcome (115; 116). Intraoperative dyes, near infrared and visible, have been proposed as a means of identifying tumor margins intraoperatively, and recently a clinical trial has demonstrated that the use of a fluorescent dye may improve the EOR and six-month PFS in GBM patients (50). A number of efforts are underway to use dye-based and label-free intraoperative microscopy to improve the surgeon's ability to distinguish tumor-infiltrated brain from noninfiltrated tissue.

Radiation Therapy

The most effective adjuvant therapy for GBM after surgery is high dose external beam RT. The optimal RT dosing regimen for GBM treats a wide margin, including nonenhancing T2-weighted (T2w) or T2w/FLAIR-hyperintense regions to a moderate dose (45-54 Gy), and boosting the resection cavity and any residual CE-T1w abnormality to a higher dose (60 Gy) (117; 118). This is generally given in thirty, 2 Gy fractions five times per week using an intensity-modulated technique

that prevents high doses from being given to critical structures like the brain stem and the optic nerves.

There are three main volumes considered in RT planning: the gross tumor volume (GTV), the clinical target volume (CTV), and the planning target volume (PTV). The GTV1 describes the position and extent of the primary tumor encompassing any contrast-enhancing tissue as well as the resection cavity if present on CE-T1w images. The CTV1 surrounds the GTV and describes the extent of microscopic, occult tumor spread; this is generally accomplished by adding a uniform margin to the GTV. Once these two volumes are established, the third volume, the PTV1, which allows for uncertainties in planning or delivery, must be added, and the normal tissue structures in the vicinity of the target must be considered. All three of these target volumes are generated for the contrast-enhancing lesion as well as any edematous T2-hyperintense abnormality surrounding it (GTV2, CTV2, and PTV3), resulting in six total tumor regions-of-interest (ROIs).

While RT has long been used in the treatment of GBMs and will delay their progression, it generally will not control these tumors long term. Recurrence is largely due to the infiltrative nature of the tumor, with cells traveling to regions distant from the central contrast-enhancing regions. Because of this, regions of nonenhancing signal abnormality on T2w images are covered in a typical RT treatment plan too, albeit with moderate doses. However, T_{2w}/FLAIR is not tumor-specific due to difficulties in differentiating nonenhancing tumor from other causes of increased FLAIR or T2 signal (e.g. radiation effects, ischemic injury, edema, and infection) (119; 120). T_{1w}-contrast-enhanced MRI displays the leaky

neovasculature associated with these tumors, indicating well-perfused tumor lesions with excellent oxygen and chemotherapeutic drug delivery. Despite the constant effort of tumor cells to recruit new blood vessels (neoangiogenesis), there is a significant gradient of oxygen. Hypoxia occurs in tumors 100 μm away from the blood supply, and tends to be widespread in GBMs. The viable hypoxic cells existing in solid tumors are associated with the failure of radiation and certain chemotherapy regimens due to the absence of reactive oxygen species (121). This combination of occult infiltration and RT resistance due to hypoxia severely limits the efficacy of RT in GBM management.

Therapy Planning: Limitations of Standard MRI

As previously stated, the primary target for resection and high dose RT is contrast-enhancing tissue on CE-T1w imaging. Contrast-enhancing tissue is targeted because diffusion of contrast into the parenchyma is indicative of the leaky neovasculature associated high-grade tumor (122). However, intravenous contrast agents do not effectively reach tumor regions beyond this neovasculature, leaving large portions of viable tumor unseen (123). Unfortunately, these occult neoplastic foci are highly infiltrative and are largely credited with initiating GBM recurrence (67). The presence of contrast-enhancement in a brain tumor is often regarded as an indication of higher grade (grade III and IV). However, Scott et al. reported that nonenhancing gliomas were malignant in approximately one third of cases, in a sample size of 314 patients (124). In a cohort of 20 patients, Kondziolka et al. found that MRI cannot be used as a reliable tool to predict the histological diagnosis of low grade versus high grade astrocytoma (50% false-positive rate)

(125). From a study of 393 patients using an international multicenter brain tumor MRI database, the value of routine MRI in the classification of brain tumors in terms of both cell type and grade was estimated to be 65% for sensitivity and 95% for specificity in high grade tumors (126). Perhaps the use of contrast-enhancement as the sole target in surgery and the primary target in RT is the reason that approximately 80% of patients with GBM recur within 2 cm of their original tumor (127).

To account for the occult infiltration not seen with CE-T1w imaging, regions of T2w/FLAIR abnormality are covered for RT with added margins. Determining the boundary of T2-hyperintensities can be challenging, however, as the edges are not discrete and fade into normal tissue especially on low resolution images. This is because changes in T2 relaxation due to disease are quite subtle and GBCAs do not have a strong T2 relaxivity (128; 129). Furthermore, T2w/FLAIR suffers from limited specificity as nonenhancing tumor is difficult to differentiate from other tumor-related abnormalities (e.g. vasogenic edema, ischemic injury, and infection) (69; 119; 120; 130; 131). Moreover, using the entire T2/FLAIR abnormality to define a GTV2 often translates into a CTV2 and PTV2 that cover a large portion of the brain resulting in doses of ionizing radiation above the dose/volume tolerance of normal tissue (132; 133).

1.4.4 MRI in Glioma Response Assessment

The evaluation of GBM treatment rests on either the duration of patient survival or some measure of radiographic response, most often the presence of tumor-associated findings on MRI (134). Thus, serial imaging with CE-T1w and

T2/FLAIR at 1-3 month intervals is the mainstay for assessing treatment response in these patients. Clinical response is generally graded using a myriad of imaging and clinical features per the guidelines set forth by the McDonald or Response Assessment in Neuro-Oncology (RANO) criteria (67; 135).

Using the product of the two largest orthogonal tumor diameters on CE-T1w images, the McDonald method denotes progression as a 25% diameter-product increase on two consecutive contrast-enhanced T1-weighted MRI scans. However, the limitations of this method have been reviewed in detail and include: a difficulty measuring irregularly shaped tumors, a lack of assessment of the non-enhancing tumor, and a lack of guidance for the assessment of multifocal tumors (136). To overcome the limitations of the McDonald criteria, the RANO criteria added the following to a diagnosis of progression: a significant increase in T2/FLAIR nonenhancing lesions on stable/increasing doses of corticosteroids compared with baseline scan or best response after initiation of therapy; the appearance of any new lesions; clear progression of non-measurable lesions; or definite clinical deterioration not attributable to other causes apart from the tumor, or to decrease in corticosteroid dose (67).

Response Assessment: Limitations of Standard MRI

The substantial dependence of the McDonald and RANO criteria on the use of CE-T1w presents a significant limitation in terms of response assessment. First, the addition of TMZ to RT severely complicates interpretation of standard imaging and increases the likelihood of false progression. About 40% of patients receiving RT and TMZ experience “early progression” seen as increased contrast-enhancing

areas on follow-up T1-weighted images using the MC (4; 137). More than half of these cases, however, turn out to be pseudoprogression (PsP) -- a TMZ+RT-induced, inflammatory reaction resulting in increased vessel permeability and larger contrast-enhancing regions that are not associated with tumor progression and clinical deterioration (57). Consequently, a large fraction of patients that would not show progression on histopathology are treated as non-responders with large steroid and TMZ doses for up to four months before pseudoprogression is determined. Lastly, enhancement can be influenced by changes in corticosteroid dose, antiangiogenic therapies, and radiologic techniques. Thus, medications and imaging studies prescribed for supportive and adjuvant reasons may affect response assessment using CE-T1w imaging.

The additions that came with the RANO criteria, along with the authors' avid recommendation of volumetric tumor measurement, broadened the definition of progression by including corticosteroid dosage, and addressed the imaging concerns associated with multifocal and non-enhancing tumor. However, the increasing use of new molecularly-targeted agents further diminishes the reliability of standard MRI in response determination. The recent addition of epigenetic and vascular modulators to GBM treatment –like histone deacetylase inhibitors (HDACi) and bevacizumab (BEV), further complicate response monitoring in this way. For example, HDACi antagonize histone deacetylases (HDAC), altering histone acetylation profiles and modulating gene expression causing vast changes in global cellular metabolism resulting in cytostasis rather than cell death (138-140). However, since HDACi's are not overtly cytotoxic, tumor and vascular morphology remains relatively unchanged, limiting the usefulness of

CE-T1w imaging. On the other hand, BEV is a monoclonal antibody directed to VEGF which ultimately decreases BBB permeability, a phenomenon that hides what limited contrast-enhancing tissue is present (67; 141; 142). This image obscuring response to BEV therapy has been termed pseudoresponse (PsR). Though BEV is FDA approved as salvage therapy due to its relief of mass effect and increase in quality of life, it unfortunately has not been shown to confer an OS benefit for GBM in randomized clinical trials (143). The gene expression and physiologic changes associated with HDACi and BVZ confound the interpretation of conventional imaging, leading to equivocal findings and, consequently, halt any meaningful changes in anti-tumor therapy during the immediate post-RT period.

Another source of confounding in GBM response assessment concerns the MR-based spatial measurement method set forth in both the McDonald and RANO response criteria. Using the product of the two largest orthogonal tumor diameters measured by a radiologist, these methods denote progression as a 25% diameter-product increase on two consecutive CE-T1w scans (67; 144). However, the limitations of this linear measurement method have been reviewed in detail and include a difficulty measuring irregularly shaped tumors and a lack of guidance for the assessment of multifocal tumors (136). Moreover, GBMs are inherently heterogeneous in shape and composition, comprised of various tumor grades, necrotic tissue, and areas of tumor-infiltrated yet morphologically normal tissue, they are incredibly difficult to classify in this manner. Additionally, gliomas are often heterogeneously enhanced upon contrast injection, and enhancement is not uniform across a patient population complicating longitudinal analysis this way. Lastly, this method does not account for the changes associated with residual

tumor volume expansion upon hemispheric debulking or the infiltration of blood products into the resection cavity postoperatively: parameters that must be considered by the attending neuroradiologist. This is both subjective and time consuming. Unfortunately, the use of these criteria for evaluating GBM response in clinical trials may result in a gross skewing of response rates and PFS measures due to this inaccurate method of volume determination.

1.5 Molecular Imaging in Glioma

Per the Society of Nuclear Medicine and Molecular Imaging (SNMMI), a community committed to the development, improvement, and expansion of molecular imaging for the betterment of health care services, molecular imaging is

> " a type of medical imaging that provides detailed pictures of what is happening inside the body at the molecular and cellular level (145)."

Where other diagnostic imaging procedures – including x-rays, CT, and ultrasound – generate images describing physical structure or physiology, molecular imaging gives insight on how the body is functioning at a chemical and cellular level. With many molecular imaging modalities these biological phenomena become quantifiable allowing clinicians and scientists to objectively evaluate the molecular and cellular ongoings within the body using all 3 spatial dimensions in a non-invasive manner. Using the information obtained from molecular imaging studies, scientists and healthcare providers are able to gain better understanding of molecular pathways in disease, quickly assess new drugs, improve and personalize the selection of therapy, accurately monitor patient response to therapy, and identify individuals at risk for certain diseases.

Glioma has received significant interest in the field of molecular imaging as a disease where the understanding of molecular and cellular phenomena is essential to effectively diagnosing and treating patients. For example, the molecular characterization of gliomas using positron emission tomography (PET), single photon emission CT (SPECT), and MR spectroscopy (MRS) are changing the way that gliomas are defined and assisting in the non-invasive determination of tumor grade and prognosis (146; 147). Intraoperatively, fluorescent dyes and probes are used as optical tracers to identify the presence of cancerous tissue in real-time and precisely guide the resections of tumor tissue at the contrast-enhancing margins (148). After surgery and/or RT, amino acid PET shows excellent promise in being able to differentiate tissue changes due to treatment and changes due to malignant transformation or infiltration. Molecular imaging has a potential role to play during every phase of glioma management, from diagnosis to response assessment. There is no doubt that the emerging molecular imaging technologies for imaging, especially those that can accurately define tumor metabolism, with have a great impact on the management of patients with glioma and will facilitate the development of more effective biological treatment strategies.

As molecular imaging is a vast, ever-evolving field, a complete discussion of each technique and its uses in glioma is beyond the scope of this thesis. However, a detailed introduction to two molecular imaging methods at the center of the dissertation work is essential for a complete understanding of the chapters to come. These two techniques are intraoperative fluorescence microscopy and high-resolution, whole-brain spectroscopic MRI (sMRI).

1.5.1 Intraoperative Optical Imaging

Intraoperative optical imaging (IOI) utilizes infrared, visible, and/or ultraviolet light to identify and describe tissue of interest in the operating room in real time. Using the physicochemical properties of compounds within tissue or exogenous tracers administered beforehand, surgeons can visualize tissue with specific metabolic characteristics or expression profiles using the light remitted after tissue excitation. Superior spatial and temporal resolution along with the ease with which it can be integrated into the operating room environment and workflow make IOI an ideal method for assisting tumor resections. This is why a significant amount of work has been done to develop and apply IOI to the resection of gliomas over the past decade (148). The IOI probe that has seen the most development and greatest clinical success in glioma surgery is 5-aminolevulinic acid (5-ALA), an oral prodrug that is converted to the fluorescent compound in glioma cells, permitting real-time intraoperative visualization of malignant tissue with fluorescence microscopy.

5-Aminolevulinic Acid

5-ALA is a naturally occurring molecule that is found in humans, and is necessary for some basic physiological processes (149-151). The metabolism of aminolevulinic acid (ALA) is the first step in the biochemical pathway resulting in heme synthesis (**Figure 1.19A**). Aminolevulinic acid is not a photosensitizer, but rather a metabolic precursor of protoporphyrin IX (PpIX), which is a photosensitizer. The synthesis of 5-ALA is normally tightly controlled by feedback inhibition of the enzyme, 5-ALA synthetase, presumably by intracellular heme

levels. 5-ALA, when provided to the cell, bypasses this control point and results in the accumulation of PpIX, which is converted into heme by ferrochelatase through the addition of iron to the PpIX nucleus (152-157).

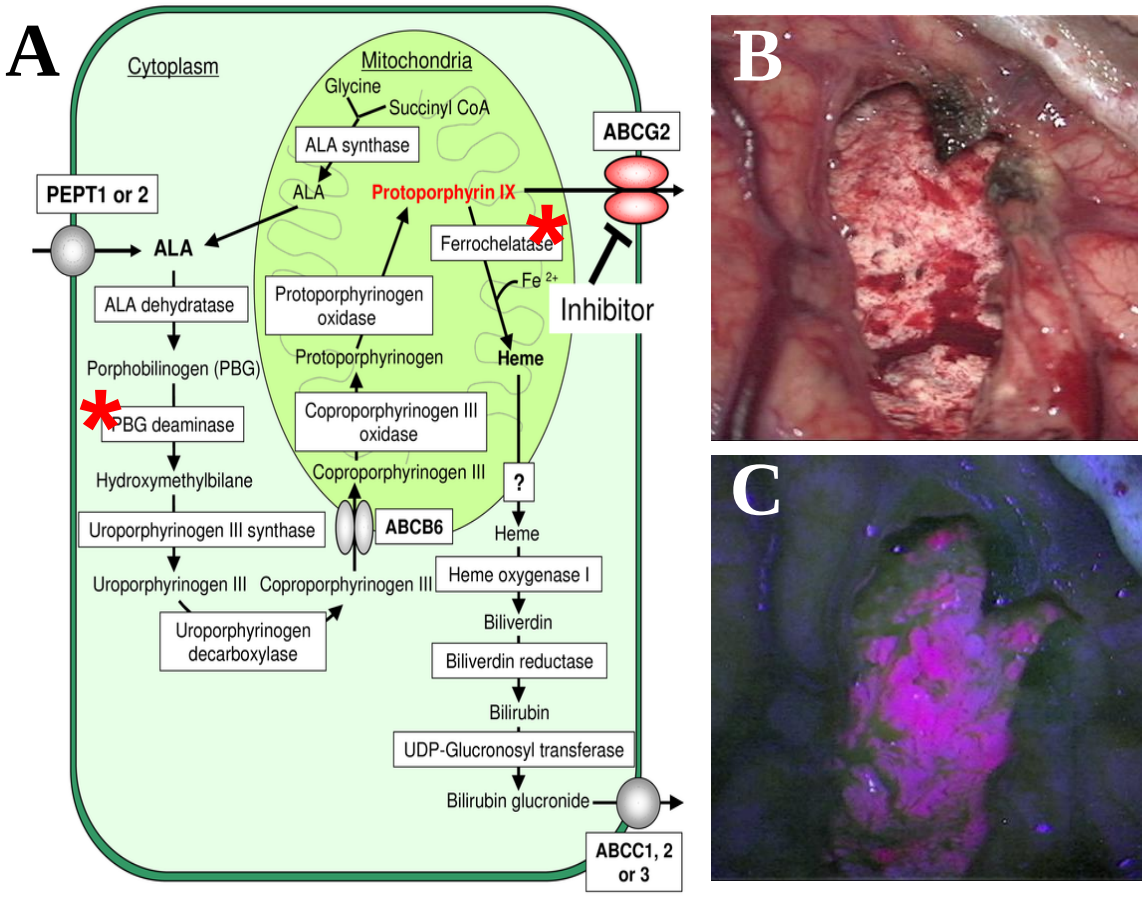

Figure 1.19. Heme biosynthetic pathway leading to the accumulation of PpIX. PpIX accumulates within glioma cells for a number of reasons, most notably decreased ferrochelatase and increased PBG deaminase activity (**A**). Upon excitation at ~405 nm, fluorescence helps the surgeon visualize infiltrating glioma tissue unseen under white light (**B** and **C**). Panel A reproduced from *Ishikawa, T., et al. (2011) Pharmaceutics 3(3), DOI:10.3390/pharmaceutics3030615* under the Creative Commons Attribution (CC BY) license (158).

Approximately 350 mg of ALA is synthesized in humans each day for endogenous heme production, and the oral administration of exogenous 5-ALA results in the production of high intracellular (mitochondrial) concentrations of PpIX (159). It is preferentially taken up by the liver, kidney, endothelia and skin as well as by malignant gliomas (WHO grade III and IV) resulting in an accumulation of PpIX in these tissues (160). Four hours after oral administration of 20 mg/kg body weight 5-ALA, the maximum PpIX plasma level is reached. This level rapidly declines during the subsequent 20 hours and is not detectable anymore 48 hours after administration. 5-ALA is eliminated quickly with a terminal half-life of 1-3 hours. Approximately 30% of an orally administered dose of 20 mg/kg body weight is excreted unchanged in urine within 12 hours.

Malignant glioma tissue (WHO grade III and IV) has also been demonstrated to synthesize and accumulate porphyrins in response to 5-ALA administration (160). The concentration of PpIX is significantly lower in white matter than in cortex and tumor, though normal tissue surrounding the tumor may also exhibit a small amount of PpIX accumulation (161; 162). Fortunately, 5-ALA induced PpIX formation is significantly higher in malignant tissue than in normal brain. At the recommended oral dose of 20 mg/kg body weight, tumor to normal brain-fluorescence ratios are usually high and offer lucid contrast for visual perception of tumor tissue under violet-blue light for at least 9 hours (**Figure 1.19B and C**). In contrast, in low-grade tumors (WHO-grade I and II) no visible fluorescence is generally observed though spectroscopic tools can identify the presence of PpIX in tumor tissue. The phenomenon of PpIX accumulation in WHO grade III and IV malignant gliomas may be explained by higher 5-ALA uptake into

the tumor tissue or an altered pattern of expression or activity of enzymes (e.g. increased PBG deaminase and decreased Ferrochelatase) involved in hemoglobin biosynthesis in tumor cells. Explanations for higher 5-ALA uptake include a disrupted blood-brain barrier, increased neo-vascularization, and the overexpression of membrane transporters in glioma tissue.

After excitation with blue light (λ=400-410 nm), PpIX is strongly fluorescent (peak at λ=635 nm) and can be visualized after appropriate modifications to a standard neurosurgical microscope (163). Fluorescence emission is generally described as intense (solid) red fluorescence for solid tumor tissue and vague pink fluorescence for infiltrating. Conversely, normal brain tissue reflects the violet-blue light and appears blue because it lacks an elevation in PpIX. The positive predictive value of tissue fluorescence for identifying malignant histology in biopsy samples is quite high, ranging from 90% to 98% in a number of qualitative and quantitative trials (161; 164-166). The sensitivity and specificity of fluorescence, though not quite as high, are still considerable ranging from 75% - 90% and 71% - 96%, respectively. Comparative studies have found that FGS can identify tumor tissue outside of contrast-enhancement, but also that the tumor detection rate (per histopathological classification) in GBM is higher for 5-ALA fluorescence than with neuronavigation or intraoperative MRI (167-169). Taken together, these studies suggested that fluorescence accurately described the presence of tumor cells in tissue, thus solidifying its utility as an intraoperative marker for malignant glioma tissue with the aim of improving the surgical resection of these tumors.

A European Phase III randomized, controlled multicenter trial demonstrated a significant clinical benefit to patients who underwent fluorescence-guided surgery (FGS) of their malignant glioma after 5-ALA administration compared to those who underwent conventional resection (50). A larger number of "complete" resections (defined as absence of contrast-enhancing tumor as revealed by early postoperative MRI) was achieved using FGS (65% vs 36 %) than with conventional microsurgery (50; 51; 170). In addition, the trial showed a significantly greater 6-month progression free period (41% vs 21%) and no significant drug-based toxicity. Interim analysis resulted in the early detection of statistical significance with primary endpoints being the number of patients without contrast-enhancing tumor on MRI (within 72 hours of surgery) and 6-month progression free survival. Continued enrollment in the pivotal trial resulted in reproduction of the endpoints upon trial completion.

The Stummer trial supported market approval and deployment under a risk management program in Europe, and ultimately a myriad of follow-up studies on the technique (171). Since then, 5-ALA studies from around the world have shown that high EOR, particularly those approaching gross-total-resection (GTR), portend significant increases in OS (≈1-8 months) relative to subtotal resection even when known confounders like age and performance status are controlled (42; 43; 52; 172-174). Furthermore, many studies that have failed to reach significance show non-significant trends in survival supporting aggressive resection (175; 176). Taken as a whole, the current collection of work sets forth evidence –at the level 2b per the Oxford Center for Evidence-based Medicine –calling for larger,

prospective GBM brain tumor resection studies in the United States to more accurately elucidate 5-ALA and EOR's effect on patient outcomes.

1.5.2 Magnetic Resonance Spectroscopy

Proton magnetic resonance spectroscopy (^{1}H-MRS) is an analytical method that enables the identification and quantification of small molecules non-invasively *in vivo*. MRS is the *in vivo* application of nuclear magnetic resonance (NMR), a technique long used by physicists and chemists to investigate the magnetic moments of nuclei and elucidate the physical structure of small organic molecules, respectively. Similar to MRI, the hydrogen atom is generally used as the signal source in MRS as it is the most abundant, naturally occurring nucleus with a magnetic moment in human tissue and has a high gyromagnetic ratio (177). MRS differs from conventional MRI, which is only sensitive to the relaxation of protons in water molecules, in that signal from unique protons on a number of small molecules is recorded over time, providing spatially-encoded chemical information (178). As such, every spatial location is filled with a chemical shift spectrum describing the signal received from a myriad of molecular species within the imaging voxel (**Figure 1.20**). These spectra are significantly altered in many neurological disorders reflecting the alteration of a number of biological processes including cellular energetics, protein synthesis, phospholipid metabolism, and more (179).

Spectra of metabolites are shown on $\boldsymbol{x}$ and $\boldsymbol{y}$ axes where $\boldsymbol{x}$ represents the chemical shift of the metabolites in units of parts per million (ppm) and $\boldsymbol{y}$ represents the arbitrary signal amplitude of the metabolites. Based on convention,

the ppm increases from right to left. The height of each metabolite peak refers to a relative concentration and the area under the curve to metabolite concentration (180). Although the resonance frequency of each nucleus changes with the main magnetic field (**Eq 1.7** and **1.8**), the shift at which a specific metabolite is seen is the same regardless of field strength (**Eq 1.9**).

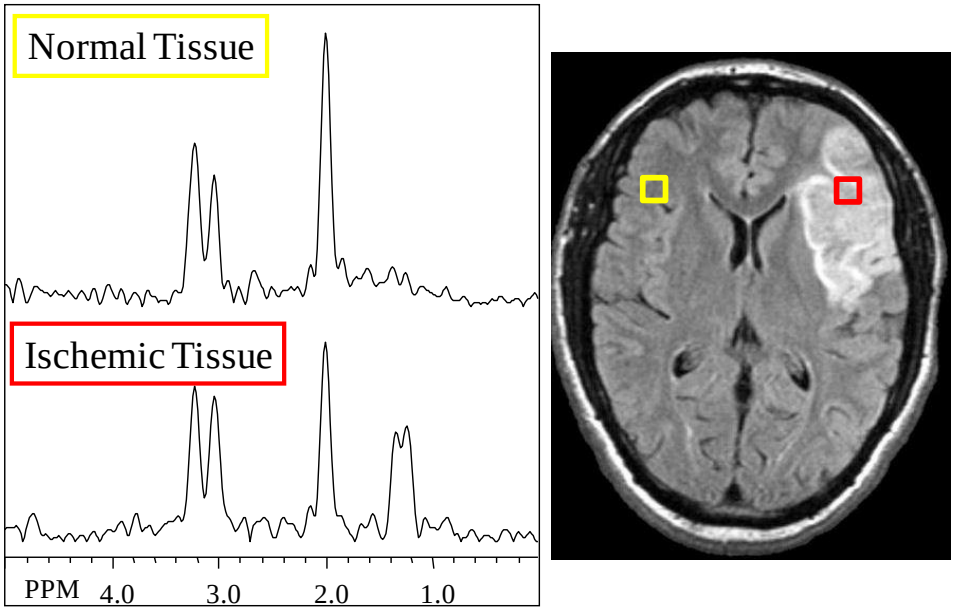

Figure 1.20. Characteristic spectra from MRS. MR spectra from normal and ischemic brain give spectra with structural differences indicating a change in the molecular profile of the tissue.

What follows is a technical discussion of the aspects that require special consideration in spectroscopy, methods used to optimize MRS acquisition, categories of MRS sequences, and important factors in data processing. It should be noted that the physics governing the signal excitation and acquisition are the same as outlined in **1.4.4** (*Chemical Shift section*), and the only difference in each technique is the RF pulse sequence and field gradient magnitude/orientation. Though this section is by no means comprehensive, it should give an adequate introduction to important concepts in spectroscopic acquisitions, the differences in spectroscopic methods, and the pros/cons of each approach.

1.5.3 Spectroscopic Magnetic Resonance Imaging

MR Spectra

Each peak in the chemical shift signal represents a proton or set of protons on a small molecule that exhibits a unique resonance frequency. However, the signal from any specific metabolite protons does not occur at a single Larmor frequency, but is spread out over a narrow range of frequencies due to the T2 relaxation and magnetic field inhomogeneity within the voxel. T2 relaxation that occurs during the acquisition period causes a spreading of the peak in the temporal frequency domain, which is characterized by the linewidth (full width at half maximum) of the peak. Also, the range of magnetic field values within the voxel result in a range of Larmor frequencies, and this range of Larmor frequencies is manifested in a spreading of the chemical shift peak. Similarly, interactions between the atomic nuclei of neighboring chemical groups within the same molecule causes each peak to be broken down, or “split”, into a set of peaks

(doublet, triplet, multiplet). This is called *J-coupling* and results in a fixed frequency shift between peaks independent of magnetic field amplitude.

There are a limited number of metabolites that can be investigated with MRS as only those with appreciable concentrations in the brain that exhibit shifts between the water and lipid resonance frequencies are considered. Even given these limitations, several small molecules describing a number of metabolic and cellular processes can be evaluated by identifying the chemical shift peak pathognomonic for each metabolite. A limited list of metabolites that are generally evaluated using standard brain MR spectroscopy can be found in **Table 1.2** along with the chemical shifts of their most descriptive peak, their T2 length, and the roles with which they are associated in tissue.

Metabolite	Abbrev	PPM	T2 length	Role
Myo-inositol	MI	3.6	Short	Glial marker/osmolyte
Choline	CHO	3.2	Long	Phospholipid biosynthesis, PLC signaling
Creatine	Cr	3.0	Long	Cellular Energtics
Glutamine/ Glutamate	Glx	2.1-2.5	Short	Excitatory neurotransmitter
N-acetylaspartate	NAA	2.0	Long	Neuronal Marker
Lactate	Lac	1.3	Long	Anaerobic glycolysis
Free Lipids	Lip	0.9	Long	Tissue Necrosis (high grade tumor)

Table 1.2. Metabolites observed with proton MRS with chemical shifts, T2 length, and role within tissue.

The Effect of TE on Spectra

As in MRI, the TE of the pulse sequence affects the information present within the chemical shift spectrum. Sequences with short TEs (20-40 ms) acquire signal from metabolites that have short and long T2 relaxation times, while those with long TEs (135-288 ms) only acquire signal from those with long T2 relaxation times (i.e. all the short T2 metabolites have reached equilibrium). Because of less signal loss due to T1 and T2 effects and the early signal acquisition, short TE sequences have higher SNR and additional metabolites in each spectrum (e.g. MI, Glx, and others) compared to long TE sequences. The addition of these short T2 metabolites allows the evaluation of a number of additional metabolic process; however, these extra metabolites can cause peak overlap in the spectrum resulting in lower spectral resolution (i.e. separation of metabolite peaks in spectrum) (179). Conversely, as the TE becomes longer, the SNR drops and the complexity of the spectrum decreases due to the suppression of short T2 metabolites. This results in spectra that are less noisy with fewer sharp resonances (**Figure 1.21**).

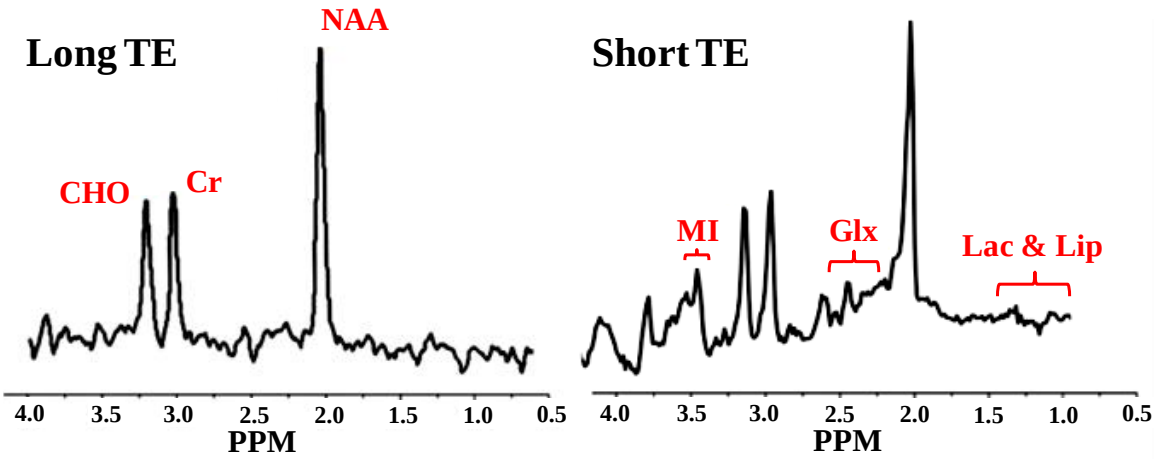

Figure 1.21. Representative spectra of long (left) and short (right) TE pulse sequences.

Water and Lipid Suppression

Metabolite levels range from approximately 1 mM to 10 mM in a normal brain while protons in brain water are approximately 80 M and lipid concentration in peri-cranial fat is quite high as well. Therefore, to acquire signal from the lower concentration metabolites without having their signal obscured by massive water and lipid peaks (4.7 ppm and 1.3 ppm, respectively), suppression techniques are used to negate the signal from these sources.

One method for nulling water and lipid signal is by the use of chemical shift selective suppression (CHESS). CHESS involves the pre-saturation of water or lipid with frequency-specific 90° RF pulses with narrow bandwidths centered at the resonance frequencies of 4.7 ppm and 1.3 ppm (**Figure 1.22**). Much like the FLAIR sequence in **1.4.2**, the initial frequency selective pulse excites the water and lipid spins into the transverse plane while leaving the metabolite spins at rest. In the transverse plane, the lipid and water spins begin to dephase, a process hastened by the addition of spoiler or dephasing gradients. As there is no longer any longitudinal component of the magnetism for water or lipid, the 90° pulse at the beginning of the spectroscopic sequence only excites protons present on the metabolites. Thus, the resultant echo is effectively devoid of lipid and water signal.

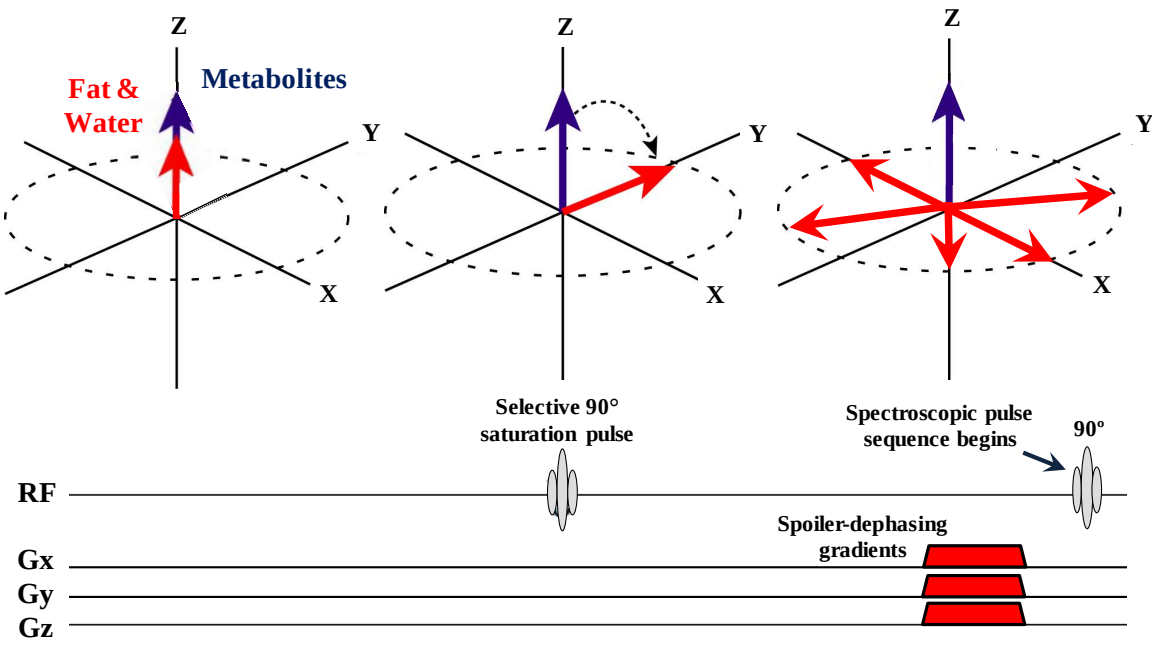

Figure 1.22. CHESS saturation sequence and its impact on different spins. CHESS is a preparatory sequence run before the spectroscopic sequence begins.

Another method by which unwanted subcutaneous lipid around the skull can be suppressed is known as outer volume suppression (OVA). OVA is a spatial saturation method similar to CHESS that allows the nulling of signal in a defined region. The regions to be saturated are generally defined by the user on anatomical images that allow visualization of lipid-laden tissue (i.e. subcutaneous and periorbital fat). Using these precisely-placed, location-specific pulses that are analogous to the frequency-specific pulses of CHESS, lipid signal is saturated before the spectroscopic pulse sequence begins to prevent the metabolite signal from being obscured by lipid contaminants.

Metabolites and their functions

The three strongest signals in *in vivo* MR spectroscopy of a normal human brain come from the molecules N-acetylaspartate (NAA), creatine (CR), and choline (Cho) (**Figure 1.23**). NAA is a free amino acid found in rather high concentrations (average: 10.3 mM) almost exclusively in the CNS and PNS (181). Though its function is not completely known, NAA has been connected with a number of intracellular processes including the storage of aspartate, an osmolyte, and a precursor to N-acetylaspartylglutamate, the most prominent excitatory dipeptide neurotransmitter in the mammalian CNS (182; 183). Although concentrations appear to differ among neuron types and it has been found in some glial cell types, NAA is commonly considered to be a marker of neuronal density and decreases in NAA concentration are associated with neuronal dysfunction and degeneration (181; 184; 185).

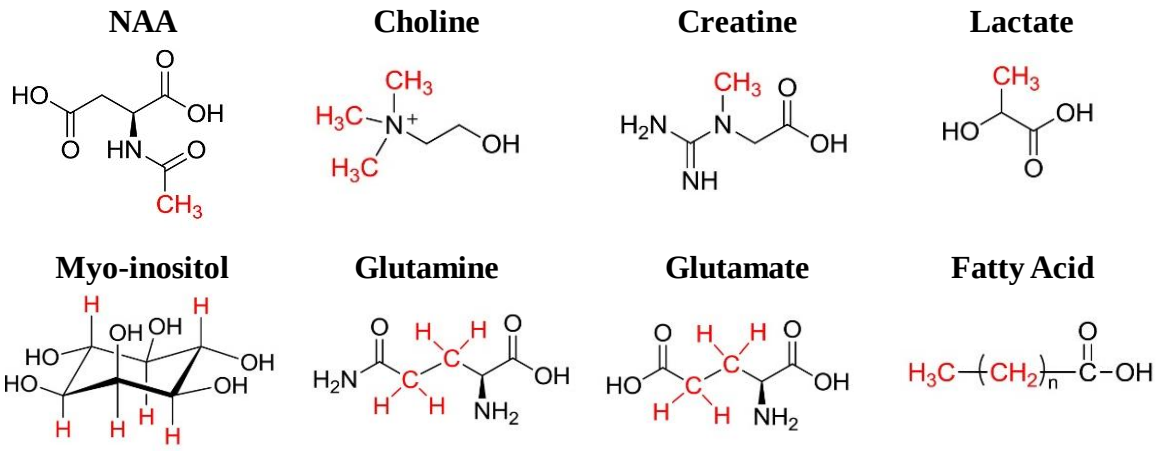

Figure 1.23. Chemical structures of small molecules commonly evaluated using in vivo MRS. The red groups in each structure demarcate the functional groups that give rise to NMR signal in the clinically evaluated ppm interval.

Unlike NAA, CR is a nitrogenous organic acid that is ubiquitous in the human body (e.g. brain, muscle, kidney, and liver) that serves as a reservoir for ATP generation through its phosphorylated intermediate, phosphocreatine. The concentrations of phosphorylated and unphosphorylated forms range from 4.0 mM – 5.6 mM in the human brain, and are relatively stable with age and disease, with the exception of tumor and stroke (183). Because of its stability, many have used CR as a reference marker to normalize other metabolites in the brain. However, this practice is losing hold as more precise, quantitative approaches are being developed. Choline is an essential nutrient that is required for the synthesis of membrane phospholipids like phosphatidylcholine and neurotransmitters like acetylcholine. The signal in MRS studies interpreted as Cho is actually composed of free choline and a number of Cho containing compounds, the primary contributors of which are glycerophosphorylcholine and phosphorylcholine. The combined concentration of these species, termed total choline (tCho) in NMR, ranges from 1.0 mM – 2.5 mM and are non-uniformly distributed in the brain with the caudal cerebrum exhibiting the lowest levels (183; 186). Though interpretations of tCho changes on MRS are complicated by the myriad of metabolites contributing to signal, changes in this peak are generally associated with alterations in phospholipid biosynthesis and membrane choline kinase activity. Increases in tCho are associated with the membrane synthesis in proliferating cells within tumor and gliosis while decreases are associated with infarct due to ischemic stroke and hepatic encephalopathy (187; 188).

There are three chemical species that are generally only present when short TE pulse sequences are used: myo-inositol (MI), glutamate (Glu), and glutamine

(Gln). These molecules have short T2 times and multiple protons with unique resonances resulting in the nullification of these signals in long TE sequences and the absorption these peak into the larger peaks of the other molecules, respectively. For example, MI is a cyclic sugar alcohol described as a glial marker, a precursor to a number of intracellular secondary messengers, and an osmolyte with a concentration similar to CR in the brain (range 4mM – 8 mM). However, MI has a number of resonant protons that exhibit extensive J-coupling, giving rise to a complex chemical shift spectrum. This splitting of signal results in low intensities of individual peaks despite relative abundance of MI as a whole. One of these peaks (resonant at 3.6 ppm) is absorbed by choline and is completely unidentifiable while another (resonant at 4.05 ppm) is nulled during CHESS as it generally falls within the bandwidth of water saturation pulses (183). Similarly, the separation of Glu and Gln, an excitatory neurotransmitter and its precursor (which range from 6.0 – 12.5 mM and 3.0-5.8 mM in the normal brain, respectively), is very difficult because of their similar structures and complex resonance profiles. Moreover, many of their resonances (those between 2.0 ppm and 2.3 ppm) are absorbed by the largest peak in the MRS spectrum, the NAA peak at 2.0 ppm. As such, most spectroscopists refer to a Glu/Gln composite waveform between 2.3 and 2.5 ppm as Glx, the combined resonance of unique protons on both Glu and Gln.

Lactate (Lac) and lipid (Lip), particularly long-chain fatty acids, have proton resonances that range from 0.9 to 2.0 ppm; however, the largest, most clinically relevant peaks for each lie at 1.3 and 1.35, respectively (183). Lac is a product of anaerobic glycolysis that is generally low in the normal brain (< 1 mM) even under conditions that increase lactate peripherally like strenuous physical exertion (189).

Increases in brain Lac levels have been reported in conditions where blood flow is restricted, such as can be seen with stroke, trauma, or tumors (188). Increased Lac is also commonly found in necrotic tissue or fluid-filled cysts. Lip, on the other hand, is highly concentrated in the subcutaneous and periorbital tissues and is composed of a number of hydrophobic compounds including mono and polyglycerides, arachidonic acid derivatives, and cholesterol derivatives. Many of these compounds have fatty acid components with a large number of methylene groups that have NMR active protons. This results in a substantial NMR signal (several orders of magnitude) at 1.35 ppm that crowds-out any of the smaller metabolite peaks including lactate. Lip saturation techniques mask much of this signal, allowing most of the metabolite signals to be retained with the exception of Lac. As such, highly specific Lip suppression techniques like spectral editing must be implemented to retain Lac signal (190).

Magnetic Field Homogeneity and Spectral Quality

To analyze the differences between metabolite resonance frequencies, excitation and signal readout must be done in a highly homogenous magnetic field. A heterogeneous field results in resonance frequency dispersion causing peak broadening, resulting in an increased linewidth. This decreases the SNR and spectral resolution, causing adjacent peaks (like Cho and CR) to merge and even a loss of small metabolite peaks (like MI or Glx) in background noise. To prevent this, sophisticated “shimming” protocols are completed before MRS acquisitions to homogenize the static field as much as possible. Shim coils in the MR scanner generate additional magnetic fields that can interfere (either constructively or

destructively) with the static magnetic field to obtain the homogenous field necessary for MRS.

Shimming becomes more difficult as the volume and complexity of the region imaged increases because of the complexity of magnetic perturbations in space. This is particularly true in regions where the magnetic susceptibility of two tissues changes (i.e. the interface of brain and bone or brain and a metallic implant). This change in susceptibility causes local field distortions that lead to frequency shifts and spin dephasing. The former can cause an absence or shifting of spin excitation resulting in either the absence of signal or the spatial shift in signal acquired, resulting in signal loss and image distortion. If the homogeneity shifts the water proton resonance outside the bandwidth of the suppression RF pulses, the unsuppressed water will drown out the metabolites, leaving little metabolic data intact. Additionally, spin dephasing can cause a decreased T2 relaxation time, ultimately resulting in the loss of short TE metabolites in the chemical shift spectrum.

Spatial Localization

There are two general categories that describe spatial localization in MR spectroscopy: single voxel spectroscopy (SVS) and multi-voxel spectroscopy, also known as magnetic resonance spectroscopic imaging (MRSI) or chemical shift imaging (CSI) (64). In the former, a single spectrum is recorded from a single voxel in a specified brain region. In the latter, an entire ROI is excited and signal from multiple regions is acquired by varying the field gradients. Each technique has advantages and disadvantages, and choosing the right one for a specific purpose is important to improve the quality of results.

SVS utilizes three orthogonal slice selection RF pulses that converge at a single voxel from which spectroscopic data will be acquired (**Figure 1.24A**). Signal from all surrounding regions is eliminated by the intentional dephasing of spins using additional gradients or dephasing RF pulses. After the dephasing is completed, the signal is read unaltered from that location only. This technique is advantageous when the investigator is only concerned with the chemical information from one voxel, requires substantial field homogeneity, and desires improved water suppression and spectral resolution.

The RF pulse intervals, flip angles, and gradient strengths differentiate SVS slice selection techniques into more specific groups including point resolved spectroscopy sequence (PRESS) and stimulated echo acquisition mode (STEAM) sequence (**Figure 1.24B** and **C**). STEAM sequences generally produce a better slice profile (i.e. sharp voxel edges), are more effective at water suppression, and are less sensitive to chemical shift artifact than PRESS because of the 90° pulse trains used and the dephasing gradient added during an interval called the "mixing time" (TM). PRESS sequences, on the other hand, generally give spectra with higher SNR and lower sensitivity to motion than STEAM at the expense of a longer TE. Though these two sequences differ in a few key points, they are generally recognized as being comparable in clinical brain spectroscopy and their use depends on the specific application required. For example, if a very short TE is required, the STEAM sequence is preferable because of its shorter 90° pulse. Conversely, if a longer TE is acceptable, PRESS may be preferable because of its higher SNR and its resilience to motion artifact.

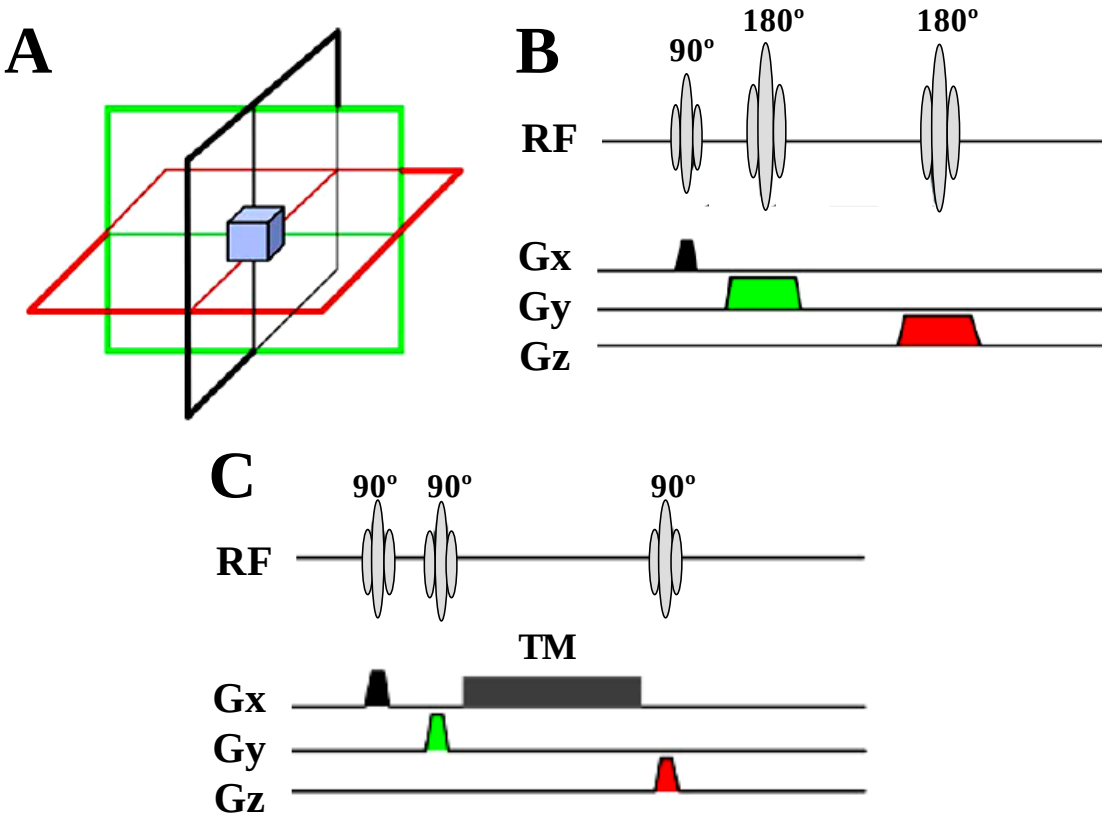

Figure 1.24. Single voxel localization techniques. Single voxel localization is accomplished by collecting signals from voxels at the intersection of three orthogonal slice selection RF pulses (**A**). This is achieved differently for different sequences. The PRESS sequence uses a 90°-180° -180° RF pulse train with the ***x***, ***y***, and ***z*** gradients on, respectively (**B**), while STEAM utilizes 90° RF pulses with shorter slice selection gradients and a large dephasing gradient (**C**). Adapted from *Progress in Nuclear Magnetic Resonance Spectroscopy, 49, Barker, P.B., Lin, D. D. M., In vivo proton MR spectroscopy of the human brain, 99-128, (2006)*, with permission from Elsevier (177).

While SVS acquires signal from a single voxel after slice selection, multi-dimensional spectroscopic sequences, or MRSI sequences, collect multiple spatially-arrayed spectra from individual slices or volumes after excitation (**Figure 1.25**). This is done by a repetition of excitation sequences with varying gradients that alter the phase of the spins before or during signal readout (**Figure 1.26B** and **C**). This procedure is called "phase encoding" and links the phase change experienced by the spins in the presence of the field gradient to their location in space. This is comparable to structural MRI sequences which encode the spatial information of the voxels in the phase of the MR signal. However, unlike MRI, MRSI does not utilize the frequency of the spins to encode the other spatial dimensions. Instead, phase is again modulated with orthogonal gradients and signal readout is performed in the absence of a frequency encoding gradient to retain the frequency information for chemical shift analysis.

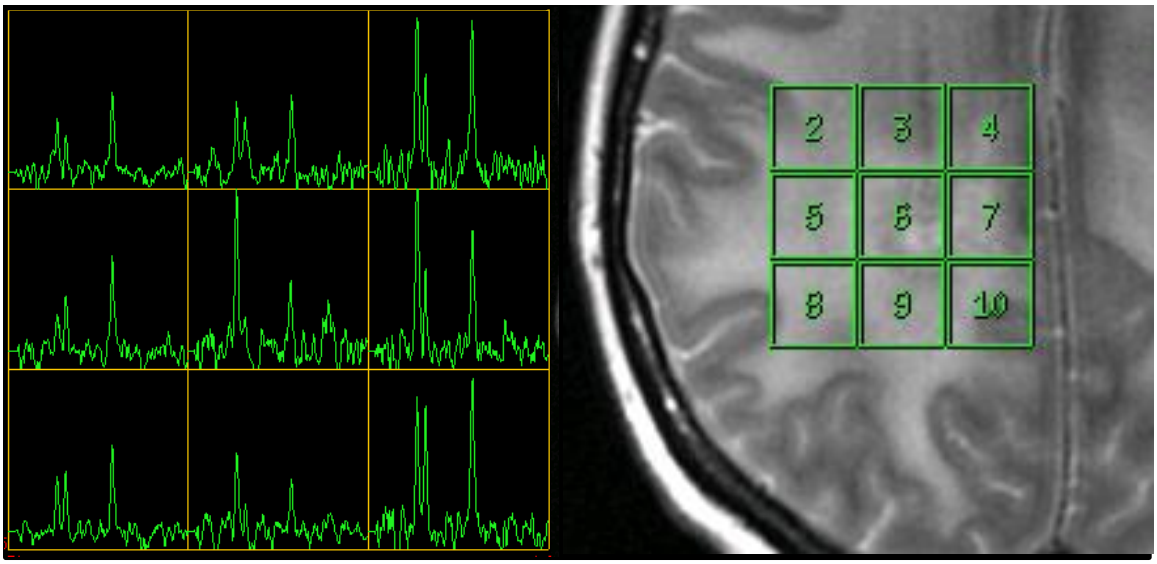

Figure 1.25. Array of spectra acquired using a 2D-MRSI sequence of a suspicious brain lesion.

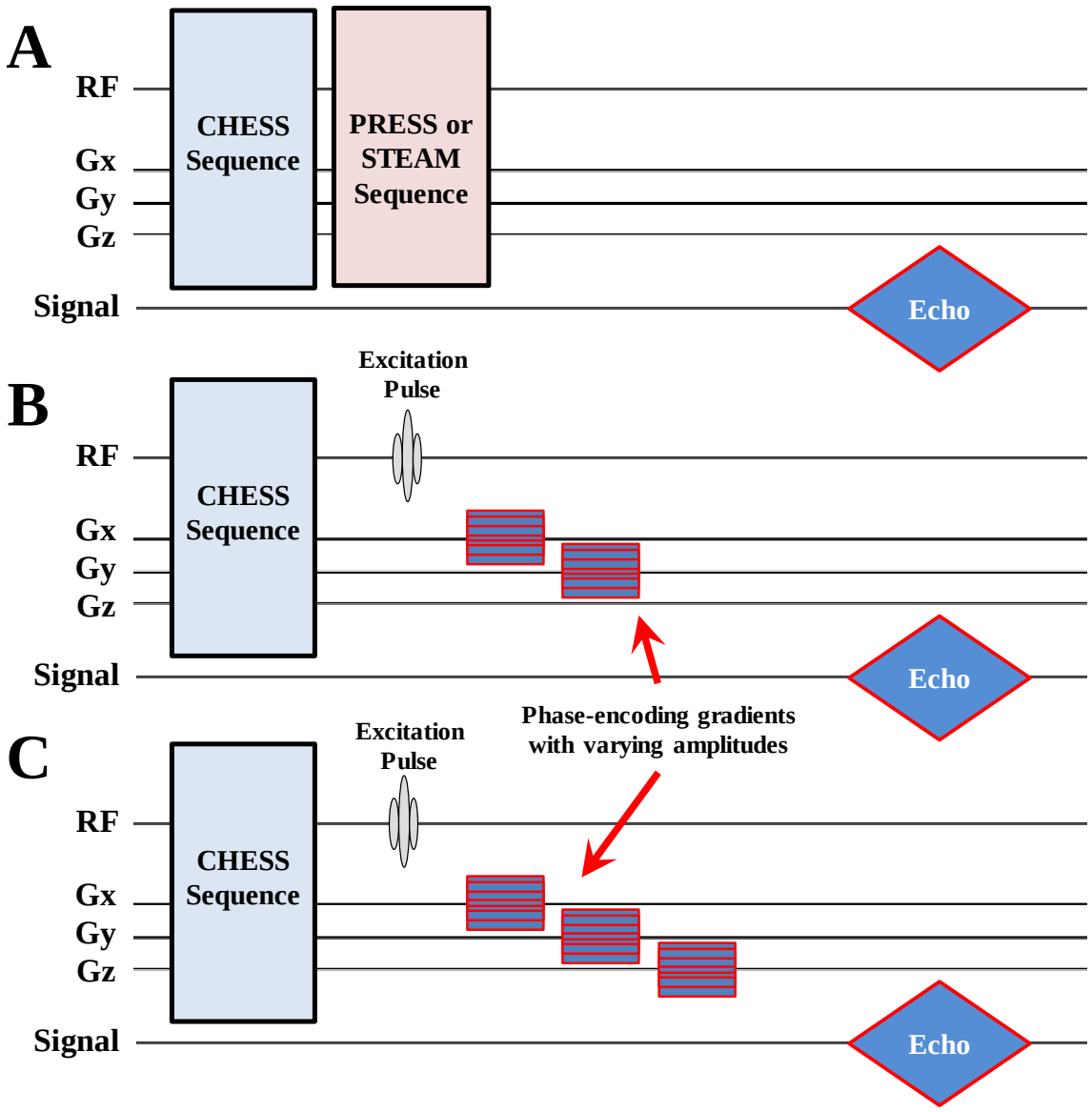

Figure 1.26. Basic pulse sequences for SVS, 2D-MRSI, and 3D-MRSI. While SVS just reads out the signal from a single voxel after water suppression and localization (**A**), MRSI sequences excite a slice or volume of interest and use the variation in gradient amplitude to link spin phase to location (**B** and **C**). The dimension of the image formed is based on the number of the gradients used for phase encoding. The spatial resolution of the spectroscopic image is related to the size of the imaged area and the number of phase-encoding increments used.

1.5.4 Overview of Spectroscopic Data Processing

Following acquisition, spectroscopic data are modified through a number of well-defined procedures to generate reliable estimates of metabolite signal and to map metabolite concentration within the human brain. A comprehensive discussion of this process is beyond the scope of this work; however, a brief explanation of the workflow and a description of the processing pipeline used for this work, the Metabolite Imaging and Data Analysis System (MIDAS), are included in the following pages.

The general workflow used to generate meaningful spectroscopic information, including the generation of chemical shift spectra or metabolite levels, from raw signal output of an MR scanner can be found in **Figure 1.27**. Though this description may vary slightly due to the hardware available or the protocol and parameters used for acquisition, the aforementioned workflow is sufficiently general and describes most of important aspects of data processing necessary for clinical utilization.

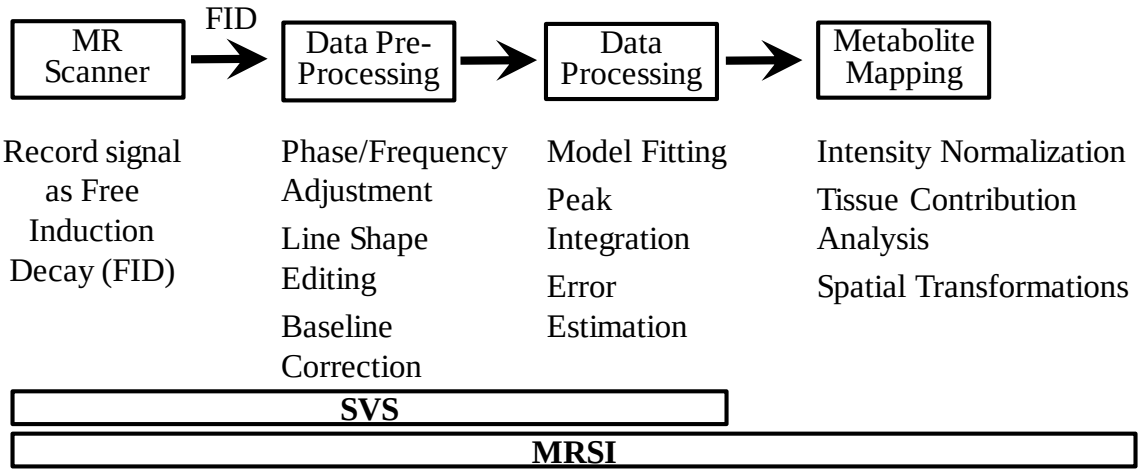

Figure 1.27. Flow chart for processing of MR signals for spectroscopic applications. The bar at the bottom defines the depth of processing for SVS and MRSI sequences.

Spectroscopic Data Pre-processing

The pre-processing of spectroscopic data serves to deconvolve the spatial-phase link between metabolite signals, generate frequency domain data (e.g. chemical shift spectra) from time domain data (e.g. free induction decay recorded by receiver coils), and correct the frequency domain data for structural obscurities that could confound further data processing (61). These processes include phase/frequency adjustment and line shape correction to prevent the loss of signal from destructive interference and line broadening associated with field homogeneities and relaxation effects (**Figure 1.28**). Baseline correction strategies are also implemented to subtract away the signal from other species that can obscure the MR signal from the small molecules of interest. Proton-dense macromolecules like non-suppressed lipids and polypeptides can cause an increase in baseline that should be accounted for.

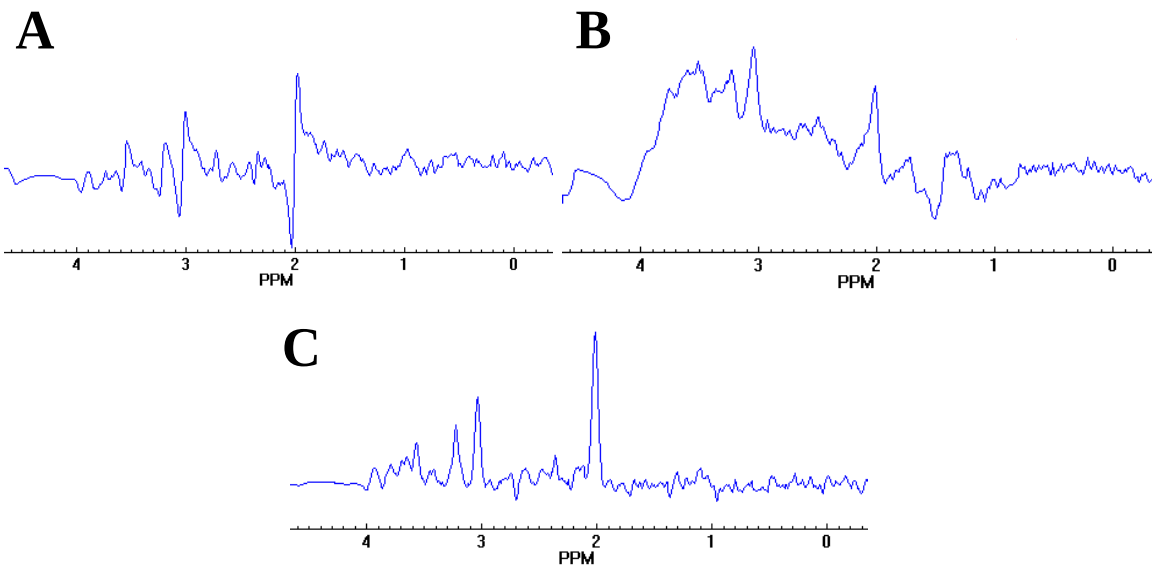

Figure 1.28. The impact of phase and baseline correction on spectral quality. Without phase correction (**A**), spectra exhibit both peaks and troughs that obscure peak amplitude. Without baseline correction (**B**), integrating peak areas become problematic as the lower limit of all peaks are not the same. When phase and baseline correction is completed (**C**), the relative amplitudes of the peaks are much easier to see and integration becomes much more accurate.

Spectroscopic Data Processing

This step of the process is generally concerned with fitting spectral data to a set of known models based on prior knowledge (e.g. known chemical shift, relative abundance, and peak profile), computing parameters for the peak models like area under the curve (AUC), and determining the confidence of the measurements using error estimation (61). The reference molecule from which chemical shift is generally measured in clinical spectroscopy is generally tetramethylsilane, though some processing schemes utilize other salts like 2,2-dimethyl-2-silapentane-5-sulfonate, primarily because of their solubility in water (183; 191). Based on this chemical shift, well-established, individual spectral profiles are used as a starting point to model the raw data (**Figure 1.29**). All estimated parameters, from peak areas to linewidth measures, are generally reported with error terms like the Cramer-Rao lower bound (CRLB): an estimate of the lowest possible estimator-independent error associated with the noise in the spectrum (192). For example, the CRLB for the NAA peak in **Figure 1.29D** (the largest peak in the spectrum) is 2.5%, meaning that the lowest possible error in the computation of the NAA AUC is 2.5%. As a general rule, parameters with CRLB < 20% are considered measured with sufficient precision while those above this threshold should be considered with caution.

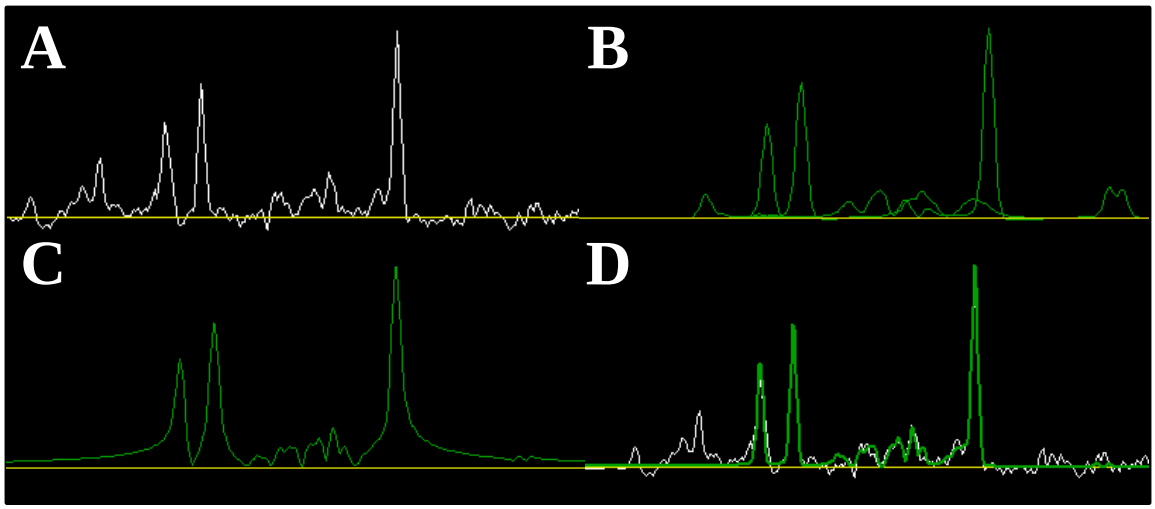

Figure 1.29. Fitting of raw frequency domain data (**A**). Estimates of peak position and height based on prior knowledge (**B**) are fitted to the raw data then combined (**C**) to generate a composite spectrum that describes the underlying spectrum (**D**).

Metabolite Mapping

Whereas SVS only maps a single spectrum to a single voxel, MRSI maps a spectrum to each voxel within the imaging volume, allowing the evaluation of the spatial relationship of metabolites within the brain. To do this, however, steps must be taken to ensure that the signals coming from adjacent voxels are based on the metabolite concentration alone and no other scan-related factors like field inhomogeneity. Additionally, voxels must be correctly oriented relative to each other in space and relative to anatomical MR images taken during the imaging protocol in space. The former requires the comparison metabolite data for each voxel to known tissue-specific populations (e.g. white matter, grey matter, or CSF) from a database of normal metabolite values or by normalizing each value to other signals intrinsic to the voxel, like voxel water. The result is a multiparametric data set, containing at each voxel the intensity-normalized spectral parameters and the tissue contributions to that voxel (**Figure 1.30**). Spatial transformation parameters are also encoded to permit image registration with an atlas or some other anatomical MRI. An additional piece of information is an estimate of the 'quality' of the data in terms of CRLB and peak linewidth at that location, which can be used to exclude spectra of inadequate quality from further analysis.

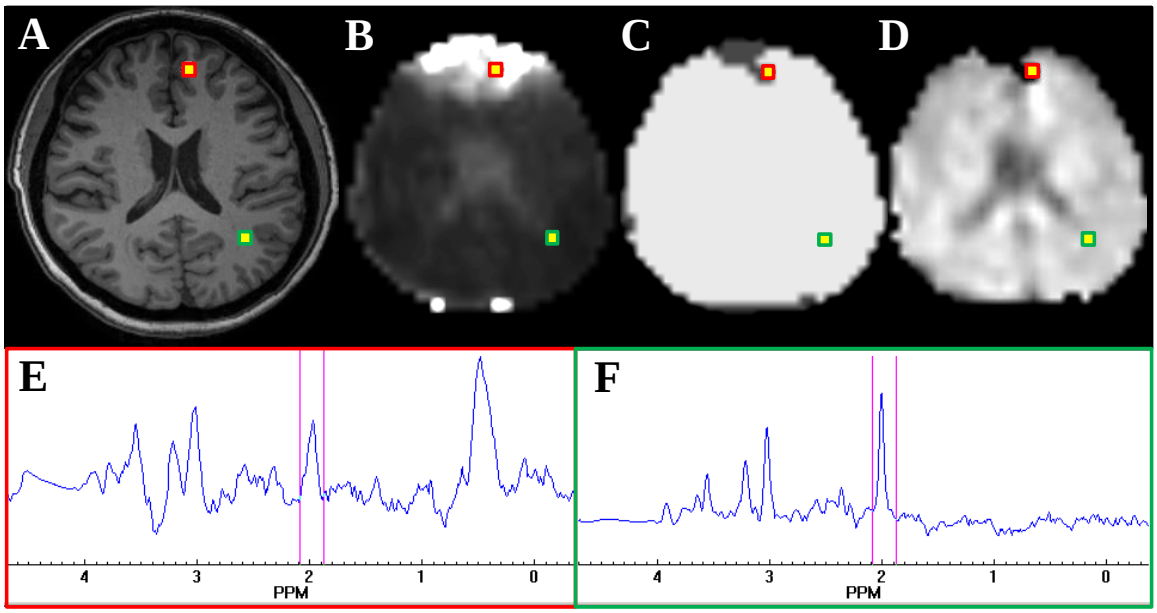

Figure 1.30. Results of MRSI spatial mapping procedure. Anatomical MRI images (**A**) are registered in space to a number of metabolite parameter maps including the CRLB for NAA area (**B**), the CRLB and linewidth-based quality map (**C**), and the normalized NAA metabolite value map (**D**). At each voxel location, a spectrum is available for manual evaluation. The spectrum in **E** comes from a voxel with a high CRLB and linewidth (yellow box with red border), while the spectrum in **F** comes from a voxel with low CRLB and linewidth (yellow box with green border). The NAA peak is bounded by the pink lines in **E** and **F**.

1.5.5 Spectroscopic Methods Used in this Work

Imaging Pulse Sequences Used in This Work

To obtain the highest resolution and sensitivity possible, our group has adapted a whole-brain Echo Planar Spectroscopic Imaging (EPSI) sequence for a Siemens 3T TRIO/TIM system with a 32-channel head coils. The basic EPSI sequence consists of a 3 pulse "WET" water suppression scheme, a slab selective short TI (198 ms) inversion recovery (STIR) lipid suppression scheme, a slab selective spin-echo with 73° excitation pulse, and an oscillating read gradient and phase-encoding in 2 dimensions (193; 194). The STIR pulse also reduces underlying macromolecule signals in the spectrum and decreases the sensitivity of the metabolite signals to potential changes in T1 relaxation times (195; 196). This sequence also includes an interleaved small flip angle (20°) water reference acquisition using generalized auto-calibrating partially parallel acquisitions (GRAPPA) to shorten scan time. Scan parameters are as follows: TR/TE/TI = 1710/70/198 ms, matrix size 50 x 50 (in-plane) x 18 partitions (along *z*); 280 x 280 mm^2 FOV, 180 mm slice thickness; 140 mm excitation slab thickness, resulting in a nominal voxel size of 4.6 mm x 4.6 mm x 5.4 mm. Prior to data acquisition, field map-based 1st order shimming was optimized manually after a vendor-based automated shim protocol. T1-weighted 3D Magnetization-Prepared Rapid-Acquisition Gradient Echo (MPRAGE, 1 mm^3, TR/TE/FA = 2300ms/3.4ms/9°), T2-weighted FLAIR (TR/TE/FA = 10,000ms/121ms/90°), and DWI (TR/TE/FA = 5400ms/105ms/90°, b=0/1000) were acquired with every scan in addition to EPSI. These scans were used for tissue segmentation and spatial registration.

Metabolite Image Analysis and Display System (MIDAS)

The MIDAS program provides an integrated set of MRI and MRSI processing functions and a whole-brain MRSI acquisition method that has been implemented on MRI systems from three major manufacturers (e.g. Siemens Medical Solutions, Phillips Medical Systems, and General Electric Healthcare). This processing can be done on either MRI or MRSI data in a modular fashion, or a full procedure can be developed to process both simultaneously with batch processing. Also, the MIDAS system provides a framework for managing large numbers and different types of data files (including image, spectroscopic, and demographic files) for managing the images acquired, the processing functions used, and the results generated from spectroscopic processing.

MIDAS is used for all spectroscopic processing in this document; as such, a brief outline of the protocol used can be found in **Figure 1.31**. In our procedure, the MIDAS program takes as input three separate data files: Digital Imaging and Communications in Medicine (DICOM) files for the T1w MRI from the imaging protocol, the DICOM MRSI metabolite files, and DICOM MRSI water reference files acquired during the metabolite signal acquisition.

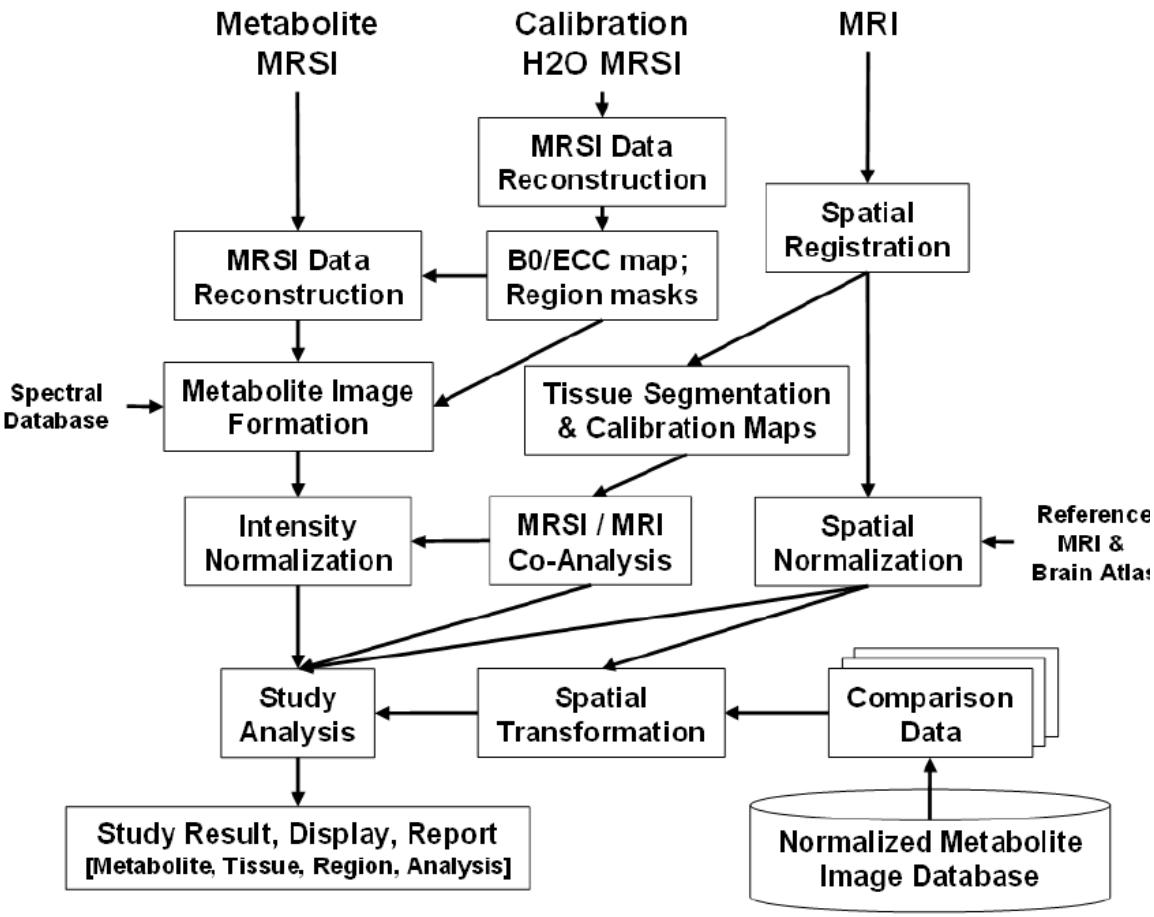

Figure 1.31. Complete MIDAS MRI and MRSI processing protocol. Reproduced by permission from John Wiley and Sons, Inc. from *Maudsley, A. A., et al. (2006) NMR in Biomedicine 19(4):* 10.1002/nbm.1025 under the Creative Commons Attribution (CC BY) license (197).

Metabolite and water reference images are reconstructed in a fully automated manner in MIDAS including spatial smoothing and interpolation to 64 x 64 x 32 points (198; 199). Spectra in voxels for which the water signal intensity linewidth was 16 Hz or less were analyzed using an automated parametric spectral analysis procedure to generate volumetric metabolic images of NAA, CR, and Cho (200). Metabolite concentrations in arbitrary units were calculated as a ratio to the brain water signal from the same ROI to adjust for tissue water content (201).

From the analyzed data format generated by MIDAS, volumetric metabolite data were generated in the DICOM format using an in-house, C++-compiled image converter. These volumes were then imported into VelocityAI (Varian Medical Systems), an FDA 510K-cleared image analysis suite for the display, registration, and annotation of multi-modal medical images. In VelocityAI, the metabolite volumes were registered to MRIs acquired clinically and resampled into this image space. Using white matter maps generated by MIDAS, ROIs of normal appear white matter (NAWM) were segmented and used to model normal brain signal. Statistical parameters derived from these models (mean, standard deviation, etc.) were used to generate standardized abnormality index maps for each metabolite. The entire process from MIDAS to index maps is a new processing step that generates novel spectroscopic images; we have termed them spectroscopic magnetic resonance images (sMRI). In this work, they will be referred to as such.

1.5.6 MR Spectroscopy in Glioma Management

Single voxel spectroscopy and MRSI have each been used extensively to evaluate human brain tumors. Though both have their merits, a key consideration for glioma imaging is tumor inhomogeneity: structural *and* metabolic. The

metabolite components present within a spectrum are highly dependent on the region of the tumor sampled. For example, the spectrum from the necrotic core of a GBM may show little to no metabolites, while a spectrum from the contrast-enhancing component may show significant Cho elevation. Using SVS, only a small piece of information about the tumor's metabolism is obtained, and it must be assumed that this "snap-shot" of metabolism is representative of the tumor as a whole. Even more troubling is the placement of the imaging ROI before spectrum acquisition. For example, peri-tumoral edema and invasive, non-enhancing tumor tissue are nearly identical on T2w imaging. Even though these two regions are known to be different metabolically, differentiating the two with conventional imaging is impossible, making the placement of a single ROI for SVS quite difficult. As such, MRSI is often favored over SVS for evaluating brain tumor metabolism. Because of this, and the sheer number of studies selecting MRSI over SVS for brain tumor evaluation, this section will focus exclusively on the use of MRSI for glioma management.

It was realized early in the development of proton MRS techniques that the spectra from regions with suspected glioma exhibited marked differences from those observed in normal brain (202). Most obvious was the fact that glioma spectra generally displayed elevated Cho and decreased NAA. As the decrease in NAA is widely interpreted as loss, dysfunction, or displacement of neuronal tissue and Cho has been linked to membrane synthesis *in vitro* and *in vivo*, the Cho/NAA ratio gained popularity early as a marker describing the proliferation and growth of non-neuronal cell types in the brain. Additionally, changes in Lac, Lip, and MI have been observed and shown to associated with the presence of glioma (203;

204). Although ischemia has been linked to Lac production and this may be playing a part in the accumulation of Lac in glioma, the greatest contributor of Lac in glioma is believed to be the unsustainable anaerobic glycolysis associated with malignant transformation (204; 205). Lip signal changes are generally associated with the accumulation of mobile lipid fractions resulting from membrane degradation, and thus are most often seen in regions of frank necrosis (206-208). Though MI signal is not as robust as any of those mentioned above and MI is not a metabolite commonly seen elevated in HGGs, some studies have found links between MI and glioma types, most notably oligodendrogliomas and low-grade astrocytomas, as well as the rare and diffusely infiltrative gliomatosis cerebri (209; 210).

MRS in Tumor Diagnosis and Classification

A commonly asked question is whether MRS can help to diagnose tumor type and grade non-invasively, as this information could have significant impact of treatment and diagnosis. Two particularly important image-based diagnoses are the differentiation between HGGs and LGGs, or between primary and metastatic brain tumors. With regards to the former, high-grade brain tumors are usually treated more aggressively than low-grade tumors, and a preoperative diagnosis of tumor grade may help guide clinical decision-making before tissue is acquired.

Several studies investigating MRS in astrocytomas have suggested there is a significant positive correlation between Cho levels and tumor grade, with more aggressive tumor having higher membrane turnover and cellular density (211-213). This, however, may not always be the case for GBM, particularly those with

necrotic regions. In these tumors, necrosis can dilute the Cho signal in surrounding areas making them difficult to differentiate from lower grade gliomas (207). This fact also underscores the need for not only proper placement of the volume of interest for spectroscopic imaging, but also a high-resolution spectroscopic modality that limits partial volume effects and signal bleed from adjacent voxels. To address tissue selection, a recent study evaluated glioma metabolism using PWI to guide volume of interest placement (214). In this work, Chawla et al. found that a number of metabolic markers, including Cho, were indeed able to differentiate high and low grade gliomas. However, this was only the case in those that were hyperperfused on PWI; no significant differences were found for any metabolites in regions that were hypoperfused or isoperfused relative to normal cerebrum.

Using machine learning and other bioinformatic techniques, several groups have shown that MRS can be used to accurately differentiate a number of tumor types including astrocytoma, oligodendroglioma, meningioma, and metastasis (215-218). For example using linear discriminant analysis, Preul et al. were able to correctly classify a preoperative tumor as a grade II astrocytoma, grade III astrocytoma, GBM, meningioma, or metastasis with spectral profiles alone with a 99% success rate (218). This was a significant improvement over the classification of these tumors using conventional imaging in the same study (77% success rate). Similarly, in a multi-institutional study, Tate et al. were able to discriminate between low grade gliomas, meningiomas, and “aggressive tumors” (GBMs and metastases) using the same method resulting in a positive classification rate of ~92% (215). Unfortunately, because of lesion variability and their dependence on

data collection and analysis techniques, these techniques have proven difficult to replicate in general clinical practice.

Because of this variability, MRS is generally used in brain tumor evaluation as an adjunct technique to be considered alongside conventional MRI and clinical findings. In particular, MRS can be very helpful in predicting the histology of a single contrast-enhancing lesion. For instance, high Cho and low NAA levels seen in a non-necrotic, contrast-enhancing tumor increase the likelihood of finding oligodendroglioma or astrocytoma histology as mobile lipid is almost exclusively seen in metastases and GBM (219). Conversely, low levels of metabolites and elevated Lip in a necrotic region surrounded by contrast enhancement with elevated Cho is more indicative of metastases or GBMs. Similarly, it has been suggested that the investigation of peri-tumoral edema on T2w imaging may be useful in differentiating metastatic and primary brain tumors. Whereas gliomas are often invasive lesions which show elevated Cho in surrounding tissue, metastatic lesions tend to be more encapsulated and do not typically show pronounced metabolic abnormalities outside of enhancement (220; 221).

MRS in Surgical and RT Planning

Because the prognosis and treatment plan is based on the histopathological grade of the tumor and the goal of local therapy (surgery and RT) is to treat tumor while minimizing treatment to normal tissue, accurate image-based guidance in glioma is incredibly important (57). The spatial-encoded metabolic information generated using MRSI may assist the surgeon in obtaining representative samples of the tumor tissue for histological diagnosis or assist the oncologist in determining

the region targeted for high-dose RT (222; 223). MRSI also describes tumor heterogeneity, allowing the differentiation of normal tissue, infiltrating tumor, and vasogenic edema, with metabolic information that would be beneficial in guiding surgical resection and RT as well (224).

MRS can enhance the diagnostic and therapeutic yield of surgical interventions by guiding surgeons to regions of high tumor metabolism during biopsy or infiltrative, yet anatomically normal margins during surgery. Many studies have investigated the role of MRSI in biopsy direction, and recognize that regions with elevated Cho and decreased NAA represent good targets for tissue sampling while regions with low Cho and NAA generally represent regions of radiation necrosis, astrogliosis, or macrophage infiltration (225-229). In one representative study in 26 patients with glioma, preoperative MRSI correctly classified all histologically confirmed WHO grade III-IV and 80% WHO grade II gliomas (223). The most definitive targets based on spectroscopy in this study, with increased Cho, decreased NAA, and isointense CR, included GBM as well as anaplastic oligodendrogliomas and astrocytomas. In another study where spectroscopy was mapped to the anatomical imaging and used in real-time during the biopsy, Cho/NAA was found to have a significant correlation with tissue cellularity with regions of intermediate invasion having lower Cho/NAA levels on average than those from bulk tumor. In a small number of subjects, however, biopsies sampled from regions with normal Cho/NAA showed tumor infiltration. The authors attributed these false negatives to the coarse spatial resolution of the spectroscopic sequence used (~0.5 cm^3) (228). Similarly, region based histologic measures like cell number per field and percent tumor in the zone immediately

outside contrast-enhancing tumor were found to have a significant inverse relationship with NAA in a more recent, retrospective study (230). No correlation with Cho was detected, and the authors concluded that NAA concentration is the most significant parameter in detecting low levels of tumor cell infiltration.

MRSI has even been evaluated as a guide for RT planning when registered with conventional MRI scans and treatment-planning CT scans (231-234). Park et al. correlated the pattern of recurrence after RT with pre-treatment MRSI findings and noted that 8 of 9 patients with a growing enhancing lesion post-RT had recurrence in regions with high Cho/NAA (235). The potential of 1H MRSI to improve the accuracy of target volumes definition based on metabolic information was evaluated in 34 patients with WHO grade II-IV gliomas (236). Comparison of the extent (and location) of active tumor as defined by MRI and MRSI demonstrated differences between the two techniques in the same study. This report and later studies documented that the area of metabolic abnormality as defined by MRSI may exceed the area of abnormal T2-weighted signal (228; 229; 237). Furthermore, a study in 26 patients with WHO grade IV gliomas treated with gamma knife surgery showed that patients in whom the volume of metabolically active lesion defined by MRSI was mostly within the radiosurgically treated volume had a longer survival time than patients with a lesser overlap (227). Lastly, Stadlbauer et al. demonstrated in gliomas that MRSI-derived Cho/NAA ratios frequently identified regions at higher risk of tumor beyond the T_{2w} signal abnormalities, and concluded that MRSI may be useful for delineating infiltrating non-enhancing tumor (beyond contrast enhancing tumor), which has clear implications for therapeutic planning (238).

In using MRS for application to brain tumors, the limited spatial resolution (~1 cm^3 for MRSI and > 4 cm^3 for single voxel) should be considered. For example, MRSI voxels containing both tumor and normal tissue have the potential to be miss-classified as normal tissue (i.e. false negative) if partial volume effects are not considered. For this reason, use of the highest possible spatial resolution is recommended (228). High resolution MRSI with good signal-to-noise ratios is best performed using high magnetic field strengths and multi-channel phased-array coils, and efficient pulse sequences. Multi-slice or 3D MRSI techniques which provide full lesion coverage, as well as including surrounding and contralateral brain regions, are also very important. While the utility of MRS in diagnosis and therapy planning for brain tumors has been documented, it has not been accepted as a routine clinical tool. Robust and automated procedures are needed to collect spectroscopic data, analyze chemical shift spectral, and display imaging results in a timely fashion. Standardization across sites and different vendors of acquisition and analysis techniques is also important.

1.6 Organization of The Dissertation

The original goal of my proposed graduate study was to establish quantitative, high-resolution, volumetric proton sMRI and associated bioinformatic techniques as reliable methods for identifying tumor infiltration and predicting outcomes in GBM. This involved attempting to predict not only the time to recurrence and expiration, but also the location of contrast-enhancing tumor after completion of therapy. During the course of my study, however, I became involved in a number of promising side projects that supplanted my original goal, and took me into image-guided surgery and RT applications instead of outcome

prediction. As a part of a surgical applications study, I had the great fortune to take part in the development of an image processing method to evaluate surgical outcomes in a trial utilizing 5-ALA. Using this method, I was then able to evaluate tumor morphology in a cohort of GBM patients receiving 5-ALA FGS and link these findings to their resection outcomes as well as their progression-free and OS. Further work with the 5-ALA clinical trial afforded me the opportunity to then validate the use of sMRI for identifying the infiltrating margin in GBM by stereotactic surgical means. Upon completion of these surgical projects, I was then able apply sMRI to RT dose planning and evaluate its impact on the dose distribution and dose constraints required for effective RT regimens.

Given the convoluted trajectory of my work, the dissertation is made up of 6 chapters organized as follows:

Chapter 1: Brief Introduction to Important Concepts (i.e. Glioma, MRI, Molecular Imaging Techniques)

Chapter 2: Quantitative tumor segmentation for the evaluation of extent of GBM resection

Chapter 3: Semi-Automated Volumetric and Morphological Assessment of GBM Resection with FGS

Chapter 4: Whole-brain spectroscopic MRI biomarkers identify infiltrating margins in GBM patients

Chapter 5. The Impact of Integrating Volumetric Whole-Brain sMRI into RT Planning for GBM

Chapter 6. Overall Discussion and Future Directions

Chapter 7. Closing Remarks

Chapters 2 through **6** have been published in peer-reviewed journals; and as such, begin with an abstract of the work followed by an Author's Contribution and Acknowledgment of Reproduction section. In the latter section the original citation can be found. Finally, this work will end with a brief discussion of the presented work and future directions for the project as well as closing remarks.

1.7 References

1. Pandey AS, Thompson BG. 2015. Neurosurgery. In *CURRENT Diagnosis & Treatment: Surgery, 14e*, ed. GM Doherty:805-83. New York, NY: McGraw-Hill Education. Number of 805-83 pp.

2. Waxman SG. 2013. Chapter 7. The Brain Stem and Cerebellum. In *Clinical Neuroanatomy, 27e*. New York, NY: The McGraw-Hill Companies. Number of.

3. D P, J AG, D F. 2001. Neuroglial Cells. In *Neuroscience*. Sunderland, MA: Sinauer Associates

4. Ostrom QT, Gittleman H, Fulop J, Liu M, Blanda R, et al. 2015. CBTRUS Statistical Report: Primary Brain and Central Nervous System Tumors Diagnosed in the United States in 2008-2012. *Neuro-oncology* 17 Suppl 4:iv1-iv62

5. Silbergeld DL, Rostomily RC, Alvord EC, Jr. 1991. The cause of death in patients with glioblastoma is multifactorial: clinical factors and autopsy findings in 117 cases of supratentorial glioblastoma in adults. *J Neurooncol* 10:179-85

6. Louis DN, Ohgaki H, Wiestler OD, Cavenee WK, Burger PC, et al. 2007. The 2007 WHO Classification of Tumours of the Central Nervous System. *Acta Neuropathologica* 114:97-109

7. Huse JT, Holland EC. 2010. Targeting brain cancer: advances in the molecular pathology of malignant glioma and medulloblastoma. *Nature reviews. Cancer* 10:319-31

8. Vigneswaran K, Neill S, Hadjipanayis CG. 2015. Beyond the World Health Organization grading of infiltrating gliomas: advances in the molecular genetics of glioma classification. *Annals of Translational Medicine* 3

9. Stupp R, Mason WP, van den Bent MJ, Weller M, Fisher B, et al. 2005. Radiotherapy plus concomitant and adjuvant temozolomide for glioblastoma. *The New England journal of medicine* 352:987-96

10. Stupp R, Hegi ME, Mason WP, van den Bent MJ, Taphoorn MJB, et al. 2009. Effects of radiotherapy with concomitant and adjuvant temozolomide versus radiotherapy alone on survival in glioblastoma in a randomised phase III study: 5-year analysis of the EORTC-NCIC trial. *Lancet Oncology* 10:459-66

11. Stupp R, Brada M, van den Bent MJ, Tonn JC, Pentheroudakis G. 2014. High-grade glioma: ESMO Clinical Practice Guidelines for diagnosis, treatment and follow-up. *Ann Oncol* 25 Suppl 3:iii93-101

12. Shonka NA, Hsu SH, Yung WKA, Mahajan A, Prabhu S. 2011. Chapter 37. Tumors of the Central Nervous System. In *The MD Anderson Manual of Medical Oncology, 2e*, ed. HM Kantarjian, RA Wolff, CA Koller. New York, NY: The McGraw-Hill Companies. Number of.

13. Ramirez YP, Weatherbee JL, Wheelhouse RT, Ross AH. 2013. Glioblastoma Multiforme Therapy and Mechanisms of Resistance. *Pharmaceuticals* 6:1475-506

14. Furnari FB, Fenton T, Bachoo RM, Mukasa A, Stommel JM, et al. 2007. Malignant astrocytic glioma: genetics, biology, and paths to treatment. *Genes & development* 21:2683-710

15. Verhaak RG, Hoadley KA, Purdom E, Wang V, Qi Y, et al. 2010. Integrated genomic analysis identifies clinically relevant subtypes of glioblastoma characterized by abnormalities in PDGFRA, IDH1, EGFR, and NF1. *Cancer cell* 17:98-110

16. Phillips HS, Kharbanda S, Chen R, Forrest WF, Soriano RH, et al. 2006. Molecular subclasses of high-grade glioma predict prognosis, delineate a pattern of disease progression, and resemble stages in neurogenesis. *Cancer cell* 9:157-73

17. 2008. Comprehensive genomic characterization defines human glioblastoma genes and core pathways. *Nature* 455:1061-8

18. Lin N, Yan W, Gao K, Wang Y, Zhang J, You Y. 2014. Prevalence and Clinicopathologic Characteristics of the Molecular Subtypes in Malignant Glioma: A Multi-Institutional Analysis of 941 Cases. *PloS one* 9:e94871

19. Haselbeck RJ, McAlister-Henn L. 1993. Function and expression of yeast mitochondrial NAD- and NADP-specific isocitrate dehydrogenases. *Journal of Biological Chemistry* 268:12116-22

20. Thompson CB. 2009. Metabolic enzymes as oncogenes or tumor suppressors. *The New England journal of medicine* 360:813-5

21. Kloosterhof NK, Bralten LB, Dubbink HJ, French PJ, van den Bent MJ. 2011. Isocitrate dehydrogenase-1 mutations: a fundamentally new understanding of diffuse glioma? *Lancet Oncology* 12:83-91

22. Bralten LB, Kloosterhof NK, Balvers R, Sacchetti A, Lapre L, et al. 2011. IDH1 R132H decreases proliferation of glioma cell lines in vitro and in vivo. *Ann Neurol* 69:455-63

23. Appin CL, Brat DJ. 2014. Molecular genetics of gliomas. *Cancer J* 20:66-72

24. Suzuki A, Nobusawa S, Natsume A, Suzuki H, Kim YH, et al. 2014. Olig2 labeling index is correlated with histological and molecular classifications in low-grade diffuse gliomas. *J Neurooncol* 120:283-91

25. Huse JT, Wallace M, Aldape KD, Berger MS, Bettegowda C, et al. 2014. Where are we now? And where are we going? A report from the Accelerate Brain Cancer Cure (ABC2) low-grade glioma research workshop. *Neuro-oncology* 16:173-8

26. Weller M, Pfister SM, Wick W, Hegi ME, Reifenberger G, Stupp R. 2013. Molecular neuro-oncology in clinical practice: a new horizon. *Lancet Oncology* 14:e370-9

27. Boots-Sprenger SH, Sijben A, Rijntjes J, Tops BB, Idema AJ, et al. 2013. Significance of complete 1p/19q co-deletion, IDH1 mutation and MGMT promoter methylation in gliomas: use with caution. *Modern pathology : an official journal of the United States and Canadian Academy of Pathology, Inc* 26:922-9

28. Appin CL, Brat DJ. 2015. Biomarker-driven diagnosis of diffuse gliomas. *Molecular aspects of medicine* 45:87-96

29. Brat DJ, Verhaak RG, Aldape KD, Yung WK, Salama SR, et al. 2015. Comprehensive, Integrative Genomic Analysis of Diffuse Lower-Grade Gliomas. *The New England journal of medicine* 372:2481-98

30. Yip S, Butterfield YS, Morozova O, Chittaranjan S, Blough MD, et al. 2012. Concurrent CIC mutations, IDH mutations, and 1p/19q loss distinguish oligodendrogliomas from other cancers. *J Pathol* 226:7-16

31. Figarella-Branger D, Mokhtari K, Colin C, Uro-Coste E, Jouvet A, et al. 2015. Prognostic Relevance of Histomolecular Classification of Diffuse Adult High-Grade Gliomas with Necrosis. *Brain Pathol* 25:418-28

32. Masui K, Cloughesy TF, Mischel PS. 2012. Review: molecular pathology in adult high-grade gliomas: from molecular diagnostics to target therapies. *Neuropathol Appl Neurobiol* 38:271-91

33. Esteller M, Garcia-Foncillas J, Andion E, Goodman SN, Hidalgo OF, et al. 2000. Inactivation of the DNA-repair gene MGMT and the clinical response of gliomas to alkylating agents. *The New England journal of medicine* 343:1350-4

34. Hegi ME, Diserens AC, Gorlia T, Hamou MF, de Tribolet N, et al. 2005. MGMT gene silencing and benefit from temozolomide in glioblastoma. *The New England journal of medicine* 352:997-1003

35. Wick W, Weller M, van den Bent M, Sanson M, Weiler M, et al. 2014. MGMT testing--the challenges for biomarker-based glioma treatment. *Nature reviews. Neurology* 10:372-85

36. Weller M, Stupp R, Reifenberger G, Brandes AA, van den Bent MJ, et al. 2010. MGMT promoter methylation in malignant gliomas: ready for personalized medicine? *Nature reviews. Neurology* 6:39-51

37. Bady P, Sciuscio D, Diserens AC, Bloch J, van den Bent MJ, et al. 2012. MGMT methylation analysis of glioblastoma on the Infinium methylation BeadChip identifies two distinct CpG regions associated with gene silencing and outcome, yielding a prediction model for comparisons across datasets, tumor grades, and CIMP-status. *Acta Neuropathol* 124:547-60

38. Graif M, Bydder GM, Steiner RE, Niendorf P, Thomas DG, Young IR. 1985. Contrast-enhanced MR imaging of malignant brain tumors. *AJNR. American journal of neuroradiology* 6:855-62

39. Weller M, van den Bent M, Hopkins K, Tonn JC, Stupp R, et al. 2014. EANO guideline for the diagnosis and treatment of anaplastic gliomas and glioblastoma. *Lancet Oncology* 15:e395-403

40. Ropper AH, Samuels MA, Klein JP. 2014. Chapter 31. Intracranial Neoplasms and Paraneoplastic Disorders. In *Adams and Victor's Principles of Neurology, 10e*. New York, NY: The McGraw-Hill Companies. Number of.

41. Bloch O, Han SJ, Cha S, Sun MZ, Aghi MK, et al. 2012. Impact of extent of resection for recurrent glioblastoma on overall survival: clinical article. *Journal of neurosurgery* 117:1032-8

42. Chaichana KL, Cabrera-Aldana EE, Jusue-Torres I, Wijesekera O, Olivi A, et al. 2014. When gross total resection of a glioblastoma is possible, how much resection should be achieved? *World Neurosurg* 82:e257-65

43. Chaichana KL, Jusue-Torres I, Navarro-Ramirez R, Raza SM, Pascual-Gallego M, et al. 2014. Establishing percent resection and residual volume thresholds affecting survival and recurrence for patients with newly diagnosed intracranial glioblastoma. *Neuro-oncology* 16:113-22

44. Hardesty DA, Sanai N. 2012. The value of glioma extent of resection in the modern neurosurgical era. *Frontiers in neurology* 3:140-50

45. Lacroix M, Abi-Said D, Fourney DR, Gokaslan ZL, Shi W, et al. 2001. A multivariate analysis of 416 patients with glioblastoma multiforme: prognosis, extent of resection, and survival. *Journal of neurosurgery* 95:190-8

46. Sanai N, Berger MS. 2008. Glioma extent of resection and its impact on patient outcome. *Neurosurgery* 62:753-64

47. Sanai N, Berger MS. 2011. Extent of resection influences outcomes for patients with gliomas. *Rev Neurol (Paris)* 167:648-54

48. Sanai N, Polley MY, McDermott MW, Parsa AT, Berger MS. 2011. An extent of resection threshold for newly diagnosed glioblastomas. *Journal of neurosurgery* 115:3-8

49. Stummer W, Meinel T, Ewelt C, Martus P, Jakobs O, et al. 2012. Prospective cohort study of radiotherapy with concomitant and adjuvant temozolomide

chemotherapy for glioblastoma patients with no or minimal residual enhancing tumor load after surgery. *J Neurooncol* 108:89-97

50. Stummer W, Pichlmeier U, Meinel T, Wiestler OD, Zanella F, Reulen HJ. 2006. Fluorescence-guided surgery with 5-aminolevulinic acid for resection of malignant glioma: a randomised controlled multicentre phase III trial. *Lancet Oncology* 7:392-401

51. Stummer W, Reulen HJ, Meinel T, Pichlmeier U, Schumacher W, et al. 2008. Extent of resection and survival in glioblastoma multiforme: identification of and adjustment for bias. *Neurosurgery* 62:564-76; discussion -76

52. Sanai N. 2012. Emerging operative strategies in neurosurgical oncology. *Curr Opin Neurol* 25:756-66

53. Hall EJ, Giaccia AJ. 2006. *Radiobiology for the Radiologist*. Lippincott Williams & Wilkins

54. Walker MD, Green SB, Byar DP, Alexander E, Jr., Batzdorf U, et al. 1980. Randomized comparisons of radiotherapy and nitrosoureas for the treatment of malignant glioma after surgery. *The New England journal of medicine* 303:1323-9

55. von Neubeck C, Seidlitz A, Kitzler HH, Beuthien-Baumann B, Krause M. 2015. Glioblastoma multiforme: emerging treatments and stratification markers beyond new drugs. *The British journal of radiology* 88:20150354

56. Laperriere N, Zuraw L, Cairncross G. 2002. Radiotherapy for newly diagnosed malignant glioma in adults: a systematic review. *Radiotherapy and*

oncology : journal of the European Society for Therapeutic Radiology and Oncology 64:259-73

57. Wen PY, Kesari S. 2008. Malignant gliomas in adults. *The New England journal of medicine* 359:492-507

58. Persano L, Rampazzo E, Basso G, Viola G. 2013. Glioblastoma cancer stem cells: Role of the microenvironment and therapeutic targeting. *Biochemical Pharmacology* 85:612-22

59. Mamourian AC. 2010. *Practical MR Physics*. Cary, GB: Oxford University Press, USA

60. de Graaf RA. 2007. Spectroscopic Imaging and Multivolume Localization. In *In Vivo NMR Spectroscopy*:349-87: John Wiley & Sons, Ltd. Number of 349-87 pp.

61. de Graaf RA. 2007. Spectral Quantification. In *In Vivo NMR Spectroscopy*:445-77: John Wiley & Sons, Ltd. Number of 445-77 pp.

62. Diaz G, Manzanera A, Ta VT, Lezoray O, Elmoataz A. 2010. Biomedical Image Understanding and Interpretation. In *Biomedical Image Analysis and Machine Learning Technologies: Applications and Techniques*, ed. F Gonzalez, E Romero:167-213. Hershey, PA: Medical Information Science Reference. Number of 167-213 pp.

63. Gowland PA, Stevenson VL. 2003. T1: The Longitudinal Relaxation Time. In *Quantitative MRI of the Brain*:111-41: John Wiley & Sons, Ltd. Number of 111-41 pp.

64. Tofts PS, Waldman AD. 2003. Spectroscopy: 1H Metabolite Concentrations. In *Quantitative MRI of the Brain*:299-339: John Wiley & Sons, Ltd. Number of 299-339 pp.

65. Nitz WR, Reimer P. 1999. Contrast mechanisms in MR imaging. *European radiology* 9:1032-46

66. Ellingson BM, Bendszus M, Boxerman J, Barboriak D, Erickson BJ, et al. 2015. Consensus recommendations for a standardized Brain Tumor Imaging Protocol in clinical trials. *Neuro-oncology* 17:1188-98

67. Wen PY, Macdonald DR, Reardon DA, Cloughesy TF, Sorensen AG, et al. 2010. Updated response assessment criteria for high-grade gliomas: response assessment in neuro-oncology working group. *J Clin Oncol* 28:1963-72

68. Lewin JS, Estes ML, Ross JS. 1992. Magnetic resonance imaging of adult intra-axial brain tumors. *Topics in magnetic resonance imaging : TMRI* 4:17-40

69. Cha S. 2006. Update on brain tumor imaging: from anatomy to physiology. *AJNR. American journal of neuroradiology* 27:475-87

70. Tynninen O, Aronen HJ, Ruhala M, Paetau A, Von Boguslawski K, et al. 1999. MRI enhancement and microvascular density in gliomas. Correlation with tumor cell proliferation. *Investigative radiology* 34:427-34

71. Garzon B, Emblem KE, Mouridsen K, Nedregaard B, Due-Tonnessen P, et al. 2011. Multiparametric analysis of magnetic resonance images for glioma grading and patient survival time prediction. *Acta Radiol* 52:1052-60

72. Aprile I, Giorgi C, Guiducci A, Conti G, Ottaviano I, Ottaviano P. 2008. Characterization of glioblastoma by contrast-enhanced flair sequences. *The neuroradiology journal* 21:196-203

73. Kelly PJ, Daumas-Duport C, Kispert DB, Kall BA, Scheithauer BW, Illig JJ. 1987. Imaging-based stereotaxic serial biopsies in untreated intracranial glial neoplasms. *Journal of neurosurgery* 66:865-74

74. Law M, Yang S, Wang H, Babb JS, Johnson G, et al. 2003. Glioma grading: sensitivity, specificity, and predictive values of perfusion MR imaging and proton MR spectroscopic imaging compared with conventional MR imaging. *AJNR. American journal of neuroradiology* 24:1989-98

75. Jain RK, di Tomaso E, Duda DG, Loeffler JS, Sorensen AG, Batchelor TT. 2007. Angiogenesis in brain tumours. *Nat Rev Neurosci* 8:610-22

76. Rees JH, Smirniotopoulos JG, Jones RV, Wong K. 1996. Glioblastoma multiforme: radiologic-pathologic correlation. *RadioGraphics* 16:1413-38

77. Naeini KM, Pope WB, Cloughesy TF, Harris RJ, Lai A, et al. 2013. Identifying the mesenchymal molecular subtype of glioblastoma using quantitative volumetric analysis of anatomic magnetic resonance images. *Neuro-oncology* 15:626-34

78. Bradley WG, Jr. 1993. MR appearance of hemorrhage in the brain. *Radiology* 189:15-26

79. Norden AD, Young GS, Setayesh K, Muzikansky A, Klufas R, et al. 2008. Bevacizumab for recurrent malignant gliomas: efficacy, toxicity, and patterns of recurrence. *Neurology* 70:779-87

80. Gallego Perez-Larraya J, Lahutte M, Petrirena G, Reyes-Botero G, Gonzalez-Aguilar A, et al. 2012. Response assessment in recurrent glioblastoma treated with irinotecan-bevacizumab: comparative analysis of the Macdonald, RECIST, RANO, and RECIST + F criteria. *Neuro-oncology* 14:667-73

81. Hajnal JV, Bryant DJ, Kasuboski L, Pattany PM, De Coene B, et al. 1992. Use of fluid attenuated inversion recovery (FLAIR) pulse sequences in MRI of the brain. *Journal of computer assisted tomography* 16:841-4

82. De Coene B, Hajnal JV, Gatehouse P, Longmore DB, White SJ, et al. 1992. MR of the brain using fluid-attenuated inversion recovery (FLAIR) pulse sequences. *AJNR. American journal of neuroradiology* 13:1555-64

83. Mabray MC, Barajas RF, Jr., Cha S. 2015. Modern brain tumor imaging. *Brain tumor research and treatment* 3:8-23

84. Kalpathy-Cramer J, Gerstner ER, Emblem KE, Andronesi OC, Rosen B. 2014. Advanced magnetic resonance imaging of the physical processes in human glioblastoma. *Cancer research* 74:4622-37

85. Ahmed R, Oborski MJ, Hwang M, Lieberman FS, Mountz JM. 2014. Malignant gliomas: current perspectives in diagnosis, treatment, and early response assessment using advanced quantitative imaging methods. *Cancer management and research* 6:149-70

86. Gerstner ER, Sorensen AG. 2011. Diffusion and diffusion tensor imaging in brain cancer. *Seminars in radiation oncology* 21:141-6

87. Schaefer PW, Grant PE, Gonzalez RG. 2000. Diffusion-weighted MR imaging of the brain. *Radiology* 217:331-45

88. Svolos P, Tsolaki E, Kapsalaki E, Theodorou K, Fountas K, et al. 2013. Investigating brain tumor differentiation with diffusion and perfusion metrics at 3T MRI using pattern recognition techniques. *Magnetic resonance imaging* 31:1567-77

89. Yamasaki F, Kurisu K, Satoh K, Arita K, Sugiyama K, et al. 2005. Apparent diffusion coefficient of human brain tumors at MR imaging. *Radiology* 235:985-91

90. Price SJ. 2010. Advances in imaging low-grade gliomas. *Advances and technical standards in neurosurgery* 35:1-34

91. Kono K, Inoue Y, Nakayama K, Shakudo M, Morino M, et al. 2001. The role of diffusion-weighted imaging in patients with brain tumors. *AJNR. American journal of neuroradiology* 22:1081-8

92. Fan GG, Deng QL, Wu ZH, Guo QY. 2006. Usefulness of diffusion/perfusion-weighted MRI in patients with non-enhancing supratentorial brain gliomas: a valuable tool to predict tumour grading? *The British journal of radiology* 79:652-8

93. O'Flynn EA, DeSouza NM. 2011. Functional magnetic resonance: biomarkers of response in breast cancer. *Breast Cancer Res* 13

94. Zaharchuk G. 2007. Theoretical basis of hemodynamic MR imaging techniques to measure cerebral blood volume, cerebral blood flow, and permeability. *AJNR. American journal of neuroradiology* 28:1850-8

95. Rutten EH, Doesburg WH, Slooff JL. 1992. Histologic factors in the grading and prognosis of astrocytoma grade I-IV. *J Neurooncol* 13:223-30

96. Samoto K, Ikezaki K, Ono M, Shono T, Kohno K, et al. 1995. Expression of vascular endothelial growth factor and its possible relation with neovascularization in human brain tumors. *Cancer research* 55:1189-93

97. Chaudhry IH, O'Donovan DG, Brenchley PE, Reid H, Roberts IS. 2001. Vascular endothelial growth factor expression correlates with tumour grade and vascularity in gliomas. *Histopathology* 39:409-15

98. Lev MH, Ozsunar Y, Henson JW, Rasheed AA, Barest GD, et al. 2004. Glial tumor grading and outcome prediction using dynamic spin-echo MR susceptibility mapping compared with conventional contrast-enhanced MR: confounding effect of elevated rCBV of oligodendrogliomas [corrected]. *AJNR. American journal of neuroradiology* 25:214-21

99. Knopp EA, Cha S, Johnson G, Mazumdar A, Golfinos JG, et al. 1999. Glial neoplasms: dynamic contrast-enhanced T2*-weighted MR imaging. *Radiology* 211:791-8

100. Sugahara T, Korogi Y, Kochi M, Ikushima I, Hirai T, et al. 1998. Correlation of MR imaging-determined cerebral blood volume maps with histologic and

angiographic determination of vascularity of gliomas. *AJR. American journal of roentgenology* 171:1479-86

101. Aronen HJ, Gazit IE, Louis DN, Buchbinder BR, Pardo FS, et al. 1994. Cerebral blood volume maps of gliomas: comparison with tumor grade and histologic findings. *Radiology* 191:41-51

102. Law M, Young RJ, Babb JS, Peccerelli N, Chheang S, et al. 2008. Gliomas: predicting time to progression or survival with cerebral blood volume measurements at dynamic susceptibility-weighted contrast-enhanced perfusion MR imaging. *Radiology* 247:490-8

103. WT Z, T K, J S. 2009. Acute effects of bevacizumab on glioblastoma vascularity assessed with DCE-MRI and relation to patient survival. In *Intl Soc Magn Reson Med*

104. Law M, Cha S, Knopp EA, Johnson G, Arnett J, Litt AW. 2002. High-grade gliomas and solitary metastases: differentiation by using perfusion and proton spectroscopic MR imaging. *Radiology* 222:715-21

105. Mitsuya K, Nakasu Y, Horiguchi S, Harada H, Nishimura T, et al. 2010. Perfusion weighted magnetic resonance imaging to distinguish the recurrence of metastatic brain tumors from radiation necrosis after stereotactic radiosurgery. *J Neurooncol* 99:81-8

106. Cicone F, Minniti G, Romano A, Papa A, Scaringi C, et al. 2015. Accuracy of F-DOPA PET and perfusion-MRI for differentiating radionecrotic from

progressive brain metastases after radiosurgery. *Eur J Nucl Med Mol Imaging* 42:103-11

107. Sugahara T, Korogi Y, Tomiguchi S, Shigematsu Y, Ikushima I, et al. 2000. Posttherapeutic intraaxial brain tumor: the value of perfusion-sensitive contrast-enhanced MR imaging for differentiating tumor recurrence from nonneoplastic contrast-enhancing tissue. *AJNR. American journal of neuroradiology* 21:901-9

108. Stupp R, Roila F. 2009. Malignant glioma: ESMO clinical recommendations for diagnosis, treatment and follow-up. *Ann Oncol* 20 Suppl 4:126-8

109. Barbosa BJ, Mariano ED, Batista CM, Marie SK, Teixeira MJ, et al. 2015. Intraoperative assistive technologies and extent of resection in glioma surgery: a systematic review of prospective controlled studies. *Neurosurg Rev* 38:217-26

110. Benardete EA, Leonard MA, Weiner HL. 2001. Comparison of frameless stereotactic systems: accuracy, precision, and applications. *Neurosurgery* 49:1409-15; discussion 15-6

111. Zamorano LJ, Nolte L, Kadi AM, Jiang Z. 1994. Interactive intraoperative localization using an infrared-based system. *Stereotactic and functional neurosurgery* 63:84-8

112. Ammirati M, Vick N, Liao YL, Ciric I, Mikhael M. 1987. Effect of the extent of surgical resection on survival and quality of life in patients with supratentorial glioblastomas and anaplastic astrocytomas. *Neurosurgery* 21:201-6

113. Albert FK, Forsting M, Sartor K, Adams HP, Kunze S. 1994. Early postoperative magnetic resonance imaging after resection of malignant glioma:

objective evaluation of residual tumor and its influence on regrowth and prognosis. *Neurosurgery* 34:45-60; discussion -1

114. Pichlmeier U, Bink A, Schackert G, Stummer W. 2008. Resection and survival in glioblastoma multiforme: an RTOG recursive partitioning analysis of ALA study patients. *Neuro-oncology* 10:1025-34

115. Hatiboglu MA, Weinberg JS, Suki D, Rao G, Prabhu SS, et al. 2009. Impact of intraoperative high-field magnetic resonance imaging guidance on glioma surgery: a prospective volumetric analysis. *Neurosurgery* 64:1073-81; discussion 81

116. Kubben PL, Scholtes F, Schijns OE, Ter Laak-Poort MP, Teernstra OP, et al. 2014. Intraoperative magnetic resonance imaging versus standard neuronavigation for the neurosurgical treatment of glioblastoma: A randomized controlled trial. *Surg Neurol Int* 5:70-9

117. Niyazi M, Brada M, Chalmers AJ, Combs SE, Erridge SC, et al. 2016. ESTRO-ACROP guideline "target delineation of glioblastomas". *Radiotherapy and oncology : journal of the European Society for Therapeutic Radiology and Oncology* 118:35-42

118. Walker MD, Strike TA, Sheline GE. 1979. An analysis of dose-effect relationship in the radiotherapy of malignant gliomas. *International journal of radiation oncology, biology, physics* 5:1725-31

119. Pope WB, Young JR, Ellingson BM. 2011. Advances in MRI assessment of gliomas and response to anti-VEGF therapy. *Current neurology and neuroscience reports* 11:336-44

120. Tsuchiya K, Mizutani Y, Hachiya J. 1996. Preliminary evaluation of fluid-attenuated inversion-recovery MR in the diagnosis of intracranial tumors. *AJNR. American journal of neuroradiology* 17:1081-6

121. Knisely JP, Rockwell S. 2002. Importance of hypoxia in the biology and treatment of brain tumors. *Neuroimaging clinics of North America* 12:525-36

122. 2010. Prescribing, Recording, and Reporting Photon-Beam Intensity-Modulated Radiation Therapy (IMRT): Contents. *Journal of the ICRU* 10:NP

123. Barajas RF, Jr., Phillips JJ, Parvataneni R, Molinaro A, Essock-Burns E, et al. 2012. Regional variation in histopathologic features of tumor specimens from treatment-naive glioblastoma correlates with anatomic and physiologic MR Imaging. *Neuro-oncology* 14:942-54

124. Scott JN, Brasher PM, Sevick RJ, Rewcastle NB, Forsyth PA. 2002. How often are nonenhancing supratentorial gliomas malignant? A population study. *Neurology* 59:947-9

125. Kondziolka D, Lunsford LD, Martinez AJ. 1993. Unreliability of contemporary neurodiagnostic imaging in evaluating suspected adult supratentorial (low-grade) astrocytoma. *Journal of neurosurgery* 79:533-6

126. Julia-Sape M, Acosta D, Majos C, Moreno-Torres A, Wesseling P, et al. 2006. Comparison between neuroimaging classifications and histopathological

diagnoses using an international multicenter brain tumor magnetic resonance imaging database. *Journal of neurosurgery* 105:6-14

127. Sherriff J, Tamangani J, Senthil L, Cruickshank G, Spooner D, et al. 2013. Patterns of relapse in glioblastoma multiforme following concomitant chemoradiotherapy with temozolomide. *The British journal of radiology* 86:20120414

128. Tofts PS, Collins DJ. 2011. Multicentre imaging measurements for oncology and in the brain. *British Journal of Radiology* 84:S213-26

129. Waldman AD, Jackson A, Price SJ, Clark CA, Booth TC, et al. 2009. Quantitative imaging biomarkers in neuro-oncology. *Nature reviews. Clinical oncology* 6:445-54

130. Klatzo I. 1967. Presidental address. Neuropathological aspects of brain edema. *Journal of neuropathology and experimental neurology* 26:1-14

131. Lu S, Ahn D, Johnson G, Cha S. 2003. Peritumoral diffusion tensor imaging of high-grade gliomas and metastatic brain tumors. *AJNR. American journal of neuroradiology* 24:937-41

132. Lawrence YR, Li XA, el Naqa I, Hahn CA, Marks LB, et al. 2010. Radiation dose-volume effects in the brain. *International journal of radiation oncology, biology, physics* 76:S20-7

133. Emami B, Lyman J, Brown A, Coia L, Goitein M, et al. 1991. Tolerance of normal tissue to therapeutic irradiation. *International journal of radiation oncology, biology, physics* 21:109-22

134. Wong ET, Hess KR, Gleason MJ, Jaeckle KA, Kyritsis AP, et al. 1999. Outcomes and prognostic factors in recurrent glioma patients enrolled onto phase II clinical trials. *J Clin Oncol* 17:2572-8

135. McDonald WI, Compston A, Edan G, Goodkin D, Hartung HP, et al. 2001. Recommended diagnostic criteria for multiple sclerosis: guidelines from the International Panel on the diagnosis of multiple sclerosis. *Ann Neurol* 50:121-7

136. van den Bent MJ, Vogelbaum MA, Wen PY, Macdonald DR, Chang SM. 2009. End point assessment in gliomas: novel treatments limit usefulness of classical Macdonald's Criteria. *J Clin Oncol* 27:2905-8

137. Taal W, Brandsma D, de Bruin HG, Bromberg JE, Swaak-Kragten AT, et al. 2008. Incidence of early pseudo-progression in a cohort of malignant glioma patients treated with chemoirradiation with temozolomide. *Cancer* 113:405-10

138. Cohen LA, Marks PA, Rifkind RA, Amin S, Desai D, et al. 2002. Suberoylanilide hydroxamic acid (SAHA), a histone deacetylase inhibitor, suppresses the growth of carcinogen-induced mammary tumors. *Anticancer research* 22:1497-504

139. Hsi LC, Xi X, Lotan R, Shureiqi I, Lippman SM. 2004. The histone deacetylase inhibitor suberoylanilide hydroxamic acid induces apoptosis via induction of 15-lipoxygenase-1 in colorectal cancer cells. *Cancer research* 64:8778-81

140. Komatsu N, Kawamata N, Takeuchi S, Yin D, Chien W, et al. 2006. SAHA, a HDAC inhibitor, has profound anti-growth activity against non-small cell lung cancer cells. *Oncology reports* 15:187-91

141. Shim H, Holder CA, Olson JJ. 2013. Magnetic resonance spectroscopic imaging in the era of pseudoprogression and pseudoresponse in glioblastoma patient management. *CNS oncology* 2:393-6

142. Brandes AA, Franceschi E, Tosoni A, Blatt V, Pession A, et al. 2008. MGMT promoter methylation status can predict the incidence and outcome of pseudoprogression after concomitant radiochemotherapy in newly diagnosed glioblastoma patients. *J Clin Oncol* 26:2192-7

143. Poulsen HS, Urup T, Michaelsen SR, Staberg M, Villingshoj M, Lassen U. 2014. The impact of bevacizumab treatment on survival and quality of life in newly diagnosed glioblastoma patients. *Cancer management and research* 6:373-87

144. Macdonald DR, Cascino TL, Schold SC, Jr., Cairncross JG. 1990. Response criteria for phase II studies of supratentorial malignant glioma. *J Clin Oncol* 8:1277-80

145. *About Nuclear Medicine and Molecular Imaging*. http://www.snmmi.org/AboutSNMMI/Content.aspx?ItemNumber=6433

146. Chung C, Metser U, Ménard C. 2015. Advances in Magnetic Resonance Imaging and Positron Emission Tomography Imaging for Grading and Molecular Characterization of Glioma. *Seminars in radiation oncology* 25:164-71

147. Chiang S. 2015. Follow-Up Imaging: Molecular Imaging is Likely Best as a Single Modality, but Multimodality Imaging is the Future. *Frontiers in neurology* 6

148. Hadjipanayis CG, Jiang H, Roberts DW, Yang L. 2011. Current and future clinical applications for optical imaging of cancer: from intraoperative surgical guidance to cancer screening. *Semin Oncol* 38:109-18

149. Yeung Laiwah AC, Moore MR, Goldberg A. 1987. Pathogenesis of acute porphyria. *The Quarterly journal of medicine* 63:377-92

150. Kennedy JC, Pottier RH, Pross DC. 1990. Photodynamic therapy with endogenous protoporphyrin IX: basic principles and present clinical experience. *J Photochem Photobiol B* 6:143-8

151. Kennedy JC, Pottier RH. 1992. Endogenous Protoporphyrin-Ix, a Clinically Useful Photosensitizer for Photodynamic Therapy. *Journal of Photochemistry and Photobiology B-Biology* 14:275-92

152. Bech Ø, Berg K, Moan J. 1997. The pH dependency of protoporphyrin IX formation in cells incubated with 5-aminolevulinic acid. *Cancer Letters* 113:25-9

153. Chang SC, MacRobert AJ, Porter JB, Bown SG. 1997. The efficacy of an iron chelator (CP94) in increasing cellular protoporphyrin IX following intravesical 5-aminolaevulinic acid administration: an in vivo study. *J Photochem Photobiol B* 38:114-22

154. Gibson SL, Cupriks DJ, Havens JJ, Nguyen ML, Hilf R. 1998. A regulatory role for porphobilinogen deaminase (PBGD) in delta-aminolaevulinic acid (delta-ALA)-induced photosensitization? *Br J Cancer* 77:235-42

155. Hinnen P, de Rooij FW, van Velthuysen ML, Edixhoven A, van Hillegersberg R, et al. 1998. Biochemical basis of 5-aminolaevulinic acid-induced protoporphyrin IX accumulation: a study in patients with (pre)malignant lesions of the oesophagus. *Br J Cancer* 78:679-82

156. Hilf R, Havens JJ, Gibson SL. 1999. Effect of delta-aminolevulinic acid on protoporphyrin IX accumulation in tumor cells transfected with plasmids containing porphobilinogen deaminase DNA. *Photochemistry and photobiology* 70:334-40

157. Gibson SL, Havens JJ, Metz L, Hilf R. 2001. Is δ-Aminolevulinic Acid Dehydratase Rate Limiting in Heme Biosynthesis Following Exposure of Cells to δ-Aminolevulinic Acid? *Photochemistry and photobiology* 73:312-7

158. Ishikawa T, Takahashi K, Ikeda N, Kajimoto Y, Hagiya Y, et al. 2011. Transporter-Mediated Drug Interaction Strategy for 5-Aminolevulinic Acid (ALA)-Based Photodynamic Diagnosis of Malignant Brain Tumor: Molecular Design of ABCG2 Inhibitors. *Pharmaceutics* 3:615-35

159. Ennis SR, Novotny A, Xiang J, Shakui P, Masada T, et al. 2003. Transport of 5-aminolevulinic acid between blood and brain. *Brain research* 959:226-34

160. Krammer B, Plaetzer K. 2008. ALA and its clinical impact, from bench to bedside. *Photochem Photobiol Sci* 7:283-9

161. Stummer W, Novotny A, Stepp H, Goetz C, Bise K, Reulen HJ. 2000. Fluorescence-guided resection of glioblastoma multiforme by using 5-aminolevulinic acid-induced porphyrins: a prospective study in 52 consecutive patients. *Journal of neurosurgery* 93:1003-13

162. Stummer W, Tonn JC, Goetz C, Ullrich W, Stepp H, et al. 2014. 5-Aminolevulinic acid-derived tumor fluorescence: the diagnostic accuracy of visible fluorescence qualities as corroborated by spectrometry and histology and postoperative imaging. *Neurosurgery* 74:310-9; discussion 9-20

163. Stummer W, Stepp H, Moller G, Ehrhardt A, Leonhard M, Reulen HJ. 1998. Technical principles for protoporphyrin-IX-fluorescence guided microsurgical resection of malignant glioma tissue. *Acta neurochirurgica* 140:995-1000

164. Idoate MA, Diez Valle R, Echeveste J, Tejada S. 2011. Pathological characterization of the glioblastoma border as shown during surgery using 5-aminolevulinic acid-induced fluorescence. *Neuropathology : official journal of the Japanese Society of Neuropathology* 31:575-82

165. Panciani PP, Fontanella M, Schatlo B, Garbossa D, Agnoletti A, et al. 2012. Fluorescence and image guided resection in high grade glioma. *Clin Neurol Neurosurg* 114:37-41

166. Valdes PA, Kim A, Brantsch M, Niu C, Moses ZB, et al. 2011. delta-aminolevulinic acid-induced protoporphyrin IX concentration correlates with histopathologic markers of malignancy in human gliomas: the need for quantitative fluorescence-guided resection to identify regions of increasing malignancy. *Neuro-oncology* 13:846-56

167. Coburger J, Engelke J, Scheuerle A, Thal DR, Hlavac M, et al. 2014. Tumor detection with 5-aminolevulinic acid fluorescence and Gd-DTPA-enhanced intraoperative MRI at the border of contrast-enhancing lesions: a prospective study based on histopathological assessment. *Neurosurgical focus* 36:E3

168. Coburger J, Hagel V, Wirtz CR, Konig R. 2015. Surgery for Glioblastoma: Impact of the Combined Use of 5-Aminolevulinic Acid and Intraoperative MRI on Extent of Resection and Survival. *PloS one* 10:e0131872

169. Roessler K, Becherer A, Donat M, Cejna M, Zachenhofer I. 2012. Intraoperative tissue fluorescence using 5-aminolevolinic acid (5-ALA) is more sensitive than contrast MRI or amino acid positron emission tomography ((18)F-FET PET) in glioblastoma surgery. *Neurological research* 34:314-7

170. Stummer W, Tonn JC, Mehdorn HM, Nestler U, Franz K, et al. 2011. Counterbalancing risks and gains from extended resections in malignant glioma surgery: a supplemental analysis from the randomized 5-aminolevulinic acid glioma resection study. Clinical article. *Journal of neurosurgery* 114:613-23

171. Liu JT, Meza D, Sanai N. 2014. Trends in fluorescence image-guided surgery for gliomas. *Neurosurgery* 75:61-71

172. Della Puppa A, De Pellegrin S, d'Avella E, Gioffre G, Rossetto M, et al. 2013. 5-aminolevulinic acid (5-ALA) fluorescence guided surgery of high-grade gliomas in eloquent areas assisted by functional mapping. Our experience and review of the literature. *Acta neurochirurgica* 155:965-72

173. Schucht P, Beck J, Abu-Isa J, Andereggen L, Murek M, et al. 2012. Gross total resection rates in contemporary glioblastoma surgery: results of an institutional protocol combining 5-aminolevulinic acid intraoperative fluorescence imaging and brain mapping. *Neurosurgery* 71:927-35

174. Schucht P, Seidel K, Beck J, Murek M, Jilch A, et al. 2014. Intraoperative monopolar mapping during 5-ALA-guided resections of glioblastomas adjacent to motor eloquent areas: evaluation of resection rates and neurological outcome. *Neurosurgical focus* 37:E16-24

175. Keles GE, Chang EF, Lamborn KR, Tihan T, Chang CJ, et al. 2006. Volumetric extent of resection and residual contrast enhancement on initial surgery as predictors of outcome in adult patients with hemispheric anaplastic astrocytoma. *Journal of neurosurgery* 105:34-40

176. Pope WB, Sayre J, Perlina A, Villablanca JP, Mischel PS, Cloughesy TF. 2005. MR imaging correlates of survival in patients with high-grade gliomas. *AJNR. American journal of neuroradiology* 26:2466-74

177. Barker PB, Lin DDM. 2006. In vivo proton MR spectroscopy of the human brain. *Prog Nucl Mag Res Sp* 49:99-128

178. Nishimura DG. 1996. *Principles of magnetic resonance imaging*. http://books.google.com/books?id=uz9BAQAAIAAJ

179. Bertholdo D, Watcharakorn A, Castillo M. 2013. Brain proton magnetic resonance spectroscopy: introduction and overview. *Neuroimaging clinics of North America* 23:359-80

180. N F, S O, H M, PJ M. 2006. Physical basis of magnetic resonance spectroscopy and its applications to central nervous system disease. *American Journal of Applied Sciences* 3:1836-45

181. Birken DL, Oldendorf WH. 1989. N-acetyl-L-aspartic acid: a literature review of a compound prominent in 1H-NMR spectroscopic studies of brain. *Neuroscience and biobehavioral reviews* 13:23-31

182. Neale JH, Bzdega T, Wroblewska B. 2000. N-Acetylaspartylglutamate: the most abundant peptide neurotransmitter in the mammalian central nervous system. *J Neurochem* 75:443-52

183. Govindaraju V, Young K, Maudsley AA. 2000. Proton NMR chemical shifts and coupling constants for brain metabolites. *NMR in Biomedicine* 13:129-53

184. Urenjak J, Williams SR, Gadian DG, Noble M. 1992. Specific expression of N-acetylaspartate in neurons, oligodendrocyte-type-2 astrocyte progenitors, and immature oligodendrocytes in vitro. *J Neurochem* 59:55-61

185. Simmons ML, Frondoza CG, Coyle JT. 1991. Immunocytochemical localization of N-acetyl-aspartate with monoclonal antibodies. *Neuroscience* 45:37-45

186. Pouwels PJ, Frahm J. 1998. Regional metabolite concentrations in human brain as determined by quantitative localized proton MRS. *Magnetic resonance in medicine* 39:53-60

187. Bluml S, Zuckerman E, Tan J, Ross BD. 1998. Proton-Decoupled 31P Magnetic Resonance Spectroscopy Reveals Osmotic and Metabolic Disturbances in Human Hepatic Encephalopathy. *Journal of Neurochemistry* 71:1564-76

188. Rudkin TM, Arnold DL. 1999. Proton magnetic resonance spectroscopy for the diagnosis and management of cerebral disorders. *Arch Neurol* 56:919-26

189. Quistorff B, Secher NH, Van Lieshout JJ. 2008. Lactate fuels the human brain during exercise. *Faseb J* 22:3443-9

190. Hurd RE, Freeman D. 1991. Proton editing and imaging of lactate. *NMR Biomed* 4:73-80

191. Wishart DS, Bigam CG, Yao J, Abildgaard F, Dyson HJ, et al. 1H, 13C and 15N chemical shift referencing in biomolecular NMR. *Journal of Biomolecular NMR* 6:135-40

192. Cavassila S, Deval S, Huegen C, van Ormondt D, Graveron-Demilly D. 2001. Cramer-Rao bounds: an evaluation tool for quantitation. *NMR Biomed* 14:278-83

193. Maudsley AA, Domenig C, Govind V, Darkazanli A, Studholme C, et al. 2009. Mapping of brain metabolite distributions by volumetric proton MR spectroscopic imaging (MRSI). *Magnetic resonance in medicine* 61:548-59

194. Ogg RJ, Kingsley PB, Taylor JS. 1994. WET, a T1- and B1-insensitive water-suppression method for in vivo localized 1H NMR spectroscopy. *J Magn Reson B* 104:1-10

195. Ebel A, Maudsley AA. 2001. Comparison of methods for reduction of lipid contamination for in vivo proton MR spectroscopic imaging of the brain. *Magnetic resonance in medicine* 46:706-12

196. Hetherington HP, Mason GF, Pan JW, Ponder SL, Vaughan JT, et al. 1994. Evaluation of cerebral gray and white matter metabolite differences by spectroscopic imaging at 4.1T. *Magnetic resonance in medicine* 32:565-71

197. Maudsley AA, Darkazanli A, Alger JR, Hall LO, Schuff N, et al. 2006. Comprehensive processing, display and analysis for in vivo MR spectroscopic imaging. *NMR Biomed* 19:492-503

198. Barefoot JC, Heitmann BL, Helms MJ, Williams RB, Surwit RS, Siegler IC. 1998. Symptoms of depression and changes in body weight from adolescence to mid-life. *Int J Obes Relat Metab Disord* 22:688-94

199. Miller GE, Freedland KE, Duntley S, Carney RM. 2005. Relation of depressive symptoms to C-reactive protein and pathogen burden (cytomegalovirus, herpes simplex virus, Epstein-Barr virus) in patients with earlier acute coronary syndromes. *Am J Cardiol* 95:317-21

200. Miller GE, Stetler CA, Carney RM, Freedland KE, Banks WA. 2002. Clinical depression and inflammatory risk markers for coronary heart disease. *Am J Cardiol* 90:1279-83

201. Alesci S, Martinez PE, Kelkar S, Ilias I, Ronsaville DS, et al. 2005. Major depression is associated with significant diurnal elevations in plasma interleukin-

6 levels, a shift of its circadian rhythm, and loss of physiological complexity in its secretion: clinical implications. *J Clin Endocrinol Metab* 90:2522-30

202. Bruhn H, Frahm J, Gyngell ML, Merboldt KD, Hanicke W, et al. 1989. Noninvasive differentiation of tumors with use of localized H-1 MR spectroscopy in vivo: initial experience in patients with cerebral tumors. *Radiology* 172:541-8

203. Hattingen E, Raab P, Franz K, Zanella FE, Lanfermann H, Pilatus U. 2008. Myo-inositol: a marker of reactive astrogliosis in glial tumors? *NMR Biomed* 21:233-41

204. Herholz K, Heindel W, Luyten PR, denHollander JA, Pietrzyk U, et al. 1992. In vivo imaging of glucose consumption and lactate concentration in human gliomas. *Ann Neurol* 31:319-27

205. Alger JR, Frank JA, Bizzi A, Fulham MJ, DeSouza BX, et al. 1990. Metabolism of human gliomas: assessment with H-1 MR spectroscopy and F-18 fluorodeoxyglucose PET. *Radiology* 177:633-41

206. Di Costanzo A, Scarabino T, Trojsi F, Popolizio T, Catapano D, et al. 2008. Proton MR spectroscopy of cerebral gliomas at 3 T: spatial heterogeneity, and tumour grade and extent. *European radiology* 18:1727-35

207. Howe FA, Barton SJ, Cudlip SA, Stubbs M, Saunders DE, et al. 2003. Metabolic profiles of human brain tumors using quantitative in vivo 1H magnetic resonance spectroscopy. *Magnetic resonance in medicine* 49:223-32

208. Kuesel AC, Sutherland GR, Halliday W, Smith IC. 1994. 1H MRS of high grade astrocytomas: mobile lipid accumulation in necrotic tissue. *NMR Biomed* 7:149-55

209. Castillo M, Smith JK, Kwock L. 2000. Correlation of myo-inositol levels and grading of cerebral astrocytomas. *AJNR. American journal of neuroradiology* 21:1645-9

210. Saraf-Lavi E, Bowen BC, Pattany PM, Sklar EM, Murdoch JB, Petito CK. 2003. Proton MR spectroscopy of gliomatosis cerebri: case report of elevated myoinositol with normal choline levels. *AJNR. American journal of neuroradiology* 24:946-51

211. Gill SS, Thomas DG, Van Bruggen N, Gadian DG, Peden CJ, et al. 1990. Proton MR spectroscopy of intracranial tumours: in vivo and in vitro studies. *Journal of computer assisted tomography* 14:497-504

212. Hourani R, Horska A, Albayram S, Brant LJ, Melhem E, et al. 2006. Proton magnetic resonance spectroscopic imaging to differentiate between nonneoplastic lesions and brain tumors in children. *J Magn Reson Imaging* 23:99-107

213. Senft C, Hattingen E, Pilatus U, Franz K, Schanzer A, et al. 2009. Diagnostic value of proton magnetic resonance spectroscopy in the noninvasive grading of solid gliomas: comparison of maximum and mean choline values. *Neurosurgery* 65:908-13

214. Chawla S, Wang S, Wolf RL, Woo JH, Wang J, et al. 2007. Arterial spin-labeling and MR spectroscopy in the differentiation of gliomas. *AJNR. American journal of neuroradiology* 28:1683-9

215. Tate AR, Majos C, Moreno A, Howe FA, Griffiths JR, Arus C. 2003. Automated classification of short echo time in in vivo 1H brain tumor spectra: a multicenter study. *Magnetic resonance in medicine* 49:29-36

216. De Edelenyi FS, Rubin C, Esteve F, Grand S, Decorps M, et al. 2000. A new approach for analyzing proton magnetic resonance spectroscopic images of brain tumors: nosologic images. *Nat Med* 6:1287-9

217. Tate AR, Griffiths JR, Martinez-Perez I, Moreno A, Barba I, et al. 1998. Towards a method for automated classification of 1H MRS spectra from brain tumours. *NMR Biomed* 11:177-91

218. Preul MC, Caramanos Z, Collins DL, Villemure JG, Leblanc R, et al. 1996. Accurate, noninvasive diagnosis of human brain tumors by using proton magnetic resonance spectroscopy. *Nat Med* 2:323-5

219. Ishimaru H, Morikawa M, Iwanaga S, Kaminogo M, Ochi M, Hayashi K. 2001. Differentiation between high-grade glioma and metastatic brain tumor using single-voxel proton MR spectroscopy. *European radiology* 11:1784-91

220. Fan G, Sun B, Wu Z, Guo Q, Guo Y. 2004. In vivo single-voxel proton MR spectroscopy in the differentiation of high-grade gliomas and solitary metastases. *Clin Radiol* 59:77-85

221. Chiang IC, Kuo YT, Lu CY, Yeung KW, Lin WC, et al. 2004. Distinction between high-grade gliomas and solitary metastases using peritumoral 3-T magnetic resonance spectroscopy, diffusion, and perfusion imagings. *Neuroradiology* 46:619-27

222. Hermann EJ, Hattingen E, Krauss JK, Marquardt G, Pilatus U, et al. 2008. Stereotactic biopsy in gliomas guided by 3-tesla 1H-chemical-shift imaging of choline. *Stereotactic and functional neurosurgery* 86:300-7

223. Martin AJ, Liu H, Hall WA, Truwit CL. 2001. Preliminary assessment of turbo spectroscopic imaging for targeting in brain biopsy. *AJNR. American journal of neuroradiology* 22:959-68

224. Di Costanzo A, Scarabino T, Trojsi F, Giannatempo GM, Popolizio T, et al. 2006. Multiparametric 3T MR approach to the assessment of cerebral gliomas: tumor extent and malignancy. *Neuroradiology* 48:622-31

225. Hall WA, Martin A, Liu H, Truwit CL. 2001. Improving diagnostic yield in brain biopsy: coupling spectroscopic targeting with real-time needle placement. *J Magn Reson Imaging* 13:12-5

226. Dowling C, Bollen AW, Noworolski SM, McDermott MW, Barbaro NM, et al. 2001. Preoperative proton MR spectroscopic imaging of brain tumors: correlation with histopathologic analysis of resection specimens. *AJNR. American journal of neuroradiology* 22:604-12

227. Chan AA, Lau A, Pirzkall A, Chang SM, Verhey LJ, et al. 2004. Proton magnetic resonance spectroscopy imaging in the evaluation of patients undergoing gamma knife surgery for Grade IV glioma. *Journal of neurosurgery* 101:467-75

228. Ganslandt O, Stadlbauer A, Fahlbusch R, Kamada K, Buslei R, et al. 2005. Proton magnetic resonance spectroscopic imaging integrated into image-guided surgery: correlation to standard magnetic resonance imaging and tumor cell density. *Neurosurgery* 56:291-8

229. McKnight TR, von dem Bussche MH, Vigneron DB, Lu Y, Berger MS, et al. 2002. Histopathological validation of a three-dimensional magnetic resonance spectroscopy index as a predictor of tumor presence. *Journal of neurosurgery* 97:794-802

230. Stadlbauer A, Nimsky C, Buslei R, Pinker K, Gruber S, et al. 2007. Proton magnetic resonance spectroscopic imaging in the border zone of gliomas: correlation of metabolic and histological changes at low tumor infiltration--initial results. *Investigative radiology* 42:218-23

231. Chang J, Thakur S, Perera G, Kowalski A, Huang W, et al. 2006. Image-fusion of MR spectroscopic images for treatment planning of gliomas. *Med Phys* 33:32-40

232. Graves EE, Pirzkall A, Nelson SJ, Larson D, Verhey L. 2001. Registration of magnetic resonance spectroscopic imaging to computed tomography for radiotherapy treatment planning. *Med Phys* 28:2489-96

233. Narayana A, Chang J, Thakur S, Huang W, Karimi S, et al. 2007. Use of MR spectroscopy and functional imaging in the treatment planning of gliomas. *Br J Radiol* 80:347-54

234. Pirzkall A, Li X, Oh J, Chang S, Berger MS, et al. 2004. 3D MRSI for resected high-grade gliomas before RT: tumor extent according to metabolic activity in relation to MRI. *Int J Radiat Oncol Biol Phys* 59:126-37

235. Park I, Tamai G, Lee MC, Chuang CF, Chang SM, et al. 2007. Patterns of recurrence analysis in newly diagnosed glioblastoma multiforme after three-dimensional conformal radiation therapy with respect to pre-radiation therapy magnetic resonance spectroscopic findings. *International journal of radiation oncology, biology, physics* 69:381-9

236. Pirzkall A, McKnight TR, Graves EE, Carol MP, Sneed PK, et al. 2001. MR-spectroscopy guided target delineation for high-grade gliomas. *International journal of radiation oncology, biology, physics* 50:915-28

237. Nelson SJ, Graves E, Pirzkall A, Li X, Antiniw Chan A, et al. 2002. In vivo molecular imaging for planning radiation therapy of gliomas: an application of 1H MRSI. *J Magn Reson Imaging* 16:464-76

238. Stadlbauer A, Buchfelder M, Doelken MT, Hammen T, Ganslandt O. 2011. Magnetic resonance spectroscopic imaging for visualization of the infiltration zone of glioma. *Cen Eur Neurosurg* 72:63-9

Chapter 2

Quantitative tumor segmentation for the evaluation of extent of GBM resection

2.1 Author's Contribution and Acknowledgement of Reproduction

The work presented here was conceptualized, organized, researched, and written by the dissertation author. Of the data presented all was collected by the author under the guidance of Dr. Shim, Dr. Holder, and many collaborators. The chapter is reproduced with minor edits from Cordova, J.S., Schreibmann, E., Hadjipanayis, C.G., Guo, Y., Shu, H.K., Shim, H., Holder, C.A. Quantitative Tumor Segmentation for Evaluation of Extent of Glioblastoma Resection to Facilitate Multisite Clinical Trials. *Trans. Onc.* (2014) 7(1), 40-47 DOI: 10.1593/tlo.13835 (239).

2.2 Abstract

Standard-of-care therapy for GBMs, the most common and aggressive primary adult brain neoplasm, is maximal safe resection, followed by radiation and chemotherapy. Since maximizing resection may be beneficial for these patients, improving tumor EOR with methods such as intraoperative 5-ALA FGS is currently under evaluation. However, it is difficult to reproducibly judge EOR in these studies due to the lack of reliable tumor segmentation methods, especially for postoperative MRI scans. Therefore, a reliable, easily distributable segmentation method is needed to permit valid comparison, especially across multiple sites. We report a segmentation method that combines versatile region-of-interest generation with automated clustering methods. We applied this to GBM cases undergoing FGS and matched controls to illustrate the method's reliability and accuracy. Agreement and inter-rater variability between segmentations were assessed using the concordance correlation coefficient, and spatial accuracy was determined using the Dice similarity index and Hausdorff distance. Fuzzy C-means clustering with three classes was the best performing method, generating volumes with high agreement with manual contouring and high inter-rater agreement pre- and postoperatively. The proposed segmentation method allows tumor volume measurements of contrast-enhanced T1-weighted images in an unbiased, reproducible fashion necessary for quantifying EOR in multicenter trials.

2.3 Introduction

GBM is the most common and most aggressive primary brain neoplasm in adults. Current imaging evaluation for GBM management relies heavily on the

subjective analysis of T1-weighted (T1W) MR images (9; 10). Simple unidimensional and bi-dimensional measurements of T1W contrast-enhancing regions of the tumor are the crux of response criteria in clinical trials, although limitations of such methods have been reviewed previously in detail, particularly with regards to post-surgical tumor analysis (67; 136; 144). For example, these linear methods of measurement are not well-suited for evaluating curvilinear tumor remnants such as those along the edges of a postoperative resection cavity. In addition, they may not accurately account for the presence of T1-hyperintense blood products (methemoglobin) in and around the resection site, which can be confused with enhancing tumor tissue. While not currently the standard-of-care, these morphological nuances can be accounted for by a neuroradiologist with 3D volume-rendering software that allows for the manual tracing of images, or "contouring"; however, this process is time-consuming, cost-prohibitive, and suffers from limited reproducibility (128; 240; 241). In order to overcome these limitations, many sophisticated algorithms have been developed for the automated segmentation of multiple images; however, few have achieved the simplicity, speed, accuracy, and limited user interaction required for routine clinical use (242-245). Moreover, many of the software environments in which these techniques have been designed are not standardized for clinical use, compounding the challenge of their implementation in clinical trials (246). Due to the inadequacies surrounding the manual and automated segmentation methods that are currently available, it would be desirable to develop a hybrid method of tumor segmentation that is adaptable to various clinically-available tools for the reproducible segmentation of contrast-enhancing tumors in multicenter neurosurgical trials.

Coupling a flexible image sampling method, such as region-of-interest (ROI) blob (ROI-blob) generation, to an unsupervised statistical classification algorithm appears to exhibit the clinically-desired balance for semi-automated tumor segmentation. Two well-established classification schemes that can be adapted for unsupervised image segmentation are Otsu's multi-level thresholding (Otsu) and Fuzzy C-means clustering (Fuzzy) (247-249). The Otsu method uses discriminant statistical analysis for image histogram intensity thresholding, exhaustively determining intensity thresholds (between tissue classes) that minimize the intraclass variance among each class of voxels (250; 251). The division algorithm modifies each threshold by fitting the histogram with a number of probability curves and iteratively computing the variances and positions of each until curve overlap is minimized. The result is a 3D map with discrete classes containing voxels that exhibit similar signal intensities. When this method is used to divide a contrast-enhanced, T1W ROI-blob into three or four classes, the resultant map differentiates strongly and weakly enhancing regions from surrounding tissues.

The Fuzzy algorithm similarly computes cluster centroids, and clusters voxels based on intra/interclass signal intensity variance. Unlike Otsu –which classifies voxels into discrete clusters (hard-clustering)– Fuzzy treats each data element as a member of all clusters with an associated level of membership in each, which can be expressed as a continuous value (soft-clustering) (252-254). Therefore, Fuzzy classification results in a set of maps, each representing a class with a similar signal intensity range, where each voxel's value indicates the degree of its residence (expressed as a probability) in that class. Fuzzy has been

investigated for tumor segmentation using multi-dimensional feature vectors over the last couple of decades with varying degrees of success (255-257); however, to our knowledge, no investigation has been done to evaluate its performance coupled to ROI-blob analysis.

In this study, we develop and validate a flexible semi-automated tumor segmentation tool for the assessment of pre- and postoperative GBM tumor burden based on contrast-enhanced T1W images. As proof of principle, we applied ROI-blob/voxel classification methods (Otsu and Fuzzy) to GBM patients receiving FGS with 5-ALA and retrospectively matched control patients in order to: 1) illustrate the reliability and accuracy of the segmentation method, and 2) corroborate the EOR findings of the ongoing Phase II 5-ALA clinical trial (50; 51; 161; 163; 170; 258; 259). The desired outcome is to develop a reliable and user-friendly segmentation method for the generation of T1W contrast-enhancing tumor volumes that may be used in multicenter neurosurgical clinical trials in GBM patients.

2.4 Methods

2.4.1 Preoperative and Postoperative Imaging

Per the institutional review board-approved 5-ALA Phase II clinical trial, high-resolution, 3D preoperative MR images, including 1 mm^3 T1W magnetization-prepared rapid gradient-echo (MP-RAGE) images (repetition time/echo time = 1900/3.52, 256 x 256 matrix, flip angle = 9°, before and after intravenous administration of gadolinium-based contrast medium) generated 48 h or less prior to surgery for 5-ALA patients were analyzed. Postoperative images

consisted of T1W MP-RAGE and/or low-resolution (1 x 1 x 5 mm, repetition time/echo time = 450-2000/9.2-20, 256 x 224-177 matrix, flip angle = 90°-130°) images acquired before and after the intravenous administration of gadolinium-based contrast medium postoperatively, within 24 h of surgery. Control patients matched for GBM tumor size and location were retrospectively selected from an Emory University/Winship Cancer Institute Department of Radiation Oncology database for case-comparison. These pre- and postoperative MR images exhibited similar characteristics in terms of the aforementioned pulse sequence parameters and the timing of the scans relative to surgery (24-48 h post-surgery).

2.4.2 Image Analysis

The 510(k), FDA-cleared medical imaging platform VelocityAI (Velocity Medical Solutions, Atlanta, GA) was used to outline tumors manually and generate ROI-blobs using pre- and postoperative T1W scans with and without intravenous contrast. As per a European randomized multicenter FGS trial, complete tumor resection was defined as ≤ 0.175 cm^3 of residual contrast-enhancing tumor after surgery using volumetric assessment (50). The conventional imaging definition of GTR (residual contrast-enhancing tumor < 1 cm^3) was also evaluated.

2.4.3 Computer-Assisted, Manual Contouring

Preoperative and postoperative tumor volumes were manually delineated using VelocityAI by an experienced board-certified neuroradiologist (CAH). Enhancing-tumor control points were initiated, and tumor regions were interactively grown or contracted in two dimensions, and post-hoc edits were made as needed. This manual method of contouring is commonplace in the generation

of tumor volumes for both radiotherapy planning and validation of simulated segmentations (243; 260; 261).

2.4.4 Semi-automated Segmentation Method

Preoperative tumor ROI-blobs for Otsu and Fuzzy processing were generated in VelocityAI by coarsely contouring around enhancing tumor on T1W images, including the first and last image on which the tumor is visible, and every sixth axial slice in between, and then automatically interpolating to a cohesive 3D structure (**Figure 2.1A** and **B**). As few as two slices (at the superior-most and inferior-most poles of the tumor, respectively) and as many as every slice containing tumor can be contoured and interpolated to give a cohesive ROI-blob; however, based on practical clinical experience, we have found that contouring every 6^{th} slice gives ROI-blobs that adequately encompass even the most complex contrast-enhancing brain tumors within a reasonable time-frame. This type of initialization can be done with any volume-rendering platform capable of exporting DICOM blobs making implementation of the method simple at multiple sites.

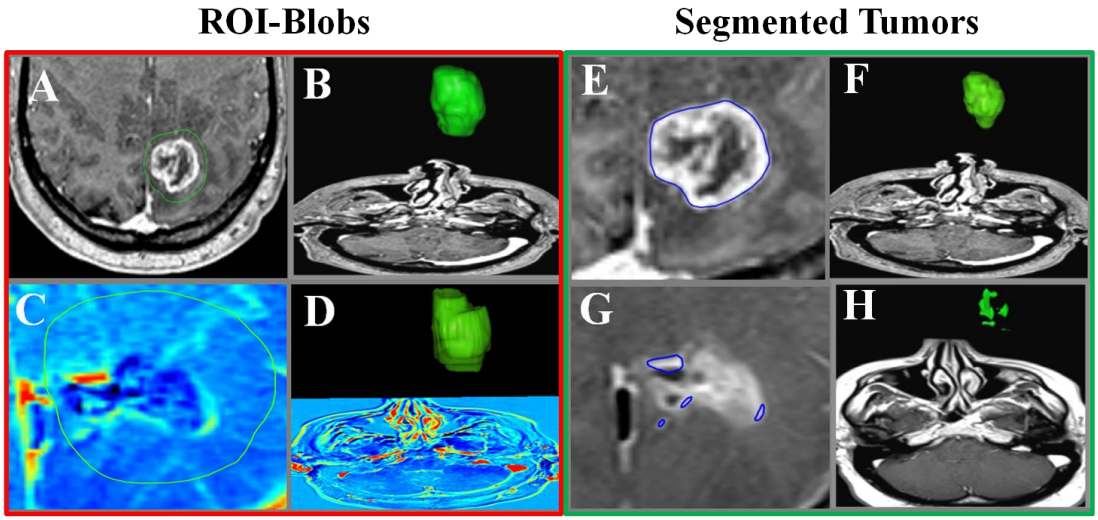

Figure 2.1. Segmentation procedure for preoperative and postoperative images. Preoperative (**A** and **B**) and postoperative (**C** and **D**) ROI-blobs (2D and 3D) generated by coarse contouring. Subtraction image (**C**) accounts for blood product accumulation in resection cavity (dark region). Resultant 2D and 3D tumor segmentations for preoperative (**E** and **F**) and postoperative (**G** and **H**) contrast-enhanced T1W images using Fuzzy3 algorithm.

ROI-blobs and parent images were then exported and processed offline using C++-generated Otsu and Fuzzy algorithms. Algorithms utilized standard code from the Insight Segmentation and Registration Toolkit (ITK), and were compiled as a command-line executable taking as input DICOM images (ROI-blobs) and outputting segmentation masks in the same format. Algorithm pre-processing included fade correction for signal differences due to magnetic field gradients in a bias-field estimation manner. No smoothing functions were utilized, epsilon was set at 0.01, and iterations set at 30 as these were found to be optimal. For these algorithms, the number of tissue classes is a definable parameter, and any number of strata represented by a positive integer can be generated; however, stratification of voxels into more than 5 classes is of limited utility, as discrete tissue types (such as contrast-enhancing tumor rims) become erroneously subcategorized. Therefore, only maps stratified into 3 or 4 classes were generated with the naming convention as follows: classification of 4 classes using the Fuzzy and Otsu algorithms are named Fuzzy4 and Otsu4, respectively, and classification of 3 classes using the Fuzzy and Otsu algorithms are named Fuzzy3 and Otsu3, respectively. It should be noted that Otsu3 was abandoned in the preliminary analysis as resultant maps did not differentiate parenchyma from enhancing tissue, and therefore is not reported herein. These maps were then imported into VelocityAI for display and evaluation.

To produce post-resection tumor volumes, image difference maps (subtraction images) were generated by subtracting white matter-normalized, spatially co-registered pre-contrast T1W images from post-contrast T1W images. This was done in order to correct for the presence of T1-hyperintense postoperative

blood products and cavity deformation. Normalization of postoperative images included fade correction and pre-contrast image signal scaling with post-contrast: pre-contrast intensity ratio. These normalized subtraction images were then used to draw coarse ROI-blobs and generate segmentation maps using both algorithms outlined above (**Figure 2.1C** and **D**). This was done for all pre- and postoperative images by two research specialists (non-radiologists), Reader 1 (JSC) and Reader 2 (JA), independently and many days apart (>20 days).

2.4.5 Statistical Methods

Statistical analyses were performed with the Statistical Analysis System (version 9; SAS Institute, Cary, NC); all were 2-sided, and statistical significance was set at $p < 0.05$. The concordance correlation coefficient (CCC), a reproducibility index evaluating the agreement of two readings by measuring their combined variation from the line $y = x$, was used to measure the agreement of tumor volumes generated by Readers 1 and 2 using Otsu4, Fuzzy4, and Fuzzy3 with those generated manually by the neuroradiologist (262-264). Spatial agreement between each segmentation and the manual contour was evaluated using the Dice Similarity Index (Dice) and the mean Euclidean distance (MED) –volume overlap and surface distance metrics, respectively– for each pair, and means between readers were subjected to analysis of variance with Tukey's correction (265; 266). It is generally accepted that Dice values > 0.70 represent a significant overlap in structures, with values > 0.80 considered to be "good" and values > 0.90 considered to be "excellent". For surface distance, a value of 0 is an ideal MED; however, for practical purposes, a mean distance of ~ 1 mm is considered very good

(~1 voxel-width error in MP-RAGE images). Inter-rater agreement, in terms of CCC, was evaluated for the method that had the highest agreement with manual contouring as a metric of inter-rater variability. Wilcoxon signed-rank test and Chi-square/Fisher's exact analysis were used to compare manually-generated and algorithm-generated volume outcomes (i.e., residual tumor volume and EOR) for 16 5-ALA: control pairs in the 37 case sample. Performance metrics (sensitivity, specificity, positive predictive value, and negative predictive value) were computed using a two-by-two contingency table for post-resection tumor volume cut-offs of ≤ 1 cm^3 and ≤ 0.175 cm^3, with manual contouring by an experienced neuroradiologist as the "ground truth" for these 16 ALA:control pairs (267).

2.5 Results

2.5.1 Fuzzy3 Shows Greatest Volume Agreement with Manual Contouring

A total of 37 cases were accrued for validation of the segmentation methods; 16 of which had received FGS in the 5-ALA trial, and 21 retrospective controls. Examples of pre- and postoperative ROI-blobs and tumor volumes generated using Fuzzy3 are shown in **Figures 2.1A-D** and **E-H**, respectively, and raw volume data for all cases and methods are in **Tables 2.1** and **2.2**. The CCC for each method with manual contouring pre- and postoperatively is shown with 95% confidence intervals in **Figure 2.2**. The extra five cases are included with 5-ALA cases for CCC, method comparison, and spatial analysis in **Figures 2-4**. Although differences in agreement between Fuzzy4 and Otsu4 were subtle preoperatively, greater differences were apparent postoperatively, with CCCs for Fuzzy4 approaching unity, while those for Otsu were below 0.84. This trend held for both

readers pre- and postoperatively suggesting a reproducible finding attributable to the method. Moreover, pre- and postoperative differences in inter-reader mean CCC between Otsu4 and Fuzzy4 were found to be statistically significant at p = 0.027 (**Table 2.3**) and p=0.002 (**Table 2.4**), respectively.

ID	Manual	Reader 1 Otsu4	Reader 2 Otsu4	Reader 1 Fuzzy3	Reader 2 Fuzzy3	Reader 1 Fuzzy4	Reader 2 Fuzzy4
Case 1	3.59	2.41	6.10	3.58	3.51	3.547	3.547
Case 2	83.98	82.08	83.21	90.36	86.15	96.88	88.83
Case 3	22.36	23.23	27.69	22.47	22.64	22.56	21.14
Case 4	41.81	48.45	47.05	41.82	41.64	39.75	39.75
Case 5	8.38	9.20	8.72	8.49	8.01	8.25	8.32
Case 6	42.73	47.31	44.71	42.12	45.09	43.89	37.23
Case 7	11.94	15.24	12.77	12.72	10.85	12.05	10.45
Case 8	51.19	61.85	50.14	50.81	48.74	51.41	50.90
Case 9	4.15	6.59	3.68	4.38	3.34	4.02	3.61
Case 10	15.95	15.77	6.91	15.73	15.17	16.27	15.69
Case 11	4.80	4.87	4.65	4.87	4.88	5.07	4.16
Case 12	76.19	88.52	77.80	80.56	77.82	76.80	75.42
Case 13	66.75	89.27	68.63	66.30	67.62	69.69	65.81
Case 14	4.13	3.31	3.94	4.17	4.05	3.98	4.04
Case 15	53.34	51.98	50.44	52.94	52.9	53.09	57.10
Case 16	18.23	16.43	19.99	18.14	18.03	18.42	16.35
Case 17	13.97	14.54	15.16	14.00	14.49	13.45	14.07
Case 18	54.13	61.69	52.58	49.30	52.01	52.45	51.18
Case 19	10.92	7.24	16.30	10.85	11.10	11.02	11.60
Case 20	20.05	14.69	34.83	20.82	21.31	19.44	19.03
Case 21	30.94	31.03	31.11	32.75	28.95	31.46	30.65
Case 22	35.72	40.71	42.84	36.35	33.79	36.65	37.51
Case 23	54.41	65.54	59.19	54.88	55.74	61.82	60.76
Case 24	89.40	126.8	84.66	92.59	89.80	87.98	95.39
Case 25	3.92	4.19	9.30	3.60	3.67	3.66	3.39
Case 26	16.23	23.51	15.84	16.38	15.14	17.29	15.47
Case 27	29.66	32.50	32.64	29.98	30.03	29.54	29.11
Case 28	101.75	121.36	112.38	112.97	95.59	106.56	78.63
Case 29	65.59	84.86	45.88	65.10	64.63	65.51	67.64
Case 30	23.88	22.29	23.16	23.82	23.38	24.09	24.58
Case 31	33.40	30.77	31.17	33.11	33.89	33.05	30.63
Case 32	54.60	53.62	52.83	54.86	54.37	53.95	53.76
Case 33	29.22	25.97	24.23	28.9	20.90	28.79	21.04
Case 34	15.01	15.51	13.88	14.70	13.83	15.22	13.15
Case 35	9.67	8.98	8.51	9.32	9.13	9.81	9.01
Case 36	34.91	31.38	30.67	33.59	34.15	33.05	32.30
Case 37	82.58	72.00	67.66	81.93	70.54	84.29	58.78

Table 2.1. Preoperative contrast-enhancing tumor volumes (cm3) generated using manual, Otsu, and Fuzzy methods. Readers 1 & 2 are remote in time. Line demarcates the end of 32 cases in 5-ALA trial.

ID	Manual	Reader 1 Otsu4	Reader 2 Otsu4	Reader 1 Fuzzy3	Reader 2 Fuzzy3	Reader 1 Fuzzy4	Reader 2 Fuzzy4
Case 1	0.22	0.41	1.46	0.43	0.30	0.28	0.29
Case 2	8.25	15.24	19.88	7.07	8.00	8.91	5.25
Case 3	1.49	2.11	2.84	1.77	1.42	1.62	1.93
Case 4	0.82	2.71	0.99	0.65	1.72	2.12	2.17
Case 5	0.62	0.47	0.90	0.62	0.69	0.39	0.75
Case 6	5.0	5.28	6.32	4.32	5.26	4.97	5.84
Case 7	0.08	0.97	0.90	0.05	0.05	0.03	0.00
Case 8	0.05	0.72	0.60	0.65	0.55	0.41	0.65
Case 9	0.01	0.28	0.33	0.11	0.19	0.10	0.31
Case 10	0.69	1.53	3.49	0.65	0.76	0.68	0.90
Case 11	0.04	1.80	3.33	0.06	0.03	0.13	0.66
Case 12	5.87	10.32	10.87	5.58	5.28	7.07	5.88
Case 13	3.94	3.93	2.59	3.66	4.95	3.60	5.01
Case 14	0.64	0.80	0.75	0.72	0.66	0.74	0.52
Case 15	0.52	1.44	6.21	0.86	1.38	0.41	1.28
Case 16	0.05	0.35	0.11	0.08	0.09	0.04	0.04
Case 17	1.28	0.61	0.70	1.26	1.97	1.44	1.58
Case 18	8.06	5.16	5.42	7.83	8.31	8.08	4.54
Case 19	1.20	0.83	2.03	1.28	1.21	1.30	0.84
Case 20	2.36	2.10	2.12	2.17	2.94	2.39	3.61
Case 21	1.58	2.07	2.59	2.02	1.95	1.98	0.96
Case 22	10.42	11.33	11.89	9.70	10.67	10.29	9.29
Case 23	8.60	9.37	10.89	8.35	8.98	8.55	9.31
Case 24	1.91	3.61	5.24	2.56	1.68	2.60	3.05
Case 25	0.64	1.11	3.18	1.38	1.21	0.84	1.71
Case 26	0.03	0.89	0.79	0.55	0.72	0.33	0.27
Case 27	2.12	1.53	1.62	2.36	2.79	2.15	1.29
Case 28	7.28	11.31	15.49	8.27	7.77	9.34	5.89
Case 29	5.77	13.0	13.64	5.70	5.14	8.33	8.80
Case 30	8.62	9.40	8.31	9.83	9.79	8.36	7.49
Case 31	2.95	1.80	6.21	2.94	2.83	3.09	4.05
Case 32	0.91	0.99	0.92	0.92	0.94	0.93	0.79
Case 33	3.73	3.95	2.84	3.16	2.35	3.70	3.46
Case 34	7.63	9.03	9.35	7.20	7.92	8.00	5.60
Case 35	0.91	0.99	0.95	0.88	1.15	1.58	1.23
Case 36	0.58	0.53	0.51	1.76	0.67	0.98	0.43
Case 37	1.14	2.29	2.54	1.93	2.17	1.56	2.01

Table 2.2. Postoperative tumor volumes generated using manual, Otsu, and Fuzzy methods. Readers 1 & 2 are separate readers remote in time. Line demarcates the end of 32 cases in 5-ALA trial.

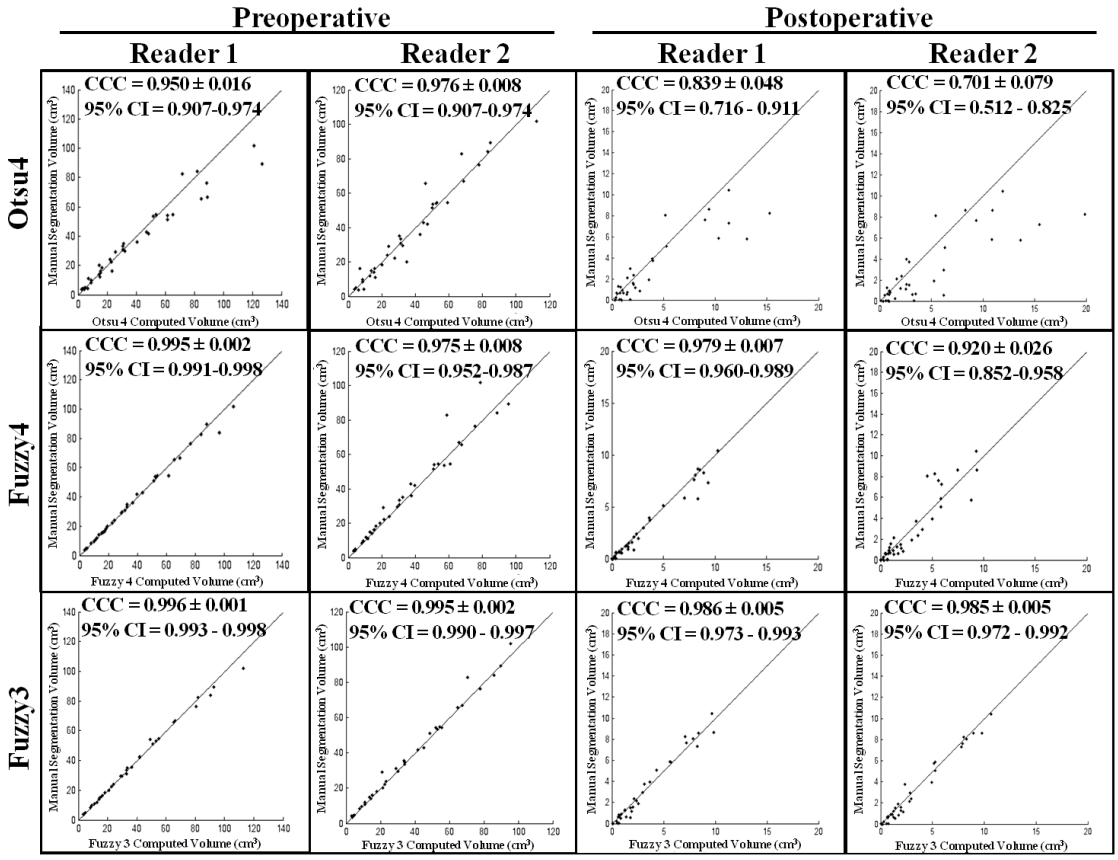

Figure 2.2. Preoperative and postoperative manual tumor contour volume vs. semi-automated segmentation (Otsu 4, Fuzzy 4, or Fuzzy3 from top to bottom) by two separate readers. CCC = Concordance Correlation Coefficient ± SEM; C.I. = Confidence Interval.

	Otsu 4	Fuzzy 4	Fuzzy 3
CCC	0.981*,**	0.993*,°	0.998**,°
SEM	0.006	0.002	0.001
95% C.I.	(0.963, 0.990)	(0.988, 0.998)	(0.997, 0.999)

Table 2.3. Mean CCCs with SEM and 95% confidence intervals for preoperative tumor volumes generated using automated methods versus manual contouring by two separate readers (Reader 1 and Reader 2). *p = 0.027, **p = 0.005, °p = 0.025. CCC = Concordance Correlation Coefficient; C.I. = Confidence Interval.

	Otsu 4	Fuzzy 4	Fuzzy 3
CCC	0.780*,**	0.971*,°	0.990**,°
SEM	0.062	0.009	0.003
95% C.I.	(0.626, 0.875)	(0.953, 0.990)	(0.983, 0.996)

Table 2.4. Mean CCCs with SEM and 95% confidence intervals for postoperative tumor volumes generated using automated methods versus manual contouring by two separate readers (Reader 1 and Reader 2). *p = 0.002, **p = 0.001, °p = 0.045. CCC = Concordance Correlation Coefficient; C.I. = Confidence Interval.

Based on its near-perfect agreement with manual contouring both pre- and postoperatively, Fuzzy clustering was selected as the most promising segmentation method, and another simulation using only three classes was then investigated in an attempt to optimize the method. With the use of only three classes, Fuzzy3 segmentation volumes (**Figure 2.2, Row 3**) exhibited higher agreement with manual contouring - in terms of CCC - than Fuzzy4 segmentations, both pre- and postoperatively. The differences in inter-rater mean CCCs were found to be statistically significant in the pre- and postoperative settings as well ($p = 0.025$ in **Table 2.3** and $p=0.045$ in **Table 2.4**, respectively).

2.5.2 Fuzzy3 Algorithm Shows Greatest Spatial Agreement with Manual Contouring

To evaluate spatial overlap of algorithm-generated tumor segmentations versus manual contours, Dice and MED metrics were used (**Figure 2.3A**). Mean Dice and MED values with SEMs and 95% confidence intervals for Otsu and Fuzzy methods versus manual contouring were computed for subjects pre- and postoperatively and reported in **Figure 2.3B**. Fuzzy4 again outperformed Otsu4, in terms of Dice and MED values, exhibiting a significantly higher mean Dice value and significantly lower MED preoperatively and postoperatively ($p < 0.05$). Subsequent Fuzzy3 simulations produced segmentations that also differed significantly in terms of Dice and MED from Otsu4; however, no significant difference in these values was found between segmentations produced using Fuzzy3 and 4. Moreover, preoperative intra-rater variability - as measured by the coefficient of variation for Dice and MED - were found to be increased in Otsu4

relative to those for Fuzzy3 and 4 which were similar (0.070/1.27 and 0.083/1.38, respectively).

A

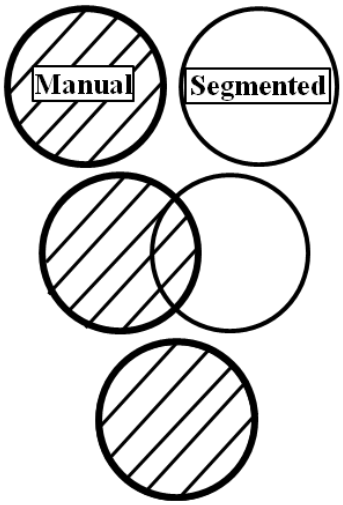

Spatial Overlap	Dice Index	Mean Euclidean Distance
No Overlap	0	Large
Partial Overlap	0 < X < 1	Small
Complete Overlap	1	0

B

	Preoperative			Postoperative		
Dice	**Otsu 4**	**Fuzzy 4**	**Fuzzy 3**	**Otsu 4**	**Fuzzy 4**	**Fuzzy 3**
Mean	0.871*,**	0.911**	0.916*	0.551°,°°	0.620°°	0.640°
SEM	0.014	0.010	0.012	0.043	0.038	0.0402
95% CI	(0.841-0.900)	(0.892-0.931)	(0.891-0.940)	(0.463-0.639)	(0.543-0.697)	(0.559-0.722)
MED						
Mean	0.265+,++	0.151++	0.142+	4.469a, aa	3.129aa	3.110a
SEM	0.039	0.024	0.023	0.882	0.808	0.837
95% CI	(0.186-0.344)	(0.101-0.200)	(0.096-0.188)	(2.676-6.263)	(1.488-4.770)	(1.408-4.811)

Figure 2.3. Pre- and postoperative Dice and MED. Two-dimensional illustration depicting impact of manual and segmented structure overlap on Dice and MED (A) along with mean pre- and postoperative Dice and MED values with SEM and 95% confidence for Otsu and Fuzzy methods versus manual contouring (B). *$p < 0.05$, **$p < 0.05$, $^{+}p < 0.05$, $^{++}p < 0.05$, $^{\circ}p < 0.05$, $^{\circ\circ}p < 0.05$, $^{a}p < 0.05$, $^{a\,a}p < 0.05$. C.I. = Confidence Interval.

2.5.3 Fuzzy3 Algorithm Exhibits Exceptionally High Inter-rater Agreement

Fuzzy3 outperformed both Otsu4 and Fuzzy4 in all measured parameters (CCC, Dice, and MED), although only non-statistically significant trends were found vs. Fuzzy4 in regards to spatial agreement with manual contouring. This, along with anecdotal evidence that Fuzzy4 requires more computation time than Fuzzy3 (as more centroids must be evaluated and more thresholds optimized), led to the selection of the Fuzzy3 method as the best candidate for inter-rater reproducibility analysis. The CCC, SEM, and 95% confidence intervals between separate readers using Fuzzy3 for tumor volume generation are reported, along with their agreement plots, in **Figure 2.4** for subjects pre- and postoperatively, as a measure of inter-rater agreement. The use of Fuzzy3 for tumor segmentation resulted in inter-rater CCCs for pre- and postoperative tumor volumes that approached unity (0.990 and 0.983, respectively), with narrow confidence intervals (0.981 - 0.995 and 0.981 - 0.995, respectively). This was particularly noteworthy postoperatively, as accurate post-surgical residual tumor measurements are typically difficult to determine, even using the most time-consuming manual segmentation methods, due to their complex morphology and the presence of T1-hyperintense blood products.

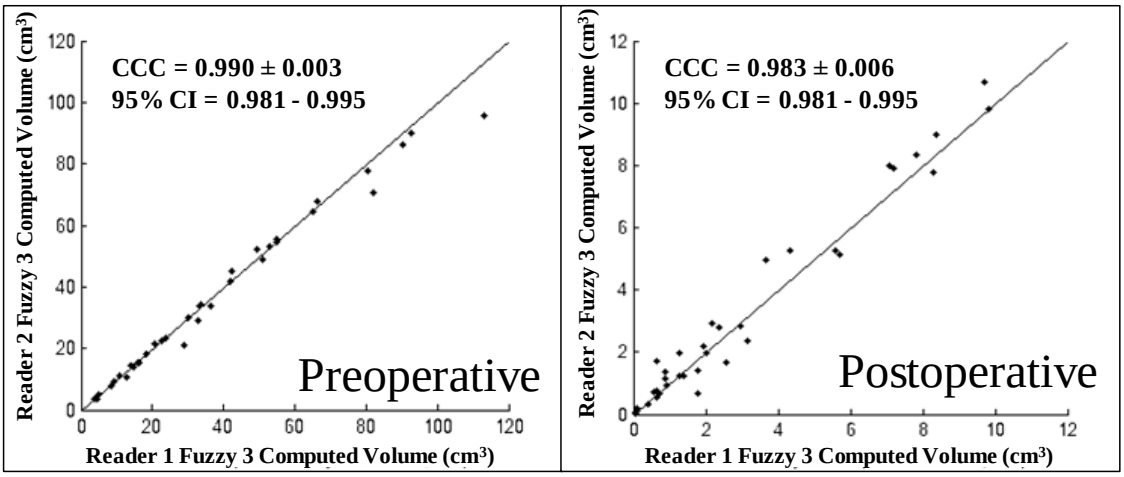

Figure 2.4. Inter-rater reliability analysis. Pre- (top) and postoperative (bottom) tumor volumes generated using Fuzzy3 by Reader 1 vs. Reader 2. CCC = Concordance Correlation Coefficient ± SEM; C.I. = Confidence Interval.

2.5.4 Fuzzy3 Algorithm Performs Well Per Diagnostic Performance Metrics

Chi-square comparison of Fuzzy3-generated postoperative tumor volumes vs. manually contoured tumor volumes by an experienced neuroradiologist (ground truth) for 16 case-control pairs showed a sensitivity of 0.929 (95% CI: 0.661-0.998) and specificity of 1.0 (95% CI: 0.815-1.0), at a volume cut-off of ≤ 1.0 cm^3. Accuracy, positive predictive value, and negative predictive value at ≤ 1.0 cm^3 were 0.969, 1.0 (95% CI: 0.753-1.00), and 0.947 (95% CI: 0.740-0.999), respectively. At a postoperative tumor volume cut-off of ≤ 0.175 cm^3, sensitivity and specificity for Fuzzy3 were found to be 0.667 (95% CI: 0.223-0.957) and 1.0 (95% CI: 0.868-1.000), respectively, with accuracy, positive predictive value, and negative predictive value of 0.938, 1.0 (95% CI: 0.398-0.1.0), and 0.929 (95% CI: 0.765-0.991). The mean EOR, as computed using Fuzzy3 volumes, was found to be 94.5 ± 4.8% for the ALA patients and 86.5 ± 11.5% for the controls. Furthermore, no statistically significant difference between EOR determined using Fuzzy3 or manual contouring was found with p = 0.313 for ALA patients (manual: 95.0 ± 1.2%) and p = 0.115 for control patients (manual EOR: 86.5 ± 3.0%).

2.6 Discussion

In any clinical trial analyzing surgical resection, a major hindrance in image analysis must be addressed: the unbiased and reproducible measurement of pre- and postoperative tumor volumes. We believe that Fuzzy C-means clustering coupled to ROI-blob initialization offers a feasible solution to this hindrance. Fuzzy3 performs as well as other complex semi- and fully-automated methods proposed in recent years. Fuzzy3's preoperative Dice values (mean of 0.92) lie well

within the range of similar values generated using edge and region-based segmentation algorithms (0.72-0.98), including content-based active contours, fuzzy connectedness, and fluid vector flow methods (268-272). This holds true for comparison of Fuzzy3 to other classification/clustering methods - utilizing neighborhood regularization, deformable models, and/or global constraints based on atlases - which exhibit Dice coefficients ranging from 0.40 to 0.90 (243). These values include those generated by newly developed methods utilizing conditional markov fields, support vector machine classification, decision forests, and expectation-maximization, and markov random field methods (273-276). Moreover, MED observed using Fuzzy3 (mean 0.142 mm) preoperatively exhibited similar comparability to other segmentation studies using this metric (0.73 – 4.5 mm) (277-280). Dice and MED values for postoperative segmentations barely failed to reach the generally known thresholds of reasonable segmentation (> 0.70 and 1 mm, respectively), but still fell within the range of those reported in other studies. These lower scores are likely due to the large volume contribution of surrounding blood vessels to end segmentation. This is currently being addressed with post-processing methods, including the use of shape-identifiers to find and remove blood vessels in T1W images.

Computer-assisted, manual contouring decreases the inter- and intra-rater variability of volume generation in multiple anatomical regions (i.e. cervix, lung, brain, pancreas and liver); however, this requires a great deal of time and effort (241; 246; 281-283). Sorensen et al. found that manual contouring of tumor volumes resulted in an average completion time of approximately 20 minutes per tumor - a time requirement that clearly limits its routine use (241). Ongoing work

shows that when a group of cases (tumor volumes 8.0 – 100.0 cm^3) are segmented by a research specialist using Fuzzy3 and a neuroradiologist using computer-assisted manual contouring, Fuzzy3 generates segmentations in significantly less time (186.7 ± 35.3 s vs. 378.5 ± 49.9 s; $p < 0.001$). Furthermore, whereas the entirety of the manual contouring time consists of user interaction, this only accounts for an average of 86.4 s ± 34.4 s (< 50% of total time) using Fuzzy3, as the most time-intensive component of the Fuzzy3 segmentation is computation. Furthermore, the Fuzzy3 and manual segmentations were equally accurate, as no statistically significant difference was found in terms of the Dice means (Dice: 0.943 ± 0.018 and 0.945 ± 0.015, $p = 0.741$, respectively). Lastly, Fuzzy3 can be used for batch processing, allowing multiple tumors to be segmented sequentially and simultaneously: an advantageous quality when data from multiple centers are analyzed at a single site. The user (most likely an imaging technician) need not laboriously contour the intricate morphology of each tumor; he or she need only draw a simple coarse blob around the tumor for each patient and process multiple cases in a single batch. The algorithm will fill in the fine morphological details of the tumor for the neuroradiologist to confirm afterward. The proposed semi-automated segmentation method delineates the intricacies of tumor morphology in a manner comparable to manual contouring with high fidelity, but in less time and with less user interaction and, consequently, with less potential for user-introduced bias.

Semi-automated segmentation methods have been developed in an attempt to combine the high-level visual processing and specialized knowledge exhibited by humans with the objectivity of computers; however, most of these methods

remain restricted to their individual development sites, having not gained widespread acceptance (257; 284-288). This is likely due to an absence of segmentation algorithm/software transparency, the technical complexity of the algorithms, and the difficulty with which input data is generated. For example, artificial neural networks are capable of identifying very complex voxel-based dependencies within large 3D MRI data sets, offering clear advantages over less sophisticated methods. However, implementing these processes is not trivial, as the algorithm must be trained - requiring a slow, tedious learning phase - and segmentation trouble-shooting requires a proficiency in data abstraction processes, such as hierarchical self-organized mapping (242; 289). Conversely, ROI-guided semi-automated segmentation methods using algorithms similar to those used here have been shown to quantify enhancing tumor reproducibly in the presence of resection cavity collapse and non-neoplastic enhancing tissues in less time than manual contouring, lending credence to the standardization and utilization of similar methods in neurosurgical trials (290-292).

Precision in image registration is crucial to postoperative tumor segmentation, as evaluating the complex morphology of residual tumor requires the ability to differentiate residual enhancing tumor tissue from T1-hyperintense blood products (methemoglobin), non-neoplastic enhancing structures, such as normal blood vessels, and parenchyma in the presence of an often deformed resection cavity. When the proposed algorithms are applied to ROI-blobs that sample image difference maps (subtraction images), misregistration of the resection cavity and surrounding tissues may result in misclassification of voxels. For example, if voxels containing post-surgical blood products, which are

hyperintense on T1W images, are slightly misregistered, these voxels may subsequently be subtracted from voxels containing enhancing tumor, resulting in incorrect lower residual tumor volumes. As the current work utilized only rigid image registration algorithms for the fusion of pre- and post-contrast images, the use of more sophisticated registration methods, including deformable registration algorithms, such as multi-resolution modified basis spline or multi-modality Demons, may prove to be advantageous. Due to the low error of VelocityAI's deformable registration algorithms, as shown by Kirby et al., a sample of cases with sub-cubic centimeter residual tumor volumes were segmented using Fuzzy3 after both rigid and B-Spline deformable image registration to investigate the impact of registration on algorithm performance (293). Although no significant difference was found, a trend in both MED and mean-percent volume error for rigid and deformable segmentation (1.61 ± 0.73 mm/50.7 ± 35.3% and 0.89 ± 0.64 mm/47.6 ± 37.3%, respectively) suggests that deformable registration may increase the accuracy of postoperative tumor segmentation, and lends credence to its use in future studies.

Although the Fuzzy3 method described herein exhibited high agreement and reproducibility for the systematic determination of contrast-enhancing tumor volumes, it did exhibit some weaknesses common to intensity-histogram thresholding. As the threshold between classes/clusters is determined solely by the intensity of the voxels within the image histogram, other strongly enhancing, non-neoplastic tissues or high-intensity noise may be misclassified as contrast-enhancing tumor. Although this is a significant problem when utilizing global thresholding techniques, it is less of an issue when using local thresholding, since

generating versatile ROI-blobs that exclude obviously non-neoplastic enhancing tissues (dura, blood vessels, etc.) can mitigate segmentation errors. Furthermore, these regions may be accounted for by the classification algorithms or simple post-processing procedures. The ROI-selection and post-processing techniques are more systematic, more reproducible, and more easily standardized than manual contouring and should be considered as important components of tumor segmentation using this methodology. Also, in this study, these algorithms were applied to a population of MR images with variable acquisition parameters and spatial resolutions. Ideally, in future work, only high-resolution 3D images (i.e. MP-RAGE) would be acquired and analyzed, as this decreases misclassification due to partial volume effects. Furthermore, as deformable registration seems to be favorable, acquiring high-resolution images is important, as registration performance is inversely proportional to image spatial resolution (294).

The proposed method, Fuzzy3, overcomes many of the perceived pitfalls of manual and other semi-automated segmentation methods by coupling a flexible shape of blob-generation method with simple, local histogram thresholding/clustering. The proposed algorithm allows for significant control of segmentation parameters - including the selection of pertinent data for analysis (i.e. ROI-blob) and the desired number of clusters to be classified - while maintaining an intuitive workflow. Moreover, Fuzzy3 is easily integrated with volume-rendering software that is currently being used for clinical purposes, such as RT planning, thereby expanding the potential for implementation across multiple sites. As such, Fuzzy3 should be considered for the generation of pre- and postoperative tumor volumes for EOR analysis in multicenter trials for GBM (or

other tumors). Future directions concerning this method consist of addressing the aforementioned drawbacks of intensity-histogram thresholding, further automating and standardizing the method, particularly in regard to ROI-blob generation and post-processing procedures, and further investigating the effect of deformable registration and spatial resolution on segmentation accuracy.

2.7 References

1. Cordova JS, Schreibmann E, Hadjipanayis CG, Guo Y, Shu HK, et al. 2014. Quantitative tumor segmentation for evaluation of extent of glioblastoma resection to facilitate multisite clinical trials. *Transl Oncol* 7:40-7

2. Stupp R, Mason WP, van den Bent MJ, Weller M, Fisher B, et al. 2005. Radiotherapy plus concomitant and adjuvant temozolomide for glioblastoma. *The New England journal of medicine* 352:987-96

3. Stupp R, Hegi ME, Mason WP, van den Bent MJ, Taphoorn MJB, et al. 2009. Effects of radiotherapy with concomitant and adjuvant temozolomide versus radiotherapy alone on survival in glioblastoma in a randomised phase III study: 5-year analysis of the EORTC-NCIC trial. *Lancet Oncology* 10:459-66

4. van den Bent MJ, Vogelbaum MA, Wen PY, Macdonald DR, Chang SM. 2009. End point assessment in gliomas: novel treatments limit usefulness of classical Macdonald's Criteria. *J Clin Oncol* 27:2905-8

5. Macdonald DR, Cascino TL, Schold SC, Jr., Cairncross JG. 1990. Response criteria for phase II studies of supratentorial malignant glioma. *J Clin Oncol* 8:1277-80

6. Wen PY, Macdonald DR, Reardon DA, Cloughesy TF, Sorensen AG, et al. 2010. Updated response assessment criteria for high-grade gliomas: response assessment in neuro-oncology working group. *J Clin Oncol* 28:1963-72

7. White DR, Houston AS, Sampson WF, Wilkins GP. 1999. Intra- and interoperator variations in region-of-interest drawing and their effect on the measurement of glomerular filtration rates. *Clin Nucl Med* 24:177-81

8. Tofts PS, Collins DJ. 2011. Multicentre imaging measurements for oncology and in the brain. *British Journal of Radiology* 84:S213-26

9. Sorensen AG, Patel S, Harmath C, Bridges S, Synnott J, et al. 2001. Comparison of diameter and perimeter methods for tumor volume calculation. *J Clin Oncol* 19:551-7

10. Gordillo N, Montseny E, Sobrevilla P. 2013. State of the art survey on MRI brain tumor segmentation. *Magnetic resonance imaging* 31:1426-38

11. Bauer S, Wiest R, Nolte LP, Reyes M. 2013. A survey of MRI-based medical image analysis for brain tumor studies. *Phys Med Biol* 58:R97-129

12. Gooya A, Pohl KM, Bilello M, Cirillo L, Biros G, et al. 2012. GLISTR: Glioma Image Segmentation and Registration. *IEEE transactions on medical imaging* 31:1941-54

13. Gu YH, Kumar V, Hall LO, Goldgof DB, Li CY, et al. 2013. Automated delineation of lung tumors from CT images using a single click ensemble segmentation approach. *Pattern Recognition* 46:692-702

14. Kumar V, Gu Y, Basu S, Berglund A, Eschrich SA, et al. 2012. Radiomics: the process and the challenges. *Magnetic resonance imaging* 30:1234-48

15. Vermes E, Childs H, Carbone I, Barckow P, Friedrich MG. 2013. Auto-Threshold quantification of late gadolinium enhancement in patients with acute heart disease. *J Magn Reson Imaging* 37:382-90

16. Stoutjesdijk MJ, Zijp M, Boetes C, Karssemeijer N, Barentsz JO, Huisman H. 2012. Computer aided analysis of breast MRI enhancement kinetics using mean shift clustering and multifeature iterative region of interest selection. *J Magn Reson Imaging* 36:1104-12

17. Liu HT, Sheu TW, Chang HH. 2013 Jun 7 [Epub ahead of print]. Automatic segmentation of brain MR images using an adaptive balloon snake model with fuzzy classification. *Med Biol Eng Comput*

18. Bindu CH. 2009. An Improved Medical Image Segmentation Algorithm Using Otsu Method. *International Journal of Recent Trends in Engineering* 2:88-90

19. Otsu N. 1979. Threshold Selection Method from Gray-Level Histograms. *Ieee Transactions on Systems Man and Cybernetics* 9:62-6

20. Ahmed MN, Yamany SM, Mohamed N, Farag AA, Moriarty T. 2002. A modified fuzzy C-means algorithm for bias field estimation and segmentation of MRI data. *IEEE Trans Med Imaging* 21:193-9

21. Pham DL, Prince JL. 1999. Adaptive fuzzy segmentation of magnetic resonance images. *IEEE Trans Med Imaging* 18:737-52

22. Bezdek JC, Hall LO, Clarke LP. 1993. Review of MR image segmentation techniques using pattern recognition. *Med Phys* 20:1033-48

23. Phillips WE, 2nd, Phuphanich S, Velthuizen RP, Silbiger ML. 1995. Automatic magnetic resonance tissue characterization for three-dimensional magnetic resonance imaging of the brain. *J Neuroimaging* 5:171-7

24. Phillips WE, 2nd, Velthuizen RP, Phuphanich S, Hall LO, Clarke LP, Silbiger ML. 1995. Application of fuzzy c-means segmentation technique for tissue differentiation in MR images of a hemorrhagic glioblastoma multiforme. *Magnetic resonance imaging* 13:277-90

25. Khotanlou H, Colliot O, Atif J, Bloch I. 2009. 3D brain tumor segmentation in MRI using fuzzy classification, symmetry analysis and spatially constrained deformable models. In *Fuzzy Sets and Systems*, pp. 1457-73. Crema, Italy

26. Stummer W, Novotny A, Stepp H, Goetz C, Bise K, Reulen HJ. 2000. Fluorescence-guided resection of glioblastoma multiforme by using 5-aminolevulinic acid-induced porphyrins: a prospective study in 52 consecutive patients. *Journal of neurosurgery* 93:1003-13

27. Stummer W, Pichlmeier U, Meinel T, Wiestler OD, Zanella F, Reulen HJ. 2006. Fluorescence-guided surgery with 5-aminolevulinic acid for resection of malignant glioma: a randomised controlled multicentre phase III trial. *Lancet Oncology* 7:392-401

28. Stummer W, Reulen HJ, Meinel T, Pichlmeier U, Schumacher W, et al. 2008. Extent of resection and survival in glioblastoma multiforme: identification of and adjustment for bias. *Neurosurgery* 62:564-76; discussion -76

29. Stummer W, Stepp H, Moller G, Ehrhardt A, Leonhard M, Reulen HJ. 1998. Technical principles for protoporphyrin-IX-fluorescence guided microsurgical resection of malignant glioma tissue. *Acta neurochirurgica* 140:995-1000

30. Stummer W, Stocker S, Novotny A, Heimann A, Sauer O, et al. 1998. In vitro and in vivo porphyrin accumulation by C6 glioma cells after exposure to 5-aminolevulinic acid. *J Photochem Photobiol B* 45:160-9

31. Stummer W, Stocker S, Wagner S, Stepp H, Fritsch C, et al. 1998. Intraoperative detection of malignant gliomas by 5-aminolevulinic acid-induced porphyrin fluorescence. *Neurosurgery* 42:518-25; discussion 25-6

32. Stummer W, Tonn JC, Mehdorn HM, Nestler U, Franz K, et al. 2011. Counterbalancing risks and gains from extended resections in malignant glioma surgery: a supplemental analysis from the randomized 5-aminolevulinic acid glioma resection study. Clinical article. *Journal of neurosurgery* 114:613-23

33. Chang HH, Zhuang AH, Valentino DJ, Chu WC. 2009. Performance measure characterization for evaluating neuroimage segmentation algorithms. *NeuroImage* 47:122-35

34. Zhang YJ. 1996. A survey on evaluation methods for image segmentation. *Pattern Recognition* 29:1335-46

35. Lin LI. 1989. A concordance correlation coefficient to evaluate reproducibility. *Biometrics* 45:255-68

36. Lin L, Hedayat AS, Sinha B, Yang M. 2002. Statistical methods in assessing agreement: Models, issues, and tools. *Journal of the American Statistical Association* 97:257-70

37. Lin L, Hedayat AS, Wu WT. 2012. *Statistical Tools for Measuring Agreement*. 233 SPRING STREET, NEW YORK, NY 10013, UNITED STATES: Springer. 1-157 pp.

38. Dice LR. 1945. Measures of the Amount of Ecologic Association between Species. *Ecology* 26:297-302

39. Deza MM. 2012. General Definitions. In *Encyclopedia of distances*:3-43. New York: Springer. Number of 3-43 pp.

40. Lalkhen AG, McCluskey, A. 2008. Clinical Tests: Sensitivity and Specificity. *Continuing Education in Anaesthesia, Critical Care, and Pain* 8:221-3

41. Harati V, Khayati R, Farzan A. 2011. Fully automated tumor segmentation based on improved fuzzy connectedness algorithm in brain MR images. *Computers in Biology and Medicine* 41:483-92

42. Rexilius J, Hahn HK, Klein J, Lentschig MG, Peitgen HO. 2007. Multispectral brain tumor segmentation based on histogram model adaptation - art. no. 65140V. *Medical Imaging 2007: Computer-Aided Diagnosis, Pts 1 and 2* 6514:V5140-V

43. Ho S, Bullitt E, Gerig G. 2002. Level-set evolution with region competition: Automatic 3-D segmentation of brain tumors. In *16th International Conference on Pattern Recognition, Vol I, Proceedings*, ed. RL Kasturi, D; Suen, C pp. 532-5: IEEE COMPUTER SOC

44. Sachdeva J, Kumar V, Gupta I, Khandelwal N, Ahuja CK. 2012. A novel content-based active contour model for brain tumor segmentation. *Magnetic resonance imaging* 30:694-715

45. Wang T, Cheng I, Basu A. 2009. Fluid vector flow and applications in brain tumor segmentation. *IEEE Trans Biomed Eng* 56:781-9

46. Bauer S, Nolte LP, Reyes M. 2011. Fully Automatic Segmentation of Brain Tumor Images Using Support Vector Machine Classification in Combination with Hierarchical Conditional Random Field Regularization. *Medical Image Computing and Computer-Assisted Intervention, Miccai 2011, Pt Iii* 6893:354-61

47. Zikic D, Glocker B, Konukoglu E, Criminisi A, Demiralp C, et al. 2012. Decision forests for tissue-specific segmentation of high-grade gliomas in multi-channel MR. *Med Image Comput Comput Assist Interv* 15:369-76

48. Ruan S, Lebonvallet S, Merabet A, Constans JM. 2007. Tumor segmentation from a multispectral MRI images by using support vector machine classification. *2007 4th Ieee International Symposium on Biomedical Imaging : Macro to Nano, Vols 1-3*:1236-9

49. Zhu Y, Young GS, Xue Z, Huang RY, You H, et al. 2012. Semi-automatic segmentation software for quantitative clinical brain glioblastoma evaluation. *Academic radiology* 19:977-85

50. Weizman L, Ben Sira L, Joskowicz L, Constantini S, Precel R, et al. 2012. Automatic segmentation, internal classification, and follow-up of optic pathway gliomas in MRI. *Medical Image Analysis* 16:177-88

51. Deoni SC, Rutt BK, Parrent AG, Peters TM. 2007. Segmentation of thalamic nuclei using a modified k-means clustering algorithm and high-resolution quantitative magnetic resonance imaging at 1.5 T. *NeuroImage* 34:117-26

52. Chen A, Deeley MA, Niermann KJ, Moretti L, Dawant BM. 2010. Combining registration and active shape models for the automatic segmentation of the lymph node regions in head and neck CT images. *Medical physics* 37:6338-46

53. Deeley MA, Chen A, Datteri R, Noble JH, Cmelak AJ, et al. 2011. Comparison of manual and automatic segmentation methods for brain structures in the presence of space-occupying lesions: a multi-expert study. *Phys Med Biol* 56:4557-77

54. Pallud J, Taillandier L, Capelle L, Fontaine D, Peyre M, et al. 2012. Quantitative morphological magnetic resonance imaging follow-up of low-grade glioma: a plea for systematic measurement of growth rates. *Neurosurgery* 71:729-39; discussion 39-40

55. Mayr NA, Taoka T, Yuh WT, Denning LM, Zhen WK, et al. 2002. Method and timing of tumor volume measurement for outcome prediction in cervical cancer using magnetic resonance imaging. *International journal of radiation oncology, biology, physics* 52:14-22

56. Grenacher L, Thorn M, Knaebel HP, Vetter M, Hassenpflug P, et al. 2005. The role of 3-D imaging and computer-based postprocessing for surgery of the liver and pancreas. *Rofo* 177:1219-26

57. Wang Y, Lin ZX, Cao JG, Li MQ. 2011. Automatic MRI Brain Tumor Segmentation System Based on Localizing Active Contour Models. In *Advanced Research on Information Science, Automation and Material System, Pts 1-6*, ed. H Zhang, G Shen, D Jin, 219-220:1342-6. LAUBLSRUTISTR 24, CH-8717 STAFA-ZURICH, SWITZERLAND: TRANS TECH PUBLICATIONS LTD. Number of 1342-6 pp.

58. Iftekharuddin KM, Zheng J, Islam MA, Ogg RJ. 2009. Fractal-based brain tumor detection in multimodal MRI. *Applied Mathematics and Computation* 207:23-41

59. Dou WB, Ruan S, Chen YP, Bloyet D, Constans JM. 2007. A framework of fuzzy information fusion for the segmentation of brain tumor tissues on MR images. *Image and Vision Computing* 25:164-71

60. Lee CH, Schmidt M, Murtha A, Bistritz A, Sander M, Greiner R. 2005. Segmenting brain tumors with conditional random fields and support vector machines. In *Computer Vision for Biomedical Image Applications*, ed. Y Liu, T Jiang, CS Zhang, 3765:469-78. Berlin, Germany: Springer. Number of 469-78 pp.

61. Prastawa M, Bullitt E, Ho S, Gerig G. 2004. A brain tumor segmentation framework based on outlier detection. *Med Image Anal* 8:275-83

62. Lashkari AE. 2012. A Neural Network-Based Method for Brain Abnormality Detection in MR Images Using Zernike Moments and Geometric Moments. *International Journal of Computer Applications* 4:1-8

63. Kanaly CW, Ding D, Mehta AI, Waller AF, Crocker I, et al. 2011. A novel method for volumetric MRI response assessment of enhancing brain tumors. *PloS one* 6:e16031

64. Tacher V, Lin M, Chao M, Gjesteby L, Bhagat N, et al. 2013. Semiautomatic volumetric tumor segmentation for hepatocellular carcinoma: comparison between C-arm cone beam computed tomography and MRI. *Academic radiology* 20:446-52

65. Chow DS, Qi J, Guo X, Miloushev VZ, Iwamoto FM, et al. 2013. Semiautomated Volumetric Measurement on Postcontrast MR Imaging for Analysis of Recurrent and Residual Disease in Glioblastoma Multiforme. *AJNR. American journal of neuroradiology*

66. Kirby N, Chuang C, Ueda U, Pouliot J. 2013. The need for application-based adaptation of deformable image registration. *Medical physics* 40:011702

67. Hajnal J, Hawkes, D., Hill, D. 2001. Section I: Methodology. In *Medical Imaging Registration*, ed. J Hajnal, Hawkes, D., Hill, D.:11-117. Boca Raton, FL: CRC Press LLC. Number of 11-117 pp.

Chapter 3

Semi-Automated Volumetric and Morphological Assessment of Glioblastoma Resection with Fluorescence-Guided Surgery

3.1 Author's Contribution and Acknowledgement of Reproduction

The work presented here was conceptualized, organized, researched, and written by the dissertation author. Of the data presented all was collected by the author under the guidance of Dr. Shim, Dr. Holder, and many collaborators. The chapter is reproduced with minor edits from Cordova, J.S., Gurbani, S.S., Holder, C.A., Olson, J.J., Schreibmann, E., Shi, R., Guo, Y., Shu, H.G., Shim, H., Hadjipanayis, C.G. Semi-Automated Volumetric and Morphological Assessment of Glioblastoma Resection with Fluorescence-Guided Surgery. Mol Imaging Biol. (2015) Oct 13. [Epub ahead of print] PMID: 26463215 (295).

3.2 Abstract

GBM neurosurgical resection relies on contrast-enhanced MRI-based neuronavigation. However, it is well-known that infiltrating tumor extends beyond contrast enhancement. FGS using 5-ALA was evaluated to improve EOR of GBMs. Pre-operative morphological tumor metrics were also assessed. Thirty patients from a Phase II trial evaluating 5-ALA FGS in newly diagnosed GBM were assessed. Tumors were segmented pre-operatively to assess morphological features as well as post-operatively to evaluate EOR and residual tumor volume (RTV). Median EOR and RTV were 94.3% and 0.821 cm^3, respectively. Pre-operative surface area to volume ratio and RTV were significantly associated with OS, even when controlling for the known survival confounders. This study supports claims that 5-ALA FGS is helpful at decreasing tumor burden and prolonging survival in GBM. Moreover, morphological indices are shown to impact both resection and patient survival.

3.3 Introduction

The goal of surgery in patients with GBM is maximum safe resection to relieve tumor mass effect, confirm diagnosis, and enhance the efficacy of adjuvant therapy. In recent years, however, the value of “more complete” resection (i.e. removal of the entire contrast-enhancing tumor) in extending PFS and OS has been recognized (41-46; 48; 49). Consequently, much work has been done to enhance tumor resection, including the development of intraoperative technologies like FGS (41-43; 46; 116; 296). One of the most well-studied fluorescent markers used for FGS in malignant gliomas is 5-ALA (297). 5-ALA is an oral prodrug that is converted to the fluorescent compound PpIX during heme

biosynthesis in glioma cells, permitting real-time intraoperative visualization of malignant tissue with fluorescence microscopy (155; 157; 171; 258; 298-300). Though the exact mechanisms of 5-ALA penetration of glioma are still uncertain, it appears that bulk flow of 5-ALA across the leaky GBM vasculature and active transport at the blood-brain and blood-CSF interfaces contribute to 5-ALA-induced fluorescence in both *in vitro* and *in vivo* tumor models (159; 299; 301-303). In a randomized Phase III study, Stummer et al. demonstrated that more extensive GBM resection and higher PFS rates were achievable with 5-ALA FGS compared to conventional resection, leading to multiple follow-up studies on the technique (42; 43; 50; 52; 148; 172-176; 304; 305).

One critical, yet often overlooked, component of determining neurosurgical efficacy is the metric(s) by which resection is evaluated (109). Since convention is to target the enhancing component of contrast-enhanced T1-weighted images (CE-T1w) for resection, most studies utilize EOR, a comparison of pre- and post-operative CE-T1w tumor volumes (41-46; 48; 50; 161). However, recent work suggests that residual contrast-enhancing tumor volume (RTV) more accurately reflects disease burden and patient survival (304). Furthermore, the measurement of GBM tumor volume at a single time point is known to be inaccurate and irreproducible (67; 136). Taking the quotient of two separate measurements compounds this error, potentially resulting in erroneous relationships between EOR and survival (306).

The method by which tumor volumes are measured is also a potential source of error in resection analyses. Linear measurements are often used to evaluate response to chemoradiation therapy, but they are poorly suited for

evaluating the curvilinear tumor remnants around a resection cavity (67; 144). Modeling RTV with ellipsoids is also known to be largely inaccurate and highly susceptible to intra- and inter-reader variability (67; 128). Some automated digital-image segmentation techniques have shown promise in measuring pre-operative tumor volumes, but few are designed to evaluate RTV where T1-hyperintense blood products (methemoglobin) and cavity collapse obscure measurements (242; 243). Such structural nuances can be accounted for using manual image contouring; however, this process is time-consuming and suffers from limited reproducibility (128; 240; 241; 307). These limitations often lead to a resection being labeled as a GTR (with an RTV of predetermined volume) despite the presence of residual contrast-enhancement, potentially skewing endpoints. Due to the inadequacies of conventional methods, careful consideration of image segmentation techniques – particularly those specially designed for the measurement of pre- and post-operative contrast-enhancing tumor volumes – is essential for the generation of accurate relationships between resection and survival outcomes.

A Phase II study of 5-ALA FGS was initiated in 2011 at Emory University to evaluate its efficacy in the resection of newly diagnosed and recurrent malignant gliomas. To overcome the tumor measurement limitations of previous studies, a rigorously validated, semi-automated segmentation method designed specifically for resection-related outcomes was utilized to measure tumor pre- and post-operative tumor volumes (239). We report the primary endpoints, EOR and RTV, for a prospective cohort of newly diagnosed GBM patients that have undergone 5-ALA FGS, and interim findings for secondary endpoints including adverse event

(AE) rates, PFS, and OS. To the best of our knowledge, this is the largest prospective 5-ALA study in North America utilizing a semi-automated volumetric method designed specifically for tumor resection analysis, and the first to show pre-operative morphological metrics are not only associated with resection outcomes, but also survival outcomes for GBM patients receiving FGS.

3.4 Materials and Methods

3.4.1 Patient Selection

All patients included in this analysis were part of a prospective Phase II 5-ALA FGS study at Emory University Hospital Midtown and Emory University Hospital (2011-2014). Patients who had newly diagnosed or recurrent malignant gliomas suspected by MRI were eligible for FGS. The trial included all patients 18 years of age or older with normal bone marrow, renal, and liver function, KPS ≥ 60%, and able to understand and sign an informed consent document before surgery. Patients with midline, basal ganglia, or brainstem tumors, and those receiving any experimental therapies prior to surgery, or with a family history of porphyria, were excluded. The inability to achieve a GTR was not an exclusion criterion. Demographic, genomic, and clinical values were recorded for each patient as potential covariates for endpoint analyses and included age (continuous and above/below 55 years), KPS before and 6 weeks after surgery, tumor location eloquence, MGMT gene promoter methylation status (methylated versus unmethylated), EGFR amplification status, and PTEN deletion status.

3.4.2 Fluorescence-Guided Surgery

5-ALA (Gliolan®; provided by photonamic GmbH & Co. KG, Wedel, Germany and manufactured by medac Gmbh, Wedel, Germany) was administered to patients orally at 20 mg/kg of bodyweight 3-5 h before induction of general anesthesia. Image-guided microsurgical resection was then carried out using a standard surgical operating microscope adapted for fluorescence excitation and emission at wavelength ranges of 400–410 nm and 480–750 nm, respectively. Fluorescence-guided microsurgical removal of tissue was performed intermittently during the tumor resection, mainly along the contrast-enhancing tumor margins on neuronavigation. Tissue sampled at regions of residual tissue fluorescence was sent for histological confirmation by neuropathology.

3.4.3 Image Acquisition and Analysis

Pre-operative, high-resolution 3D MR images, including 1 mm^3 T1w MPRAGE images (TR/TE = 1900/3.52, 256 x 256 matrix, FA = 9°) before and after i.v. administration of gadolinium-based contrast agent (GBCA), were generated ≤ 7 days prior to surgery for neuronavigation and tumor segmentation. The same high-resolution T1w 3D MP-RAGE images were acquired post-operatively, within 48 h (usually within 24 h) of surgery, to evaluate EOR and RTV.

The 510(k) FDA-cleared image analysis platform VelocityAI (Varian Medical Systems, Palo Alto, CA) was used to semi-automatically segment contrast-enhancing tumors with a highly-sensitive fuzzy c-means clustering algorithm (Fuzzy) on pre- and post-operative CE-T1w images as previously described (239). Spatially co-registered segmentation masks for contrast-enhancing tumor and

necrotic tissue were generated for volume and surface area (SA) measurements (Figure 3.1). An experienced neuroradiologist confirmed all final segmentations. This method of verification is commonplace for the generation of tumor segmentations for radiotherapy planning and segmentation algorithm validation (243; 260).

Based on the European Phase III 5-ALA FGS trial criterion, a "complete" resection of the contrast-enhancing tumor (CRET) was defined as ≤ 0.175 cm^3 of residual contrast-enhancement after surgery using volumetric assessment (50). The traditional definition of GTR (residual contrast-enhancing tumor volume ≤ 1 cm^3) was also considered. Tumor EOR calculations were determined by comparison of tumor volumes from pre- and post-operative volumetric MRI studies. Morphological indices based on segmentation results were generated as measures of tumor structure and included surface area (SA), percent of necrosis in tumor volume (NV%), and tumor surface area-to-volume ratio (SAVR). Patients were monitored by CE-T1w and T2w/FLAIR at 3, 6, and 9 months post-surgery, or until tumor progression was confirmed per RANO criteria (67).

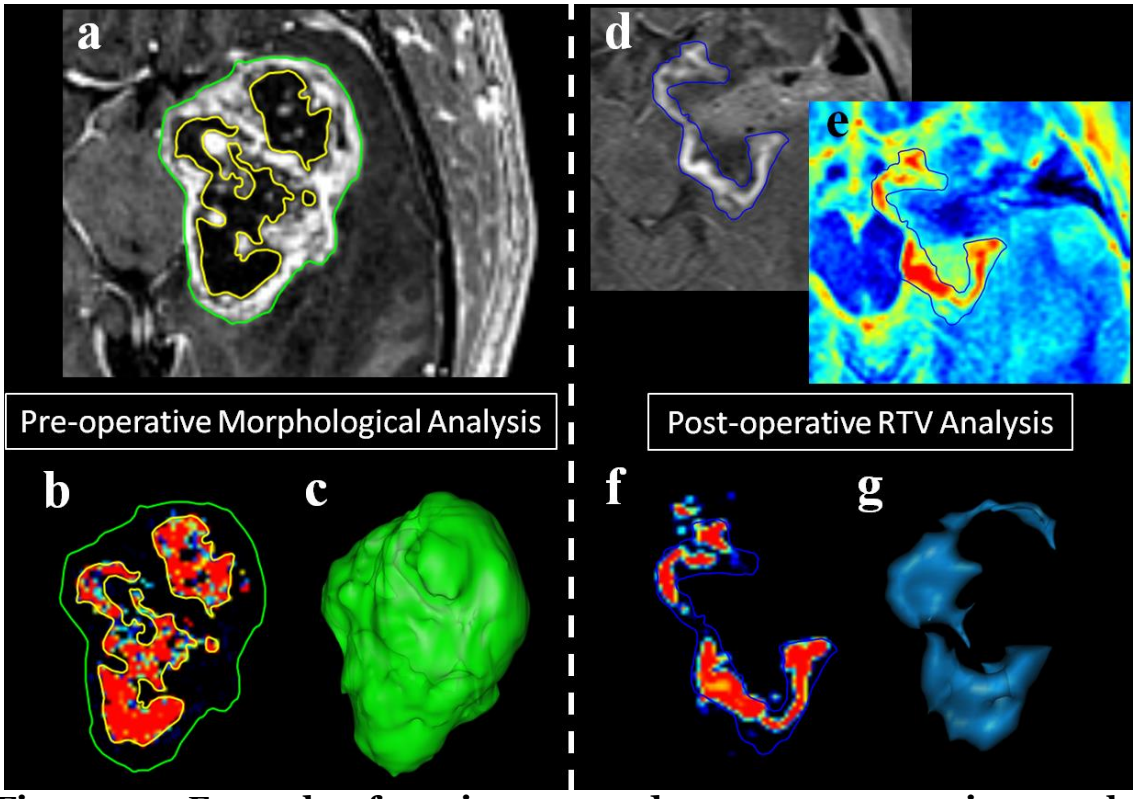

Figure 3.1. Example of semi-automated tumor segmentation results used for volumetric and morphological analysis. Preoperative CE-T1W images of GBM patients are segmented using a semi-automated method to generate volumes for contrast-enhancing (green contour) and necrotic (yellow contour) components (**a**). Voxels are classified into one of three tissue types (normal, contrast-enhancing, and necrotic) and image masks are generated for volumetric comparison (necrotic class pictured with contours, **b**). 3-Dimensional tumor surface reconstructions show the structural complexity of each tumor and can be used for surface area measurement **(c)**. Pre-contrast images are subtracted from post-contrast enhancing images (**d**) to account for non-neoplastic enhancing blood products in the resection cavity (methemoglobin in blood) and to generate T1 difference maps (**e**)**.** This subtraction image is then segmented using the same semi-automated method to generate contrast-enhancing tumor masks (**f**) and calculate residual contrast-enhancing tumor volumes (RTVs) (blue contour, **d-f**). Post-operative tumor morphology can also be visualized using this method (**g**).

3.4.4 Statistical Methods

Statistical analyses were performed with the Statistical Analysis System (version 9; SAS Institute, Cary, NC), were all 2-sided, and with statistical significance set at $p < 0.05$. Univariate analyses were first used to evaluate the association of individual covariates with EOR and RTV. The impact on primary endpoint of dichotomous covariates was evaluated by conducting paired t-tests on group means and that of continuous covariates was evaluated by testing Pearson's correlation coefficients (ρ) versus no correlation (H_0: $\rho = 0$). Multivariate analysis was then performed using a general linear model to assess the effects of multiple covariates on RTV. As RTV is the summation of contrast-enhancing voxels after surgery, it can be modeled as a Poisson process. Thus, a Poisson distribution was used for regression. A general, step-wise model selection procedure was used to select covariates to be included in the final model with the controlling variables age, pre-operative tumor volume, and MGMT gene promoter methylation status (308).

PFS and OS were evaluated using a right-censored univariate Cox regression model, and corresponding hazard rate ratios (HR) are reported with 95% confidence intervals. Covariates in Cox regression survival analysis were the same as those of the primary endpoint analysis, with the addition of EOR, RTV, pre-operative KPS, and 6 week KPS. The univariate and multivariate analysis procedures used for the survival outcomes were the same as those used for the primary endpoint analysis with controlling variables age, pre-operative KPS, and MGMT gene promoter methylation status. Pre-operative and 6-week KPS values

were compared using the Wilcoxon signed-rank test to evaluate post-surgical functional outcomes.

3.5 Results

3.5.1 Study Accrual

Between October 2011 and December 2014, 56 patients were enrolled in the Phase II 5-ALA FGS trial. Four patients were excluded as histology failed to confirm HGG (metastasis, n = 2; LGG, n = 2), and two patients consented for the study, but dropped out before surgery. A total of 31 newly-diagnosed GBM, 7 recurrent GBM, 4 newly-diagnosed WHO grade III (anaplastic) glioma, and 8 recurrent WHO grade III glioma patients were enrolled and completed 5-ALA FGS. Newly-diagnosed GBM patients were the only group analyzed in the currently reported study, as they were the largest, most homogenous group in the cohort. One patient was excluded from endpoint analysis due to an exceptionally large RTV (25.1 cm^3) that was found to be an extreme outlier (> 3 interquartile ranges (IQRs) above the third quartile). Pertinent baseline clinical characteristics of analyzed data from 30 patients are shown in **Table 3.1**.

3.5.2 Primary endpoints: EOR and RTV

Median EOR and RTV were found to be 94.8% (IQR: 11.1%; range: 70% - 100%) and 0.76 cm^3 (IQR: 5.8 cm^3; range: 0 - 15.3 cm^3), respectively. CRET resection was achieved in 9 patients (30%), and GTR (≤ 1cm^3) was achieved in 16 patients (53.3%). Age (> 55 or ≤55 yrs.) was the single strongest covariate for predicting EOR and RTV with p = 0.003 and 0.004, respectively **(Table 3.2)**. No other covariate was found to be significantly associated with EOR, although NV% exhibited a moderate positive trend. Pre-operative SAVR showed statistically

significant negative correlation with RTV ($\rho = -0.43$, $p = 0.02$), while pre-operative SA and volume exhibited a positive correlation with RTV ($\rho = 0.37$, $p = 0.04$ and $\rho = 0.50$, $p = 0.01$).

			% of patients (n = 30)
Gender	**Male**	20.0	66.7%
	Female	10.0	33.3%
Age	**Range**	24-79	
	Median	60.0	
	SD	12.2	
	> 55	10.0	33.3%
	≤ 55	20.0	66.7%
Preoperative KPS	**Range**	60-90	
	Mean	78.0	
	SD	9.5	
	< 80	11.0	36.7%
	80-100	19.0	63.3%
Preoperative Tumor Volume (cm^3)	**Range**	1.6-132	
	Mean	43.9	
	SD	27.3	
Tumor Location	**Eloquent**	26.0	86.7%
	Non-Eloquent	4.0	13.3%
Histology	**Primary**	28.0	93.3%
	Secondary	2.0	6.7%
Therapy after FGS	**RT + TMZ**	24.0	80.0%
	Other Therapy	4.0	13.3%
	No TX	2.0	6.7%

Table 3.1. Patient and tumor characteristics for 5-ALA FGS trial. **Other therapy* includes TMZ only, RT only, experimental treatment, or any combination of these excluding RT + TMZ.

			EOR (%)		RTV (cm^3)	
Dichotomous		**N**	**Group Mean (SEM)**	***p*-value**	**Group Mean (SEM)**	***p*-value**
Age	**> 55**	20	89.66 (2.23)	<0.01*	4.78 (1.09)	<0.01*
	≤ 55	10	97.66 (0.68)		0.88 (0.39)	
Site	**Eloquent**	27	91.95 (1.80)	0.44	3.66 (0.89)	0.40
	Non-eloquent	3	95.70 (1.27)		1.87 (0.54)	
MGMT Promoter	**Methylated**	20	91.61 (2.13)	0.53	4.30 (1.14)	0.08
	Unmethylated	10	93.78 (1.89)		1.85 (0.50)	
EGFR	**Amplification**	14	90.51 (2.77)	0.32	5.18 (1.45)	0.06
	No Amplification	16	93.92 (2.09)		1.99 (0.78)	
PTEN	**Deletion**	25	92.09 (1.90)	0.72	3.58 (0.93)	0.77
	Intact	5	93.54 (1.51)		2.97 (0.80)	
Continuous		**N**	**ρ (SEM)**	***p*-value**	**ρ (SEM)**	***p*-value**
Age (yrs.)		30	-0.34 (0.18)	0.07	0.26 (0.18)	0.17
SA (mm^2)		30	-0.08 (0.19)	0.67	0.37 (0.18)	0.04*
Preoperative Tumor Volume (cm^3)		30	-0.13 (0.19)	0.49	0.50 (0.16)	<0.01*
NV% (%)		30	0.33 (0.18)	0.07	-0.12 (0.19)	0.52
SAVR (mm^2/cm^3)		30	0.26 (0.18)	0.17	-0.43 (0.17)	0.02*

Table 3.2. Univariate analyses of EOR and RTV outcomes. **Significant at $p \leq 0.05$.*

The final set of variables included in the multivariable RTV model with their coefficients and p-values can be found in **Table 3.3**. The controlling variables, although either significant or nearly significant in the univariate analysis, all failed to reach significance when considered with more morphological descriptors. Pre-operative SA and SAVR both retained their significance, with very small weights, in the multivariable model. Notably, although non-significant when analyzed alone, NV% reached significance in this model, exhibiting a very strong, negative correlation with RTV (coefficient = -5.55, p = 1E-5). Taken as a whole, morphological indices describing tumor shape, complexity, and composition appear to have a substantial impact in determining the residual tumor burden after 5-ALA FGS.

	Coefficient (SEM)	*p*-value
Age (yrs.)**	0.01 (0.01)	0.56
SA (mm^2)	0.01 (0.01)	<0.01*
Preoperative Tumor Volume (cm^3)**	-0.03 (0.02)	0.09
NV% (%)	-5.55 (1.03)	<0.01*
SAVR (mm^2/cm^3)	-0.04 (0.01)	<0.01*
MGMT Gene Promoter Methylation**	0.48 (0.38)	0.21

Table 3.3. Final multivariate, general linear model describing RTV.

**Significant at $p \leq 0.05$. **Controlling Variables.*

3.5.3 Secondary Endpoint: PFS and OS

Two patients who underwent 5-ALA FGS opted not to have chemoradiation, and were not included in the secondary endpoint analysis (n = 28). The proportions of patient's progression-free at 6, 9, and 12 months were 45%, 29%, and 23%, respectively. In the Cox proportional hazard regression of PFS for these patients, MGMT gene promoter methylation decreased the risk of true tumor progression by 75.9% (HR: 0.24, 95% CI: 0.09–0.68, p = 0.01), while no significant effect was found for the previously associated covariates of age and KPS **(Table 3.4)**. Furthermore, no significant impact of EOR, RTV, or morphological indices was found on PFS. These findings were recapitulated in the multivariate analysis, with MGMT gene promoter methylation status being the only variable significantly associated with PFS (**Table 3.5**).

		PFS		OS	
Dichotomous		**HR (95% CI)**	***p*-value**	**HR (95% CI)**	***p*-value**
Age	**> 55 vs ≤ 55**	0.97 (0.38, 2.45)	0.94	1.45 (0.54, 3.89)	0.11
Site	**Eloquent vs Non-eloquent**	0.53 (0.15, 1.87)	0.32	0.95 (0.21, 4.25)	0.94
MGMT Promoter	**Methylated vs Unmethylated**	0.24 (0.09, 0.68)	0.01*	0.45 (0.16, 1.31)	0.14
EGFR	**Amplification vs No Amplification**	0.78 (0.30, 2.03)	0.61	0.70 (0.26, 1.91)	0.48
PTEN	**Deletion vs Intact**	0.85 (0.19, 3.86)	0.84	0.42 (0.12, 1.54)	0.19
Continuous		**HR (95% CI)**	***p*-value**	**HR (95% CI)**	***p*-value**
Age (yrs.)		1.01 (0.97, 1.05)	0.63	1.03 (0.98, 1.07)	0.24
KPS before surgery		0.99 (0.93, 1.04)	0.61	0.93 (0.87, 0.99)	0.04*
KPS after surgery		0.99 (0.95, 1.04)	0.87	0.95 (0.92, 0.99)	0.01*
SA (mm^2)		1.00 (1.00, 1.00)	0.23	1.00 (1.00,1.00)	0.86
Preoperative Tumor Volume (cm^3)		0.99 (0.97, 1.01)	0.12	1.00 (0.98, 1.02)	0.83
NV% (%)		0.10 (0.01, 2.98)	0.18	0.04 (0.01, 1.48)	0.08
SAVR (mm^2/cm^3)		1.00 (1.00, 1.01)	0.39	1.002 (1.00, 1.01)	0.56
EOR (%)		0.99 (0.93, 1.05)	0.65	0.94 (0.89, 0.99)	0.03*
RTV (cm^3)		0.99 (0.91, 1.08)	0.82	1.09 (1.00, 1.18)	0.06

Table 3.4. Univariate Cox proportional hazard regression analysis for PFS and OS. **Significant at $p \leq 0.05$.*

	PFS		OS	
	Coefficient (95% CI)	***p*-value**	**Coefficient (95% CI)**	***p*-value**
Age (yrs.)**	1.01 (0.97, 1.06)	0.52	1.05 (0.98, 1.12)	0.14
RTV (cm^3)	-	-	1.17 (1.03, 1.34)	0.02*
SAVR (mm^2/cm^3)	-	-	1.01 (1.01, 1.02)	0.03*
NV% (%)	0.04 (0.01, 1.93)	0.11	0.06 (0.01, 3.33)	0.17
KPS before surgery**	1.00 (0.94, 1.06)	0.99	0.95 (0.87, 1.04)	0.29
MGMT promoter methylation vs no methylation**	0.19 (0.06, 0.57)	<0.01*	0.14 (0.03, 0.63)	<0.01*

Table 3.5. Final multivariate Cox proportional hazard regression models of PFS and OS. **Significant at $p \leq 0.05$. **Controlling Variables.*

The proportion of patients alive at 6, 9, and 12 months was 81%, 52%, and 39%, respectively. Cox proportional hazard modeling showed higher KPS before and 6 weeks after surgery, as well as EOR, all moderately decreased the risk of death in the follow-up period, with RTV trending toward significance (**Table 3.4**). When considered in a multivariable model alongside age and morphological measures, pre-operative and 6-week post-operative KPS lost their significant association with OS (**Table 3.5**). Instead, MGMT gene promoter methylation, SAVR, and RTV reached significance. Notably, NV% showed strong association with OS in the univariate and multivariate analyses, but fell short of statistical significance in both (HR: 0.04, 95% CI: 0.01-1.48, p= 0.08 and HR: 0.06, 95% CI: 0.01-3.33, p= 0.17, respectively).

3.5.4 Adverse events (AEs)

One severe adverse event potentially attributable to 5-ALA was observed in all 30 patients. A patient with a history of gastrointestinal perforation exhibited a second perforation within 24 h of 5-ALA administration. Surgical correction of the perforation resulted in a return to baseline shortly thereafter.

Substance-specific side effects associated with 5-ALA (cardiac, gastrointestinal, and dermatological) were infrequent (**Table 3.6**). Dermatological abnormalities were mild and rare (10% of patients) and did not include photodermatosis. Cardiac AEs were slightly more common, yet equally mild, with 5 patients exhibiting arrhythmias (sinus bradycardia, n = 4; sinus tachycardia, n = 1) and 2 patients exhibiting exacerbation of hypertension. Nausea, constipation, and gastroesophageal reflux were the most common gastrointestinal AEs, but were well-managed with standard pharmacotherapy.

Type of AE Recorded	Number AEs recorded	Percentage of total AEs (%)
Hematological	39	9.8
Cardiac Arrhythmia	5	1.3
Cardiac General	6	1.5
Coagulation	0	0.0
Dermatology/Skin	4	1.0
Gastrointestinal	24	6.1
Metabolic/Laboratory	165	41.7
Neurology	58	14.6
Ocular/Visual	3	0.8
Pain	17	4.3
Surgery/Operative Injury	4	1.0
Unknown Syndrome	1	0.3
Vascular	0	0

Table 3.6. Adverse events recorded during trial.

Hematological and blood chemistry abnormalities were generally mild, and resolved without treatment or with supportive therapy. Anemia was the most common abnormality, affecting 50% of patients, followed by thrombocytopenia and leukocytosis, affecting 23% and 3% of patients, respectively. Mild supportive therapy restored baseline values for most of these patients within 6 weeks. Aminotransferases (AST and ALT) and alkaline phosphatase (Alk Phos) were elevated in nearly one-third of patients after surgery, but this number dropped substantially when evaluated at 6 weeks (**Table 3.7**). Hypoalbuminemia was the most common hepatobiliary disturbance observed, but returned to baseline in most patients. Few patients with AST and bilirubin perturbations were observed, most of which normalized to baseline by week 6. Of note, the majority of patients received adjuvant chemoradiation (starting at 4-5 weeks post-surgery) and steroids (immediately after surgery as needed). These therapies are known to cause blood dyscrasias and likely contribute to these abnormalities.

Neurological AEs made up 14.6% of those identified, varying in severity from digital numbness to hemiplegia, and affected 60% of patients at some point in time. Most deficits normalized within the post-operative stay, with a single patient exhibiting ongoing deficits (i.e. dysphasia, visual field cut, and gait disturbance). Median pre-operative and 6-week post-operative KPS were found to be significantly different at $p = 0.03$ (80% and 70%, respectively), implying poor outcomes. However, when stratified ($\geq$ 80% and $<$ 80% groups), no difference in medians was observed ($p = 0.08$). This is due to the low pre-operative KPS and significant drop at 6 weeks seen in 3 patients with tumors in eloquent brain regions.

	≤48 H after surgery		6 weeks after surgery	
	Number of patients	**Range**	**Number of patients**	**Range**
AST	5	13 – 103 Units/L	3	15 – 37 Units/L
ALT	9	13 - 165 Units/L	6	16 – 74 Units/L
GGT	9	6 - 316 Units/L	4	22 – 182 Units/L
Albumin	22	2.5 – 4.1 g/dL	7	2.3 – 4.3 g/dL
Bilirubin	2	0.3 – 2.8 mg/dL	0	0.3 – 1.8 mg/dL
Alkaline Phosphatase	7	20 - 116 Units/L	0	44 – 118 Units/L

Table 3.7. Patients with hepatobiliary laboratory disturbances at 48 h and 6 weeks post-surgery

3.6 Discussion

The randomized, phase III European study provided evidence for the efficacy of 5-ALA FGS with more resections of GBM and better PFS in comparison to conventional resection (50). However, FDA approval of 5-ALA for FGS of malignant gliomas requires separate trials carried out in the United States. Our trial is the first in North America to utilize 5-ALA FGS for malignant gliomas. Our study supports previous results and provides additional spatial metrics to describe the relationship between tumor morphology and resection. Furthermore, we have found that more complete resection of newly diagnosed GBM is associated with better OS, and that pre-operative tumor structure may impact survival by modulating the likelihood of complete resection.

While minimal interaction was found between pre-operative tumor volume measurements and EOR, the association of pre-operative tumor morphological metrics with RTV was notable. Structural indices could outperform current methods for predicting the complete resection of contrast-enhancing tumor. As pre-operative tumor volume is the most salient feature in imaging, it is generally used to determine tumor resectability (309). However, this single metric can be misleading, particularly in the case of large, high NV% and SAVR tumors, which were shown here to be associated with more complete resections. A more suitable method for determining resectability would require the incorporation of morphological factors describing tumor shape and complexity. A more accurate representation of tumor resectability is possible with the type of segmentation tool used here, and represents a paradigm shift in the pre-operative methods used for evaluating resection feasibility.

Our study also supports previous finding that more complete tumor resections ultimately result in greater OS (41-43; 46-48; 296). In our sample, we found an increase in risk of death by 17.5% per cm^3 of residual tumor. Moreover, morphological analysis allowed the identification of moderate association between SAVR and OS (1.1% increase in risk of death for every mm^2 increased at constant volume). Thus SAVR could potentially be interpreted as a quantitative marker of infiltrative capacity, with a large SAVR representing complexity at the tumor margin and an increased interaction of tumor with surrounding tissue. Further, the survival-SAVR association in this study could result from some unknown interaction between biological growth characteristics and morphological features (i.e. high SAVR tumors may be intrinsically more aggressive than low SAVR tumors). This association becomes even more relevant when considered in concert with the strongest potential confounders of this comparison: MGMT gene promoter methylation status and RTV (310). Also of note is the seemingly protective effect exhibited NV% on OS, a finding largely attributed to gene expression patterns previously (311). The current work suggests that the protective effect of NV% may also be associated with the increased likelihood of complete resection via NV%'s modulation of RTV. Further studies investigating the differences in morphology and growth patterns among biologically-distinct GBM subtypes could potentially shed light on these biology-resection-survival interactions and should be considered in larger, multi-site FGS trials investigating survival outcomes.

Though our study supports much of what others have set forth concerning the utility and safety of 5-ALA FGS, there are some points of disagreement. The

current study exhibited CRET in only 30% of cases, a rate lower than that reported by other studies (50; 161). Although it is possible these differences are due to surgeon experience and hardware, these differences are likely due to the combination of three unique factors in this study: the high proportion of patients with eloquent tumors, the high post-operative MR image resolution, and the high-sensitivity tumor measurement method. Our study included over 25% more eloquent cases than the European multicenter study (86.7% vs 61.0%, respectively), increasing the likelihood of subtotal resections from the outset. Further, the post-operative MRI voxel volume used in that study (0.175 cm^3) was orders of magnitude larger than that in our study (0.001 cm^3). With such coarse spatial resolution and the lack of a sensitive segmentation tool, small RTVs approaching the size of a voxel (0.175 – 1 cm^3) could be falsely labeled as "no tumor". Seven patients in our study fall within this RTV range (23%), all of which could have been misclassified as CRET based on lower resolution images. Second, modeling contrast-enhancing tumors with spheroids based on tumor diameters is known to be grossly inaccurate and highly susceptible to intra- and inter-reader variability (67; 128). The segmentation method used for measurement in this study was validated previously and showed high intra- and inter-reader reproducibility, as well as strong volume and spatial agreement with expert-segmented tumors (239). Moreover, the combination of high-resolution MRI with voxel-level tissue classification allows the measurement of morphological parameters, like SA, that are highly sensitive to fine changes in tumor structure. This combination bolsters the novelty of the tumor structure/complexity claims in this work, as few studies

have described such metrics utilizing measurement methods specifically designed for resection analysis (312; 313).

5.6.1 Limitations and Strengths

The absence of a control group, the small sample size, and inhomogeneity in salvage therapies after chemoradiation are clear limitations of this study. Our study does, however, represent one of the largest single-center, prospective studies analyzing resection and survival outcomes of 5-ALA FGS for newly diagnosed GBM in North America using a validated, semi-automated tumor segmentation method. Most studies to date, have used linear diameter or manual segmentation for this end, both of which are heavily user-biased and subject to inaccuracies (50; 67; 128; 144; 240). Lastly, using precision segmentation, this study demonstrates the impact that morphological tumor features (SA, SAVR, and NV%) have on resection and survival outcomes. In a higher-powered study, these indices could be used to evaluate the biology-morphology relationships in distinct GBM subtypes to evaluate the specific impact of tumor structure and resection on survival outcomes in each type.

3.6.2 Conclusions

This clinical study supports the previous randomized, European trial where 5-ALA FGS is helpful at decreasing RTV and providing more complete tumor resections in GBM. We have also found that 5-ALA FGS does increase OS in patients with GBM. Multi-center FGS studies may provide further evidence to support 5-ALA FGS efficacy and safety in a larger, more diverse cohort, and more precisely define the relationship between pre-/post-operative imaging features

and resection/survival outcomes in the US to support FDA approval of Gliolan®. Features investigated in these studies should include morphological indices describing tumor complexity and composition, like SA, SAVR, and NV%, as they have been shown here to impact not only tumor resection, but also patient survival.

3.7 References

1. Cordova JS, Gurbani SS, Holder CA, Olson JJ, Schreibmann E, et al. 2015. Semi-Automated Volumetric and Morphological Assessment of Glioblastoma Resection with Fluorescence-Guided Surgery. *Molecular imaging and biology : MIB : the official publication of the Academy of Molecular Imaging*

2. Bloch O, Han SJ, Cha S, Sun MZ, Aghi MK, et al. 2012. Impact of extent of resection for recurrent glioblastoma on overall survival: clinical article. *Journal of neurosurgery* 117:1032-8

3. Stummer W, Meinel T, Ewelt C, Martus P, Jakobs O, et al. 2012. Prospective cohort study of radiotherapy with concomitant and adjuvant temozolomide chemotherapy for glioblastoma patients with no or minimal residual enhancing tumor load after surgery. *J Neurooncol* 108:89-97

4. Hardesty DA, Sanai N. 2012. The value of glioma extent of resection in the modern neurosurgical era. *Frontiers in neurology* 3:140-50

5. Chaichana KL, Cabrera-Aldana EE, Jusue-Torres I, Wijesekera O, Olivi A, et al. 2014. When gross total resection of a glioblastoma is possible, how much resection should be achieved? *World Neurosurg* 82:e257-65

6. Chaichana KL, Jusue-Torres I, Navarro-Ramirez R, Raza SM, Pascual-Gallego M, et al. 2014. Establishing percent resection and residual volume thresholds affecting survival and recurrence for patients with newly diagnosed intracranial glioblastoma. *Neuro-oncology* 16:113-22

7. Lacroix M, Abi-Said D, Fourney DR, Gokaslan ZL, Shi W, et al. 2001. A multivariate analysis of 416 patients with glioblastoma multiforme: prognosis, extent of resection, and survival. *Journal of neurosurgery* 95:190-8

8. Sanai N, Berger MS. 2008. Glioma extent of resection and its impact on patient outcome. *Neurosurgery* 62:753-64

9. Sanai N, Polley MY, McDermott MW, Parsa AT, Berger MS. 2011. An extent of resection threshold for newly diagnosed glioblastomas. *Journal of neurosurgery* 115:3-8

10. Vogelbaum MA, Jost S, Aghi MK, Heimberger AB, Sampson JH, et al. 2012. Application of novel response/progression measures for surgically delivered therapies for gliomas: Response Assessment in Neuro-Oncology (RANO) Working Group. *Neurosurgery* 70:234-43

11. Kubben PL, Scholtes F, Schijns OE, Ter Laak-Poort MP, Teernstra OP, et al. 2014. Intraoperative magnetic resonance imaging versus standard neuronavigation for the neurosurgical treatment of glioblastoma: A randomized controlled trial. *Surg Neurol Int* 5:70-9

12. Hadjipanayis CG, Widhalm G, Stummer W. 2015. What is the Surgical Benefit of Utilizing 5-Aminolevulinic Acid for Fluorescence-Guided Surgery of Malignant Gliomas? *Neurosurgery [Epub Ahead of Print] DOI: 10.1227/NEU.0000000000000929*

13. Hinnen P, de Rooij FW, van Velthuysen ML, Edixhoven A, van Hillegersberg R, et al. 1998. Biochemical basis of 5-aminolaevulinic acid-induced protoporphyrin IX accumulation: a study in patients with (pre)malignant lesions of the oesophagus. *Br J Cancer* 78:679-82

14. Stummer W, Stocker S, Novotny A, Heimann A, Sauer O, et al. 1998. In vitro and in vivo porphyrin accumulation by C6 glioma cells after exposure to 5-aminolevulinic acid. *J Photochem Photobiol B* 45:160-9

15. Gibson SL, Havens JJ, Metz L, Hilf R. 2001. Is δ-Aminolevulinic Acid Dehydratase Rate Limiting in Heme Biosynthesis Following Exposure of Cells to δ-Aminolevulinic Acid? *Photochemistry and photobiology* 73:312-7

16. Collaud S, Juzeniene A, Moan J, Lange N. 2004. On the selectivity of 5-aminolevulinic acid-induced protoporphyrin IX formation. *Curr Med Chem Anticancer Agents* 4:301-16

17. Novotny A, Xiang J, Stummer W, Teuscher NS, Smith DE, Keep RF. 2000. Mechanisms of 5-aminolevulinic acid uptake at the choroid plexus. *J Neurochem* 75:321-8

18. Liu JT, Meza D, Sanai N. 2014. Trends in fluorescence image-guided surgery for gliomas. *Neurosurgery* 75:61-71

19. Olivo M, Wilson BC. 2004. Mapping ALA-induced PPIX fluorescence in normal brain and brain tumour using confocal fluorescence microscopy. *International Journal of Oncology* 25:37-45

20. Rud E, Gederaas O, Hogset A, Berg K. 2000. 5-aminolevulinic acid, but not 5-aminolevulinic acid esters, is transported into adenocarcinoma cells by system BETA transporters. *Photochemistry and photobiology* 71:640-7

21. Ennis SR, Novotny A, Xiang J, Shakui P, Masada T, et al. 2003. Transport of 5-aminolevulinic acid between blood and brain. *Brain research* 959:226-34

22. Zhao SG, Chen XF, Wang LG, Yang G, Han DY, et al. 2013. Increased expression of ABCB6 enhances protoporphyrin IX accumulation and photodynamic effect in human glioma. *Annals of surgical oncology* 20:4379-88

23. Xiang J, Hu Y, Smith DE, Keep RF. 2006. PEPT2-mediated transport of 5-aminolevulinic acid and carnosine in astrocytes. *Brain research* 1122:18-23

24. Sanai N. 2012. Emerging operative strategies in neurosurgical oncology. *Curr Opin Neurol* 25:756-66

25. Della Puppa A, De Pellegrin S, d'Avella E, Gioffre G, Rossetto M, et al. 2013. 5-aminolevulinic acid (5-ALA) fluorescence guided surgery of high-grade gliomas in eloquent areas assisted by functional mapping. Our experience and review of the literature. *Acta neurochirurgica* 155:965-72

26. Schucht P, Beck J, Abu-Isa J, Andereggen L, Murek M, et al. 2012. Gross total resection rates in contemporary glioblastoma surgery: results of an institutional protocol combining 5-aminolevulinic acid intraoperative fluorescence imaging and brain mapping. *Neurosurgery* 71:927-35

27. Schucht P, Seidel K, Beck J, Murek M, Jilch A, et al. 2014. Intraoperative monopolar mapping during 5-ALA-guided resections of glioblastomas adjacent to motor eloquent areas: evaluation of resection rates and neurological outcome. *Neurosurgical focus* 37:E16-24

28. Keles GE, Chang EF, Lamborn KR, Tihan T, Chang CJ, et al. 2006. Volumetric extent of resection and residual contrast enhancement on initial surgery as predictors of outcome in adult patients with hemispheric anaplastic astrocytoma. *Journal of neurosurgery* 105:34-40

29. Pope WB, Sayre J, Perlina A, Villablanca JP, Mischel PS, Cloughesy TF. 2005. MR imaging correlates of survival in patients with high-grade gliomas. *AJNR. American journal of neuroradiology* 26:2466-74

30. Grabowski MM, Recinos PF, Nowacki AS, Schroeder JL, Angelov L, et al. 2014. Residual tumor volume versus extent of resection: predictors of survival after surgery for glioblastoma. *Journal of neurosurgery* 121:1115-23

31. Stummer W, Pichlmeier U, Meinel T, Wiestler OD, Zanella F, Reulen HJ. 2006. Fluorescence-guided surgery with 5-aminolevulinic acid for resection of malignant glioma: a randomised controlled multicentre phase III trial. *Lancet Oncology* 7:392-401

32. Hadjipanayis CG, Jiang H, Roberts DW, Yang L. 2011. Current and future clinical applications for optical imaging of cancer: from intraoperative surgical guidance to cancer screening. *Semin Oncol* 38:109-18

33. Van Meir EG, Hadjipanayis CG, Norden AD, Shu HK, Wen PY, Olson JJ. 2010. Exciting new advances in neuro-oncology: the avenue to a cure for malignant glioma. *CA Cancer J Clin* 60:166-93

34. Barbosa BJ, Mariano ED, Batista CM, Marie SK, Teixeira MJ, et al. 2015. Intraoperative assistive technologies and extent of resection in glioma surgery: a systematic review of prospective controlled studies. *Neurosurg Rev* 38:217-26

35. Stummer W, Novotny A, Stepp H, Goetz C, Bise K, Reulen HJ. 2000. Fluorescence-guided resection of glioblastoma multiforme by using 5-aminolevulinic acid-induced porphyrins: a prospective study in 52 consecutive patients. *Journal of neurosurgery* 93:1003-13

36. van den Bent MJ, Vogelbaum MA, Wen PY, Macdonald DR, Chang SM. 2009. End point assessment in gliomas: novel treatments limit usefulness of classical Macdonald's Criteria. *J Clin Oncol* 27:2905-8

37. Wen PY, Macdonald DR, Reardon DA, Cloughesy TF, Sorensen AG, et al. 2010. Updated response assessment criteria for high-grade gliomas: response assessment in neuro-oncology working group. *J Clin Oncol* 28:1963-72

38. Hughes I, Hase T. 2010. Error Propagation. In *Measurements and their Uncertainties: A Practical Guide to Modern Error Analysis*:37-52. New York: Oxford University Press Inc., New York. Number of 37-52 pp.

39. Macdonald DR, Cascino TL, Schold SC, Jr., Cairncross JG. 1990. Response criteria for phase II studies of supratentorial malignant glioma. *J Clin Oncol* 8:1277-80

40. Tofts PS, Collins DJ. 2011. Multicentre imaging measurements for oncology and in the brain. *British Journal of Radiology* 84:S213-26

41. Gordillo N, Montseny E, Sobrevilla P. 2013. State of the art survey on MRI brain tumor segmentation. *Magnetic resonance imaging* 31:1426-38

42. Bauer S, Wiest R, Nolte LP, Reyes M. 2013. A survey of MRI-based medical image analysis for brain tumor studies. *Phys Med Biol* 58:R97-129

43. White DR, Houston AS, Sampson WF, Wilkins GP. 1999. Intra- and interoperator variations in region-of-interest drawing and their effect on the measurement of glomerular filtration rates. *Clin Nucl Med* 24:177-81

44. Sorensen AG, Patel S, Harmath C, Bridges S, Synnott J, et al. 2001. Comparison of diameter and perimeter methods for tumor volume calculation. *J Clin Oncol* 19:551-7

45. Chow DS, Qi J, Guo X, Miloushev VZ, Iwamoto FM, et al. 2014. Semiautomated volumetric measurement on postcontrast MR imaging for analysis of recurrent and residual disease in glioblastoma multiforme. *AJNR. American journal of neuroradiology* 35:498-503

46. Cordova JS, Schreibmann E, Hadjipanayis CG, Guo Y, Shu HK, et al. 2014. Quantitative tumor segmentation for evaluation of extent of glioblastoma resection to facilitate multisite clinical trials. *Transl Oncol* 7:40-7

47. Chang HH, Zhuang AH, Valentino DJ, Chu WC. 2009. Performance measure characterization for evaluating neuroimage segmentation algorithms. *NeuroImage* 47:122-35

48. Collett D. 2003. Strategy for model selection. In *Modeling Binary Data*, ed. C Chatfield, J Lindsey, M Tanner, J Zidek:91-7. Boca Raton, FL: Chapman & Hall/CRC. Number of 91-7 pp.

49. Orringer D, Lau D, Khatri S, Zamora-Berridi GJ, Zhang K, et al. 2012. Extent of resection in patients with glioblastoma: limiting factors, perception of resectability, and effect on survival. *Journal of neurosurgery* 117:851-9

50. Sanai N, Berger MS. 2011. Extent of resection influences outcomes for patients with gliomas. *Rev Neurol (Paris)* 167:648-54

51. Paravati AJ, Heron DE, Landsittel D, Flickinger JC, Mintz A, et al. 2011. Radiotherapy and temozolomide for newly diagnosed glioblastoma and anaplastic astrocytoma: validation of Radiation Therapy Oncology Group-Recursive Partitioning Analysis in the IMRT and temozolomide era. *J Neurooncol* 104:339-49

52. Gutman DA, Cooper LA, Hwang SN, Holder CA, Gao J, et al. 2013. MR imaging predictors of molecular profile and survival: multi-institutional study of the TCGA glioblastoma data set. *Radiology* 267:560-9

53. Crawford FW, Khayal IS, McGue C, Saraswathy S, Pirzkall A, et al. 2009. Relationship of pre-surgery metabolic and physiological MR imaging parameters to survival for patients with untreated GBM. *J Neurooncol* 91:337-51

54. Saraswathy S, Crawford FW, Lamborn KR, Pirzkall A, Chang S, et al. 2009. Evaluation of MR markers that predict survival in patients with newly diagnosed GBM prior to adjuvant therapy. *J Neurooncol* 91:69-81

Chapter 4

Whole-Brain Spectroscopic MRI Biomarkers Identify Infiltrating Margins in Glioblastoma Patients

4.1 Author's Contribution and Acknowledgement of Reproduction

The work presented here was conceptualized, organized, researched, and written by the dissertation author. Of the data presented all was collected by the author under the guidance of Dr. Shim, Dr. Hadjipanayis, and many collaborators. The chapter is reproduced with minor edits from Cordova, J.S., Shu, H.K.G., Liang, Z., Gurbani, S.S., Cooper, L.A.D., Holder, C.A., Olson, J.J. Kairdolf, B., Schreibmann, E., Neill, S., Hadjipanayis, C.G., Shim, H. Whole-Brain Spectroscopic MRI Biomarkers Identify Infiltrating Margins in Glioblastoma Patients, Neuro Oncol. 2016 Mar 15. pii: now036. [Epub ahead of print](314).

4.2 Abstract

The standard-of-care for GBM is maximal safe resection followed by RT with chemotherapy. Currently, contrast-enhanced MRI is used to define primary treatment volumes for surgery and RT. However, enhancement does not identify the tumor entirely resulting in limited local control. Proton sMRI may better define the tumor margin. Here, we develop a whole-brain sMRI pipeline and validate sMRI metrics with quantitative measures of tumor infiltration. Whole-brain sMRI metabolite maps were co-registered with surgical planning MRI and imported into a neuronavigation system to guide tissue sampling in GBM patients receiving 5-ALA FGS. Samples were collected from regions with metabolic abnormalities in a biopsy-like fashion before bulk resection. Tissue fluorescence was measured *ex vivo* using a hand-held spectrometer. Tissue samples were immunostained for SOX2 and analyzed to quantify the density of staining cells using a novel digital pathology image analysis tool. Correlations between sMRI markers, SOX2 density, and *ex vivo* fluorescence were evaluated. sMRI biomarkers exhibit significant correlations with SOX2-positive cell density and *ex vivo* fluorescence. Clinically, sMRI metabolic abnormalities predated contrast-enhancement at sites of tumor recurrence and exhibited an inverse relationship with PFS. As it identifies tumor infiltration and regions at high-risk for recurrence, sMRI could complement conventional MRI to improve local control in GBM patients.

4.3 Introduction

Approximately 15,000 new cases of GBM are diagnosed each year in the United States, making it the most common primary malignant brain tumor in

adults (315). The standard-of-care for GBM is maximal safe surgical resection followed by RT with concurrent and adjuvant TMZ chemotherapy. Despite such aggressive management, the tumor recurrence rate is high –approximately 70% within 6 months of RT – and the median OS is 13-15 months (10). Currently, both surgery and RT are based on T1-weighted contrast-enhanced (CE-T1w) MRI using the intravenous injection of gadolinium-based contrast agents. While contrast agent accumulates in regions where GBM tumors have compromised the blood-brain barrier or exhibit leaky neovasculature, they cannot effectively reach infiltrating tumor where perfusion is limited (67; 123). Multiple studies have found infiltrating tumor cells centimeters away from the contrast-enhancing mass (73). One study found that tissue extracted from a zone 6-14 mm outside of the CE-T1w region was composed of 60–100% tumor cells (316). Furthermore, these nonenhancing regions are biologically distinct, with varying oncogenic profiles that appear to influence treatment efficacy and recurrence (123; 317). Due to the remaining infiltrating cancer cells, nearly 80% of patients recur within 2 cm of the original CE-T1w tumor after therapy (127).

Molecular imaging techniques, including MR spectroscopy and fluorescence microscopy, have shown promise in identifying and directing therapy to tumor-infiltrated regions beyond the CE-T1w lesion (129). Proton spectroscopy, which includes 2D-chemical shift and 3D magnetic resonance spectroscopic imaging, is a molecular imaging technique that maps the metabolism of native small molecules to tumor regions *in vivo* without the need for exogenous tracers (193; 318). Using tumor metabolism, physicians can identify and target regions of significant tumor infiltration beyond contrast diffusion even when edema is

present (206; 224; 230; 318; 319). Additionally, infiltrating tumor cells can be identified intraoperatively using 5-ALA fluorescence microscopy (109). 5-ALA is an orally administered pro-drug that is readily metabolized by malignant gliomas to PpIX: a molecular species that fluoresces red (600-700 nm) under blue-violet light (400-410 nm). FGS with 5-ALA allows for the real-time visualization of tumor-infiltrated tissue with exceptionally high sensitivity, specificity, and positive predictive values (297). This technique has enabled surgeons to achieve significantly more complete malignant glioma resections compared to conventional methods and, consequently, has become indispensable in neurosurgical oncology departments around the world (297).

The complementary nature of MR spectroscopy and 5-ALA FGS is clear: spectroscopy allows the identification of tumor-infiltrated tissue via metabolic perturbations ***preoperatively***, while FGS provides a method for confirming infiltration and directing the resection of tissue ***intraoperatively***. However, the clinical use of spectroscopy has been limited due to various technical pitfalls including low spatial resolution, limited field-of-view, and insufficient tools for spectral display and analysis. To overcome these limitations, we have developed an imaging pipeline utilizing state-of-the-art, high-resolution (0.1cm^3 nominal voxel size) spectroscopic imaging and automated analysis tools to allow the addition of whole-brain metabolic maps to intraoperative neuronavigation (193). Using this novel whole-brain spectroscopic MRI (sMRI) method, we performed 5-ALA FGS in a cohort of GBM patients with sMRI scans and evaluated the relationship between metabolic markers, *ex vivo* tissue fluorescence, and histological measures of tumor infiltration. We also measured recurrence and

survival outcomes in patients on trial. Our aims are to provide quantitative evidence that sMRI non-invasively identifies infiltrating GBM tissue beyond the margin of contrast enhancement and to set forth clinical evidence for the use of sMRI to assist in directing surgery and RT in malignant gliomas.

4.4 Materials and Methods

4.4.1 Study Design

The objective of the surgical study was to describe the relationship between sMRI metrics, *ex vivo* fluorescence, and histological markers to test if sMRI is capable of identifying infiltrating GBM tissue. Patients included in this pilot study (n = 20) were part of an Institutional Review Board-approved, prospective Phase II 5-ALA FGS trial at Emory University (2011-2014) for patients with malignant glioma. The trial included patients ≥18 years of age with normal bone marrow, renal, and liver function; KPS ≥ 60%; and able to provide written informed consent. Patients with deep-seated tumors, receiving experimental therapies before surgery, and with a family history of porphyria were excluded. Tissue excised in a biopsy-like fashion from metabolically abnormal regions was analyzed as the primary endpoint. PFS (in days) was measured as a secondary outcome in those patients who had recurred after the standard-of-care (n=11) per the updated Response Assessment in Neuro-Oncology (RANO) criteria.(67) Survival data was frozen at August 2015 and the date of recurrence was retrospectively determined by a board-certified neuroradiologist backdating to the earliest known recurrence. Preoperative necrotic, contrast enhancing, and T2w-hyperintense tissue along with contrast enhancing tissue at recurrence were segmented semi-automatically

with a previously described method and confirmed by a neuroradiologist (239). Banked non-neoplastic tissue (n = 24 slides) from patients who had received surgery on a previous Institutional Review board-approved study for treatment-refractory seizures were collected as controls.

The RT-recurrence study was meant to survey the location of recurrence relative to sMRI abnormalities before the start of RT. All patients (n = 13) were part of a separate Institutional Review Board-approved, prospective Phase II sMRI-RT trial at Emory University (2014-2015). Inclusion criteria were the same as the FGS trial, and individuals with MRI-incompatible implants, medical conditions that compromise RT tolerance, or previous cranial radiation were excluded. Patients were scanned with the sMRI sequence ≤ 1 week prior to the beginning of RT and monitored every 1-3 months after completion of RT with standard MRI. Recurrence was determined according to the RANO criteria, and location of recurrence was noted relative to preRT metabolic abnormalities.

4.4.2 Image Acquisition and Processing

Whole-brain sMRI combining 3D echo-planar spectroscopic imaging, generalized auto-calibrating partially-parallel acquisitions, and elliptical k-space encoding was conducted (TE/TR/FA = 17.6ms/1551ms/71°) on 3T MRI scanner with 32-channel head coil array (Siemens Medical). This single average sMRI sequence has a scan time of approximately 19 minutes. Intracellular water signal was collected in an interleaved manner for signal normalization and registration with anatomical images. Raw data were processed using the MIDAS (193; 197) to give DICOM images with nominal voxel size of 4.4 mm x 4.4 mm x 5.6 mm.

Metabolite maps generated include choline (Cho), Creatine (CR), and N-acetylaspartate (NAA), as well as Cho/NAA, Cho/CR, and NAA/CR ratio maps. T1-weighted 3D MPRAGE (1 mm^3, TR/TE/FA = 2300ms/3.4ms/9°), T2w/FLAIR (TR/TE/FA = 10,000ms/121ms/90°), and diffusion-weighted images (DWI, TR/TE/FA = 5400ms/105ms/90°, b=0/1000) were also acquired. sMRI maps were then imported into VelocityAI (Varian Medical Systems), an FDA 510K-cleared image analysis suite for the processing of multi-modal medical images, for registration to the surgical planning MRI and resampling into the planning MRI image space.

4.4.3 Tissue Sampling and Fluorescence Measurement

5-ALA (Gliolan® Medac) was administered to patients orally (20 mg/kg bodyweight) 3-5 hours before surgery. Cho/NAA ratio maps were co-registered with surgical planning MRIs and imported into a neuronavigation system (Stealth Surgical Navigation System) to guide tissue sampling. Anatomy from water signal maps was visually compared to high-resolution anatomical imaging to verify co-registration accuracy. Specimens (1-2 per patient) were sampled in a biopsy-like fashion from areas exhibiting elevated Cho/NAA and visible fluorescence using a location-reporting probe before surgical debulking, in order to minimize navigation error due to resection-related brain shift (**Figure 4.1A-C**). Twenty-six tissue specimens (11 from contrast-enhancing tissue, 11 from T2w/FLAIR abnormal tissue, and 4 from tissue devoid of either abnormality) were sampled in this manner. Multiple fluorescence measurements (3-5 per sample) were made immediately *ex vivo* using a hand-held spectrometer with tip 5-10 mm from the tissue (320).

4.4.4 SOX2 Immunohistochemistry

Paraffin-embedded 5-µm sections of sampled tissue were stained for tumor infiltration using a SOX2 marker. Immunohistochemistry against SOX2 was performed with rabbit monoclonal antibody (1:500, ab92494, Abcam) according to the manufacturer's instructions (DAKO). Visualization was established using DAKO EnVision+ Dual (mouse and rabbit) Link System-HRP (K4061, DAKO) and DAB (K3467, DAKO), and slides were counter-stained with hematoxylin. Samples from control patients were stained similarly.

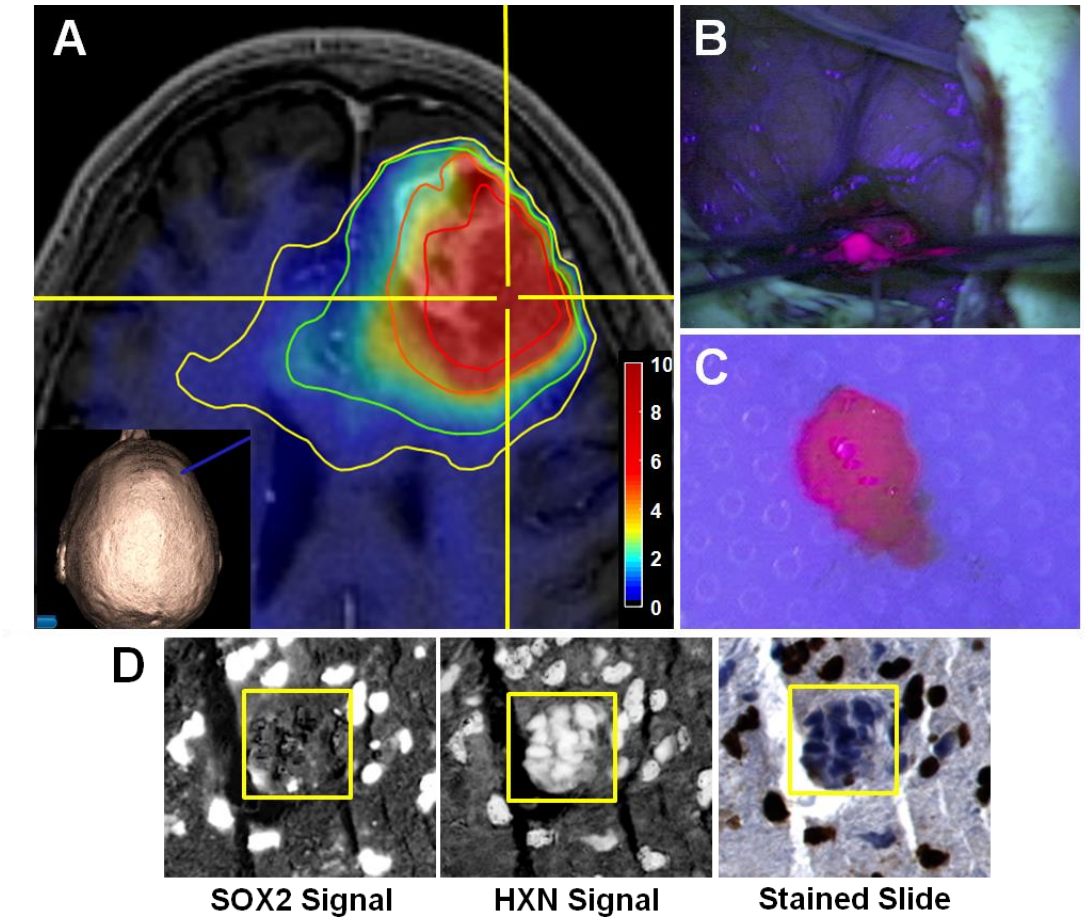

Figure 4.1. Procedure for tissue sampling and histological analysis using sMRI and 5-ALA FGS. View of anatomical and metabolic data in neuronavigation station with Cho/NAA ratio contours (yellow, 1.5-fold; green, 2-fold; orange, 5-fold; red, 10-fold increases in Cho/NAA over normal contralateral white matter) **(A)**. The inset image shows the 3D reconstruction of the patient surface anatomy along with the navigation probe (blue). The region of metabolic abnormality was identified using a stereotactic technique with a location-reporting probe and fluorescence was visualized using intraoperative microscopy **(B)**. Tissue was sampled in a biopsy-like fashion before debulking, and fluorescence was measured *ex vivo* **(C)**. Automated nuclear segmentation, digital unmixing (pictured), and nuclear classification using machine-learning techniques allowed the generation of a SOX2 density metric that were correlated with sMRI and *ex vivo* fluorescence signal **(D)**. HXN, hematoxylin. Color bar depicts fold changes.

4.4.5 Automated Histology Slide Analysis

Tumor infiltration in terms of SOX2 density (SOX2-positive area/total tissue area) was quantified using automated, whole-slide image analysis. SOX2-stained sections were digitized at 40X magnification using Hamamatsu's High-Resolution Nanozoomer 2.0HT Whole-slide Scanner. Automatic segmentation of nuclear boundaries was performed by digitally deconvolving hematoxylin and SOX2 signals into separate image channels (**Figure 4.1D**). An adaptive Gaussian mixture model was trained to classify image pixels into glass, tissue, and nuclear regions using maximum likelihood optimization of the hematoxylin. A graph-cutting approach was used to smooth nuclear segmentation, while a marker-based watershed method was used to separate nuclei. Nuclear features were used to train a random forest classifier to label each as SOX2-positive or negative. Total tissue area was computed as the sum of nuclear and tissue areas. SOX2 and total tissue areas were generated by multiplying the number of pixels classified as SOX2-positive or tissue, respectively, by the pixel dimensions (0.5 μm x 0.5 μm).

4.4.6 sMRI-SOX2 Analysis

Each set of co-registered metabolite volumes was imported into MATLAB (version 8.4.0; MathWorks,) for preprocessing and analysis. Contralateral white matter contours were used to estimate normal brain signal parameters and generate standardized abnormality index (AI_{metab}) maps for each metabolite (**Figure 4.2**). To account for potential navigation error, sMRI values to be correlated with SOX2 density were sampled from AI_{metab} maps using an 8 mm isotropic ROI centered on the location of tissue extraction (**Figure 4.2C**, **blue box**).

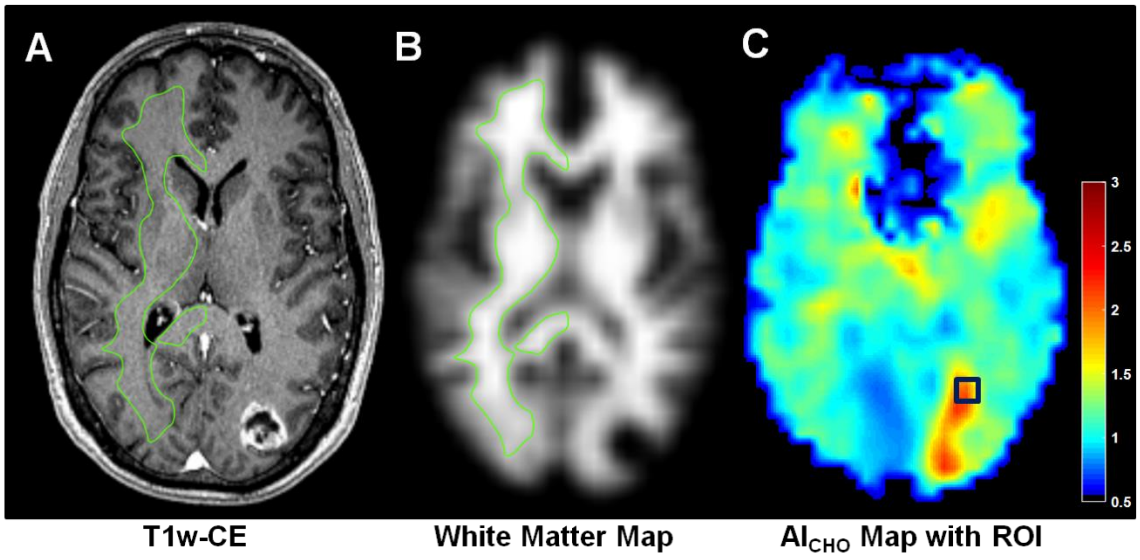

$$AI_{metab}^{linear} = \frac{S_{metab}^{voxel}}{mean_{metab}^{NAWM}}$$

Figure 4.2. Metabolite signal normalization scheme used for sMRI analyses. Normal appearing white matter (**A** and **B**) in hemisphere contralateral to the tumor was segmented using a white matter probability map to estimate mean normal brain signal. Normalized abnormality index (AI) maps **(C)** by linear scaling using the value in this contour. These are presurgical images of the patient in **Figure 5C.** ROI, region-of-interest; AI_{Cho}, normalized choline abnormality index map; NAWM, normal appearing white matter; green contour, NAWM segmentation. Color bars depict fold changes.

4.4.7 Statistical Methods

Statistical analyses were performed with the MATLAB Statistics and Machine Learning Toolbox, were 2-sided, and had significance set at $p \leq 0.05$. Differences in normal and tumor tissue SOX2 densities were evaluated using one-way analysis of variance with Tukey-Kramer's multiple comparisons correction. Standardized AI_{metab} maps were generated for each sMRI volume using a linear scaling function (**Figure 4.2)**. Mean differences and effect size for metabolite abnormalities in necrotic, contrast-enhancing, and T2w-hyperintense regions were evaluated using multivariate analysis of variance. All fluorescence measurements for a piece of tissue were averaged to generate mean fluorescent signal. Correlations between sMRI markers, mean *ex vivo* fluorescence, SOX2 density, and PFS were evaluated using Pearson's correlation coefficient (ρ) with a null hypothesis of no correlation.

4.5 Results

4.5.1 sMRI shows metabolic abnormalities beyond anatomical MRI

Co-registration of sMRI maps with conventional MRI allows the display of sMRI-detectable metabolites throughout the entire brain and illustrates the metabolic heterogeneity within GBM tumors (**Figure 4.3A** and **B**). The signal-to-noise ratio for the sMRI sequence, calculated as the mean area under the NAA peak divided by the peak-to-peak noise, is outstanding (SNR = 39.7 ± 14.7) resulting in highly sensitive, quantitative metabolite maps (see **Figure 4.4** for spectra). In the case pictured, increases in Cho, a marker of membrane synthesis and cellular proliferation, and decreases in NAA, a marker of neuronal integrity, expand well

beyond the CE-T1w and T2w signal abnormalities, indicating the potential infiltration of tumor cells across the genu of the corpus callosum. Conversely, CR, a marker of cellular energetics, remains relatively unchanged with the exception of the central necrotic portion of the tumor, where it is nearly absent. The intracellular water signal is acquired in an interleaved fashion with the spectral data (**Figure 4.3C**) and serves as a source of anatomical features for affine image registration, as well as a denominator for the absolute quantification of metabolite concentrations.

Over 1.3 million voxels from segmented necrotic, contrast-enhancing, and T2w-hyperintense tissue ROIs were evaluated for metabolic abnormalities. The average fold-change in each metabolite for all 20 presurgical patients can be found in **Table 4.1** along with the percent variance in each region explained by metabolic changes (i.e. effect size for group mean difference, $\boldsymbol{\eta^2}$**)**. There was a statistically significant difference in the mean metabolite abnormalities observed in each ROI from these patients indicating that each exhibits a distinct metabolic profile (Wilk's Λ [1st dimension] = 0.64, $p < 0.001$; Wilk's Λ [2nd dimension] = 0.94, $p < 0.001$). Though each imaging value exhibited a statistically significant contribution, only Cho/NAA, Cho/CR, and NAA exhibited moderate to strong effect in differentiating each ROI ($\boldsymbol{\eta^2}$**=** 0.11, 0.21, and 0.10, respectively).

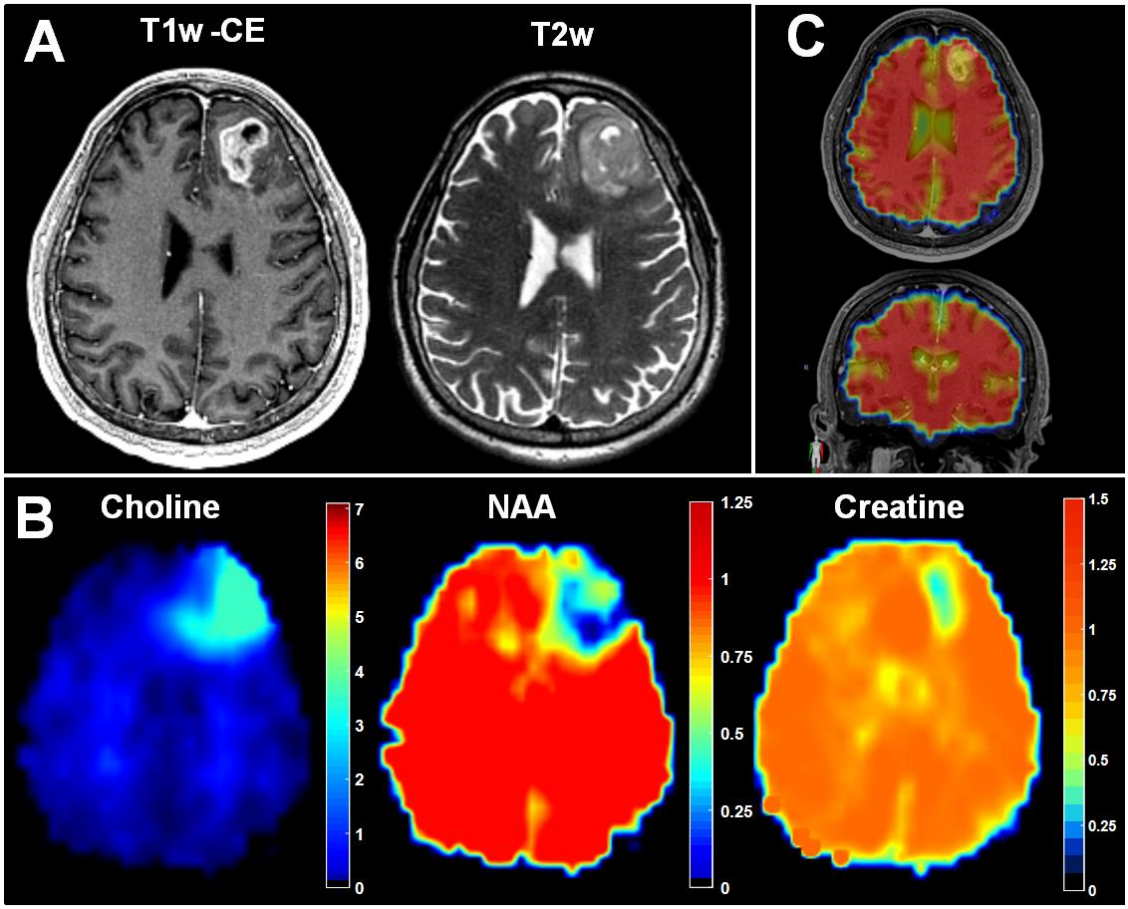

Figure 4.3. sMRI quantitatively maps small-molecule metabolism throughout the entire brain and describes metabolic abnormalities outside of conventional anatomical MR imaging. Metabolite maps (choline, NAA, and creatine) show abnormalities beyond CE-T1w or T2w imaging, and give insight into the metabolic heterogeneity of the tumor and surrounding tissue **(A** and **B)**. Internal water signal is used as a denominator of metabolite signal, allowing the generation of absolute metabolite concentrations **(C).** Color bars depict fold changes.

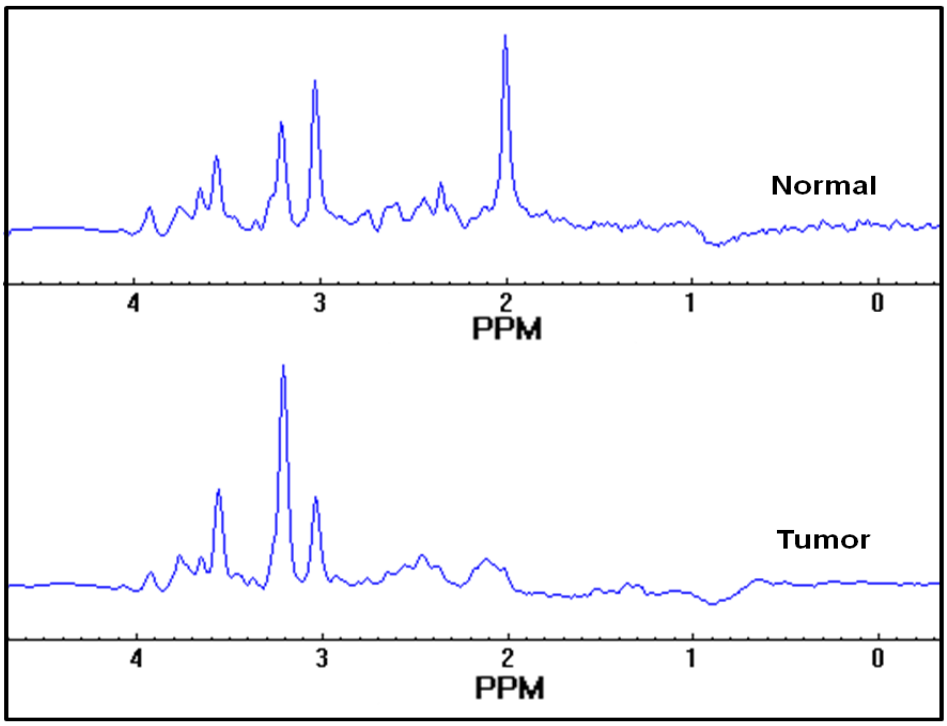

Figure 4.4. Representative sMRI spectra from normal and tumor tissue. Spectra were generated from patient in Figure 3**.** The spectroscopic technique used gives chemical shift data with SNR of ~ 40, on average. SNR is calculated as the mean area under the NAA peak divided by the peak-to-peak noise.

Tumor Region	Cho		Cho/NAA		Cho/CR		NAA		NAA/CR		CR		ADC	
	Mean	SD	Mean	SD	Mean	SD	Mean	SD	Mean	SD	Mean	SD	Mean	SD
Necrosis (n = 20)	0.821	0.627	2.830	2.094	2.352	1.755	0.270	0.392	1.163	1.565	0.390	0.354	1.531	0.408
CE (n = 20)	1.477	0.964	4.146	3.695	2.181	1.446	0.382	0.413	0.856	1.314	0.743	0.519	1.363	0.343
T2W (n = 20)	1.103	0.920	1.779	2.413	1.039	0.763	0.711	0.373	0.757	0.697	1.029	0.625	1.395	0.348
η^2	0.04		0.11		0.21		0.10		0.01		0.09		0.01	

Table 4.1. Fold-change of each metabolite in different tumor regions on CE-T1w MRI for all preoperative patients. The ADC was included for comparison. Eta-squared (η^2) is a measure of effect size and can be interpreted as the proportion of variance in the ROIs explained by the metabolite evaluated. Statistically significant differences were found between each ROI using a multivariate ANOVA (Wilk's Λ [1st dimension] = 0.64, $p < 0.001$; Wilk's Λ [2nd dimension] = 0.94, $p < 0.001$). CE, Contrast-enhancing regions; T2W, T2w-hyperintense regions.

4.5.2 Integration of sMRI into neuronavigation system

sMRI maps were integrated into the surgical neuronavigation station by fusion with standard anatomical MR images to allow real-time guidance of surgeons to metabolically abnormal tissue (**Figure 4.1A**). Each sMRI map was resampled into the anatomical MRI space for transfer to the neuronavigation system. Fusion of these images with the neuronavigation system's fiducial coordinate system allows the real-time guidance of surgical instruments to a selected target with exceptional accuracy. Contours representing various degrees of metabolic abnormality to be targeted are generated to describe abnormality thresholds.

4.5.3 Automated histology image analysis gives objective marker of tumor infiltration

An automated whole-slide image analysis approach was developed to objectively quantify the density of immunostained tumor cells in tissue specimens. SOX2 is a transcription factor known to maintain pluripotency in stem cells; however, immunohistochemistry for SOX2 shows remarkable specificity for infiltrating neoplastic cells in glioma (321). A hematoxylin counterstain allows the delineation of nuclear boundaries, and the deconvolution of hematoxylin and SOX2 signals into separate image channels with digital unmixing allows the automated classification of SOX2-positive and negative populations (**Figure 4.1D**) (322). SOX2 density (mm^2 SOX2 / mm^2 tissue), a quantitative metric of tumor infiltration in a tissue section, can then be calculated as the area of SOX2-positive nuclei over the area of total tissue on each slide. Using this method, the

SOX2 densities in GBM (contrast-enhancing and nonenhancing regions) from Cho/NAA abnormal regions and control tissue samples were found to be 0.037 ± 0.048, 0.035 ± 0.040, and 0.001 ± 0.0009 mm^2 SOX2 / mm^2 tissue, respectively. SOX2 density in nonenhancing and enhancing tissue were found to be significantly elevated relative to tissue acquired from controls ($p < 0.01$ and $p < 0.001$, respectively) though no significant difference in SOX2 density was observed between them ($p = 0.97$). Though too few were acquired for a properly-powered comparison ($n = 4$), as sampling was generally targeted within T2w abnormal regions, tissue samples outside of T2w hyperintensities also exhibited elevated SOX2 density with a mean of 0.065 ± 0.040 mm^2 SOX2 / mm^2 tissue (**Figure 4.5A-D**). Objective histological analysis not only confirms that tumor infiltration occurs in regions with Cho/NAA abnormalities regardless of contrast-enhancement, but it also suggests that elevations in Cho/NAA may be able to identify infiltration beyond T2w abnormalities.

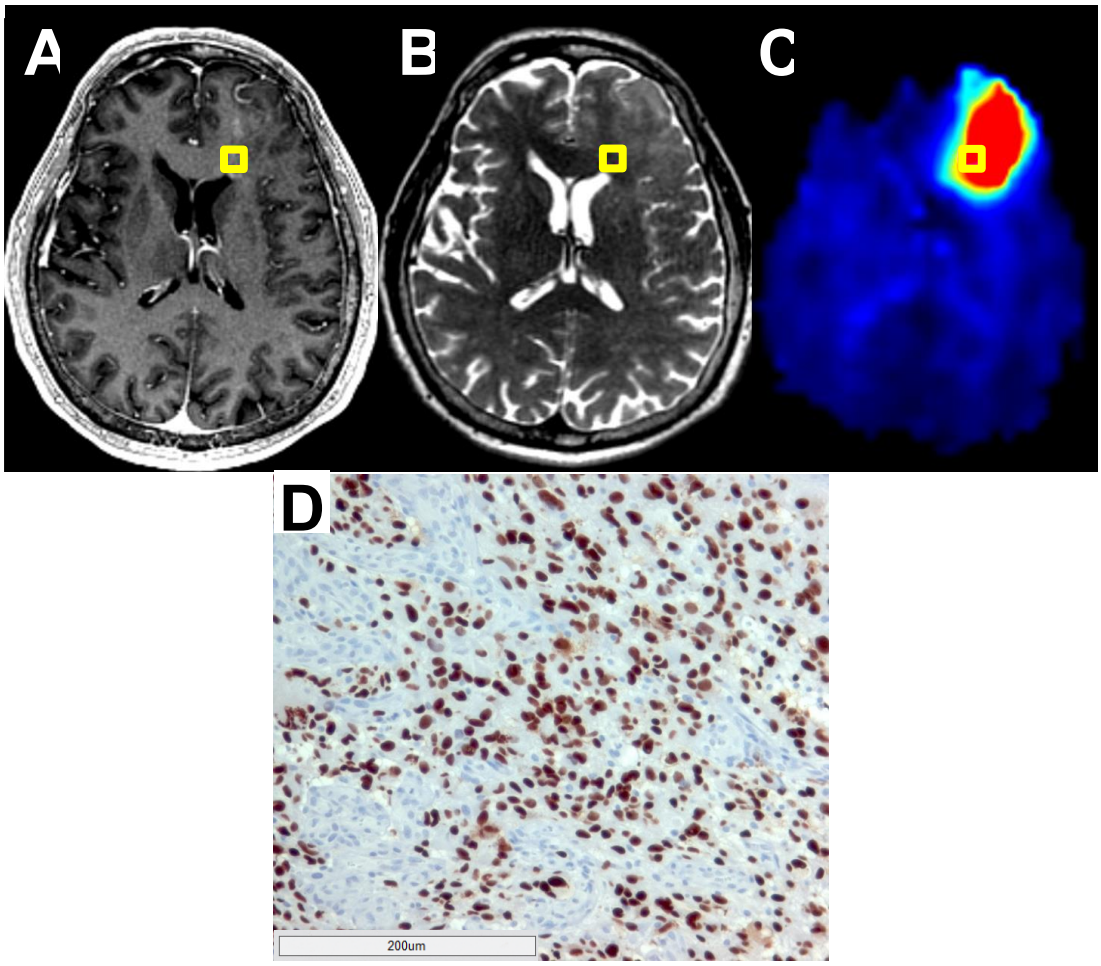

Figure 4.5. A normalized metric of tumor infiltration, SOX2 density, identifies tumor outside of conventional imaging. Though no obvious abnormality can be found on preoperative CE-T1w (**A**) or T2w imaging (**B**) in this patient, a striking elevation in Cho/NAA (**C**) on sMRI suggests substantial tumor infiltration. A light micrograph of tissue (including 200 μm scale bar) from the gold box showed elevations in SOX2 density along with the microvascular proliferation and nuclear atypia suggestive of GBM (**D**).

4.5.4 sMRI markers exhibit significant correlations with SOX2 density

AI_{metab} maps depicting standardized metabolic changes between patients were used to evaluate the correlation between sMRI markers and SOX2 density. Significantly elevated SOX2 densities were found in all tissues from Cho/NAA abnormal regions exhibiting CE-T1w and T2w abnormalities, as well as in tissue outside of both abnormalities. Cho/NAA and Cho were the markers most highly correlated with SOX2 density, exhibiting strong, statistically significant associations (**Table 4.2**). NAA and NAA/CR maps both exhibited moderate negative correlations while Cho/CR and CR did not exhibit significant correlations with SOX2 density ($\rho = 0.35$, $p = 0.08$; $\rho = 0.24$, $p = 0.23$, respectively). In addition, the ADC, a DWI marker generally associated with the cellularity of tissue, did not exhibit significant correlation with SOX2 density ($\rho = 0.18$, $p = 0.39$). The coupling of stereotactic tissue sampling with objective histological analysis suggests a striking relationship between sMRI metabolic abnormalities and the infiltration of GBM into normal-appearing brain.

Biomarker	ρ	p-value
NAA	-0.42	0.04*
NAA/CR	-0.56	<0.01*
Cho	0.69	<0.001*
Cho/NAA	0.82	<0.0001*
Cho/CR	0.35	0.08
CR	0.24	0.23
DWI-ADC	0.18	0.39

Table 4.2. Pearson's correlation coefficients for all sMRI metabolites and SOX2 density. *Significant at $p < 0.05$.

4.5.5 Ex vivo tissue fluorescence correlates with sMRI markers and SOX2 density

The average fluorescence signal measured in tumor specimens *ex vivo* was compared to both sMRI markers and SOX2 density. Fluorescence was measurable in all tissues from Cho/NAA abnormal regions with an average fluorescence signal of $2.15 \times 10^6 \pm 1.29 \times 10^6$. These measurements exhibited a strong, statistically significant correlation with SOX2 density ($\rho = 0.64$, $p = 5E\text{-}6$). Furthermore, Cho/NAA and Cho exhibited statistically significant associations with *ex vivo* fluorescence ($\rho = 0.36$, $p < 0.0001$; $\rho = 0.40$, $p < 0.001$). Thus, not only is *ex vivo* fluorescence highly associated with a histological marker of tissue infiltration (SOX2 density), but it also exhibits significant associations with metabolic markers generated preoperatively with sMRI.

4.5.6 Cho/NAA identifies regions at high-risk for tumor recurrence

All patients in this analysis had histopathologically-confirmed GBM, completed RT (30 fractions of 2 Gy), and received follow-up care at a single institution. Five of the thirteen patients on trial had documented CE-T1w progression (38.5%) as of August 2015, and each recurrence was confirmed by serial imaging or histopathology. While both Cho and Cho/NAA measures showed high correlations with infiltration, Cho/NAA was chosen to evaluate recurrence as it is a more sensitive marker for identifying regions at risk for recurrence (323; 324). Red contours depicting 2-fold elevations in Cho/NAA (compared to contralateral normal-appearing white matter) are shown on each image to depict regions with a high likelihood of tumor infiltration (325). This level of elevation

equates to a mean Z-score of 6.62 in these patients, suggesting the identification of metabolic abnormalities with > 99.999% confidence.

All patients who had tumor recurrence in the follow-up period showed contrast-enhancement in regions that exhibited Cho/NAA abnormalities before RT; a few examples of this can be found in **Figure 4.6**. In row **4.6A**, Cho/NAA elevation at the posterior aspect of the tumor resection cavity predates the appearance of a CE-T1w lesion in that region by roughly 5 months. This lesion continued to grow after the recurrence date, resulting in increased spatial agreement with the preRT 2-fold Cho/NAA abnormality [Z-score = 7.57 (tissue classified as abnormal with > 99.999% confidence)]. Similarly, in a patient with a large frontal GBM, preRT Cho/NAA abnormalities anterior to the resection cavity and even across the midline approximate later tumor recurrence volumes nearly 5 months after completion of RT (**Figure 4.6B**). The morphology of the CE-T1w lesion continued to evolve throughout the follow-up period to further approximate the morphology of the preRT 2-fold Cho/NAA abnormality [Z-score = 5.75 (tissue classified as abnormal with > 99.999% confidence)].

In some cases where GBM recurrence was observed, the recurrence sites exhibited clear metabolic abnormalities before surgical resection. For example, the 40-year-old patient depicted in **Figure 4.6C** exhibited a striking tail of Cho/NAA elevation that coursed along the occipital horn of the left lateral ventricle even before surgery (**Figure 4.2C**). This abnormality continued to grow through the duration of RT, ultimately resulting in overt tumor invasion along the trajectory of the 2-fold Cho/NAA abnormality [Z-score = 6.53 (tissue classified as abnormal with > 99.999% confidence)].

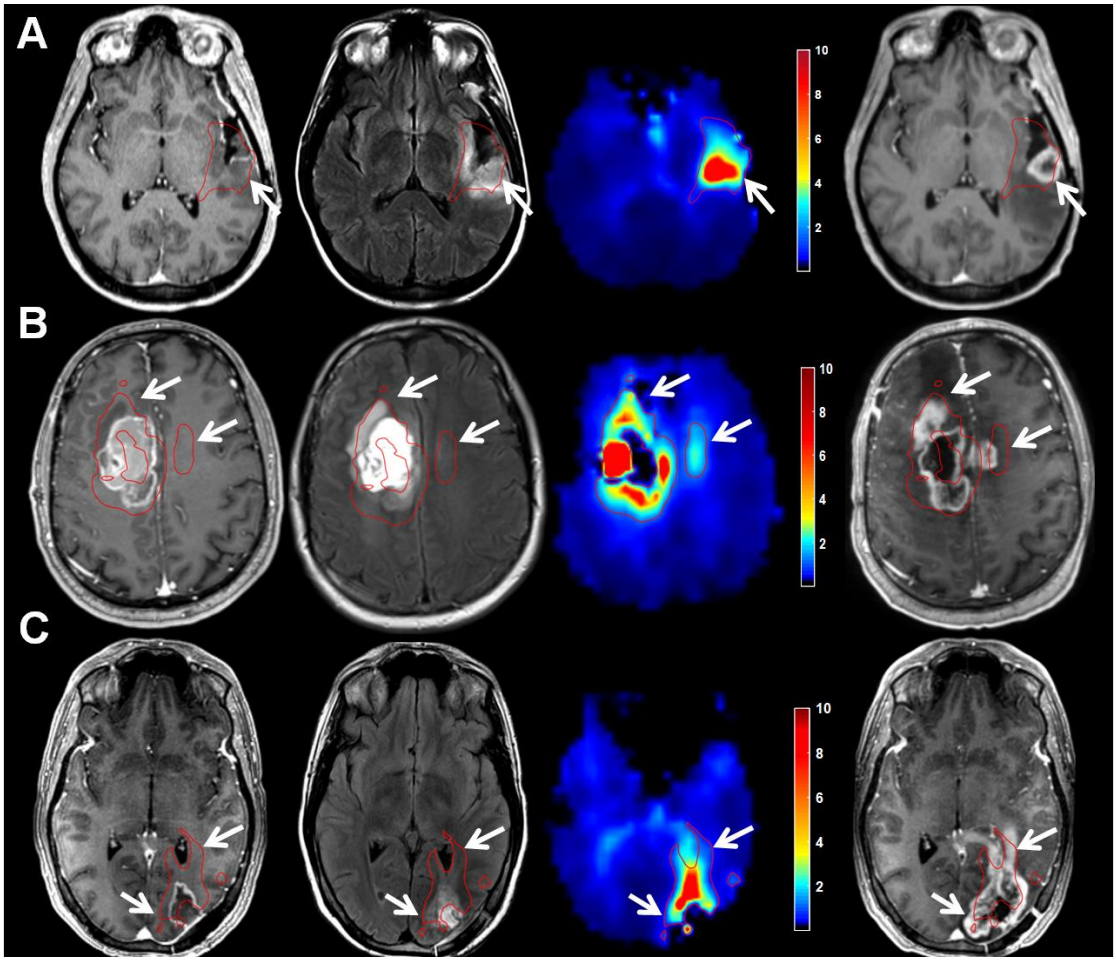

Figure 4.6. Abnormalities in Cho/NAA describe regions at high risk for recurrence before RT in GBM. CE-T1w (first column), T2w/FLAIR (second column), and Cho/NAA (third column) images taken before RT are shown with first recurrence on CE-T1w imaging after RT (fourth column). In a patient with no residual contrast-enhancement and T2W abnormality that surrounded the entire resection cavity, increased Cho/NAA posterior to the resection cavity is coherent with the site of first recurrence 5 months after RT (**A**). Cho/NAA abnormalities anterior and contralateral to enhancing tumor before RT predate expansion into these regions 4 months after RT (**B**). Though no T2w abnormality was found contralateral before RT, the metabolic signature of tumor was present. PreRT Cho/NAA map clearly shows infiltration of subependymal space that becomes contrast-enhancing 4 months later (**C**). The red contour illustrates the regions that exhibit a Cho/NAA abnormality ≥ 2-fold higher than normal contralateral brain. Color bars depict fold changes.

4.5.7 Cho/NAA ratio in T2-hyperintense regions correlates with PFS

Segmentation of necrotic, CE-T1w, and T2w abnormalities using a previously described semi-automated, blob-based algorithm allowed the comparison of quantitative sMRI findings with survival outcomes (239). When Cho/NAA statistics in each segmentation were analyzed (mean, median, maximum, etc.), a striking relationship between Cho/NAA values in the T2w abnormality and PFS was identified (**Figure 4.7**). Patients that exhibited high maximum Cho/NAA values within the T2w abnormality (not including necrosis or contrast-enhancing tissue) preoperatively had shorter PFS than those with lower values in this region (ρ = -0.74, p = 0.012). No trend between Cho/NAA values within necrotic or enhancing regions and PFS were found, however.

4.6 Discussion

GBM is a devastating disease with the vast majority of patients exhibiting recurrence within 6 months despite aggressive treatment (10). It has long been suspected that the standard treatment regimen is not optimally effective because conventional imaging does not allow reliable targeting of the entire GBM tumor: CE-T1w imaging does not identify infiltrative margins and T2w imaging is not specific for tumor tissue (69; 119; 326). Conversely, spectroscopic techniques are not limited by contrast diffusion (unlike CE-T1w imaging) and are not obscured by the presence of edema (unlike T2w imaging) (206; 224). Although prospective spectroscopy-histology studies have generated compelling results in the past, the low spatial resolution and limited field-of-view of sequences used in these studies, and even those currently available clinically, hinder the

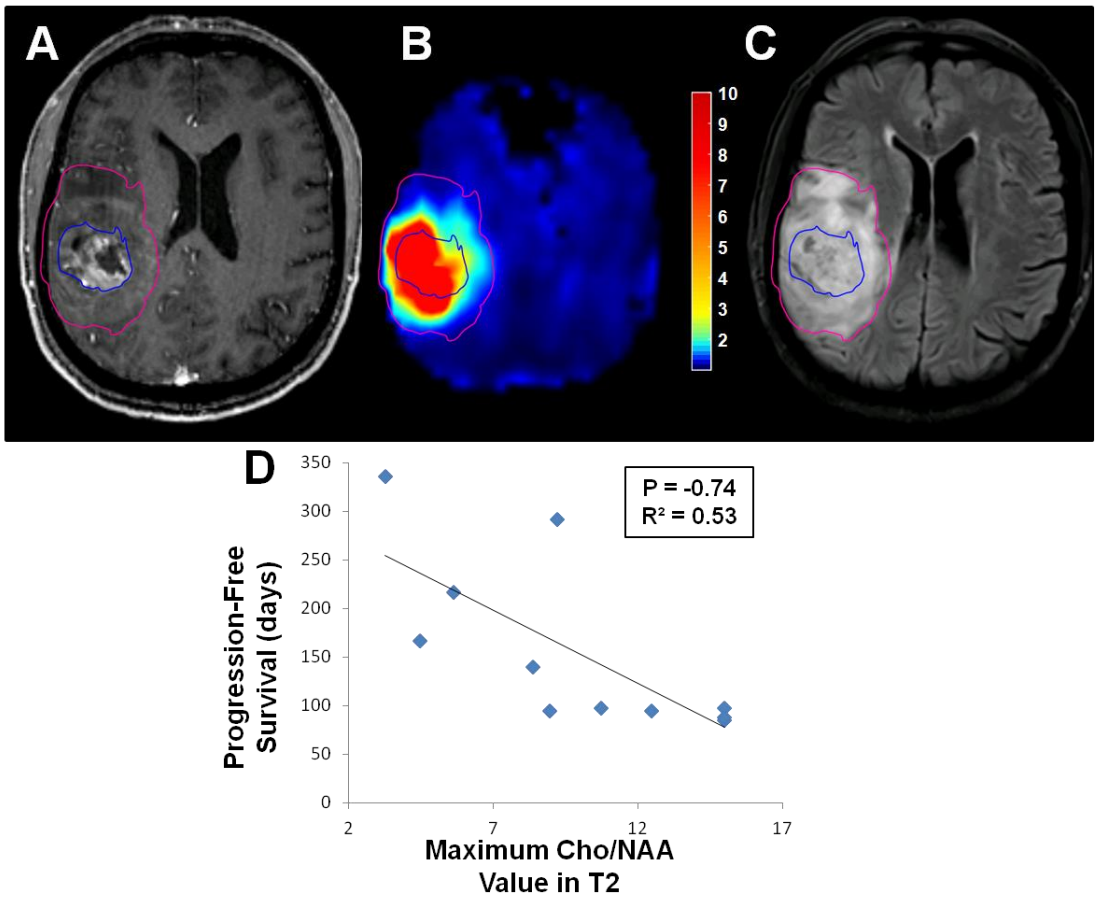

Figure 4.7. Peritumoral Cho/NAA abnormalities are associated with PFS. Patients with high maximum Cho/NAA values within the T2w hyperintense region outside of contrast-enhancing and necrotic tissue before RT (**A–C**) appear to exhibit poorer survival, in terms of PFS, than those who have lower maximal Cho/NAA values in this region (**D**). Pink contour, T2w hyperintense region; Blue contour, CE-T1w region. Color bar depicts fold changes.

clinical use of the technology severely (230; 319; 327-329). As such, spectroscopy has been relegated to a supportive role in glioma diagnosis only. To overcome such imaging limitations, a spectroscopy pipeline utilizing a state-of-the-art pulse sequence and processing tools was developed for the generation of high-resolution, whole-brain sMRI images that are easily imported into standard intraoperative neuronavigation stations. Moreover, to overcome bias in histological interpretation, quantitative image analysis techniques were used for the objective and automated evaluation of microscopic tumor infiltration.

The combination of standardized, high-resolution metabolic mapping, precise stereotactic tissue extraction, and quantitative tissue section analysis allows the correlation of metabolic abnormality with histology at an unprecedented level of accuracy. Combining these tools, we confirm the presence of tumor-infiltrated tissue beyond CE-T1w and T2w lesions, as well as the similarity of tumor infiltration in metabolically abnormal contrast-enhancing and nonenhancing peritumoral regions. These results imply substantial tumor infiltration beyond regions conventionally targeted for resection or RT. The results also suggest the absence of contrast-enhancement does not signify the absence of bulk tumor, thus supporting previous suspicions concerning the inadequacy of anatomical imaging for therapy planning in GBM. Furthermore, sMRI metrics exhibit significant associations with two quantitative measures of tissue infiltration –SOX2 density and *ex vivo* tissue fluorescence –supporting the hypothesis that sMRI identifies tumor-infiltrated tissue *in vivo*. Lastly, Cho/NAA not only identifies regions at high-risk for contrast-enhancing recurrence, but also shows a significant association with PFS in a small cohort of GBM patients. Taken

together, this work represents the first in-human study to: combine high-resolution, whole-brain sMRI and 5-ALA FGS for real-time intraoperative neuronavigation in GBM; describe sMRI abnormalities using both *ex vivo* fluorescence and quantitative histological metrics; and survey the capacity that sMRI may have for assessing clinical outcomes such as the location of recurrence and time to recurrence.

4.6.1 Study Strengths and Limitations

This study has limitations common to other pilot neurosurgical studies: small sample sizes for both tissue sampling and recurrence analyses. However, even given the sample size, the analytical techniques are robust enough to describe striking relationships between histology, tissue fluorescence, and sMRI markers. Moreover, the recurrence and PFS data remain unchanged further supporting the claim that sMRI can identify tumor infiltrated tissue. Lastly, we were unable to sample normal tissue outside of Cho/NAA abnormal and fluorescent region in FGS patients making it impossible to determine baseline SOX2 densities and diagnostic accuracy. This is a problem common to neurosurgical studies as it is considered negligent to acquire normally functioning tissue, which often requires sampling of the contralateral hemisphere in GBM, at the risk of causing extensive neurological injury. Though unfortunate, this is a component of neurosurgical studies that is insurmountable, and thus is accepted in the field. Even in light of these limitations, the data support the claims that sMRI can identify brain regions that are tumor-infiltrated, regions that are at high-risk for recurrence, and regions that could be

specifically targeted with surgery and RT in an attempt to decrease the likelihood of local progression in GBM.

4.6.1 Conclusions

High-resolution, whole-brain sMRI could prove to be an excellent method for obtaining the complementary metabolic information necessary to preoperatively identify sites of significant tumor infiltration and to direct 5-ALA FGS to tumor-infiltrated regions that appear normal on conventional MRI. Furthermore, as the intensity of metabolic abnormality in the T2w-hyperintense component of the tumor is shown to be associated with progression, the expansion of high-dose RT boost volumes (≥ 60 Gy) to encompass these regions may possibly decrease the rate of local recurrence as well. Apart from GBM, sMRI has exciting potential to improve the diagnosis, targeting, and response assessment for a number of other intracranial tumors. This is especially true for lower grade gliomas which often do not contrast-enhance on CE-T1w MR imaging, making surgery and RT target planning difficult. Thus, the addition of sMRI to RT dosage planning in low grade glioma could result in a brand new, clinically important target ROI. Most importantly, the addition of sMRI to the surgical and RT management of gliomas would represent a paradigm shift in the field of image-guided therapy away from targeting surrogate markers using tracer-based imaging techniques (e.g. contrast-enhancement, standardized tracer uptake in PET) to targeting abnormal tissue regions by measuring endogenous biological processes.

Encouragingly, many of the technical pitfalls of sMRI implementation that have plagued its clinical implementation in the past have now been surmounted,

and further development of more sophisticated sMRI analysis and integration pipelines appears promising. Although further standardization and automation of the clinical workflow is required, tracer-independent metabolic mapping with sMRI would provide accurate brain tumor metabolism information to neurosurgeons and radiation oncologists treating glioma patients. The clinical integration of sMRI into therapy planning and response assessment in glioma would represent a paradigm shift in the management of these patients, potentially giving physicians a new tool to improve survival with this debilitating disease beyond the current standard-of-care.

4.7 References

1. Cordova JS, Shu HG, Liang Z, Gurbani SS, Cooper LA, et al. 2016. Whole-brain spectroscopic MRI biomarkers identify infiltrating margins in glioblastoma patients. *Neuro-oncology* 15

2. Ostrom QT, Gittleman H, Liao P, Rouse C, Chen Y, et al. 2014. CBTRUS statistical report: primary brain and central nervous system tumors diagnosed in the United States in 2007-2011. *Neuro-oncology* 16 Suppl 4:iv1-63

3. Stupp R, Hegi ME, Mason WP, van den Bent MJ, Taphoorn MJB, et al. 2009. Effects of radiotherapy with concomitant and adjuvant temozolomide versus radiotherapy alone on survival in glioblastoma in a randomised phase III study: 5-year analysis of the EORTC-NCIC trial. *Lancet Oncology* 10:459-66

4. Barajas RF, Jr., Phillips JJ, Parvataneni R, Molinaro A, Essock-Burns E, et al. 2012. Regional variation in histopathologic features of tumor specimens from treatment-naive glioblastoma correlates with anatomic and physiologic MR Imaging. *Neuro-oncology* 14:942-54

5. Wen PY, Macdonald DR, Reardon DA, Cloughesy TF, Sorensen AG, et al. 2010. Updated response assessment criteria for high-grade gliomas: response assessment in neuro-oncology working group. *J Clin Oncol* 28:1963-72

6. Kelly PJ, Daumas-Duport C, Kispert DB, Kall BA, Scheithauer BW, Illig JJ. 1987. Imaging-based stereotaxic serial biopsies in untreated intracranial glial neoplasms. *Journal of neurosurgery* 66:865-74

7. Yamahara T, Numa Y, Oishi T, Kawaguchi T, Seno T, et al. 2010. Morphological and flow cytometric analysis of cell infiltration in glioblastoma: a comparison of autopsy brain and neuroimaging. *Brain tumor pathology* 27:81-7

8. Toussaint LG, 3rd, Nilson AE, Goble JM, Ballman KV, James CD, et al. 2012. Galectin-1, a gene preferentially expressed at the tumor margin, promotes glioblastoma cell invasion. *Molecular cancer* 11:32

9. Sherriff J, Tamangani J, Senthil L, Cruickshank G, Spooner D, et al. 2013. Patterns of relapse in glioblastoma multiforme following concomitant chemoradiotherapy with temozolomide. *The British journal of radiology* 86:20120414

10. Waldman AD, Jackson A, Price SJ, Clark CA, Booth TC, et al. 2009. Quantitative imaging biomarkers in neuro-oncology. *Nature reviews. Clinical oncology* 6:445-54

11. Law M. 2004. MR spectroscopy of brain tumors. *Topics in magnetic resonance imaging : TMRI* 15:291-313

12. Maudsley AA, Domenig C, Govind V, Darkazanli A, Studholme C, et al. 2009. Mapping of brain metabolite distributions by volumetric proton MR spectroscopic imaging (MRSI). *Magnetic resonance in medicine* 61:548-59

13. Stadlbauer A, Buchfelder M, Doelken MT, Hammen T, Ganslandt O. 2011. Magnetic resonance spectroscopic imaging for visualization of the infiltration zone of glioma. *Cent Eur Neurosurg* 72:63-9

14. Stadlbauer A, Nimsky C, Buslei R, Pinker K, Gruber S, et al. 2007. Proton magnetic resonance spectroscopic imaging in the border zone of gliomas: correlation of metabolic and histological changes at low tumor infiltration--initial results. *Investigative radiology* 42:218-23

15. Di Costanzo A, Scarabino T, Trojsi F, Popolizio T, Catapano D, et al. 2008. Proton MR spectroscopy of cerebral gliomas at 3 T: spatial heterogeneity, and tumour grade and extent. *European radiology* 18:1727-35

16. Di Costanzo A, Scarabino T, Trojsi F, Giannatempo GM, Popolizio T, et al. 2006. Multiparametric 3T MR approach to the assessment of cerebral gliomas: tumor extent and malignancy. *Neuroradiology* 48:622-31

17. Barbosa BJ, Mariano ED, Batista CM, Marie SK, Teixeira MJ, et al. 2015. Intraoperative assistive technologies and extent of resection in glioma surgery: a systematic review of prospective controlled studies. *Neurosurg Rev* 38:217-26

18. Hadjipanayis CG, Widhalm G, Stummer W. 2015. What is the Surgical Benefit of Utilizing 5-Aminolevulinic Acid for Fluorescence-Guided Surgery of Malignant Gliomas? *Neurosurgery [Epub Ahead of Print] DOI: 10.1227/NEU.0000000000000929*

19. Cordova JS, Schreibmann E, Hadjipanayis CG, Guo Y, Shu HK, et al. 2014. Quantitative tumor segmentation for evaluation of extent of glioblastoma resection to facilitate multisite clinical trials. *Transl Oncol* 7:40-7

20. Maudsley AA, Darkazanli A, Alger JR, Hall LO, Schuff N, et al. 2006. Comprehensive processing, display and analysis for in vivo MR spectroscopic imaging. *NMR Biomed* 19:492-503

21. Kairdolf BA, Bouras A, Kaluzova M, Sharma AK, Wang MD, et al. 2016. Intraoperative Spectroscopy with Ultrahigh Sensitivity for Image-Guided Surgery of Malignant Brain Tumors. *Analytical chemistry* 88:858-67

22. de la Rocha AM, Sampron N, Alonso MM, Matheu A. 2014. Role of SOX family of transcription factors in central nervous system tumors. *American journal of cancer research* 4:312-24

23. Ruifrok AC, Johnston DA. 2001. Quantification of histochemical staining by color deconvolution. *Analytical and quantitative cytology and histology / the International Academy of Cytology [and] American Society of Cytology* 23:291-9

24. Go KG, Kamman RL, Mooyaart EL, Heesters MA, Pruim J, et al. 1995. Localised proton spectroscopy and spectroscopic imaging in cerebral gliomas, with comparison to positron emission tomography. *Neuroradiology* 37:198-206

25. Nelson SJ, Vigneron DB, Dillon WP. 1999. Serial evaluation of patients with brain tumors using volume MRI and 3D 1H MRSI. *NMR Biomed* 12:123-38

26. Guo J, Yao C, Chen H, Zhuang D, Tang W, et al. 2012. The relationship between Cho/NAA and glioma metabolism: implementation for margin delineation of cerebral gliomas. *Acta neurochirurgica* 154:1361-70; discussion 70

27. Cha S. 2006. Update on brain tumor imaging: from anatomy to physiology. *AJNR. American journal of neuroradiology* 27:475-87

28. Young GS. 2007. Advanced MRI of adult brain tumors. *Neurologic clinics* 25:947-73, viii

29. Pope WB, Young JR, Ellingson BM. 2011. Advances in MRI assessment of gliomas and response to anti-VEGF therapy. *Current neurology and neuroscience reports* 11:336-44

30. Matsumura A, Isobe T, Anno I, Takano S, Kawamura H. 2005. Correlation between choline and MIB-1 index in human gliomas. A quantitative in proton MR

spectroscopy study. *Journal of clinical neuroscience : official journal of the Neurosurgical Society of Australasia* 12:416-20

31. Nafe R, Herminghaus S, Raab P, Wagner S, Pilatus U, et al. 2003. Preoperative proton-MR spectroscopy of gliomas--correlation with quantitative nuclear morphology in surgical specimen. *J Neurooncol* 63:233-45

32. Croteau D, Scarpace L, Hearshen D, Gutierrez J, Fisher JL, et al. 2001. Correlation between magnetic resonance spectroscopy imaging and image-guided biopsies: semiquantitative and qualitative histopathological analyses of patients with untreated glioma. *Neurosurgery* 49:823-9

Chapter 5

Impact of Integrating Whole-Brain Spectroscopic MRI into Radiation Treatment Planning for Glioblastoma

5.1 Author's Contribution and Acknowledgement of Reproduction

The work presented here was conceptualized, organized, researched, and written by the dissertation author. Of the data presented all was collected by the author under the guidance of Dr. Shim, Dr. Shu, and many collaborators. The chapter is reproduced with minor edits from Kandula, S., Cordova, J.S., Gurbani, S.S., Zhong, J., Tejani, M. Kayode, O., Patel, K., Prabhu, R., Schreibmann, E., Crocker, I., Holder, C.A., Shim, H., Shu, H.K.G. Impact of Integrating Whole-Brain Spectroscopic MRI into Radiation Treatment Planning for Glioblastoma (*In preparation for submission to the International Journal of Radiation Oncology*Biology*Physics May* 2016).

5.2 Abstract

Incorporating spectroscopic magnetic resonance imaging (sMRI) for radiation treatment (RT) planning has been challenging due to processing and technical limitations. Here, we evaluate the feasibility of integrating 3D high-resolution, whole-brain sMRI into RT planning for GBM, and determine the degree to which sMRI modifies RT target volumes. Eleven patients with newly-diagnosed GBM obtained sMRI immediately prior to RT. 3D sMRI was acquired using a volumetric spin-echo EPSI sequence and parallel imaging (GRAPPA), with a 32-channel head coil on a 3T (Siemens TRIO/TIM) system, and processed to give whole-brain metabolite maps with 0.1 mL resolution. sMRI maps depicting choline (Cho) to N-acetylaspartate (NAA) ratios were registered to corresponding T1-weighted post-contrast MRI (T1c) for each patient. sMRI-modified target volumes were created based on quantitative assessment of elevated Cho/NAA ratios, and analytically compared to the target volumes defined by conventional MRI sequences. The addition of sMRI data increased the median size of the 60 Gray CTV by 55.3% (range, 19.1-216.1%), 37.8% (range, 9.8-113.1%), and 28.1% (range, 5.9-58.2%) for Cho/NAA thresholds describing 1.5-fold, 1.75-fold, and 2.0-fold increases, respectively. Decreased spatial overlap was noted between the conventional CTVs and sMRI volumes. Of six patients who have experienced recurrence, five exhibited out-of-field recurrences which were covered by sMRI-based plans. Integration of 3D high-resolution whole-brain sMRI into RT planning was feasible, resulted in considerably modified RT target volumes, and predicted post-RT recurrences. Thus, sMRI may serve as an additional treatment planning tool for improving RT target definition for the benefit of GBM patients.

5.3 Introduction

GBM is the most aggressive and common type of adult brain tumor, representing 80% of primary malignant central nervous system tumors (330; 331). Multiple therapeutic advancements and clinical trials have helped formulate the current treatment paradigm for GBM patients: maximal safe resection followed by RT with concurrent and adjuvant TMZ. Nonetheless, median OS is poor at just 14.6 months, indicating that enhanced therapies are necessary (9).

Optimal RT targeting of GBM remains challenging due to its infiltrative nature and poorly defined margins on conventional CT and MRI. Traditionally, two RT target volumes are created on the planning CT simulation: one volume based on abnormalities defined by the enhancing tissue on CE-T1w imaging plus the resection cavity, and another volume defined by the T2w/FLAIR sequence. However, evidence from histological analyses indicates that modern imaging fails to capture the true extent of active disease due to the presence of infiltrative, non-enhancing tumor tissue (229; 233; 332-334). Furthermore, MRI provides limited info on tumor physiology and lacks specificity, often misrepresenting normal brain tissue as tumor (333). This lack of precision in tumor identification and target delineation remains a limiting factor in RT planning for GBM.

Progressive research has led to the development of more sophisticated imaging modalities (molecular and physiologic) to better evaluate tumor pre- and post-treatment (335). Spectroscopic MRI noninvasively characterizes metabolic profiles of brain tissue by detecting resonance frequency shifts in molecules with MRI active nuclei, such as ^{1}H (336). This chemical shift phenomenon results in spectral data which describe a number of small molecules in the brain, some of

which are associated with tumor metabolism. The metabolites associated with tumor tissue include: Cho (a marker of membrane synthesis which is generally elevated in tumor tissue); NAA (a marker of neuronal cell activity/function which is typically decreased in tumor tissue); CR (a marker of cellular energy metabolism and often decreased in tumor tissue); and Lac (a metabolic byproduct of anaerobic glycolysis that is generally seen in regions of necrosis and hypoxia in higher grade tumors) (325; 337).

sMRI techniques have evolved from single to multi-voxel methods, which have permitted improved anatomical coverage, spectral resolution, and data of biochemical transformations. Prior studies have incorporated sMRI as a tool in RT planning (234; 237; 338-340). however poor spatial resolution, partial-brain sMRI coverage, and/or lack of a software platform for reliable multimodality image registration/transfer of data, were notable limitations of such studies. To overcome these limitations, we have developed an imaging pipeline utilizing state-of-the-art, high-resolution (0.1 mL nominal voxel size) spectroscopic imaging and automated analysis tools to allow the addition of whole-brain metabolic maps to intraoperative neuronavigation (193). Herein, we evaluate the feasibility of integrating 3D high-resolution full-brain sMRI into the RT planning process for GBM and determine the degree to which sMRI modifies RT target volumes.

5.4 Methods and Materials

5.4.1 Patients

Following approval by the internal review board, an institutional protocol enrolled patients with newly-diagnosed, pathologically-confirmed GBM (following

resection or biopsy) to receive a sMRI study at three different time points: immediately prior to the start of concurrent chemoradiation therapy, two weeks into chemoradiation, and four weeks after chemoradiation was completed. Eligible patients must also have been ≥ 18 years old with KPS of at least 70, had normal bone marrow, renal, and liver function, and planned to receive the standard of care adjuvant treatment for GBM (RT with concurrent TMZ followed by adjuvant TMZ). Patients with MRI-incompatible implants, medical conditions that compromised RT tolerance, or received investigational agents or enrolled on other protocols (cooperative group or institutional) were excluded. A total of 11 patients enrolled between 7/2014-3/2015.

5.4.2 sMRI data acquisition and registration

Whole-brain sMRI combining 3D-EPSI with parallel imaging was conducted for each patient (TE/TR/FA = 17.6ms/1551ms/71°). A brief optimization of first order shims to a water linewidth of <25 Hz before SMRI-acquisition was completed before acquisition. Internal water signal was collected in concert with metabolite data in an interleaved manner, and was used to normalize the signal from each metabolite. Raw data was then processed using the MIDAS to give metabolite maps with a nominal voxel size of 4.4 mm x 4.4 mm x 5.6 mm (0.108 cm^3) (http://mrir.med.miami.edu:8000/midas). Contrast-enhanced T1w MPRAGE (1 mm^3, TR/TE/FA = 2300/3.4/9°) and T2/FLAIR images (TR/TE/FA = 10,000/121/90°) from the same imaging study were processed and co-registered with the metabolite maps. sMRI data was exported from MIDAS into VelocityAI (Varian Medical Systems) and co-registered to the

pre-treatment CE-T1w images. Metabolite maps were scaled by the mean Cho/NAA ratio obtained from a ROI segmented on normal-appearing white matter in the hemisphere contralateral to the tumor to generate fold-normal (-fold) measures.

5.4.3 Target and sMRI volume definitions

For each patient, CT and MRI treatment volumes were delineated within VelocityAI by a radiation oncologist. The GTV1 was the tumor volume as defined by the MRI T2w FLAIR abnormality. The CTV1 was defined as the GTV1 with a 0.7 centimeter (cm) modified margin. The PTV1 consisted of the CTV1 with a 0.3 cm margin. GTV2 corresponded to an enhancing lesion or resection cavity (defined on the contrast-enhanced T1w MRI), and was expanded by a 0.5 cm modified margin to generate CTV2 to account for microscopic disease. PTV2 consisted of the CTV2 with a 0.3 cm margin to account for set-up uncertainties. PTV1 was prescribed to 51 Gy in 30 fractions (10 patients) or 54 Gy in 30 fractions (1 patient). PTV2 was prescribed to 60 Gy in 30 fractions (simultaneous integrated boost technique) in all patients.

Prior histological studies of HGG tumor samples have indicated that Cho/NAA threshold values ≥ 1.0 can be considered pathologic (325; 329; 341). Based on this data, sMRI-guided target volumes were generated as follows: three Cho/NAA fold values were selected (1.5-fold, 1.75-fold, and 2.0-fold [which correspond to Cho/NAA ratio values of approximately 0.9-1.2]) to generate autosegmented volumes. A radiation oncologist minimally edited these volumes to account for anatomical structures and to remove image artifact. The

autosegmented sMRI-guided contour was merged with the CTV2 to create "sMRI_CTV2" for each threshold value. An additional 0.3 cm margin was added to create the "sMRI_PTV2". For replanning purposes, each sMRI_CTV2 was merged with CTV1 to create sMRI_CTV1, of which an additional 0.3 cm margin was added to generate sMRI_PTV1.

5.4.4 Data Analysis, Re-planning, and Recurrence Evaluation

For each patient, three sets of sMRI contours were exported as DICOM-RT structure sets and imported into Matlab (The Mathworks, Inc.) with co-registered T1w images. All contours were then rasterized into the T1w image space. For each of the three threshold Cho/NAA ratio values, sMRI_CTV2 and CTV2 were compared in terms of absolute volume and spatial overlap (Dice similarity coefficient [DICE]). Additionally, the absolute volume of each sMRI contour that extended beyond the traditional CTV1 and CTV2 was calculated. Additionally, the absolute volume and percentage of the sMRI contour that extended outside of 100% prescription isodose lines (51 Gy or 54 Gy [corresponding to PTV1]), and 60 Gy [PTV2]) were also calculated.

Each set of sMRI-based CTVs and PTVs were transferred to the Eclipse Treatment Planning System (Varian Medical Systems, Palo Alto, CA) for re-planning by medical dosimetrists. This was performed to determine the feasibility of meeting conventional planning objectives with respect to target volume coverage and organ and risk (OAR) RT dose constraints. For treatment planning, the goal was for 100% of the prescription dose to cover 95% of the respective target volume, while limiting the maximum dose to the brainstem, optic chiasm, and

optic nerves to less than 54 Gy. A maximum point dose of 60 Gy to the brainstem and 90% coverage of the PTV60 was allowable in cases in which the two structures were in close proximity.

Follow-up imaging was assessed to determine and compare whether recurrent tumor was encompassed by the original and/or sMRI-modified target volumes. Follow-up MRI scans were evaluated by radiation oncologists and neuroradiologists for evidence of tumor progression following the RANO criteria (67). In patients with evidence of radiographic disease progression, the MRI at the time of tumor recurrence or progression was co-registered with the treatment planning CT, and location of recurrence was compared among the conventional and sMRI-guided treatment plans.

5.5 Results

Table 5.1 displays patient and tumor characteristics. Whole-brain 3D sMRI was successfully obtained in all 11 patients. Data was processed in MIDAS and exported into VelocityAI in which co-registration with the pre-treatment T1w MRI sequences was performed. See **Figure 5.1** for a representation of the methodology workflow.

Patient	Age	Tumor location	Brain Volume (cm^3)
1	63	Right frontal	1427
2	61	Left parieto-occipital	1534
3	55	Right frontal	1427
4	56	Right temporal	1391
5	45	Right parietal	1665
6	82	Right temporo-parietal	1223
7	43	Left temporal	1417
8	60	Right temporo-parietal	1470
9	45	Left temporal	1425
10	71	Left temporal	1409
11	40	Left occipital	1517

Table 5.1. sMRI-RT patient characteristics.

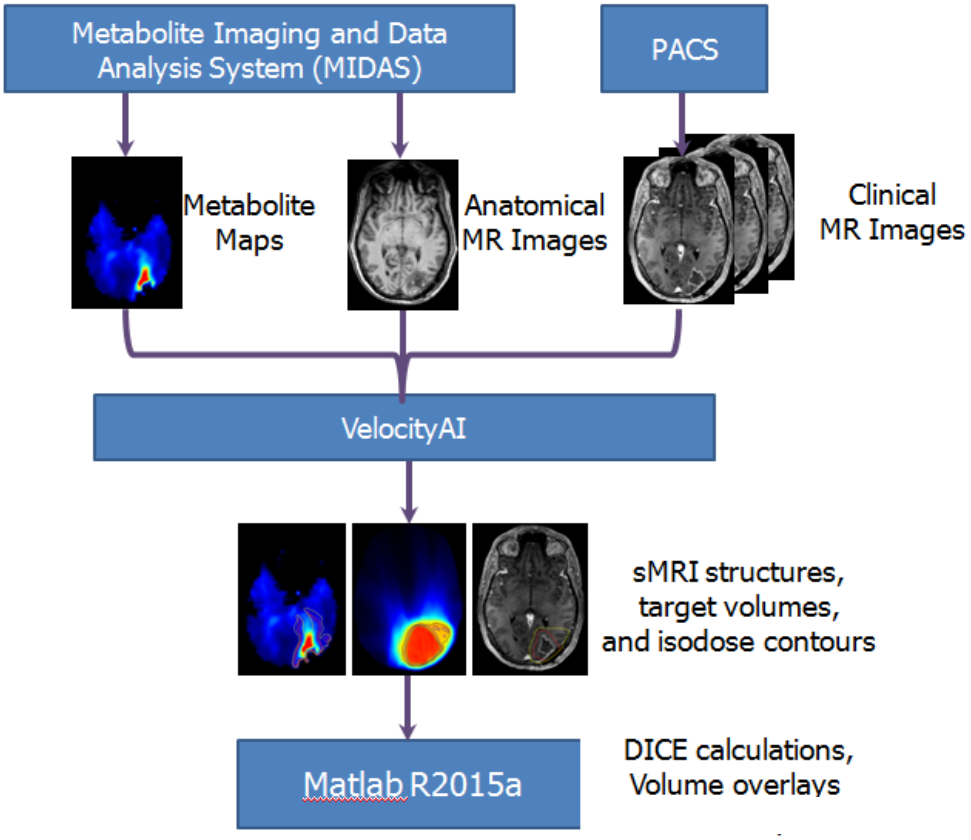

Figure 5.1. Image processing and analysis pipeline. Spectral processing in MIDAS includes signal normalization, tissue segmentation, quality evaluation, etc. Anatomical and metabolite maps are co-registered in MIDAS as well. Contrast-enhanced and T2/FLAIR images used for target planning were exported from PACS. Anatomical, metabolite, and clinical images were then imported into VelocityAI for co-registration and RT volume contouring. Normal contralateral white matter was contoured at baseline for determining fold changes in tumor metabolite levels. Contours depicting normalized metabolite changes were overlaid onto clinical images to assist in target delineation. RT structures generated in VelocityAI (GTV, CTV, Cho/NAA contours, etc.) were imported into Matlab to quantitatively evaluate spatial overlap and volume differences between conventional target volumes and those generated with sMRI maps.

5.5.1 Volumetric and Spatial Analysis

The incorporation of sMRI data into RT planning resulted in larger CTV volumes (**Table 5.2**). The median percentage increase in the sMRI_CTV2 (60 Gy prescription volume) was 55.3% (19.1-216.1%), 37.8% (range, 9.8-113.1%), and 28.1% (5.9-58.2%) for Cho/NAA threshold values of 1.5-fold, 1.75-fold, and 2.0-fold, respectively. sMRI_CTV1 also increased, but to a smaller extent (median increase of 3.8% [range, 1.4-70.8%], 2.4% [0.8-35.7%], and 1.7% [range, 0.7-18.5%] with Cho/NAA values of 1.5-fold, 1.75-fold, and 2.0-fold, respectively). Decreased spatial overlap, as demonstrated by lower DICE values, was noted between the CTVs and segmented sMRI volumes. Median DICE scores for CTV2 were 0.51 (range, 0.21-0.75), 0.55 (range, 0.26-0.79), and 0.51 (range, 0.31-0.79) for Cho/NAA values of 1.5, 1.75, and 2.0, respectively. See **Figure 5.2 and Figure 5.3** for representative case examples.

	Patient	CTV1 (cm^3)	sMRI CTV1 (cm^3)	% diff	DICE	CTV2 (cm^3)	sMRI CTV2 (cm^3)	% diff	DICE
Cho/ NAA 1.5-fold	1	276.5	287.0	3.8	0.60	95.7	148.5	55.3	0.67
	2	298.3	306.5	2.7	0.53	93.1	153.6	70.0	0.54
	3	187.2	247.1	32.0	0.62	90.9	191.7	111	0.50
	4	289.7	295.1	1.86	0.34	103.8	123.6	19.1	0.50
	5	415.7	449.6	8.2	0.47	148.6	219.7	47.8	0.58
	6	417.2	462.9	11.0	0.29	91.4	127.1	39.0	0.45
	7	178.7	184.9	3.5	0.42	43.3	72.8	68.2	0.51
	8	343.9	349.0	1.5	0.53	90.3	134.9	49.3	0.75
	9	347.1	352.1	1.4	0.37	88.1	123.2	39.8	0.55
	10	138.5	163.4	18.0	0.46	44.9	89.4	99.1	0.32
	11	111.1	189.8	70.8	0.38	45.6	144.2	216	0.21
	Median	289.7	295.1	3.8	0.46	90.9	134.9	55.3	0.51
Cho/ NAA 1.75-fold	1	276.5	283.0	2.4	0.53	95.7	131.9	37.8	0.69
	2	298.3	302.3	1.3	0.44	93.1	132.0	41.7	0.55
	3	187.2	216.4	15.6	0.62	90.9	153.1	68.5	0.57
	4	289.7	294.3	1.6	0.28	103.8	114.0	9.8	0.50
	5	415.7	432.9	4.1	0.41	148.6	186.2	25.3	0.62
	6	417.2	462.8	10.9	0.19	91.4	108.0	18.1	0.41
	7	178.7	183.0	2.4	0.35	43.3	63.5	46.7	0.52
	8	343.9	347.7	1.1	0.45	90.3	115.5	27.8	0.79
	9	347.1	350.0	0.8	0.29	88.1	106.1	20.4	0.56
	10	138.5	153.5	10.8	0.36	44.9	69.5	54.7	0.34
	11	111.1	150.8	35.7	0.34	45.6	97.2	113	0.26
	Median	289.7	294.3	2.4	0.36	90.9	114.0	37.8	0.55
Cho/ NAA 2.0-fold	1	276.5	281.3	1.7	0.48	95.7	122.5	28.1	0.68
	2	298.3	300.5	0.7	0.38	93.1	120.0	28.7	0.54
	3	187.2	202.8	8.3	0.57	90.9	128.9	41.9	0.60
	4	289.7	293.7	1.4	0.23	103.8	109.9	5.9	0.46
	5	415.7	425.1	2.3	0.35	148.6	167.4	12.7	0.62
	6	417.2	462.8	10.9	0.14	91.4	100.9	10.3	0.34
	7	178.7	181.6	1.6	0.30	43.3	57.3	32.4	0.51
	8	343.9	346.3	0.7	0.39	90.3	105.1	16.4	0.79
	9	347.1	349.6	0.7	0.20	88.1	96.0	8.9	0.50
	10	138.5	150.1	8.4	0.27	44.9	59.6	32.6	0.31
	11	111.1	131.7	18.5	0.29	45.6	72.2	58.2	0.31
	Median	289.7	293.7	1.7	0.3	90.9	10.1	28.1	0.51

Table 5.2. Volumetric and spatial data. Abbreviations: CTV –based on CT and MRI findings; sMRI_CTV – union of sMRI contour and CTV; DICE - Dice similarity coefficient between sMRI contour alone and respective CTV1 or CTV2.

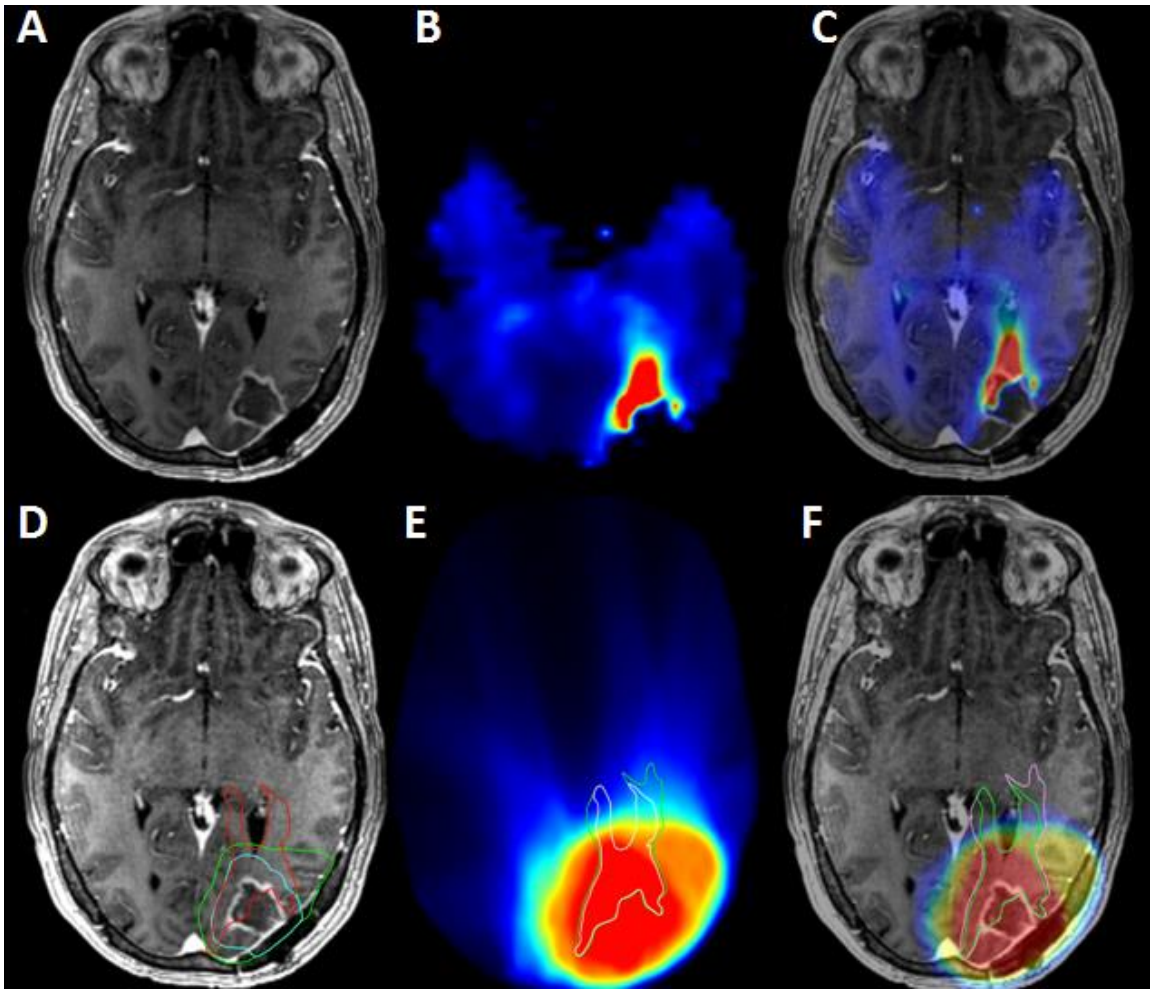

Figure 5.2. Co-registered CE-T1w MRI and Cho/NAA images of 40-year-old male with occipital GBM who received RT. A visible Cho/NAA abnormality extend beyond the contrast-enhancing border, passing along white matter tracks towards the posterior horn of the left lateral ventricle (**A-C**). A region of Cho/NAA greater than or equal to a 2-fold increase above normal falls well outside the CTV2 (turquoise contour) and CTV1 (green contour) (**D**). An overlay of the cumulative RT dose on the anatomical image with 2-fold (green contour) and 1.75-fold (pink contour) Cho/NAA changes shows that a substantial portion of metabolic abnormality falls outside of the regions receiving the highest dose (**E** and **F**).

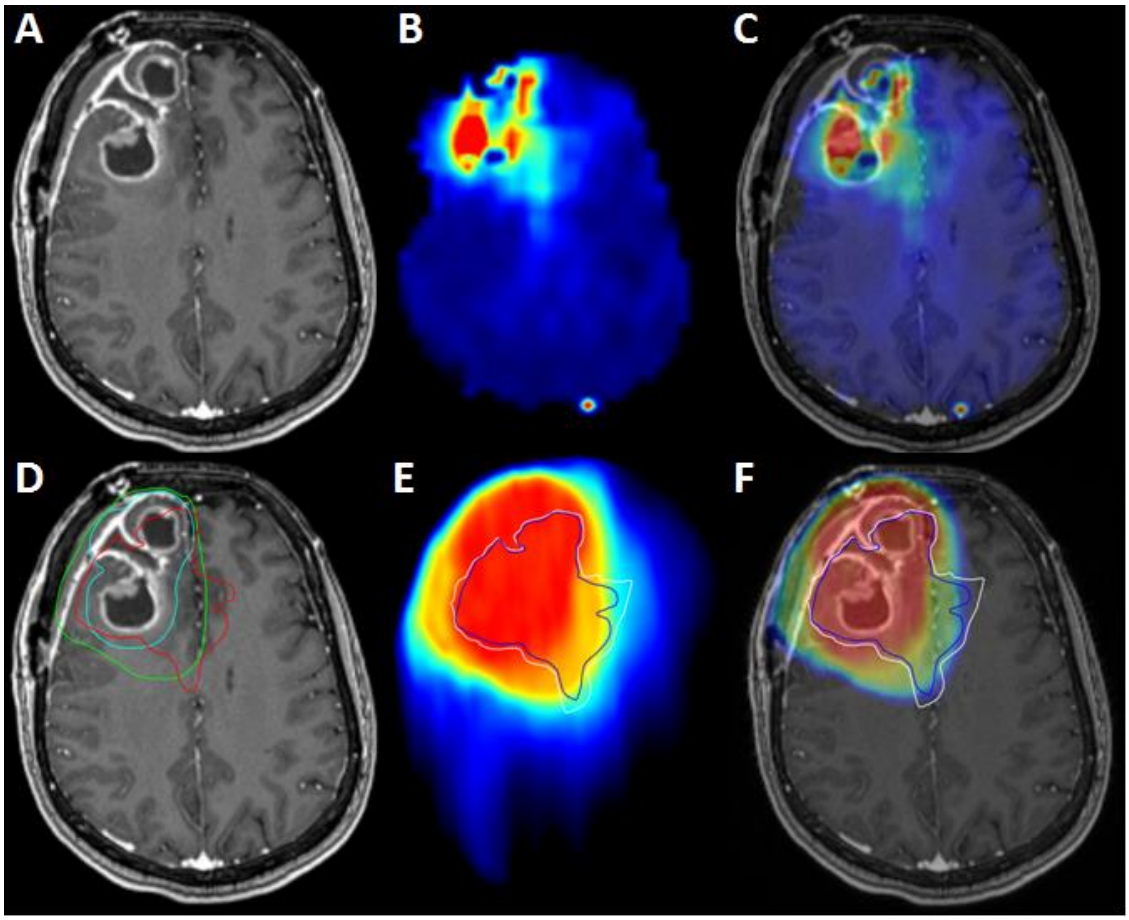

Figure 5.3. Co-registered CE-T1w MRI and Cho/NAA images of 56-year-old female with frontal GBM who received chemoradiation. Cho/NAA abnormalities extend medially and posteriorly beyond contrast-enhancement (**A-C**). A region of Cho/NAA greater than or equal to a 2-fold increase above normal falls well outside the CTV2 (turquoise contour) and CTV1 (green contour) (**D**). An overlay of the cumulative RT dose on the anatomical image with 2-fold (blue contour) and 1.75-fold (white contour) Cho/NAA changes shows that a substantial portion of metabolic abnormality falls outside of the regions receiving the highest dose (**E** and **F**).

Table 5.3 displays the respective volumes and percentages of each sMRI structure extending outside of the prescription isodoses. The median absolute sMRI volume extending outside of the 100% IDL of PTV1 and PTV2 were 3.5 and 36.4, 2.1 and 18, and 0.9 and 10.2 for Cho/NAA values of 1.5-fold, 1.75-fold, and 2.0-fold, respectively. See **Figure 5.2D-F** and **Figure 5.3D-F** for representative case examples. **Figure 5.4** demonstrates the associated boxplots reflecting the percentage of the respective sMRI structure volume extending outside of the RT prescription isodoses.

5.5.2 Replanning

RT plans incorporating the sMRI-modified PTVs were replanned to assess the feasibility of meeting planning objectives and determining plan acceptability. For all plans, the planning goal was for 100% of the prescription dose to cover 95% of the respective target volume, while limiting the maximum dose to the brainstem, optic chiasm, and optic nerves to less than 54 Gy. A maximum point dose of 60 Gy to the brainstem was a hard constraint. **Table 5.4** details target coverage and brainstem maximum dose for each patient. Despite considerably larger target volumes with MRSI data, replanning was successful and deemed acceptable for all patients with incorporation of all Cho/NAA levels. Of the 11 patients, only two patients' revised plans did not closely meet desired target coverage parameters (for PTV2[60 Gy]) due to brainstem proximity and respect for threshold tolerance. However, PTV2 coverage in the original plan was also not achieved in these cases. In two patient cases, the max brainstem dose increased from 7 and 13 Gy to 58 and 59 Gy, respectively as a result of the larger targets. In all plans, the maximum doses to the optic nerves and chiasm met specified constraints.

	Patient	Volume 100% PTV1 IDL (cm^3)	% outside 100% IDL PTV1	Volume 100% PTV2 IDL (cm^3)	% outside 100% IDL PTV2
Cho/NAA 1.5-fold	1	2.8	2.2	36.5	28.4
	2	4.6	4.0	45.5	38.9
	3	39.9	24.2	81.5	49.6
	4	0.4	0.7	20.4	33.3
	5	10.5	6.5	49.2	30.5
	6	0.0	0.0	36.4	50.1
	7	3.5	6.4	15.3	28.1
	8	0.1	0.1	16.4	13.0
	9	1.2	1.5	25.9	31.6
	10	9.1	14.8	34.8	56.7
	11	64.1	55.7	90.1	78.2
Cho/NAA 1.75-fold	1	1.5	1.5	24.5	23.0
	2	2.2	2.5	28.5	31.8
	3	15.9	12.9	45.3	36.7
	4	0.1	0.3	12.6	26.3
	5	3.2	2.7	22.1	18.3
	6	0	0	17.5	39.4
	7	2.1	4.9	9.5	22.2
	8	0.1	0.1	7.5	7.5
	9	0.4	0.7	13.6	22.8
	10	3.0	7.7	18.0	46.6
	11	30.5	46.0	45.5	68.4
Cho/NAA −2.0-fold	1	1.0	1.1	17.2	19.1
	2	0.9	0.9	19.8	27.6
	3	6.8	6.8	25.6	27.5
	4	0.03	0.03	8.9	23.0
	5	0.6	0.6	9.0	9.5
	6	0	0	10.2	33.6
	7	1.2	3.4	6.0	17.9
	8	0.01	0.02	4.0	4.7
	9	0.03	0.07	6.2	15.7
	10	1.5	5.8	10.5	40.9
	11	14.0	35.1	22.1	55.4

Table 5.3. Autosegmented sMRI contour extending outside of prescription isodoses. Abbreviations: IDL – isodose line; PTV1 – planning target volume 1 (corresponding to PTV51 or PTV54); PTV2 – planning target volume 2 (corresponding to PTV60).

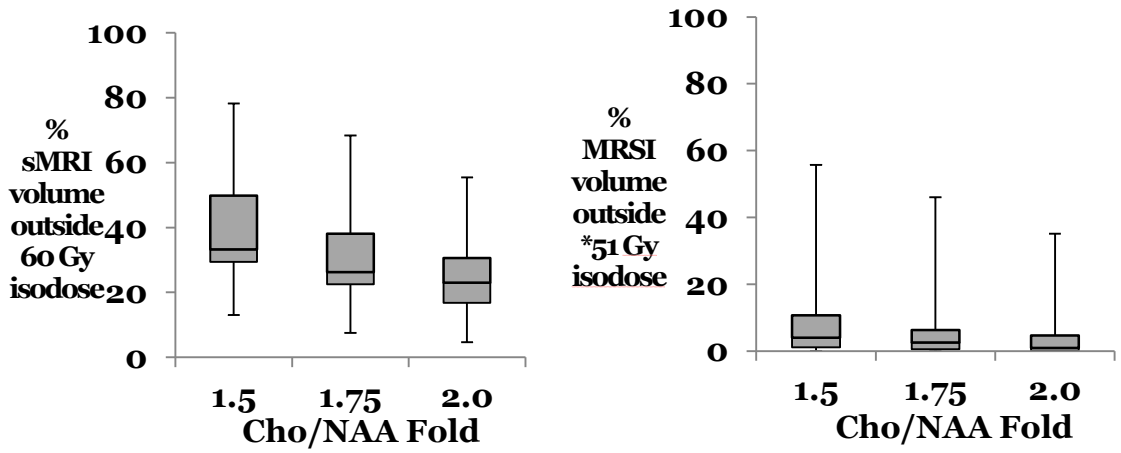

Figure 5.3. Boxplots reflecting the percentage of the sMRI structure volume extending outside of the RT prescription isodoses. *54 Gy in 1 patient

	Patient	1	2	3	4	5	6	7	8	9	10	11
Target Volume coverage of PTV1 by 54 Gy (%)	Conv PTV1	98.0	98.5	100	99.9	99.5	94.6	97.9	99.9	97.5	98.8	99.9
	sMRI-PTV1 (1.50-fold)	99.5	99.9	100	99.9	100	98.7	99.1	99.4	98.3	100	99.9
	sMRI-PTV1 (1.75-fold)	99.9	100	100	99.9	99.9	98.7	99.1	96.7	98.1	100	99.9
	sMRI-PTV1 (2.0-fold)	99.9	100.0	100	99.9	99.7	97.8	98.8	99.2	99.1	99.7	99.9
Target Volume coverage of PTV2 by 60 Gy (%)	Conv PTV1	98.0	96.8	97.9	86.2	98.9	96.5	98.9	98.7	89.5	99.9	99.4
	sMRI-PTV1 (1.50-fold)	91.0	93.5	95.5	83.0	94.7	94.5	95.0	94.6	80.0	95.0	95.0
	sMRI-PTV1 (1.75-fold)	95.0	94.9	95.0	84.0	95.4	94.3	95.0	95.0	85.1	95.1	94.1
	sMRI-PTV1 (2.0-fold)	96.0	95.0	95.0	86.0	95.9	94.0	95.0	94.9	91.3	95.5	94.8
Brainstem Max Dose (Gy)	Conv PTV1	53.5	55.0	13.0	59.3	52.8	53.9	59.4	58.3	58.0	52.9	7.3
	sMRI-PTV1 (1.50-fold)	58.9	59.9	59.8	57.9	57.8	59.4	58.7	59.6	58.3	58.8	58.0
	sMRI-PTV1 (1.75-fold)	58.7	58.8	58.1	58.9	58.1	59.2	59.0	59.4	59.2	58.4	58.4
	sMRI-PTV1 (2.0-fold)	58.7	59.2	55.4	58.2	57.8	58.7	58.6	58.9	59.3	58.7	58.2

Table 5.4. Comparison of Target Coverage and Brainstem Doses. Abbreviations: PTV1 – planning target volume 1 (corresponding to PTV51 or PTV54); PTV2 – planning target volume 2 (corresponding to PTV60); Gy –Gray; Conv – conventional.

5.5.3 Preliminary Recurrence analysis

Of the 11 patients, six have experienced recurrent disease with a median time to recurrence of 3.1 months from the completion of RT. Preliminary analysis suggests that in five of the six cases of recurrence, the expanded MRSI-guided target volumes encompassed regions of tumor recurrence which were not originally covered by the standard target volumes.

5.6 Discussion

Our report demonstrates that 3D high-resolution whole-brain sMRI can be effectively integrated into RT planning to serve as an additional tool for improving RT target definition in GBM patients. sMRI has previously been integrated in RT planning, however these reports acknowledged limitations of low spatial resolution and lack of robust multimodality image registration/transfer of data (233; 234; 237; 338-340; 342). Moreover, the most recent of these analyses was the only one in which whole-brain volumetric 3D sMRI was utilized (340). In this study, data for 19 GBM patients using volumetric acquisition resulted in sMRI coverage of the brain between 70-76%. Field of view was 280 x 280 x 180 mm^3 and 64 x 64 x 32 voxels with effective voxel size of approximately 1.0 mL. In comparison, the resolution of our data set was finer with nominal voxel size of 4.4 x 4.4 x 5.6 mm^3 (0.108 mL). This helps surmount the partial volume effects often seen with lower resolution sequences. Therefore, the higher resolution affords increased fidelity in the sMRI data.

The incorporation of sMRI data considerably modified conventionally-delineated RT target volumes. Even at the higher threshold Cho/NAA abnormality

(2.0-fold), sMRI_CTV2 (CTV60) volumes increased by a median of 28% and up to 58%. DICE scores were as low as 0.31, suggesting significant spatial discrepancy between the sMRI abnormality and the conventional target volume. Moreover, an appreciable portion of the sMRI volume extended outside of the 60 Gy prescription isodose in nearly all patients (**Table 5.3** and **Figure 5.3**). This indicates that metabolically active disease may be unaccounted for by conventional MRI, and consequently, not receive appropriate RT coverage. Similar results were noted in a 2003 report (234), in which the authors found that metabolic activity (defined by spectroscopy) extended beyond the contrast enhancement in 19/30 patients with HGG, averaging 21 cm^3 and extending 8–33 mm beyond the contrast enhancement. A more recent study from 2014 demonstrated that approximately one-third of patients had metabolically active tumor outside of CTV60 (340). Furthermore, in some cases, the 51 or 54 Gy prescription isodose (representing coverage of edema and microscopic disease based on standard MRI) did not encompass the sMRI abnormality.

The sMRI-modified target volumes were re-planned successfully, further supporting the feasibility of incorporating the data into the treatment planning process. In our study, the same target doses and margins (as originally delivered) were utilized in re-planning. Nonetheless, there are many implications of utilizing sMRI data with respect to customizing RT dosing and margins. More precise, high resolution data may enable selective dose escalation and account for tumor heterogeneity based on metabolite levels. Recently, partial brain 3D sMRI [with voxel resolution of 6.25×6.25×25.0 mm^3 (1.0 mL)] was incorporated for GBM dose painting to guide simultaneous integrated boost (SIB) to 72 Gy based on

spectroscopic abnormalities (339). Clinical trials investigating this approach are currently in their early stages (ClinicalTrials.gov NCT01507506 and NCT02394665). Another possible ramification relates to utilizing sMRI data to more selectively define target volume margins. Current protocols commonly require 2 cm margins from GTV to CTV, which can result in irradiation of substantial volumes of normal brain tissue. With sMRI aiding in the definition of metabolically active disease, margins can be optimally designed and objectively minimized to reduce neurotoxicity even with dose escalation.

Fundamentally, the addition of sMRI in treatment planning should help prevent tumor recurrence and translate into improvements in survival and quality of life of GBM patients. Preliminary recurrence analysis suggests that sMRI abnormality at pre-RT encompasses post-RT recurrences, as the sMRI-modified target volumes contained regions of tumor recurrence which were not originally covered by the standard target volumes. Similarly, Pirzkall et al. found a correspondence between areas of new contrast enhancement and the initial spectroscopic abnormalities in 8 of 10 non–contrast-enhancing patients (234). Additionally, they found that the choline-to-N-acetyl-aspartate index volumes correlated inversely with the time to onset of new contrast enhancement. We intend to continue analyzing recurrence patterns in these patients to help further validate and define the role of sMRI in RT planning and recurrence prediction.

5.6.1 Study Strengths and Limitations

Several strengths and weaknesses of this study warrant consideration. High resolution scans, quality methodology, and logical processing of sMRI data were

seamlessly executed within the framework of the RT planning process. Notwithstanding, the resolution and processing of our sMRI scans could be further improved. Though the study was retrospective, consisted of a small sample size, and served primarily as a feasibility analysis, it yielded provocative volumetric and recurrence data which necessitate more evaluation. In our study, we examined multiple Cho/NAA fold levels, but the optimal cutoff for use in planning requires further elucidation by the evaluating finer Cho/NAA intervals. A pathognomonic Cho/NAA signature(s) is necessary to help standardize sMRI data utilization.

5.6.2 Conclusions

In conclusion, integration of 3D high-resolution whole-brain sMRI into RT planning is feasible, resulted in considerably modified RT target volumes, and predicted post-RT recurrences. sMRI may serve as an additional treatment planning tool for improving RT target definition for the benefit of GBM patients.

5.7 References

1. Ostrom QT, Bauchet L, Davis FG, Deltour I, Fisher JL, et al. 2014. The epidemiology of glioma in adults: a "state of the science" review. *Neuro-oncology* 16:896-913
2. Schwartzbaum JA, Fisher JL, Aldape KD, Wrensch M. 2006. Epidemiology and molecular pathology of glioma. *Nat Clin Pract Neurol* 2:494-503; quiz 1 p following 16
3. Stupp R, Mason WP, van den Bent MJ, Weller M, Fisher B, et al. 2005. Radiotherapy plus concomitant and adjuvant temozolomide for glioblastoma. *The New England journal of medicine* 352:987-96
4. Burger PC, Dubois PJ, Schold SC, Jr., Smith KR, Jr., Odom GL, et al. 1983. Computerized tomographic and pathologic studies of the untreated, quiescent, and recurrent glioblastoma multiforme. *J Neurosurg* 58:159-69
5. McKnight TR, von dem Bussche MH, Vigneron DB, Lu Y, Berger MS, et al. 2002. Histopathological validation of a three-dimensional magnetic resonance spectroscopy index as a predictor of tumor presence. *Journal of neurosurgery* 97:794-802
6. Narayana A, Chang J, Thakur S, Huang W, Karimi S, et al. 2007. Use of MR spectroscopy and functional imaging in the treatment planning of gliomas. *Br J Radiol* 80:347-54
7. Farace P, Giri MG, Meliado G, Amelio D, Widesott L, et al. 2011. Clinical target volume delineation in glioblastomas: pre-operative versus post-operative/pre-radiotherapy MRI. *Br J Radiol* 84:271-8

8. Burger PC, Heinz ER, Shibata T, Kleihues P. 1988. Topographic anatomy and CT correlations in the untreated glioblastoma multiforme. *J Neurosurg* 68:698-704

9. Cao Y, Sundgren PC, Tsien CI, Chenevert TT, Junck L. 2006. Physiologic and metabolic magnetic resonance imaging in gliomas. *J Clin Oncol* 24:1228-35

10. Nelson SJ. 2003. Multivoxel magnetic resonance spectroscopy of brain tumors. *Mol Cancer Ther* 2:497-507

11. McKnight TR, Lamborn KR, Love TD, Berger MS, Chang S, et al. 2007. Correlation of magnetic resonance spectroscopic and growth characteristics within Grades II and III gliomas. *J Neurosurg* 106:660-6

12. Guo J, Yao C, Chen H, Zhuang D, Tang W, et al. 2012. The relationship between Cho/NAA and glioma metabolism: implementation for margin delineation of cerebral gliomas. *Acta neurochirurgica* 154:1361-70; discussion 70

13. Nelson SJ, Graves E, Pirzkall A, Li X, Antiniw Chan A, et al. 2002. In vivo molecular imaging for planning radiation therapy of gliomas: an application of 1H MRSI. *J Magn Reson Imaging* 16:464-76

14. Einstein DB, Wessels B, Bangert B, Fu P, Nelson AD, et al. 2012. Phase II trial of radiosurgery to magnetic resonance spectroscopy-defined high-risk tumor volumes in patients with glioblastoma multiforme. *Int J Radiat Oncol Biol Phys* 84:668-74

15. Pirzkall A, Li X, Oh J, Chang S, Berger MS, et al. 2004. 3D MRSI for resected high-grade gliomas before RT: tumor extent according to metabolic activity in relation to MRI. *Int J Radiat Oncol Biol Phys* 59:126-37

16. Ken S, Vieillevigne L, Franceries X, Simon L, Supper C, et al. 2013. Integration method of 3D MR spectroscopy into treatment planning system for glioblastoma IMRT dose painting with integrated simultaneous boost. *Radiat Oncol* 8:1

17. Parra NA, Maudsley AA, Gupta RK, Ishkanian F, Huang K, et al. 2014. Volumetric spectroscopic imaging of glioblastoma multiforme radiation treatment volumes. *Int J Radiat Oncol Biol Phys* 90:376-84

18. Maudsley AA, Domenig C, Govind V, Darkazanli A, Studholme C, et al. 2009. Mapping of brain metabolite distributions by volumetric proton MR spectroscopic imaging (MRSI). *Magnetic resonance in medicine* 61:548-59

19. Widhalm G, Krssak M, Minchev G, Wohrer A, Traub-Weidinger T, et al. 2011. Value of 1H-magnetic resonance spectroscopy chemical shift imaging for detection of anaplastic foci in diffusely infiltrating gliomas with non-significant contrast-enhancement. *J Neurol Neurosurg Psychiatry* 82:512-20

20. Croteau D, Scarpace L, Hearshen D, Gutierrez J, Fisher JL, et al. 2001. Correlation between magnetic resonance spectroscopy imaging and image-guided biopsies: semiquantitative and qualitative histopathological analyses of patients with untreated glioma. *Neurosurgery* 49:823-9

21. Wen PY, Macdonald DR, Reardon DA, Cloughesy TF, Sorensen AG, et al. 2010. Updated response assessment criteria for high-grade gliomas:

response assessment in neuro-oncology working group. *J Clin Oncol* 28:1963-72

22. Chang J, Thakur SB, Huang W, Narayana A. 2008. Magnetic resonance spectroscopy imaging (MRSI) and brain functional magnetic resonance imaging (fMRI) for radiotherapy treatment planning of glioma. *Technol Cancer Res Treat* 7:349-62

Chapter 6

General Discussion and Future Directions

6.1 General Discussion

Molecular imaging has made substantial impacts on disease in every major organ system and is playing an increasingly important role in patient care, medical research, and drug design. By developing and utilizing the vast array of molecular imaging techniques available, scientists and physicians are not only gaining a greater understanding of the biological processes underlying disease but also learning how to manipulate those critical processes that give rise to pathological states. This is especially true in cancer, where a myriad of normal cellular processes are altered, and sometimes interact a complementary manner, to generate overt disease. In no solid tumor known is the biological diversity so great and is there a population in such need of advancement of new, effective therapeutic options than in glioma, especially GBM. As such, this work lies at the interface of molecular imaging, MR imaging, and image analysis as it attempts to exploit the unique

information acquired from each to gain understanding of GBM biology and to integrate each part into a cohesive whole for the advancement of GBM therapy.

FGS with 5-ALA and sMRI are two vastly different techniques in terms of physics and biology, yet they can be used in a way to provide complementary information for the management of gliomas. While the former relies on electronic transitions in a large, highly conjugated molecule and the latter relies on the nuclear spin in small molecules, both describe the proliferative capacity of tissues at the molecular level. While FGS exploits specific aberrations of a single pathway within glioma cells and sMRI describes a myriad of metabolites linked to a number of molecular cascades, both define tissue regions that never seen before and describe regions of potential recurrence. The advent of FGS fundamentally changed the way that neurosurgical oncologists approach glioma resection. Similarly, the use of sMRI for preoperative planning and RT targeting represents a paradigm shift in the field of image-guided glioma therapy; one away from targeting surrogate markers using tracer-based imaging techniques to targeting abnormal tissue regions by measuring endogenous biological processes. Together with the right analytical and computational techniques, these techniques have the potential to not only expand our understanding of the molecular phenomena central to gliomagenesis and recurrence, but to also slow recurrence and extend the survival for patients with the disease.

This work starts with the development and utilization of a bioinformatics-based imaging analysis technique for evaluating molecular and MR imaging methods. In **Chapter 2** a clustering method generally used in genomics was adapted for the grouping of MRI voxels to evaluate its use as an image

segmentation method. A validation procedure showed that, indeed, such a method would be equally as accurate as manual segmentations, though in much less time and with less variability. In **Chapter 3**, this segmentation method is applied to a cohort of patients receiving GBM resection using the first molecular imaging technique described, 5-ALA FGS. Using this objective image analysis technique, we presented data that support the previous claims by Stummer et al. and others that the more complete resection achieved with 5-ALA FGS can increase survival in patients with GBM (49-51; 170). Moreover, using the morphological tumor features alongside resection and survival outcomes, we were able to show strong associations between tumor structure, resection outcomes, and survival outcomes. It is our understanding that this piece of information is novel, having never been shown with an automated segmentation method before. Since **Chapter 3**, two papers have substantiated our claims by showing significant relationships between survival and tumor features similar to those defined in this work using automated and manual segmentation techniques (343; 344). Interestingly the authors of Yang et al., were also able to show that certain features were also predictive of the molecular subtype (i.e. mesenchymal, neural, proneural) observed for each tumor (344).

In **Chapter 4**, we outlined the procedure for combining 5-ALA with sMRI and validated the capacity of sMRI for identifying normal brain matter infiltrated with glioma cells. Although spectroscopy-histology studies have been completed in the past, **Chapter 4** describes not only the validation of the highest resolution, whole-brain sMRI maps to date, but also the first study to do so by combining *ex vivo* fluorescence and automated histological analysis (230; 319; 327-329). All

other studies compare findings from low resolution MRS images (~1 cm^3) with qualitative or semi-quantitative metrics of tumor cell density or proliferation. Moreover, the identification of SOX2-positive cells in Cho/NAA abnormal tissue outside of T2w/FLAIR hyperintense regions parallels similar results from a recent study in LGG (345). Furthermore, we set forth evidence that Cho/NAA abnormalities may be able to identify regions that are at high risk for recurrence following therapy in regions that may appear normal on conventional MRI. By using a whole-brain method, we show this is even true for recurrence sites contralateral to the original tumor. This is novel and of great significance as clinically-available MRS protocols have a restricted coverage and generally miss large portions of contralateral brain.

On a separate note, using the protocol outline in **Chapter 5**, integrating sMRI into the presurgical workup of patients with HGG that are receiving 5-ALA FGS is quite easy and would likely guide surgeons to regions of infiltration not apparent on conventional MRI. As the study in Chapter 3 suggested the presence of residual tumor increase the likelihood of death, extending the resection to these regions may result in better survival outcomes. However, the power of this preoperative-intraoperative molecular imaging combination lies not only in the ability to identify these infiltrated regions, but to confirm the presence of infiltrating cells in real-time using intraoperative fluorescence. The combination of two quantitative imaging modalities suggesting the presence of tumor cells will likely give the surgeon more confidence in furthering tumor resection in these areas if such an expansion is viewed as safe. If this type of combination becomes more common, it is foreseeable that more molecular imaging information,

potentially that from PET imaging or infrared dye fluorescence, could be added to this protocol resulting in an even more accurate method for identifying the distribution of tumor cells in normal brain tissue (346).

In **Chapter 5**, the semi-automatic delineation of target volumes based on whole-brain sMRI was evaluated for planning RT. Spectroscopy has been used to plan RT in previous studies; however, only one other has used whole-brain volumetric 3D MRSI making this study the second of its kind (227; 235; 347; 348). Just as in recurrence prediction, full coverage of the brain and tumor regions is essential for spectroscopic findings to have an impact on RT planning. The manual placement of an FOV before MRS acquisition, like that pictured in **Figure 1.25**, not only leads to incomplete tumor and normal tissue characterization but also introduces an amount of selection bias into data acquisition (340). Using sMRI, we avoid these limitations thereby enabling better sampling of all tissue regions without selection bias and with better visualization of the metabolically active tumor throughout the brain. The greater accuracy afforded by sMRI may allow the generation of new dosage volumes based on the presence of unique molecular make up of existing RT targets. This would represent the development of new RT target volumes based on molecular phenotype. Such an addition of whole-brain metabolic information into RT planning may lead to the development of innovative RT treatment strategies personalized to the metabolic profile of each patient's tumor.

Although volumetric spectroscopic imaging methods are not uniformly available in the clinical setting currently, there are many implications of utilizing sMRI data with respect to customizing RT dosing and margins in current clinical

trials. For example, the increased precision afforded by high resolution data may enable selective dose escalation by accounting for tumor heterogeneity based on metabolite levels. Recently, partial brain 3D MRSI [with a low voxel resolution of ~1 cm^3] was incorporated for GBM dose painting to guide RT boosts to 72 Gy based on spectroscopic abnormalities (339), and other trials investigating similar approaches with low resolution data are currently in their early stages (ClinicalTrials.gov NCT01507506 and NCT02394665). Thus, the addition of our precise, high resolution technique may add additional information to the trials. Such precise mapping may be most interesting when coupled with dose escalation using proton-based RT therapy; a technique known to have a highly controllable energy deposition profile (349). Another possible ramification relates to utilizing sMRI data to more selectively define volume margins. Current protocols commonly require the addition of uniform 2 cm margins from GTV to resulting in irradiation of substantial volumes of normal brain tissue. With sMRI aiding in the definition of metabolically active disease, margins can be optimally designed to encompass metabolic abnormalities and reduce potential neurotoxicity even in the presence of dose escalation.

A potential shortcoming for all the projects described in this work, particularly those describing patient outcomes or using tissue specimens, is the limited sample size. This is a shortcoming common to pilot clinical studies; however, that is difficult to control. Even given the limited samples in each of the studies, the sample size was high enough and the analytical tools sensitive enough to give meaningful and interesting results. Ideally, the studies presented in **Chapters 3**, **4**, and **5** would be reproduced in clinical trials with larger enrollment.

As such, clinical trials are currently being proposed or revised with aims similar to those in each of these chapters to allow more definitive conclusions to be made. Image quality is also a particular concern in those studies that utilized sMRI. Though the imaging and processing procedures used attempt to limit spectral artifact, it is possible that spectral abnormalities could have altered the data without our knowing. Because of this, we are currently developing more robust methods to filter spectroscopic data in the hopes of preventing this in future studies. A more detailed description of this spectral quality work can be found in **6.2.2**.

In conclusion, the culmination of the work presented in this dissertation has demonstrated the molecular imaging techniques, more specifically 5-ALA FGS and sMRI, add value to the management of patients with GBM and should be studied further in larger clinical trials. Moreover, the developed methodologies in this work are also expected to be useful for other applications and tumor types. The segmentation method in **Chapter 2** could assist in measuring the growth of contrast-enhancing tumor for response determination while sMRI could potentially be used to differentiate brain tumors of cellular origins (i.e. oligodendroglioma vs astrocytoma). Although this dissertation focused on GBM, the principles, approaches, and use of the molecular imaging techniques therein can be applied to other brain tumors as the technologies are directed at the biochemical processes that underlie normal brain function and their alterations in disease.

6.2 Future Directions

The future directions from the work of this dissertation are to some extent unlimited. However, there are a few promising studies that are already in progress or near initiation in our laboratory that should be noted. These include the application sMRI to LGG biopsy targeting, the development of spectral quality analysis models for filtering poor spectra before volumetry, and the validation of automated metabolic segmentations for RT planning.

6.2.1 sMRI for Lower Grade Glioma Targeting

In cases where resection is not indicated, needle biopsy is chosen to confirm diagnosis in suspected glioma. Though biopsy guidance for contrast-enhancing tumors relies on CE-T1w, the guidance for nonenhancing gliomas (100% of grade II and 40% of grade III) relies on T2w/FLAIR images. For correct glioma grading, the biopsy should be obtained from the most anaplastic portion of the tumor; however, this is often difficult to determine using anatomic T2w/FLAIR (**Figure 6.1,** *left-most panel*) due to the considerable intratumoral heterogeneity seen in nonenhancing gliomas (350; 351). Kondziolka et al. found that the combination of T1w, T2w, and CT could not reliably predict histological diagnosis of LGG versus HGG, exhibiting a 50% false-positive rate (125). Additionally, Scott et al. reported that approximately one third of nonenhancing gliomas exhibit highly malignant (grade III) foci (124). The inability to identify the highest grade regions of the tumor could result in its under grading and ultimately cause under treatment. Thus, the field of neuro-oncology is in dire need of an imaging modality that can accurately describe the heterogeneous nature of nonenhancing tumors, and can direct biopsy to the most malignant component of the glioma.

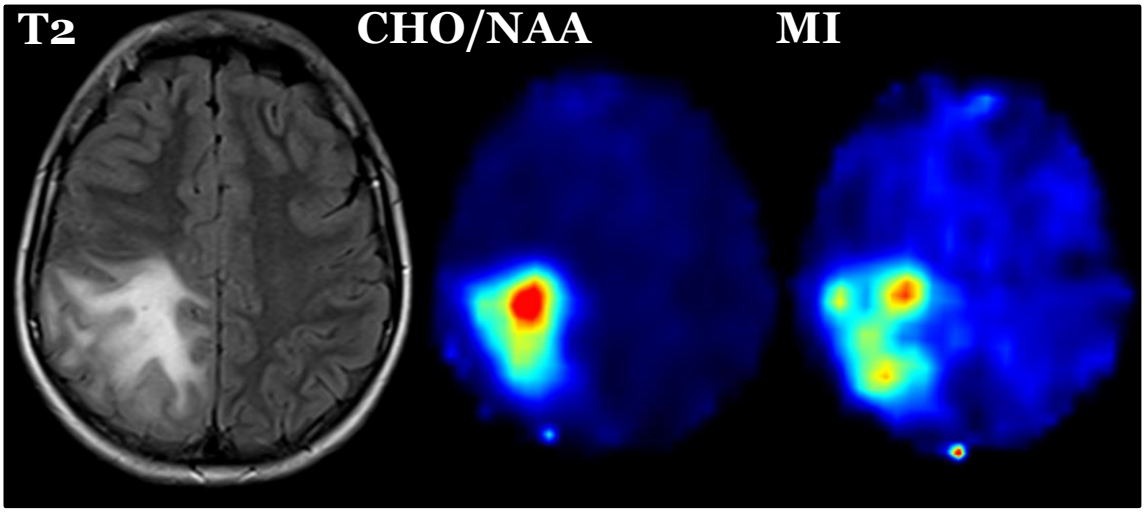

Figure 6.1. Spectroscopic MRI in LGG. T2w/FLAIR, Cho/NAA, and MI images for patient with IDH mutant, 1p19q intact, WHO grade II glioma. Note the punctate elevations in MI relative to the uniform elevation of Cho/NAA.

As sMRI-based metabolite metrics describe significant metabolic heterogeneity in HGG and we have shown that sMRI metrics correlate with infiltration in GBM, we hypothesize that sMRI metrics will correlate with infiltration in LGG and that sMRI is a viable imaging modality biopsy direction in nonenhancing lesions. To do this, we would propose a small clinical trial of approximately 20 patients for which we would obtain whole-brain sMRI before the biopsy of their suspected nonenhancing glioma (presumed grade II or III). In addition to NAA, Cho, CR and their derivatives, we would also quantify MI as it has been shown in a few studies to be associated with LGG (**Figure 6.1**) (209; 352; 353). Then, in a procedure similar to that outlined in **Chapter 3,** we would sample tissue from metabolically abnormal regions using a biopsy needle (2-4 per patient) and conduct neuropathological assessment on these specimens. Neuropathological assessment would include the evaluation of MGMT, 1p19q, EGFR, and PTEN as well as immunohistochemistry for SOX2, IDH, and MIB1 (a nuclear marker of proliferation). Histological grade and cellular features would then be correlated with metabolite metrics and used as a gold standard for an ROC analysis evaluating the sensitivity, specificity, positive predictive value (PPV), and negative predictive value (NPV) of sMRI for differentiating WHO grade II and III gliomas. Once validated, this histology and sMRI sequence/processing protocol could be easily disseminated to other institutions for a larger, multi-center clinical trial.

6.2.2 Automated Spectral Quality Analysis

The fitting of spectroscopic data works best when spectral quality is good (e.g. spectral resolution and SNR are high). However, spectral quality is based on the physical characteristics of the tissue examined, some of which can change during the treatment and natural course of glioma. For example, magnetic susceptibility changes at tissue interfaces, oftentimes resulting in uninterpretable spectra. This is of significant consequence in glioma imaging, as one of the greatest sources of susceptibility artifact –the cavity-tissue interface caused by surgical resection –is also a region of great importance in glioma response assessment. Due to the variance in spectral quality at this interface, automated spectral processing may produce inaccurate curve fits resulting in erroneous signal abnormalities in image volumes (**Figure 6.2**). To prevent poor data from generating misleading volumes and potentially affecting clinical decision making, a tool for quantifying and automatically classifying spectral quality is necessary. As such, we have begun to develop an automated method for determining spectral quality based on curve-fitting metrics using machine-learning methods to create a data-driven model for spectral filtering.

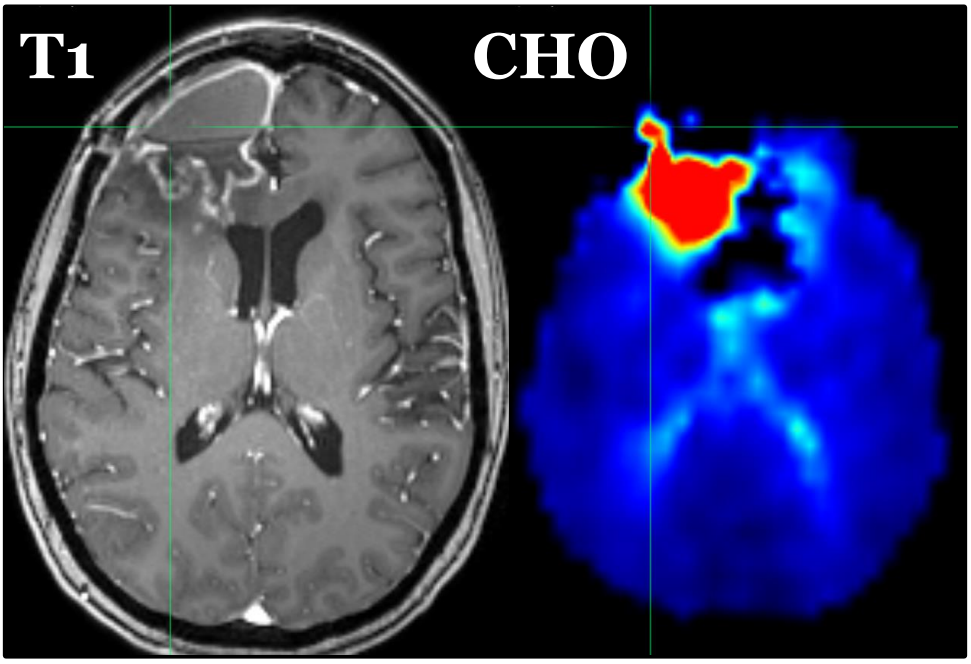

Figure 6.2. Example of sMRI artifact. Magnetic susceptibility variations in the head distort spectral line shape sometimes resulting in erroneous volumetry. In this case, susceptibility changes at the edge of a resection cavity results in a spectral artifact suggesting a pronounced increase in Cho.

As no consensus for spectral quality is available, one must be built using an automated system that allows an individual or group of individuals to review and grade numerous spectra. To do this, we have developed a web-based spectral evaluation platform that is distributable to a number of MR spectroscopy experts around the world to generate training data for building a spectral quality filter that best represents “ground truth”. In an initial single-reviewer pilot study, this tool was used to visually review and label each of 6243 spectra from 7 separate patients as having adequate (A) or inadequate (I) spectral quality. sMRI curve-fitting parameters describing 115 characteristics from each spectrum were used as features to train random forest classifiers. Classifiers were trained on the following scenarios: 1) A vs I in tumor & normal voxels; 2) A vs I in tumor voxels only; and 3) A vs I in normal voxels only. Strict cross-validation was performed to evaluate generalizability, training each classifier on six patients and evaluating on the seventh in a rotating, leave-one-out manner. Classifiers were also trained to discriminate between tumor and normal tissue in 1) voxels with adequate SQ and 2) voxels with inadequate SQ. Classifier performance was evaluated using receiver operator characteristic (ROC) analysis to determine area-under-the-curve (AUC), and feature salience was evaluated by summing the split criterion for each variable over all trees in each forest of the classifier.

In this pilot study, AUC values for classifying signal quality and tumor (in A voxels) were rather high, 0.94 and 0.79, respectively. The most salient features for signal quality included the Cramer-Rao bounds of the NAA peak, a metric often used by spectroscopists to evaluate quality, and the Cramer-Rao bounds for Cho and CR peak frequencies. Not surprisingly, the most salient features for

differentiation of normal and tumor tissue included Cho/NAA, Cho/CR, and NAA/CR: ratios used for tumor evaluation clinically. The high AUCs for tumor classification suggest training machine-learning algorithms with curve-fit metrics may result in accurate spectral quality and metabolic abnormality classifiers.

These classification data sparked our interest and triggered a larger, multi-reviewer experiment which is currently underway. Physicist and clinicians throughout the United States and Great Britain with MRS expertise are grading spectra to be compiled as training set for a convolutional neural network. We anticipate that developing a classifier based on the consensus of several expertly-trained reviewers will result in a more generalizable, and widely accepted model of spectral quality. Such a model could be integrated seamlessly as an additional module to the existing spectroscopic processing pipeline, and would hopefully limit the number of artifacts present in the resulting volumetric maps. A decrease in artifact would likely eliminate the ambiguity that is sometimes present when determining RT target volumes, and would hopefully give physicians more confidence in evaluating metabolic abnormalities with sMRI.

6.2.3 RT Target Volume Segmentation and Automatic Metabolic Profiling

Our group has also been working to develop an automated segmentation algorithm for defining sMRI abnormalities that could be used for RT target planning. The pipeline that is currently being developed considers metabolic data from sMRI maps alongside anatomical abnormalities derived from standard T2w/FLAIR images. The pipeline begins by skull stripping the T2w/FLAIR image using the water reference map from the EPSI acquisition. Next, an initial tumor

region, or blob, is identified by searching for regions that exhibit both T2w/FLAIR hyperintensities and reduced NAA signal using a mean ratio correlation method and morphological filters. These regions are then used as a starting point for a geodesic level-set refinement that adapts the initial blob to the fine details specific to each metabolite (354). The result of this process is a set of spatially-coherent, objectively-delineated ROIs describing a number of metabolic abnormalities that can be viewed in parallel with conventional MRI (**Figure 6.3**). Moreover, these ROIs are formatted such that they can be imported in the treatment planning system to specifically increase the RT target volumes to encompass metabolically abnormal tissue outside of standard CE-MRI.

In a pilot study, this automatic pipeline successfully generated ROIs describing NAA, Cho, and CR abnormalities in 12 patients with pre, mid, and postRT sMRI scans. Upon visual inspection, the ROIs approximated the metabolic abnormalities with little error. A study is soon to be underway to quantitatively compare the manual segmentation of metabolic abnormalities in patients with GBM with those ROIs generated by this algorithm (using a procedure similar to that found in **Chapter 2**), and to evaluate the feasibility of adding these ROIs with full margins to RT planning in terms of coverage and dose constraints (using a procedure similar to that found in Chapter 5). The further development and validation of such an sMRI segmentation technique would not only make the integration of sMRI metabolite maps into RT planning easier, but may also potentially streamline the acceptance of this metabolic imaging modality into clinical practice.

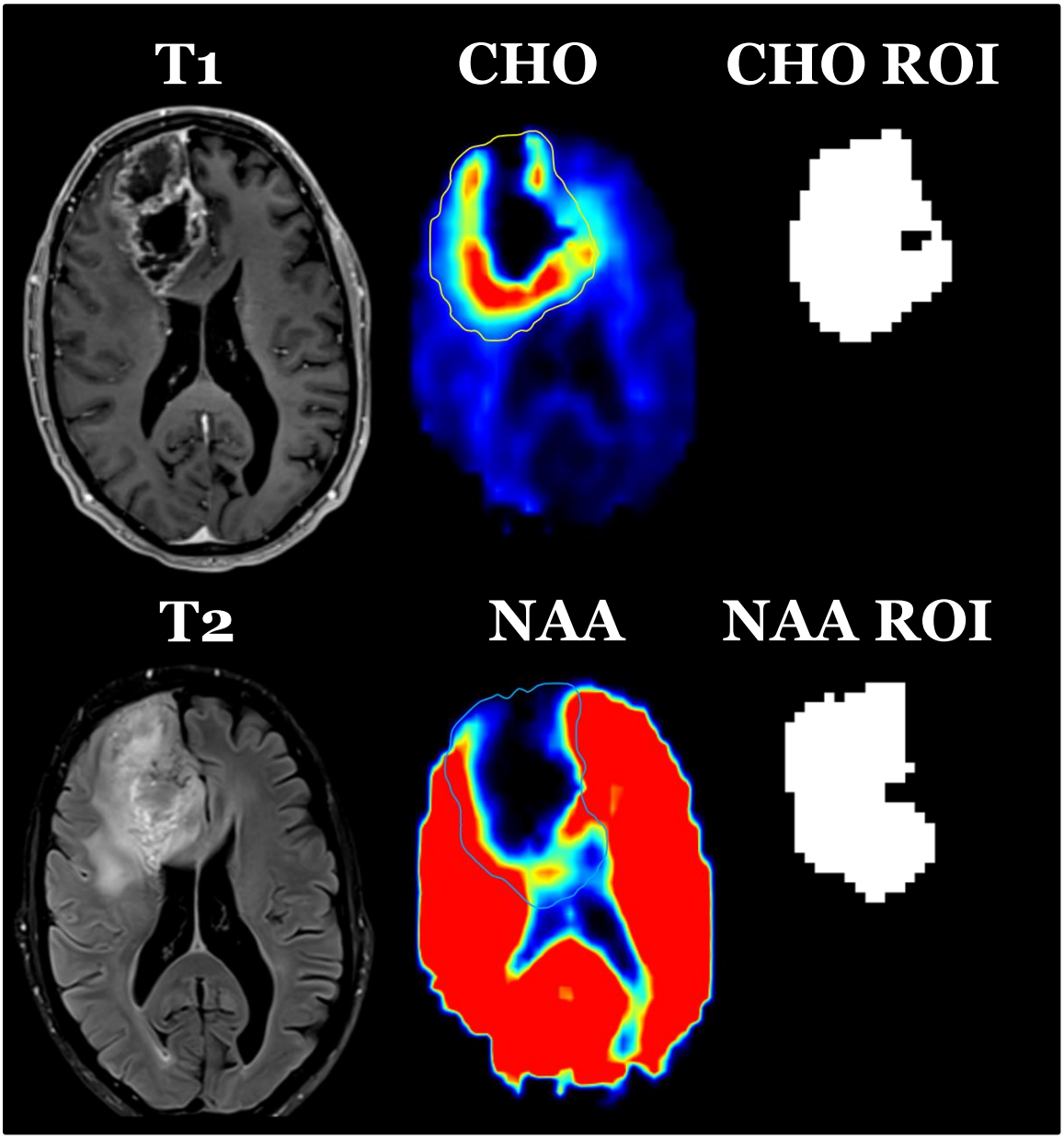

Figure 6.3. Automatic metabolic ROI segmentation for RT target volume planning. Color contours overlaid onto the Cho and NAA maps describe the distribution of the automatically segmented ROIs in sMRI space.

6.4 References

1. Stummer W, Pichlmeier U, Meinel T, Wiestler OD, Zanella F, Reulen HJ. 2006. Fluorescence-guided surgery with 5-aminolevulinic acid for resection of malignant glioma: a randomised controlled multicentre phase III trial. *Lancet Oncology* 7:392-401
2. Stummer W, Tonn JC, Mehdorn HM, Nestler U, Franz K, et al. 2011. Counterbalancing risks and gains from extended resections in malignant glioma surgery: a supplemental analysis from the randomized 5-aminolevulinic acid glioma resection study. Clinical article. *Journal of neurosurgery* 114:613-23
3. Stummer W, Reulen HJ, Meinel T, Pichlmeier U, Schumacher W, et al. 2008. Extent of resection and survival in glioblastoma multiforme: identification of and adjustment for bias. *Neurosurgery* 62:564-76; discussion -76
4. Stummer W, Meinel T, Ewelt C, Martus P, Jakobs O, et al. 2012. Prospective cohort study of radiotherapy with concomitant and adjuvant temozolomide chemotherapy for glioblastoma patients with no or minimal residual enhancing tumor load after surgery. *J Neurooncol* 108:89-97
5. Rios Velazquez E, Meier R, Dunn WD, Jr., Alexander B, Wiest R, et al. 2015. Fully automatic GBM segmentation in the TCGA-GBM dataset: Prognosis and correlation with VASARI features. *Sci Rep* 5
6. Yang D, Rao G, Martinez J, Veeraraghavan A, Rao A. 2015. Evaluation of tumor-derived MRI-texture features for discrimination of molecular

subtypes and prediction of 12-month survival status in glioblastoma. *Med Phys* 42:6725-35

7. Croteau D, Scarpace L, Hearshen D, Gutierrez J, Fisher JL, et al. 2001. Correlation between magnetic resonance spectroscopy imaging and image-guided biopsies: semiquantitative and qualitative histopathological analyses of patients with untreated glioma. *Neurosurgery* 49:823-9
8. Matsumura A, Isobe T, Anno I, Takano S, Kawamura H. 2005. Correlation between choline and MIB-1 index in human gliomas. A quantitative in proton MR spectroscopy study. *Journal of clinical neuroscience : official journal of the Neurosurgical Society of Australasia* 12:416-20
9. Nafe R, Herminghaus S, Raab P, Wagner S, Pilatus U, et al. 2003. Preoperative proton-MR spectroscopy of gliomas--correlation with quantitative nuclear morphology in surgical specimen. *J Neurooncol* 63:233-45
10. Stadlbauer A, Buchfelder M, Doelken MT, Hammen T, Ganslandt O. 2011. Magnetic resonance spectroscopic imaging for visualization of the infiltration zone of glioma. *Cent Eur Neurosurg* 72:63-9
11. Stadlbauer A, Nimsky C, Buslei R, Pinker K, Gruber S, et al. 2007. Proton magnetic resonance spectroscopic imaging in the border zone of gliomas: correlation of metabolic and histological changes at low tumor infiltration--initial results. *Investigative radiology* 42:218-23
12. Zetterling M, Roodakker KR, Berntsson SG, Edqvist PH, Latini F, et al. 2016. Extension of diffuse low-grade gliomas beyond radiological borders

as shown by the coregistration of histopathological and magnetic resonance imaging data. *Journal of neurosurgery* 26:1-12

13. Warram JM, de Boer E, Korb M, Hartman Y, Kovar J, et al. 2015. Fluorescence-guided resection of experimental malignant glioma using cetuximab-IRDye 800CW. *Br J Neurosurg* 29:850-8
14. Ken S, Vieillevigne L, Franceries X, Simon L, Supper C, et al. 2013. Integration method of 3D MR spectroscopy into treatment planning system for glioblastoma IMRT dose painting with integrated simultaneous boost. *Radiat Oncol* 8:8-1
15. Chan AA, Lau A, Pirzkall A, Chang SM, Verhey LJ, et al. 2004. Proton magnetic resonance spectroscopy imaging in the evaluation of patients undergoing gamma knife surgery for Grade IV glioma. *Journal of neurosurgery* 101:467-75
16. Park I, Tamai G, Lee MC, Chuang CF, Chang SM, et al. 2007. Patterns of recurrence analysis in newly diagnosed glioblastoma multiforme after three-dimensional conformal radiation therapy with respect to pre-radiation therapy magnetic resonance spectroscopic findings. *International journal of radiation oncology, biology, physics* 69:381-9
17. Ozturk-Isik E, Pirzkall A, Lamborn KR, Cha S, Chang SM, Nelson SJ. 2012. Spatial characteristics of newly diagnosed grade 3 glioma assessed by magnetic resonance metabolic and diffusion tensor imaging. *Transl Oncol* 5:10-8
18. Parra NA, Maudsley AA, Gupta RK, Ishkanian F, Huang K, et al. 2014. Volumetric spectroscopic imaging of glioblastoma multiforme radiation

treatment volumes. *International journal of radiation oncology, biology, physics* 90:376-84

19. Ken S, Vieillevigne L, Franceries X, Simon L, Supper C, et al. 2013. Integration method of 3D MR spectroscopy into treatment planning system for glioblastoma IMRT dose painting with integrated simultaneous boost. *Radiat Oncol* 8:1
20. Mizumoto M, Yamamoto T, Takano S, Ishikawa E, Matsumura A, et al. 2015. Long-term survival after treatment of glioblastoma multiforme with hyperfractionated concomitant boost proton beam therapy. *Pract Radiat Oncol* 5:19
21. Henson JW, Gaviani P, Gonzalez RG. 2005. MRI in treatment of adult gliomas. *Lancet Oncology* 6:167-75
22. Jacobs AH, Kracht LW, Gossmann A, Ruger MA, Thomas AV, et al. 2005. Imaging in neurooncology. *NeuroRx* 2:333-47
23. Kondziolka D, Lunsford LD, Martinez AJ. 1993. Unreliability of contemporary neurodiagnostic imaging in evaluating suspected adult supratentorial (low-grade) astrocytoma. *Journal of neurosurgery* 79:533-6
24. Scott JN, Brasher PM, Sevick RJ, Rewcastle NB, Forsyth PA. 2002. How often are nonenhancing supratentorial gliomas malignant? A population study. *Neurology* 59:947-9
25. Castillo M, Smith JK, Kwock L. 2000. Correlation of myo-inositol levels and grading of cerebral astrocytomas. *AJNR. American journal of neuroradiology* 21:1645-9

26. Howe FA, Barton SJ, Cudlip SA, Stubbs M, Saunders DE, et al. 2003. Metabolic profiles of human brain tumors using quantitative in vivo 1H magnetic resonance spectroscopy. *Magnetic resonance in medicine : official journal of the Society of Magnetic Resonance in Medicine / Society of Magnetic Resonance in Medicine* 49:223-32

27. Hattingen E, Raab P, Franz K, Zanella FE, Lanfermann H, Pilatus U. 2008. Myo-inositol: a marker of reactive astrogliosis in glial tumors? *NMR in biomedicine* 21:233-41

28. Paragios N, Deriche R. Geodesic Active Regions and Level Set Methods for Supervised Texture Segmentation. *International Journal of Computer Vision* 46:223-47

Chapter 7

Some Final Thoughts

While the whole of this work will be read as scholarly text and is most easily characterized as molecular imaging, this was not my intention, in its entirety, from the outset. As a young man having been privileged with a great many opportunities --many that others are often denied --I feel it my duty to take on a work in great need. Similar to a Bible verse my grandmother recited religiously about love (John 13:33-34), I feel I have been charged to "give unto others as [I] have been given". And as I have been given very much, I am expected to give very much. Thus I am convicted by the skills and resources that have been afforded me during my lifetime to forward a cause that is both meaningful and formidable. In this work, the cause that I found was the treatment and overall care of patients with GBM.

I see those with this dreaded illness as swimmers battling an unforgiving undertow. Though they stride just as valiantly as others in more manageable

waters, they rarely escape and are invariably pulled under by the tide. No matter weak or strong, poor or rich, old or young (sadly, some even younger than myself), they break themselves against the rolling waves as their rescuers scramble to steal them from a certain doom. Unfortunately for those in these most treacherous waters, their rescuers, the men and women who have pledged their time and energy to the care of their fellow man, have their hands roped behind their backs. Such is the plight of patients with GBM--try as they may, they throw themselves against a seemingly impenetrable obstacle, a foe which they cannot overcome alone. All the while, their physicians, those with the skills needed to help them, those who stand at-the-ready in their service, must watch on woefully, unable to reach out to them.

At the conclusion of this text, after a great deal of assessing methods and scrutinizing results, I would like to leave with you a final vision of this work--my vision. In part, this work describes small, technical developments in the integration and use of imaging technologies in GBM management, though as a whole, it describes one young man's meager, yet ardent attempt to advance the care for a population that many have given up on. Not only do I hope that each chapter explicitly describes a problem, a potential solution, and an attempted resolution, but also that each gives some measure of comfort to those feeling helpless in the shadow of this grave illness. Were each chapter to be just the refining of a known technique, like the honing of steel to an edge, I hope the whole is seen as a blade, small but sharp. To me, the work described herein is more than just a log of my efforts over my time in training. To me, this is also a tool. To me, this is an attempt

at loosing the spectators at the water's edge, providing them the means they need to reach those souls enduring the waves.

I would like to end with one final remark: it has been the greatest privilege of my life so far to work with and study the awe-inspiring population that suffers from this grave disease. The hope that they have in the face of such a daunting adversary is astonishing, and their willingness to support the advancement of therapy for GBM, which they know will likely not benefit them, is altruism at its finest. Even in the shadow of their own demise, these amazing people wish to offer hope to those unfortunate souls who follow and subject themselves to scan after whirling scan in the spirit of giving and kindness. It is with these amazing, benevolent individuals that my final thoughts lie. For without their efforts and sacrifices, not only would the outcomes of this work have been trivial, but also the advancement of imaging in the service of GBM patients of the future would be impossible.